University of Alberta

Development and Applications of an Electrospray Ionization Ion Trap/Linear Time-of-Flight Mass Spectrometer

by

Wojciech Gabryelski

A thesis submitted to the Faculty of Graduate Studies and Research in partial fulfillment of the requirements for the degree of Doctor of Philosophy

Department of Chemistry

Edmonton, Alberta

Fall 2000

National Library of Canada
Acquisitions and Bibliographic Services
395 Wellington Street
Ottawa ON K1A 0N4
Canada

Bibliothèque nationale du Canada
Acquisitions et services bibliographiques
395, rue Wellington
Ottawa ON K1A 0N4
Canada

Your file Votre référence

Our file Notre référence

The author has granted a non-exclusive licence allowing the National Library of Canada to reproduce, loan, distribute or sell copies of this thesis in microform, paper or electronic formats.

L'auteur a accordé une licence non exclusive permettant à la Bibliothèque nationale du Canada de reproduire, prêter, distribuer ou vendre des copies de cette thèse sous la forme de microfiche/film, de reproduction sur papier ou sur format électronique.

The author retains ownership of the copyright in this thesis. Neither the thesis nor substantial extracts from it may be printed or otherwise reproduced without the author's permission.

L'auteur conserve la propriété du droit d'auteur qui protège cette thèse. Ni la thèse ni des extraits substantiels de celle-ci ne doivent être imprimés ou autrement reproduits sans son autorisation.

0-612-59588-9

Canada

University of Alberta

Library Release Form

Name of Author: Wojciech Gabryelski

Title of Thesis: Development and Applications of an Electrospray Ionization Ion Trap/Linear Time-of-Flight Mass Spectrometer

Degree: Doctor of Philosophy

Year this Degree Granted: 2000

Permission is hereby granted to the University of Alberta Library to reproduce single copies of this thesis and to lend or sell such copies for private, scholarly, or scientific research purposes only.

The author reserves all other publication and other rights in association with the copyright in the thesis, and except as hereinbefore provided, neither the thesis nor any substantial portion thereof may be printed or otherwise reproduced in any material form whatever without the author's prior written permission.

Wojciech Gabryelski

#218, 10511-92 Street
Edmonton, AB.
T5H 4E6

29, May, 2000

University of Alberta

Faculty of Graduate Studies and Research

The undersigned certify that they have read, and recommend to the Faculty of Graduate Studies and Research for acceptance, a thesis entitled "Development and Applications of an Electrospray Ionization Ion Trap/Linear Time-of-Flight Mass Spectrometer" submitted by Wojciech Gabryelski in partial fulfillment of the requirements for the degree of Doctor of Philosophy.

Dr. L. Li, Professor of Chemistry

Dr. C. A. Lucy, Professor of Chemistry

Dr. M. T. McDermott, Assistant Professor of Chemistry

Dr. M. Palcic, Professor of Chemistry

Dr. L. McMullen, Assistant Professor of Agricultural, Food and Nutritional Science

Dr. K. W. M. Siu, Professor of Chemistry

May 14, 2000

Abstract

The work presented in this thesis involves the development and application of an electrospray ionization ion trap/time-of-flight mass spectrometer (ESI IT/TOFMS). The instrument combines the most universal ionization technique with the tandem mass spectrometry capability of an ion trap and rapid and sensitive detection provided by a time-of-flight detector.

Capabilities and limitations of this mass analyzer used for quantification of sulfonamides are presented. Compared to the performance of a single quadrupole mass spectrometer, the ESI IT/TOFMS is superior in analyses of multicomponent samples and applications requiring high rates of data acquisition. The instrument was also evaluated as a detector for identification of phenylthiohydantoin (PTH)-amino acids, the final products in the Edman sequencing of proteins. Detectability of PTH-amino acids in ESI IT/TOFMS is at least 10 times better than in commonly used liquid chromatography with UV-detection.

Implementation of tandem mass spectrometry (MS/MS) methods (e.g., source fragmentation, collision-induced dissociation (CID), and photo-induced dissociation (PID)) on the ESI IT/TOFMS is described. These techniques have been used to solve a number of challenging problems in structural analysis. Results from an in-depth investigation of the fragmentation pathways of PTH-amino acids have significance in understanding the fundamentals of ion chemistry and can be utilized for identification of nonstandard PTH-amino acids and differentiation of PTH-amino acid isomers.

A new method used to obtain unambiguous structural identification of polymer end groups is presented. This method, applied to the end-group analysis of two slow-releasing drugs, could become an essential part of a polymer characterization program.

The requirement for and limitation of MS/MS methods used in sequential analysis of biopolymers such as peptides, proteins, saccharides are evaluated and illustrated with examples. Time-resolved detection is used to characterize dissociation processes inside the

ion trap in submillisecond time frame. This unique technique allowed for the first time to monitor time-resolved laser-induced dissociation of a protein inside the ion trap. The application of this method for dissociation kinetics of different conformers of cytochrome c and differentiation of disaccharide anomers is presented.

for Beata and Pawel

Acknowledgments

I would like thank my supervisor Dr. Liang Li for his advice, support and enthusiasm during the course of my research. I also thank all members of Dr. Li's research group with whom I have worked with. In particular, I wish to thank Dr. R. W. Purves for his assistance in the early stage of my research and Dr. T. Yalcin for his significant contributions to work presented in Chapters 4 and 5. The support of the machine and electronic shops have been instrumental in my work. I especially thank Mr. L. Coulson for his assistance in the development of the instrument.

I would also like to acknowledge NSERC and the University of Alberta for providing me with graduate scholarships. Also, I have appreciated the additional financial support of the Chemistry Department throughout the duration of my program.

Table of Contents

Chapter 1 1

Introduction: Electrospray Ionization Ion Trap/Time-of-Flight Mass Spectrometry 1

1.1 Soft ionization techniques 1

1.2 Electrospray ionization 3

1.2.1 The quantitative aspect of electrospray 5

1.2.2 Applications of electrospray ionization 7

1.3 Quadrupole ion trap 8

1.3.1 Operational principles of the ion trap 8

1.3.2 Resonant excitation 12

1.3.3 Ion trap with stretched geometry 13

1.4 Interfacing electrospray ionization to the quadrupole ion trap 14

1.5 Mass analysis using the quadrupole ion trap 17

1.5.1 Detection principles for IT-linear TOFMS 19

1.6 An Electrospray Ionization Ion Trap/linear Time-of-Flight Mass Spectrometer 22

1.7 Literature cited 24

Chapter 2 28

Investigation of the Quantitative Capabilities of an Electrospray Ionization Ion Trap/Linear Time-of-flight Mass Spectrometer 28

2.1 Introduction 28

2.2 Experimental 30

2.2.1 Instrumentation 30

2.2.2 Sulfonamides and chemicals 32

2.3 Results and Discussion 33

2.3.1 Solution properties..... 33
2.3.2 Detection limits and linear range..... 35
2.3.3 Reproducibility..... 39
2.3.4 Multicomponents analyses..... 41
2.3.5 Detectability of ion trap/TOFMs versus quadrupole MS..... 48
2.4 Summary..... 49
2.5 Literature cited..... 49

Chapter 3..... 52
Characterization of an an Electrospray Ionization Ion Trap/Linear Time-of-flight Mass Spectrometer for Phenylthiohydantoin (PTH)-Amino Acid Analysis..... 52
3.1 Introduction..... 52
3.2 Experimental..... 54
3.2.1 ESI IT/TOFMS Instrument..... 54
3.2.2 Electrospray ionization source..... 56
3.2.3 Chemicals and sample preparation..... 57
3.3 Results and Discussion..... 57
3.3.1 Soft ionization of PTH-amino acids..... 57
3.3.2 Differentiation of PTH-Leu and PTH-Ile..... 59
3.3.3 Fragmentation patterns of PTH-amino acids..... 63
3.3.4 Detection of non-standard PTH-amino acids..... 66
3.3.5 Isobaric interferences in mixture analysis..... 68
3.3.6 Detectability of PTH-amino acids..... 68
3.3.7 Chemical background..... 73
3.4 Comparison with other studies..... 74
3.5 Summary..... 80
3.6 Literature cited..... 81

Chapter 4..... 84

Dissociation of Protonated Phenylthiohydantoin-Amino Acids

and Phenylthiocarbamoyl-Dipeptides..... 84

4.1 Introduction..... 84

4.2 Experimental..... 85

4.2.1 High-energy CID experiments..... 85

4.2.2 Low-energy CID experiments..... 86

4.2.3 Chemicals..... 86

4.3 Results and Discussion..... 87

4.4 Summary..... 99

4.5 Literature cited..... 102

Chapter 5..... 104

Structural Analysis of Polymer End Groups by ESI MS/MS..... 104

5.1 Introduction..... 104

5.2 Experimental..... 106

5.2.1 High-energy CID experiments with source fragmentation..... 106

5.2.2 Polymers and chemicals..... 106

5.3 Results and Discussion..... 107

5.3.1 Poly(oxyethylene) bis(ephedrine)..... 107

5.3.2 Poly(oxyethylene) bis(acetaminophen)..... 111

5.3.3 Other considerations..... 114

5.3.4 The origin of the fragment ions in CID spectra of the polymers.... 115

5.3.5 Ion stability diagrams in source fragmentation..... 116

5.3.6 ESI IT/TOFMS in end group determination of polymers..... 118

5.4 Summary..... 122

5.5 Literature cited..... 124

Chapter 6..... 127

Photo-Induced Dissociation of Electrospray Generated Ions in an Ion Trap/Time-of-Flight Mass Spectrometer using a Nd:YAG Laser..... 127

6.1 Introduction..... 127

6.2 Experimenal..... 129

6.2.1 Modifications of the instrument..... 129

6.2.2 Excitation experiments..... 132

6.2.3 Chemicals and electrospray conditions..... 135

6.3 Results and Discussion..... 135

6.3.1 Selectivity of PID at 266-nm wavelength..... 135

6.3.2 PID of peptides..... 136

6.3.2.1 The effect of multiple laser pulses on PID spectra..... 137

6.3.2.2 The effect of the laser power on PID spectra..... 136

6.3.2.3 The effect of the ion trap buffer gas pressure on PID spectra.. 139

6.3.2.4 PID of oxytocin..... 144

6.3.3 Time-dependent detection in PID..... 145

6.4 Summary..... 149

6.5 Literature cited..... 149

Chapter 7..... 150

Photo-Induced Dissociation of Electrospray Generated Ions in an Ion Trap/Time-of-Flight Mass Spectrometer using a Pulsed CO_2 Laser..... 151

7.1 Introduction..... 151

7.2 Experimental..... 153

7.2.1 IRMPD and time-resolved CID experiments..... 153

7.2.2 Chemicals and electrospray conditions..... 156

7.3 Results and Discussion..... 156

7.3.1 IRMPD of peptides..... 156
7.3.2 IRMPD of equine cytochrome c..... 159
7.3.3 IRMPD of PTH-isoleucine..... 168
7.3.4 Time-resolved CID of PTH-isoleucine..... 174
7.3.5 Analysis of disaccharide isomers by IRMPD and CID..... 178
7.4 Summary..... 186
7.5 Literature cited..... 188

Chapter 8..... 190
Conclusions and Future Work..... 190

Appendix A..... 194
Fragmentation of peptide ions..... 194

List of Tables and Charts

Table 2.1 Detection limits for 5 sulfonamides examined in this study.....36

Table 3.1 Source fragmentation products of PTH-amino acids in ESI IT/TOFMS...60

Table 3.2 Detectability of PTH-amino acids in ESI IT/TOFMS.....73

Chart 2.1 Structure of the five sulfonamides used in this study.....32

Chart 5.1 Structures of the polymers used in this study.....107

List of Figures

Figure 1.1. Schematic of electrospray ionization process.....4

Figure 1.2. The quadrupole ion trap. (A) A cross-sectional view of the quadrupole ion trap. (B) A part of the a_z versus q_z stability diagram.....9

Figure 1.3. A schematic diagram of TOF mass analysis for ions stored in the quadrupole ion trap.....19

Figure 1.4. Schematic of electrospray ionization ion trap/linear time-of-flight mass spectrometer. Drawing is not to scale.....22

Figure 2.1. Effect of different concentrations of ammonium acetate on the mass spectra of 1 μM SDM in 80% acetonitrile/20% water. (A) No ammonium acetate added, (B) 0.5 mM ammonium acetate, (C) 2 mM ammonium acetate and (D) 10 mM ammonium acetate.....34

Figure 2.2. Mass spectrum obtained from an injection of a mixture of SDM, SCP, SMZ, SMR, and STZ. The mixture contained 100 fmol of each sulfonamide.....35

Figure 2.3. Calibration curve for a series of loop injections of SDM with an expanded view of the low end of the plot shown in the inset.....37

Figure 2.4. Mass spectrum of an injection of 5 fmol of SDM showing the limitations due to the chemical background noise using an electrospray ionization ion trap/linear TOFMS. 25 ion extraction events were summed to obtain this mass spectrum.....38

Figure 2.5. Comparison of calibration curves of SDM using ion trap/linear TOFMS and quadrupole MS. Linearity at the low end is shown in the inset. The lines connect the points representing the average of 7 measurements.....40

Figure 2.6. Reproducibility of the electrospray ionization ion trap TOFMS illustrated using repeat injections of SDM at 10 fmol, 100 fmol, and 1 pmol.....41

Figure 2.7. Repeat injections of SDM over an eight hour period. (A) A peak area of SDM as a detector response. (B) A ratio of peak areas (SDM/SMZ) as a detector response (SMZ used as an internal standard).....42

Figure 2.8. Calibration curves for a multicomponent analysis using ion trap/linear TOFMS. (A) The entire calibration range. (B) The linear range at the low end of the calibration curve. The lines connect the points representing the average of 3 measurements.....44

Figure 2.9. Calibration curves for a multicomponent analysis using quadrupole MS. (A) The entire calibration range. (B) The linear range at the low end of the calibration curve. The lines connect the points representing the average of 3 measurements.....45

Figure 2.10. Signal correlation for a multicomponent analysis using ion trap/linear TOFMS. (A) The entire calibration range. (B) The linear region.....46

Figure 3.1. Phenylthiohydantoin (PTH)-amino acid. R is the side chain of an amino acid.....52

Figure 3.2. Schematic of the two-stage electrospray interface of the ESI IT/TOFMS instrument. Drawing is not to scale.....55

Figure 3.3. Molecular ion regions of mass spectra of PTH-amino acids. (A) PTH-alanine, (B) PTH-glutamic acid, (C) PTH-(PTC-lysine), and (D) PTH-(PTC-cysteine). 5 μM sample solutions in 80% acetonitrile/20% 0.25 mM ammonium acetate in water (v/v) were analyzed at V_{CID}=25 V.....58

Figure 3.4. Mass spectra of PTH-leucine (A), (B), (C) and PTH-isoleucine (D), (E), (F) at different source voltages. (A) and (D) V_{CID} = 25 V, (B) and (E) V_{CID} = 35 V, (C) and (F) V_{CID} = 45 V.....61

Figure 3.5. Mass spectra of two isomeric non-standard PTH-amino acids obtained at V_{CID} = 45 V. (A) PTH-α-aminoisobutyric acid and (B) PTH-α-aminobutyric acid.....67

Figure 3.6. Mass spectra of a mixture of PTH-S(serine), PTH-T(threonine), PTH-Y(tyrosine) and PTH-W(tryptophan) obtained at different source voltages: (A) V_{CID} = 25 V and (B) V_{CID} = 28 V. MH^+ represents the protonated molecule and MNa^+ represents the sodium adduct. M is the single letter code of an amino acid.....69

Figure 3.7. Mass spectra of a mixture of PTH-I(isoleucine) and PTH-H(histidine) obtained at (A) V_{CID} = 25 V and (B) V_{CID} = 45 V. MH^+ represents the protonated molecule and M is the single letter code of an amino acid.....70

Figure 3.8. Signal intensities of PTH-amino acids obtained from an injection of 500 femtomoles of each compound in a flow injection experiment. One letter abbreviation represents the corresponding PTH-amino acid.....71

Figure 3.9. Mass spectrum of the mixture containing PTH-P(Proline), PTH-L(Leucine) and PTH-F(Phenylalanine) at 50 fmol/μL obtained by using continuous sample introduction. The sample was delivered at 1 μL/min in the buffer-solvent (80% acetonitrile and 20% 0.25 mM ammonium acetate in water by volume). The spectrum was acquired by summing 100 scans for a period of 25 seconds and smoothed using a 15-point Savitzky-Golay algorithm.....76

Figure 3.10. Ion trap CID spectra of PTH-isoleucine obtained in IT/TOFMS. (A) Spectrum obtained at q_z = 0.149 and V_{P-P} = 920 V. (B) Spectrum obtained at q_z = 0.210 and V_{P-P} = 1300 V.....79

Figure 4.1. Low-energy CID mass spectra of the m/z 237 ion derived from (A) PTH-Thr-Leu and (B) PTH-Thr.....88

Figure 4.2. High-energy CID mass spectra of the protonated PTH-amino acids: (A) PTH-Thr, (B) PTH-Ser, (C) PTH-Trp, and (D) PTH-Tyr.....89

Figure 4.3. High-energy CID mass spectra of the thiazalone ions derived from (A) PTC-Thr-Leu, (B) PTC-Ser-Leu, (C) PTC-Trp-Leu, and (D) PTC-Tyr-Leu.....91

Figure 4.4. High-energy CID mass spectra of the m/z 193 ions derived from (A) PTH-Thr, (B) PTH-Ser, (C) PTH-Trp, and (D) PTH-Tyr.....92

Figure 4.5. High-energy CID mass spectra of the m/z 193 ion derived from PTH-Gly.....93

Figure 4.6. Structures of neutral species eliminated from the side chains of X during the formation of the m/z 193 ion from PTH-X.....95

Figure 4.7. Proposed mechanism of fragmentation of the m/z 193 ions derived from PTH-X using PTH-Ser as an example.....96

Figure 4.8. Proposed mechanism of fragmentation of the m/z 193 ion derived from PTH-Gly.....97

Figure 4.9. High-energy CID mass spectra of the m/z 193 ions derived from (A) PTC-Thr-Leu, (B) PTC-Trp-Leu, and (C) PTC-Gly-Leu.....99

Figure 4.10. Proposed mechanism of formation and fragmentation of the m/z 193 ions derived from PTC-Thr-Leu and PTC-Trp-Leu using PTC-Thr-Leu as an example.....100

Figure 4.11. Proposed mechanism of fragmentation of the m/z 193 ion derived from PTC-Gly-Leu.....101

Figure 5.1. CID spectra of poly(oxyethylene) bis(ephedrine) using tandem sector/time of flight MS. (A) High-energy CID spectrum of the m/z 1014 oligomer at +4 charge state, (B) Source CID of the polymer at V_{CID} = 10 V, and (C) Source CID of the polymer at V_{CID} = 40 V.....108

Figure 5.2. High-energy CID spectra of ions generated in source fragmentation. (A) G_2 ion at m/z 236, (B) G_1 ion at m/z 192 and (C) G_0 ion at m/z 148, all derived

from poly(oxyethylene) bis(ephedrine). (D) The m/z 148 ion originating from ephedrine.....110

Figure 5.3. CID spectra of poly(oxyethylene) bis(acetaminophen) using tandem sector/time of flight MS. (A) High-energy CID spectrum of the m/z 1007 oligomer at +4 charge state, (B) Source CID of the polymer at V_{CID} = 10 V and (C) Source CID of the polymer at V_{CID} = 40 V.....112

Figure 5.4. High-energy CID spectra of ions generated in source fragmentation. (A) G_4 ion at m/z 310, (B) G_2 ion at m/z 222 and (C) G_0 ion at m/z 134, all derived from poly(oxyethylene) bis(acetaminophen). (D) The m/z 134 ion originating from acetaminophen.....113

Figure 5.5. Proposed mechanism of polymer fragmentation. (A) Formation of G_n and B_m ions and (B) Formation of A_n ions.....116

Figure 5.6. Ion stability diagrams in source fragmentation. (A) Poly(oxyethylene) bis(ephedrine) and ephedrine, (B) Poly(oxyethylene) bis(acetaminophen) and acetaminophen.....117

Figure 5.7. CID spectra of poly(oxyethylene) bis(ephedrine) using ion trap/time-of-flight MS. (A) Ion trap CID spectrum of the m/z 1014 oligomer at +4 charge state and (B) Source CID of the polymer at V_{CID} = 40 V.....119

Figure 5.8. Ion trap CID spectra of ions generated in source fragmentation. (A) G_2 ion at m/z 236, (B) A_4 ion at m/z 177 and (C) G_0 ion at m/z 148, all derived from poly(oxyethylene) bis(ephedrine). (D) The m/z 148 ion originating from ephedrine.....120

Figure 6.1. SWIFT waveforms used in isolation of the protonated ion of leucine-enkephalin at m/z 556.6. (A) Time-domain SWIFT notched waveform used for ion isolation. (B) Magnitude spectrum of the SWIFT notched waveform used for isolation.....130

Figure 6.2. SWIFT waveforms used in activation of the protonated ion of leucine-enkephalin at m/z 556.6. (A) Time-domain SWIFT waveform used for excitation. (B) Magnitude spectrum of the SWIFT waveform used for excitation.....131

Figure 6.3. Sequence of events of an ion trap/time-of-flight mass spectrometer for (A) CID, (B) PID with multiple laser pulses and (C) PID with a single laser pulse and time-dependent detection. See text for details.....133

Figure 6.4. PID spectra of protonated Trp-Ala at $q_z = 0.133$ with helium as a buffer gas at P = 0.6 μTorr in the TOF tube and laser energy of 40 mJ per pulse: (A) 2 pulses, (B) 5 pulses and (C) 10 pulses.....137

Figure 6.5. Dissociation spectra of protonated Tyr-Gly at $q_z = 0.154$ with helium as a buffer gas: at P = 0.6 μTorr in the TOF tube. (A) PID from 5 laser pulses with laser energy of 40 mJ per pulse. (B) PID from 5 laser pulses with laser energy of 50 mJ per pulse and (C) CID. The buffer gas pressure in the TOF tube was 0.6 μTorr.....138

Figure 6.6. Dissociation spectra of protonated Tyr-Gly-Gly at $q_z = 0.124$ with helium as a buffer gas: (A) PID at P = 0.8 μTorr in the TOF tube, (B) PID at P = 0.6 μTorr, (C) PID at P = 0.4 μTorr, (D) CID at P = 0.8 μTorr. 5 laser pulses with laser energy of 50 mJ per pulse were used for PID.....140

Figure 6.7. Dissociation spectra of protonated morphiceptin (YPFP) at $q_z = 0.141$ with helium as a buffer gas: (A) PID at P = 0.8 μTorr in the TOF tube, (B) PID at P = 0.6 μTorr, (C) PID at P = 0.4 μTorr, (D) CID at P = 0.8 μTorr. 5 laser pulses with laser energy of 50 mJ per pulse were used for PID.....141

Figure 6.8. PID spectra of protonated leucine-enkephalin (YGGFL) at $q_z = 0.132$ with helium as a buffer gas at P = 0.6 μTorr in the TOF tube: (A) PID and (B) Background-subtracted PID. The major background ion peaks are labeled

as "B". 5 laser pulses with laser energy of 50 mJ per pulse were used for PID.....142

Figure 6.9. Dissociation spectra of protonated leucine-enkephalin (YGGFL) at q_z = 0.132 with helium as a buffer gas at P = 0.6 μTorr in the TOF tube: (A) PID, (B) Background-subtracted PID and (C) CID. (A) and (B) were obtained after buffer gas "purging" step. The major background ion peaks are labeled as "B". 5 laser pulses with laser energy of 50 mJ per pulse were used for PID.....143

Figure 6.10. PID spectrum of protonated oxytocin (CYIQNCPLG) at q_z = 0.073 with helium as a buffer gas at P = 0.6 μTorr in the TOF tube. 10 laser pulses with laser energy of 50 mJ per pulse were used for PID. The CID spectrum at q_z = 0.110 is shown in the inset.....145

Figure 6.11. Relative intensities of PID products as a function of time after the laser pulse for protonated Trp-Ala at q_z = 0.133. Helium was used as a buffer gas at P = 0.4 μTorr in the TOF tube and the laser energy was 40 mJ per pulse. (A) Logarithmic time scale, (B) Linear time scale. The lines connect the points representing the average of 3 measurements.....146

Figure 6.12. Relative intensities of PID products as a function of time after the laser pulse for protonated Tyr-Gly-Gly at q_z = 0.124. Helium was used as a buffer gas at P = 0.4 μTorr in the TOF tube and the laser energy was 50 mJ per pulse. (A) Logarithmic time scale, (B) Linear time scale. The lines connect the points representing the average of 3 measurements.....148

Figure 7.1. Sequence of events of an ion trap/time-of-flight mass spectrometer for (A) IRMPD with a pulsed CO_2 laser, and (B) Time-resolved CID. See text for details.....154

Figure 7.2. IRMPD spectra using a pulsed CO_2 laser with helium as a buffer gas at P = 0.6 μTorr in the TOF tube. (A) Trp-Ala at q_z = 0.1332 and a single laser

pulse with laser energy of 80 mJ per pulse, (B) Morphiceptin (YPFP) at q_z = 0.141 and a single laser pulse with laser energy of 100 mJ per pulse, (C) Leucine-enkephalin (YGGFL) at q_z = 0.132 and a single laser pulse with laser energy of 100 mJ per pulse.....158

Figure 7.3. IRMPD spectra of equine cytochrome c at +13 charge state with helium as a buffer gas at P = 1 μTorr in the TOF tube and a single laser pulse with laser energy of 180 mJ per pulse. (A) 1 μs after excitation, (B) 100 μs after excitation, (C) 1 ms after excitation, (D) 10 ms after excitation.....160

Figure 7.4. IRMPD spectra of equine cytochrome c at +13 charge state acquired 10 ms after excitation with helium as a buffer gas at P = 1 μTorr in the TOF tube and a single laser pulse. (A) Laser energy of 130 mJ per pulse, (B) Laser energy of 180 mJ per pulse, (C) Laser energy of 460 mJ per pulse.....161

Figure 7.5. IRMPD spectra of equine cytochrome c at +12 charge state with helium as a buffer gas at P = 1 μTorr in the TOF tube and a single laser pulse with laser energy of 180 mJ per pulse. (A) 1 μs after excitation, (B) 100 μs after excitation, (C) 1 ms after excitation, (D) 10 ms after excitation.....163

Figure 7.6. Time-resolved detection in IRMPD of equine cytochrome following a single excitation laser pulse. (A) Laser energy of 180 mJ per pulse, (B) Laser energy of 130 mJ per pulse, (C) The log (A / A_0) versus time plots for +12 and +8 charge state molecular ions at laser energy of 130 mJ per pulse and for the +12 molecular ion at laser energy of 180 mJ per pulse.....165

Figure 7.7. Time-resolved detection in IRMPD of PTH-isoleucine following a single excitation laser pulse with helium as a buffer gas at P = 0.8 μTorr in the TOF tube and a single laser pulse with laser energy of 180 mJ per pulse. (A) The IRMPD spectrum acquired 1 μs after excitation, (B) The IRMPD spectrum acquired 10 ms after excitation, (C) Relative intensities of IRMPD products as a function of time after excitation.....169

Figure 7.8. Time-resolved detection in IRMPD of PTH-isoleucine following a single excitation laser pulse with helium as a buffer gas at P = 0.8 μTorr in the TOF tube and a single laser pulse with laser energy of 180 mJ per pulse. (A) The total intensity of the ions after the excitation, (B) Relative intensities of the molecular ion after the excitation. See text for details.....171

Figure 7.9. IRMPD spectra of PTH-amino acid isomers acquired 1 μs after excitation with helium as a buffer gas at P = 1 μTorr in the TOF tube and a single laser pulse with laser energy of 180 mJ per pulse. (A) PTH-isoleucine, (B) PTH-leucine , (C) PTH-norleucine.....175

Figure7.10. Time-resolved detection in CID of PTH-isoleucine. (A) The total intensity of the ions present in the ion trap during CID, (B) Relative intensities of ions involved in CID. The inset shows the CID used for excitation of the molecular ion of PTH-isoleucine.....176

Figure 7.11. Structures and fragmentation pathways of linkage isomers (βGal(1→3)βGlcNAcR, βGal(1→4)βGlcNAcR) and anomers (βGlc(1→2)βGalR and αGlc(1→2)βGalR) analyzed by IRMPD.....179

Figure 7.12. Dissociation spectra of disaccharide linkage isomers. (A), (C), (E) βGal(1→4)βGlcNAcR. (B), (D), (F) βGal(1→3)βGlcNAcR. (A), (B) CID of the protonated molecular ion. (C), (D) CID of the m/z 366 ion. (E), (F) IRMPD spectra of the protonated molecular ion acquired 1 ms after excitation with helium as a buffer gas at P = 0.8 μTorr in the TOF tube and a single laser pulse with laser energy of 180 mJ per pulse.....181

Figure 7.13. Dissociation spectra of disaccharide anomers. (A), (C), (E) αGlc(1→2)βGalR. (B), (D), (F) βGlc(1→2)βGalR. (A), (B) CID of the ammoniated molecular ion. (C), (D) CID of the m/z 351 ion. (E), (F) IRMPD spectra of the ammoniated molecular ion acquired 1 ms after

excitation with helium as a buffer gas at P = 0.8 μTorr in the TOF tube and a single laser pulse with laser energy of 180 mJ per pulse.....183

Figure 7.14. Time-resolved detection in IRMPD of βGlc(1→2)βGalR and αGlc(1→2)βGalR anomers following a single excitation laser pulse with helium as a buffer gas at P = 0.8 μTorr in the TOF tube and a single laser pulse with laser energy of 180 mJ per pulse.....185

Figure A.1. Nomenclature for the backbone fragmentation of peptide ions. Subscripts refer to the amino acid position in the sequence, determined from the N-terminal (for **a**, **b**, **c** ions) or C-terminal (for **x**, **y**, **z** ions). R refers to the amino acid side chain.....194

List of Abbreviations

AS	aerospray
AWG	arbitrary waveform generator
CID	collision-induced dissociation
Da	daltons, 1 Da ≡ 1 u (atomic mass units)
dc	direct current
EBE	electric-magnetic-electric
ESI	electrospray ionization
eV	electron volt, 1 eV = 1.602×10^{-19} J
FT-ICR	Fourier transform-ion cyclotron resonance
fwhm	full width at half maximum
Gal	galactose
Glc	glucose
HPLC	high performance liquid chromatography
ID	internal diameter
IRMPD	infrared multiphoton dissociation
IR	infrared
IT	ion trap
LC	liquid chromatography
LMCO	low-mass cut-off
MALDI	matrix-assisted laser desorption/ionization
MCP	microchannel plate
MS	mass spectrometry
MS/MS	tandem mass spectrometry (one stage)
MS/MS/MS	tandem mass spectrometry (two stages)
MS^n	molecular weight (n-1 stages)

m/z	mass-to-charge ratio
Nd:YAG	neodymium-dopped yttrium aluminium garnet
OA	orthogonal acceleration
OD	outer diameter
PC	personal computer
PEG	poly(ethylene glycol)
PID	photo-induced dissociation
PITC	phenylisothiocyanate
ppm	parts per million
PTC	phenylthiocarbamyl
PTH	phenylthiohydantoin
QIT	quadrupole ion trap
rf	radio frequency
RSD	relative standard deviation
SCP	sulfachlorpyridazine
SDM	sulfadimethoxine
SMR	sulfamerazine
SMZ	sulfamethazine
STZ	sulfathiazole
SWIFT	stored waveform inverse Fourier transform
S/N	signal-to-noise
TOF	time-of-flight
TS	thermospray
UV	ultraviolet
V_{CID}	source fragmentation voltage
V_{P-P}	magnitude of radio frequency voltage (peak-to-peak)
v/v	volume-to-volume ratio

Chapter 1

Introduction: Electrospray Ionization Ion Trap/Time-of-Flight Mass Spectrometry

The application of mass spectrometry to the analysis of fragile compounds had been hampered by the difficulties in transforming these species into intact gas-phase ions. The development of soft ionization techniques, such as electrospray, has resulted in a variety of applications and an enormous contribution to modern mass spectrometric methodology. The majority of the electrospray literature involves utilization of quadrupole mass spectrometers. Installation of an electrospray source on an ion trap time-of-flight instrument presents some advantages which could be accomplished with recent improvements in technology. The performance of a mass spectrometer capable of sensitive and fast analyses is of interest to the mass spectrometry community. Subsequent sections will discuss the implementation of electrospray ionization ion trap/time-of-flight mass spectrometry.

1.1 Soft ionization techniques

The need to generate intact molecular ions of large, complex and fragile molecules that play such an important role in many areas of science and technology has resulted in a number of "soft" ionization techniques. These techniques fall into two general categories [1].

Sudden energy methods, such as Matrix Assisted Laser Desorption (MALDI), Plasma Desorption (PD), Fast Atom Bombardment (FAB), Secondary Ion Mass Spectrometry (SIMS), depend upon the nearly instantaneous achievement of a high-energy density in a sample of analyte dispersed on or in a solid or liquid surface. In spite of their highly energetic and irreversible nature these energy sudden techniques are "soft" in the

sense that they have been able to produce intact ions of nonvolatile parent species. By current standards MALDI is the most popular and most successful technique in generating high mass intact molecular ions [2]. Energy sudden methods are restricted in the way that they can not sample ions directly from solutions. Direct sampling of solution is important in a variety of circumstances ranging from monitoring the progress of chemical reactions to the determination of trace components of biological fluids.

Field desorption methods rely on the application of very strong electric fields to extract ions from a substrate into the gas phase. Desorption of analytes at useful rates from a condensed phase into vacuum produced ions with various degrees of solvation and a wide range of energies [3]. A major advance in the generation of analyte gas-phase ions from liquid solutions was achieved in new techniques that depend upon dispersing analyte solution as a cloud of small charged droplets from which ions desorb into a bath gas rather than into vacuum. The bath gas provides enthalpy for vaporizing the solvent from the droplets and acts as a moderator to maintain both the internal and translational energies of the desorbed ions at a level corresponding to the bath gas temperature [1].

Spray techniques, such as Aerospray (AS), Thermospray (TS), and Electrospray (ES), can be distinguished by the method that charged droplets are formed. In AS [4] the mechanical energy from a high velocity gas flow assists in aerodynamic nebulization of a liquid and droplet formation. Thermospray [5] involves heating a capillary tube containing an analyte solution to vaporize the majority of solvent and generate a dispersion of charged droplets in vapor that emerges from the exit of the capillary. In ES the voltage is applied to the metallic capillary continuously filled with a solution containing the analyte. The presence of the field leads to electrophoretic separation of charges in a dipolar layer at the meniscus of the liquid at the capillary tip. A cone and a liquid jet form, and the jet emits small charged droplets. In AS and TS charging is brought about by atomization of a liquid. Statistical fluctuation in the distribution of cation and anions among the droplets accounts for their charge. In ES, atomization is brought about by charging the surface of the liquid.

1.2 Electrospray ionization

Electrospray is a method by which ions, present or generated in solution, can be transfered to the gas phase. Electrospray existed as a method for the electrostatic dispersion of liquids and the creation of aerosols long before its application to mass spectrometry. In 1917 Zeleny [6] observed and photographed nebulization occurring from drop surfaces of ethanol and glycerin solutions when they were exposed to high electric fields.

In late 1960's, Malcolm Dole carried out some pioneering experiments that were pretty much ignored for a long time. During these experiments [7, 8] he combined electrospray ionization of polymers and free jet molecular beam technique to measure ion currents and mass-to-charge ratios of gas-phase macroions with an ion-drift mass spectrometer.

The increase in popularity of electrospray ionization mass spectrometry followed the report by Fenn and coworkers [9] on application of this technique to the analysis of protein samples. The scope of applications of the electrospray method is now such that one can not be ignorant of the fundamental principles of the technique. The essence of the electrospray process can be described with simplicity. However, details of the mechanism involved in the production of isolated ions remain imperfectly understood.

The most common implementation of the general ESI process for positive ion generation is illustrated in Figure 1.1 [10]. A metallic, narrow-bore capillary, continuously filled with a solution containing the analyte, is connected to the positive terminal of a high-voltage direct current (dc) power supply. The negative terminal of this power supply is connected to the counter-electrode located a few millimeters away from the capillary tip. The counter-electrode may be a plate with an orfice or a capillary mounted on a plate leading to a mass spectrometric sampling system. Because the electrospray capillary tip is very thin, the electric field penetrating the solution at the capillary tip is very high [11].

Under the influence of the field, positive ions drift downfield toward the meniscus of the liquid and negative ions drift away from the surface.

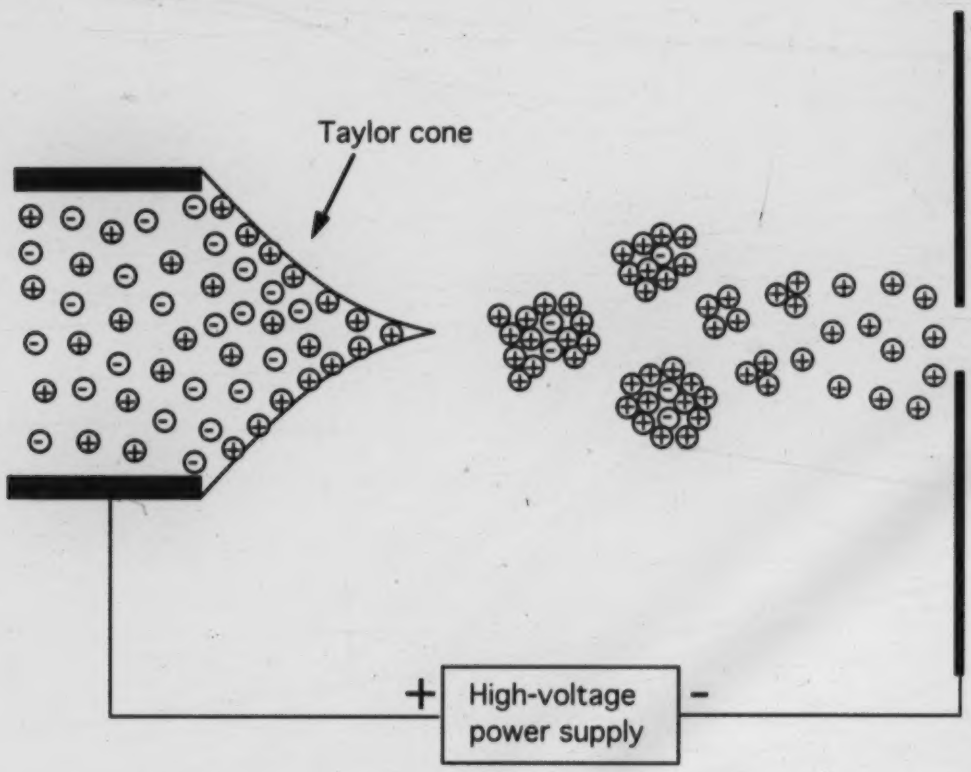

Figure 1.1. Schematic of electrospray ionization process.

The repulsion between positive ions at the surface overcomes the surface tension of the liquid and the surface begins to expand. The Tylor cone [12] forms and if the applied field is sufficiently high, a fine jet emerges from the cone tip which breaks into small charged droplets. Initial droplets, rich in positive charges, shrink in size as solvent molecules evaporate. To assist in this process, a cross-current flow of a drying gas is used [13].

Two principal mechanisms for the formation of observed gas-phase ions from small

and highly charged droplets have been proposed. In the charged residue model [7, 14], the repulsive effect of the increasing surface charge density completely offsets the droplet surface tension. The evaporating droplet divides, increasing the overall surface-to-volume ratio. The fission process may result in relatively large droplets of roughly equal size [15] or it may spawn the ejection of a series of much smaller ones in a process called "droplet jet fission" [16]. The fission process continues until the remaining particles contains only a single charged species.

Alternatively, the ion evaporation model [4, 17] assumes that the increase in surface charge density as a result of solvent evaporation produces a Coulombic repulsion that exceeds the adhesion of the charged species to the drop surface. Thus some ions are expelled from the surface. Ion evaporation is assumed to be the principal mechanism for droplets 10 nm or less in radius. A detailed discussion on the mechanism of electrospray was presented by Kebarle and Ho [18].

1.2.1 The quantitative aspect of electrospray

The introduction of electrospray ionization to mass spectrometry created a great number of opportunities for greater application of this method. At the same time, the technique sometimes seems capricious in the types of molecules amenable to ESI and the wide range of response factors attained. In addition, it has been difficult to predict the effects of changes in the solvent composition, the electrolyte employed, or the presence of other analytes. It is generally the case that the relative intensities of ions in the spectrum do not reflect the relative concentration of these ions in solution, sometimes by several orders of magnitude [19]. The lack of a successful predictive model for the response function of analytes in electrospray has hampered its application in quantitative analyses and has been a significant part of the motivation to understand the electrospray process in greater detail.

In much of the literature on this topic, it has been assumed that the basis for quantitation lay in the way in which the gas phase ions are formed from charged droplets.

Tang and Kebarle [18, 20] proposed a model for the response function of strong electrolyte analytes based on the hypothesis that the ion evaporation rate from the droplet is proportional to the ion concentration in the droplet. They assumed that the Irbane-Thomson ion evaporation model [4, 17] is the principal mechanism for the ion transfer to the gas phase. The mass spectrometrically detected ion intensity I_A of an ion A is expressed by:

$$I_A = pf \frac{k_A C_A}{k_A C_A + k_B C_B} I \qquad (1.1)$$

Where f (fraction of the droplet charge converted into gas-phase ions) and p (ion-sampling efficiency) are independent of the chemical nature of the ions. C_A and C_B are concentrations of the analyte A and B in the solution to be electrosprayed, k_A and k_B are sensitivity coefficients. I is the electrospray capillary current.

The presented equation works well only at high analyte concentrations. It predicts the plateau in response and the inter-analyte competition that exists at higher concentrations. However, the sensitivity coefficients obtained at the high concentration do not predict the response function at low concentrations.

An equilibrium model postulated by Enke [21] is based on competition among the ions in the solution for the limited number of excess charge sites at the surface of a formed droplet. The unconventional aspect of this approach assumes a distribution of ions between the charged surface and the interior of the droplet. The partition between two "separate phases" is well established while the solution is in the Taylor cone and is essentially complete before the desolvation process begins. The desolvation does not alter the surface charge composition and does not create the new charge separation. The relative abundances of observed gas-phase ions are proportional to the relative concentrations of ions in the surface excess charge phase. This model accurately predicts the response of

singly charged analytes as a function of the concentration of electrolyte and other analytes. It provides an explanation for the selective effectiveness of ESI.

1.2.2 Applications of electrospray ionization

The significance of the development of the electrospray technique and the reason for its enormous popularity is a logical coupling of sample solution introduction to mass analysis. The interfacing of ESI to Liquid Chromatography [22] and Capillary Electrophoresis [23] solved the problem of incompabilites in combining liquid separation methods with on-line mass spectrometry detection.

Specific properties of this ionization method for large, highly polar, involatile, and very fragile compounds present some advantages over other soft ionization techniques. Since the electrospray process results in formation of multiple-charged species, conventional mass spectrometers can be employed to detect large ions in accessible mass-to-charge (m/z) range [24]. Multiple charging has allowed the application of tandem mass spectrometry to generate sequence information from highly charged ions of large species [25]. Electrospray, as the very gentle ionization method, can preserve the structure of noncovalently bound complexes existing in solution and facilitate their mass detection [26].

The explosion of ESI applications took place in research areas poorly accessible by previous mass spectrometric ionization techniques. Recent review articles demonstrate the widespread use of electrospray ionization. In biochemistry, ESI is applied to the analysis of peptides and proteins [27], nucleic acids and constituents [28], carbohydrates and lipids [29]. In pharmacology, ESI is used for drug metabolism and pharmacokinetics studies [30]. In organometallic and inorganic chemistry, it is used for studying gas-phase properties of compounds [31].

Despite its many successful applications, wider acceptance of ESI has been hindered by a few key restrictions. ESI can not handle volumetric flow rates greater than a few μL/min or solutions that are high either in conductivity or surface tension. To

surmount these shortcomings modified ESI sources have been developed. The use of an aerodynamic [32] or an ultrasonic [33] nebulizer to assist electrospray and a nano-electrospray source [34] are examples of such modifications. The nano-electrospray, a popular ultrasensitive technique, is a form of the electrospray with a reduction of volumetric flow rates (from μL/min to nL/min) and smaller dimensions of a capillary tip (from 100 μm to 1-3 μm ID). Due to the formation of very small droplets the nano-electrospray process offers higher tolerance for high conductivity solutions, improved desolvation, ionization efficiency and lower sample consumption.

1.3 Quadrupole ion trap

For years the physics community has used the quadrupole ion trap in a variety of fundamental studies [35]. The chemistry community had largely ignored the ion trap until Stafford and coworkers [36, 37] developed this device as a mass spectrometer. A number of features of the ion trap make it attractive not only as a mass analyzer but also as an ion storing device, where a wide variety of chemical processes can occur [38]. They involve electron ionization, photoionization, electron transfer, proton transfer, collision-induced dissociation, photodissociation, and ion/ion or ion/neutral molecule reaction. Ion traps are particularly well suited for studying these phenomena because the reaction time can be varied over six orders of magnitude (from microseconds to seconds).

1.3.1 Operational principles of the ion trap

Figure 1.2 A shows a cross-sectional view of a quadrupole ion trap. The quadrupole ion trap consists of two identical endcap electrodes of hyperboloidal geometry separated by a distance of $2z_0$. One ring electrode of hyperboloidal geometry with internal radius (r_0) is positioned symmetrically between two end-cap electrodes. During the operation of the quadrupole ion trap, a radio frequency (rf) voltage V and dc voltage U are applied to the ring electrode. The end-cap electrodes are grounded.

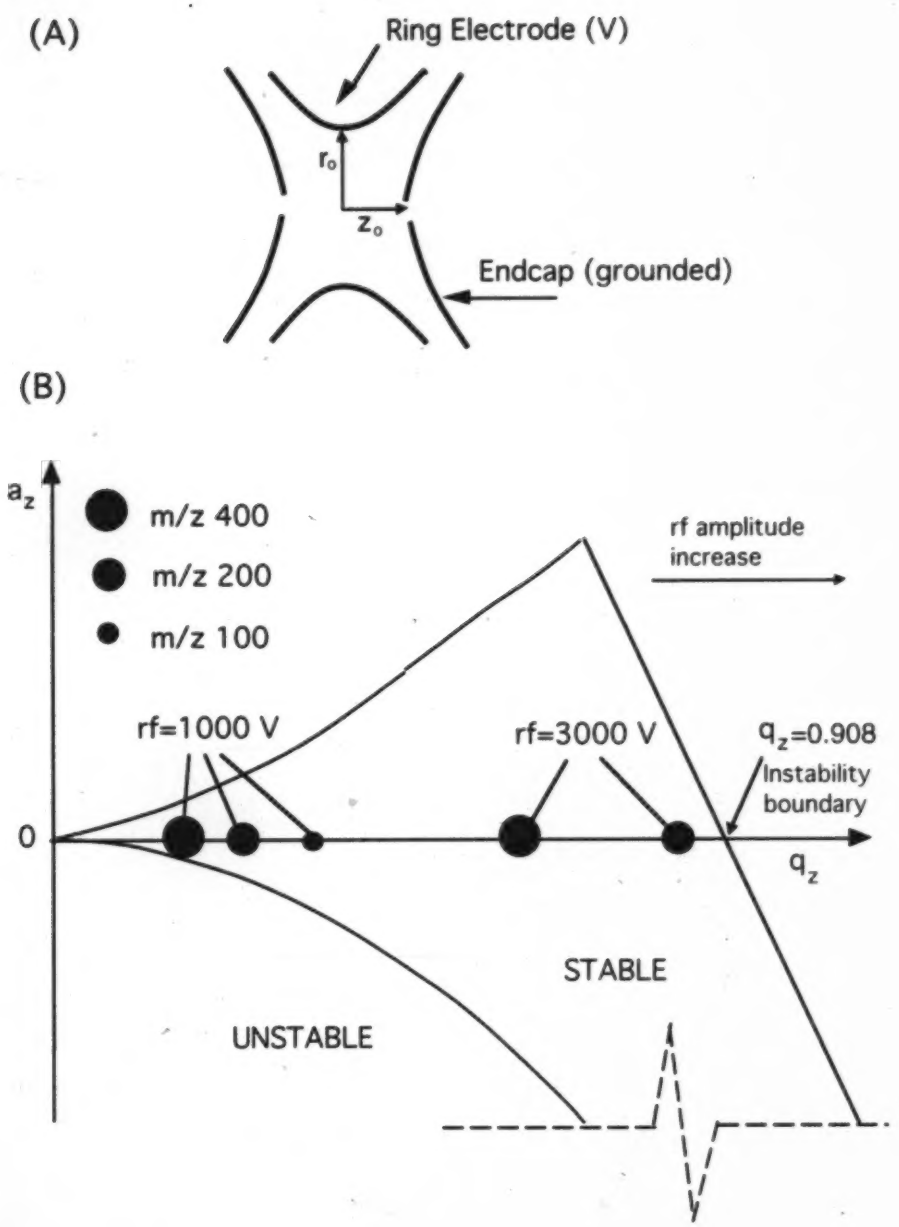

Figure 1.2. The quadrupole ion trap. (A) A cross-sectional view of the quadrupole ion trap. (B) A part of the a_z versus q_z stability diagram.

The geometries of the electrodes are defined so as to produce an ideal quadrupole field [39]:

$$r_0^2 = 2z_0^2 \tag{1.2}$$

Once the magnitude of r_0 is given, the size of all three electrodes and the electrode spacings is fixed.

An ion in a quadrupole field experiences a strong restoring force, which drives the ion toward the center of the trap and increases as the ion deviates from the center of the device. The motion of ions in the quadrupole field can be described mathematically by the solutions to the second-order linear differential equation, known as the Mathieu equation [40]. In this equation, dimensionless parameters q_z and a_z:

$$q_z = \frac{4zeV}{mr_0^2\Omega^2} \tag{1.3}$$

$$a_z = \frac{-8zeU}{mr_0^2\Omega^2} \tag{1.4}$$

are related to operational parameters of the ion trap:

- Ω frequency of rf voltage,
- V magnitude of rf voltage,
- U magnitude of dc voltage,
- r_0 internal radius of ring electrode,
- m mass of ion,
- z charge of ion,
- e elementary charge.

The solutions to Mathieu's equation determine whether an ion has a stable or unstable trajectory within the ion trap. Ions can be stored when their trajectories are stable in the r- and z-directions. Figure 1.2 B shows a small portion of the stability diagram for

quadrupole ion trap in a_z and q_z space . The section of simultaneous stability in both r- and z-directions is called a stability region. Under conventional operating conditions of the ion trap, a dc potential is not used ($a_z = 0$) and the stability region represents points that lie along the q_z axis with q_z values smaller than 0.908. Ions with q_z values smaller than 0.908 are stored in the trap, whereas those with q_z equal or bigger than 0.908 will be axially unstable and lost. Ions of different m/z may inhabit the stability zone simultaneously and be distributed at different points in the zone. The resulting dispersion according to m/z allows ions to be selectively stored. As shown in the Figure 1.2 B, ions are moved along the q_Z axis by increasing the rf voltage until they become unstable at the boundary, where q_z = 0.908, and they exit the trap. An ion with a high m/z becomes unstable at a higher rf amplitude than one with a lower m/z. Thus, as the rf voltage is raised, ions of increasing m/z are ejected in sequence and can be detected.

Trapped ions of a specific mass-to-charge have fundamental frequencies of motion unique to their q value. The frequencies of ion motion in the z-direction are defined by equation 1.5:

$$f_{h,z} = (h\Omega + \beta_z \Omega / 2) \qquad \text{for} \qquad h = \{0, +1, +2, \ldots\} \qquad (1.5)$$

Where $f_{h,Z}$ is a frequency component of the ion motion, Ω is the frequency of the rf voltage applied to the ring electrode, and β_z is a parameter related to ion motion that varies with ion's position on the stability diagram.

The higher-order frequency components (h>0) usually have negligible effect on ion motion and are not utilized.

At $q_z < 0.4$, β_z is approximately given by:

$$\beta_z \approx \sqrt{q_z^2 / 2} \qquad (1.6)$$

and the fundamental resonant frequency $f_{0,z}$ can be calculated based on the operating parameters of the trap.

1.3.2 Resonant excitation

The motion of ions confined in a quadrupole ion trap can be excited upon resonant irradiation. Such irradiation can be effected by applying a small supplementary oscillating potential across the end-cap electrodes. The frequency of this auxiliary signal is chosen to match the fundamental frequency of z-motion. In such axial (z-direction) resonant excitations ions move away from the ion trap center experiencing a greater trapping field. The ions are accelerated further so that they can achieve high kinetic energies. When the magnitude of the auxiliary oscillating potential is high, excursions in z-direction rapidly increase and after just a few cycles of application of the supplementary voltage, ions are ejected through the apertures in the end-cap electrodes. Resonant axial excitation has become a powerful technique in quadrupole ion trap mass spectrometry by the utilization of predetermined waveforms composed of specified frequencies or frequency ranges [41]. Resonant excitation can be used to affect the population of trapped ions in many ways:

Ion isolation

Broad bands of frequencies are applied to the end-cap electrodes to excite and remove many ionic species, leaving a single type of ions isolated within the ion trap.

Collision induced dissociation

The kinetic energy of an ion is increased in order to deposit internal energy to the ion through momentum-exchange collisions with buffer gas molecules. As a result the ion dissociates.

Energy deposition

The kinetic energy of an ion is increased in order to promote endothermic ion-molecule reactions.

1.3.3 Ion trap with stretched geometry

A theory of ion motion inside the ion trap assumes its purely quadrupolar geometry. However ion trap electrodes are truncated to obtain a practical working instrument. This introduces higher-order multipole components to the potential experienced by trapped ions [39]. To compensate for these adverse effects, the distance between the end-cap electrodes has been increased without modification of the shapes of the electrodes. Mathieu parameters (q_z, a_z) for "stretched" ion traps lacking quadrupole geometry can be calculated using the actual values of z_0 and r_0:

$$q_z = \frac{8zeV}{m(r_0^2 + 2z_0^2)\Omega^2} \tag{1.7}$$

$$a_z = \frac{-16zeU}{m(r_0^2 + 2z_0^2)\Omega^2} \tag{1.8}$$

Where Ω is the frequency of the rf voltage, V is the magnitude of the rf voltage, U is the magnitude of the dc voltage, r_0 is the internal radius of the ring electrode, z_0 is the distance from the center of the trap to the end-cap electrode, m is the mass of the ion, z is the charge of the ion, e is the elementary charge. With this modification, some crucial parameters related to the operation of the "real" ion trap can be determined.

The fundamental secular frequency $f_{0,Z}$ utilized in axial resonant excitation at $q_z < 0.4$ can be expressed as:

$$f_{0,z} = \frac{2.83zeV}{m(r_0^2 + 2z_0^2)\Omega} \tag{1.9}$$

Determination of secular frequencies is more complex in practice since the frequencies change slightly as an ion moves away from the ion trap center and are also dependent on the number and the nature of other ions present in the ion trap.

The low-mass cut-off value (LMCO) determines the low m/z trapping limit for ions inside the ion trap:

$$LMCO = \frac{8.81eV}{(r_0^2 + 2z_0^2)\Omega^2} \tag{1.10}$$

Ions with m/z lower than LMCO cannot be trapped. They are accelerated from the center of the trap and strike an electrode before the phase of rf voltage changes. The presented theory of a trapped ion deals with the ion localized in the center of the ion trap and possessing no initial kinetic energy. In this model all ions with m/z bigger than LMCO, including large m/z ions, are stored in the trap. For ions introduced into the quadrupole ion trap from external ionization source additional factors are important and they will be discussed later.

The rf potential applied to the ring electrode generates a parabolic potential well. The magnitude of the potential well depth in z-direction D_z (the direction of the resonant excitation) may be estimated from:

$$D_z \approx \frac{zeV^2}{m(r_0^2 + 2z_0^2)\Omega^2} \tag{1.11}$$

The potential well in which ions are trapped at a fixed V becomes increasingly shallow for larger m/z ions. The essential importance of the potential well depth is that it determines the amount of kinetic energy which an ion may acquire through resonant excitation prior to being ejected from the ion trap.

1.4 Interfacing electrospray ionization to the quadrupole ion trap

The coupling of electrospray ionization to mass spectrometry was reported simultaneously by Yamashita and Fenn [42] and Alexandrov et al. [43] in 1984. Soviet

researchers, in contrast to all other researchers acquiring mass spectral data with quadrupole mass filters in the early stage of electrospray ionization mass spectrometry, used a magnetic sector instrument. More demanding instrumental requirements for analyzing electrospray-generated ions resulted in interfacing electrospray ionization to a variety of mass analyzers. Electrospray ionization was combined with time-of-flight-mass spectrometry (TOFMS) [44-46] to achieve the high data acquisition rates required for monitoring fast separation techniques and to extend the m/z range of analyzed species. The potential for tandem mass spectrometry of ions formed by electrospray as well as a high resolution detection of large m/z ions were reported after the spectacular coupling of electrospray ionization with a Fourier transform-ion cyclotron resonance mass spectrometry [47].

Initial results obtained with a quadrupole ion trap and an electrospray source [48] demonstrated the capability of multiple-stage tandem mass spectrometry and good sensitivity for small ionic species. The major concern, however, was a relatively low trapping efficiency, especially for high mass ions. Two factors disfavor trapping of an injected ion. Entering ions have initial kinetic energy that is greater than the thermal energy. Also they are admitted to the trap from the boundary of the stability region. Namely, through a hole in the center of one of the end-caps. The interactions between ions and an electric field originate at the entrance point and result in ion trajectories influenced by a set of time-dependent forces. An injected ion is trapped only if it enters the trap during the correct phase angle of the applied rf voltage. Furthermore, unless some of its energy at the entrance is removed, the ion will not be captured. The most common method of removing energy from ion entering the quadrupole ion trap involves a low molecular weight buffer gas (i.e., helium). Ions entering the quadrupole ion trap collide with the buffer gas effectively transferring some of their energy to the gas. As a result, ions are forced to occupy the central region of the trap. An inappropriate phase relationship and/or magnitude of rf voltage during a trapping event results in ions having too high a velocity

and passing through the trap. An ion may be rejected upon the entrance when its velocity is so small that the ion can not penetrate the rf potential barrier.

A qualitative description of ion trapping within rf fields is given in a simple three-stage "swinging door" model [49]. At the first stage, the hole in the entrance end-cap acts as a "swinging door" resulting in the change of the ion energy upon the entrance. In the second stage which lasts several microseconds, ions are or are not trapped depending on their energy after interaction with the "swinging door". Gradually over many milliseconds the energy of the trapped ions is dissipated via collisions with buffer gas molecules. The change of the kinetic energy due to the interaction of ions with rf field at the early stage of injection near the entrance hole is much more important for ion trapping than the losses of energy in collisions with buffer gas molecules. The fate of the ion (whether it is trapped or not) is determined within the first few microseconds after injection.

The progress on efficient injection of ions into a trap has not been significant. Trapping efficiencies for continuous ion sources do not exceed 10 percent [50]. Further, they are strongly dependent on a number of instrumental factors as well as the mass-to charge and chemical properties of ions. It is difficult to optimize collection of ions in a wide range of masses.

An alternative method of "cooling" ions in the injection step is "electrical ion cooling". In this method electrical fields are used to focus ions into the center of the ion trap without the assistance of a buffer gas [51, 52]. Unfortunately, although this approach was evaluated as effective in ion simulation studies, it was never practically implemented. More efficient trapping of ions inside the ion trap was achieved by increasing the trapping voltage during the ion introduction [53]. The trapping efficiency for externally generated MALDI ions was about an order of magnitude higher for the ramped rf voltage procedure. However, this method can only be applied with pulsed ion sources.

Despite the fact that ion injection into quadrupole ion traps is not very effective, most ESI-IT systems work better now than at the time of the first ESI-IT coupling [48].

The enhancement of performance has been achieved by the use of rf electrodynamic ion guides [54] instead of electrostatic ion focusing lenses as ion optics devices. Rf ion guides involved in transport of ions to the entrance of mass analyzers include quadrupole [55], hexapole [56], and octopole [57]. Their focusing systems consists of an even number of rods parallel to the central axis and accurately positioned in a radial array. When the combination of rf voltages is applied to the rod electrodes, a two-dimensional multipole oscillatory electric field is generated inside the rod arrangement. Ions traveling along the rod assembly are compressed to the center of the device by the focusing action of the field and through collisions with gas molecules [58]. The focusing power of a multipole increases with the number of electrodes. An octapole seems to be the best compromise for good performance and limited complexity. The octopole ion guide offers several advantages over static lens configurations. The major advantage is the efficient transport of ions from a high pressure region (ESI source) to a region of lower pressure with minimal scattering losses. Secondly, since the ions are accelerated directly into the ion trap from the octopole, the kinetic energy of the ions can be controlled to any practical level to optimize ion injection efficiency. The octopole can also be also used as a preliminary mass filter to select the ions to be injected into the trap. Finally, this ion guide has the ability to shield the low energy ions from stray electric fields.

1.5 Mass analysis using the quadrupole ion trap

Mass analysis using the quadrupole ion trap can be performed using several different techniques. Traditional methods of detection include mass-selective instability scan and resonant ejection scan. In the mass-selective instability mode of detection [36, 37], according to the principles presented in Section 1.3.1, the amplitude of the rf potential is ramped causing the q_z values of all ions to increase throughout the ramp. As the q_z value for each ion reaches a value of 0.908, the ions are ejected axially through the end-caps electrodes and detected by an electron multiplier located behind one of the end-caps. The

mass range of detection (m/z smaller than 700 Da) is determined by the operational limit to the amplitude of rf voltage.

The resonant ejection mode of detection [59] uses a supplementary ac voltage, at a frequency smaller than the fundamental rf frequency, applied across the end-cap electrodes. Resonant ejection of the ions for detection occurs therefore at a q_z value below the normal stability limit ($q_z < 0.908$). The mass range of detection achieved by ramping the amplitude of rf voltage is considerably greater than the normal limit. Mass spectra for m/z 75 000 ions can be recorded by using rf supplementary signals of appropriately low frequency.

A scanning character of mass detection when sequential ejection of ions is used puts some restrains on the mass analysis process. Scan rates for a given scan range determine scan time. Because fast scan rates result in low mass resolution, the tradeoff has to be made between mass resolution and duration of a detection event. The shortest time to acquire a mass spectrum using traditional detection methods is in a range of milliseconds.

In an alternative approach, time-of-flight (TOF) detection method was used for the mass analysis of ions trapped inside the ion trap. TOF detection of electrospray-generated ions temporarily stored in the ion trap was first used by Lubman and coworkers [60]. Extraction of ions was performed by applying a voltage pulse to one of the end-cap electrodes. Ejected ions were accelerated entering the flight tube of a reflectron time-of-flight mass analyzer. The detection of electrospray-generated ions accumulated in the ion trap with a linear time-of-flight mass analyzer was implemented by Purves and Li [61].

The TOF mass analyzer is unique in its ability to analyze ions of all m/z ratios simultaneously. Mass spectra are generated in a very short time, thereby very fast data acquisition rates can be used. The high ion transmission allows for sensitive detection. TOF has a theoretically unlimited m/z range, but is limited in practice by the detection system. The main factor determining the performance of TOF detection is the quality of the ion beam after extraction from the trap.

1.5.1 Detection principles for IT-linear TOFMS

The principles of TOF mass analysis for ions stored in the quadrupole ion trap are briefly explained using the schematic diagram in Figure 1.3.

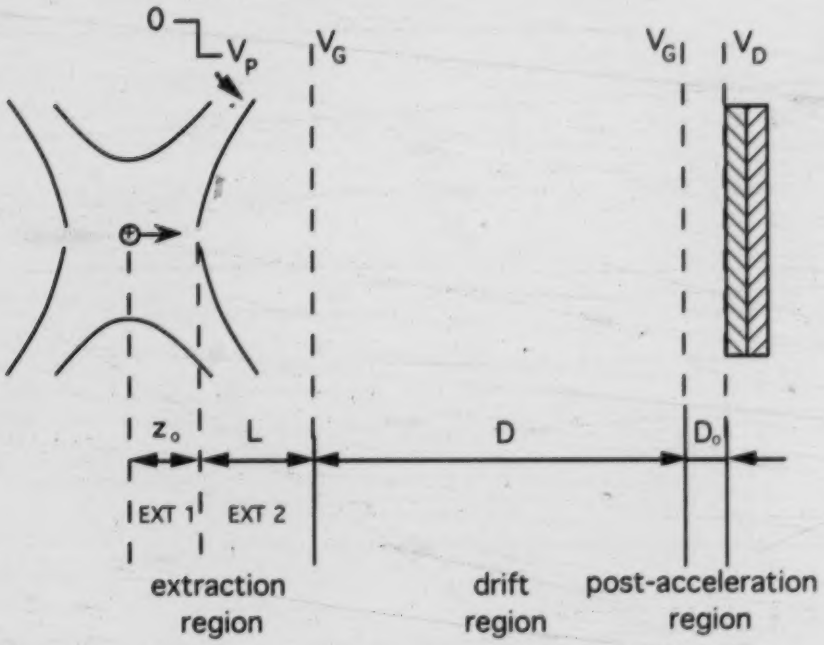

Figure 1.3. A schematic diagram of TOF mass analysis for ions stored in the quadrupole ion trap.

The TOF mass analyzer consists of an extraction region, a drift region (i.e., the flight tube) and a post acceleration (detection) region. Positive ions occupy the center of the ion trap. Their initial velocities in the direction parallel to the flight tube are assumed to be zero (v_0=0). At time zero, a few hundred of nanoseconds after the rf trapping voltage was turned off, a negative pulse (V_p) is applied to the exit end-cap electrode. Ions are

accelerated from the center of the ion trap toward the exit end-cap electrode . They exit the end-cap electrode with the velocity v_1:

$$v_1 = \sqrt{\frac{2ez(-V_P)}{m}} \tag{1.12}$$

Where m is the mass of the ion, z is the charge of the ion, and e is the elementary charge. Upon exiting the ion trap they experience the field between the end-cap (V_p) and the extraction grid (V_G). This accelerates the ions further to the velocity v_2:

$$v_2 = v_1 + \sqrt{\frac{2ez(V_P - V_G)}{m}} \tag{1.13}$$

The ions exit the extraction region with velocity v_2 and enter the field-free drift region where they are separated based on differences in their velocity. If the detector is operated at the lower potential (V_D) than the drift region grid (V_G), the ions are post-accelerated to the final velocity v_3:

$$v_3 = v_2 + \sqrt{\frac{2ez(V_G - V_D)}{m}} \tag{1.14}$$

The flight time through each field region can be calculated from:

$$t = \frac{v_f - v_0}{a} \tag{1.15}$$

Where v_f is the final velocity of the ion, v_0 is the initial velocity of the ion, and a is the acceleration of the ion.

The acceleration a can be related to the electric field strength E as:

$$a = \frac{ezE}{m} \tag{1.16}$$

The flight time through the field free region can be expressed as:

$$t_{DRF} = \frac{D}{v_2} \tag{1.17}$$

The total flight time of an ion, t_{TOT}, is a sum of the time the ion spends in all regions:

$$t_{TOT} = t_{EXT1} + t_{EXT2} + t_{DRF} + t_{DET} \tag{1.18}$$

$$t_{TOT} = \left(\frac{2z_0}{\sqrt{(-V_P)}} + \frac{2L}{\sqrt{(V_P - V_G)}} + \frac{D}{\sqrt{(-V_P)} + \sqrt{(V_P - V_G)}} + \frac{2D_0}{\sqrt{V_G - V_D}} \right) \sqrt{\frac{m}{2ez}} \tag{1.19}$$

Where m is the mass of the ion, z is the charge of the ion, and e is the elementary charge, z_0 is the distance from the center of the trap to the end-cap electrode, L is the length of the extraction region outside the ion trap, D is the length of the flight tube, D_0 is the length of the post-acceleration region, V_P is the amplitude of the ejection pulse, V_G is the voltage applied to the extraction grid, and V_D is the detector post-acceleration voltage.

Equation (1.19) shows that the time of flight (t) is proportional to the square root of the mass to charge ratio. Consequently, a calibration involving two time points with known m/z values determines the parameters in following equation:

$$t = k\sqrt{m/z} + b \tag{1.20}$$

Where k represents instrumental parameters and b corresponds to the time delay between the voltage pulse and the start of the data acquisition.

1.6 An Electrospray Ionization Ion Trap/linear Time-of-Flight Mass Spectrometer

Figure 1.4 shows a schematic diagram of the electrospray ionization ion trap/linear time-of-flight mass spectrometer [62] used in my research.

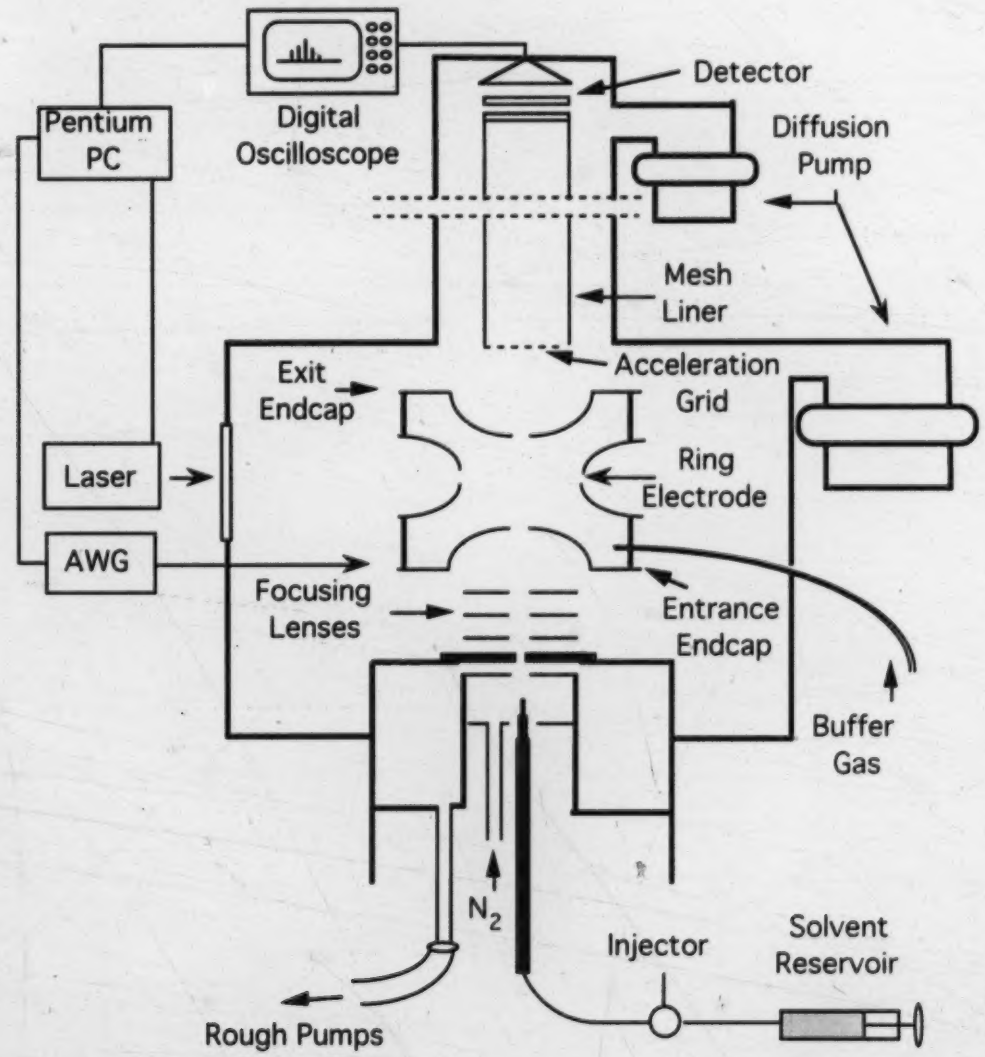

Figure 1.4. Schematic of electrospray ionization ion trap/linear time-of-flight mass spectrometer. Drawing is not to scale.

Solution from a syringe pump flows through a sample injector to an electrospray needle. A high dc voltage (~4 kV) is applied to the electrospray needle and the needle tip is positioned a few millimeters from the entrance to vacuum (nozzle plate). The region, in which charged droplets are formed is flushed constantly with heated dry nitrogen to facilitate solvent evaporation. Desolvated ions enter the two-stage interface. In the first stage, between the nozzle and the sampling plate, a relatively low vacuum is maintained by two mechanical pumps. In the second stage, operated at much higher vacuum, ions are focused into the quadrupole ion trap by a set of lenses. Ions are confined in the ion trap by applying a radio frequency (rf) voltage to the middle (ring) electrode while maintaining both end-cap electrodes at ground potential. A buffer gas (helium) is continuously introduced inside the trap rings to assist in the trapping process. After a specific time of ion accumulation, the trapping rf voltage is turned off and the ions are ejected from the ion trap by applying a negative pulse to the exit end-cap electrode. A high negative voltage, applied to the acceleration grid, pushes the ions into the field free region of the flight tube. The time of flight for all ions of different m/z values is detected by a dual multichannel plate (MCP) detector. The ion signal is amplified and captured by a digital oscilloscope with high time resolution. The spectra are transfered directly from the oscilloscope to a computer for storage.

In the basic operation of the instrument, the ion trap is used as a storing device to couple a continuous ESI source with the pulse nature of a TOF detector. This basic function of the ion trap has been expanded to a variety of procedures providing new applications presented in further chapters. In this case, the personal computer (PC) serves also as a controller in operation of a laser and the ion trap.

Characterization of the ESI IT/linear TOFMS [63] show that the instrument is most suited for the analysis of small analytes (i.e., less than ~20 000 Da). For these analytes, the optimal mass resolution of ~ 1200 fwhm can be obtained. The mass measurement can be performed with mass accuracy errors within 10 ppm when an internal standard is used

and the peaks are isotopically resolved. For an external standard without isotopic resolution, the error is less than 100 ppm. The application of the instrument to the analysis of large analytes presents problems. Adverse effects of the helium buffer gas, ion trap space charge saturation and limited efficiency of trapping results in decreased quality of mass spectra [63].

1.7 Literature cited

[1] Fenn, J. B.; Mann, M.; Meng, C. K.; Wong, S. F.; Whitehouse, C. M. *Mass Spectrom. Rev.* **1990**, 9, 37.

[2] Karas, M.; Hillenkamp, F. *Anal. Chem.* **1988**, 60, 2299.

[3] Cook, K. D. *Mass Spec. Rev.* **1986**, 5, 467.

[4] Thomson, B. A.; Iribarne, J. V. *J. Chem. Phys.* **1979**, 71, 4451.

[5] Blakley, C. R.; McAdams, M. J.; Vestal, M. L. *J. Chromatogr.* **1978**, 158, 261.

[6] Zeleny, J. *Phys. Rev.* **1917**, 10, 1.

[7] Dole, M.; Mack, L. L.; Hines, R.L. *J. Chem. Phys.* **1968**, 49, 2240.

[8] Mack, L. L.; Kralik, P.; Rheude, A.; Dole, M. *J. Chem. Phys.* **1970**, 52, 4977.

[9] Meng, C. K.; Mann, M.; Fenn, J. B. *Proceedings of the 36th Annual Conference on Mass spectrometry and Allied Topics*, San Francisco, CA, **1988**, p.771.

[10] Kebarle, P.; Tang, L. *Anal. Chem.* **1993**, 65, 972A.

[11] Loeb, L. B.; Kip, A. F.; Hudson, G. G.; Bennet, W. H. *Phys. Rev.* **1941**, 60, 714.

[12] Taylor, G. I. *Proc. R. Soc. London A* **1964**, A280, 383.

[13] Yamashita, M.; Fenn, J. B. *J. Phys. Chem.* **1984**, 88, 4451.

[14] Schmelzeisen-Redeker, G.; Butfering, L.; Rolgen, F. W. *Int. J. Mass Spectrom. Ion Proc.* **1989**, 90, 139.

[15] De Juan, L.; De la Mora, J. Fernandes J. *Polym. Mater. Sci. Eng.* **1995**, 73, 29.

[16] Gomez, A.; Tang, L. *Phys. Fluids* **1994**, 6, 404.

[17] Iribarne, J. V.; Thomson, B. A. *J. Chem. Phys.* **1976**, 64, 2287.

[18] Kebarle, P.; Ho, Y. *Electrospray Ionization Mass Spectrometry*; Cole, R. B., Ed.; Wiley Interscience: New York, **1997**; Chapter 1.

[19] Cheng, Z. L.; Siu, K. W. M.; Guevrement, R.; Berman, S. S. *J. Am. Soc. Mass Spectrom.* **1992**, 3, 281.

[20] Tang, L.; Kebarle, P. *Anal. Chem.* **1991**, 63, 2709.

[21] Enke, C. G. *Anal. Chem.* **1997**, 69, 4885.

[22] Whitehouse, C. M.; Dryer, R. N.; Yamashita, M.; Fenn, J. B. *Anal. Chem.* **1985**, 57, 675.

[23] Smith, R. D.; Olivares, J. A.; Nguyen, N. T.; Udseth H. R. *Anal. Chem.* **1988**, 60, 436.

[24] Fenn, B. J.; Mann, M.; Meng, C. K.; Wong, S. F.; Whitehouse, C. M. *Science* **1989**, 246, 64.

[25] Smith, R. D.; Loo, J. A.; Edmonds, C. G.; Barinaga, C. J.; Udseth, H. R. *Anal. Chem.* **1990**, 62, 882.

[26] Przybylski, M.; Glocker, M. O. *Agnew. Chem. Int. Ed. Engl.* **1996**, 35, 806.

[27] Loo, J. A.; Ogorzalek Loo, R. R. *Electrospray Ionization Mass Spectrometry*; Cole, R. B., Ed.; Wiley Interscience: New York, **1997**; Chapter 11.

[28] Crain, P. F. *Electrospray Ionization Mass Spectrometry*; Cole, R. B., Ed.; Wiley Interscience: New York, **1997**; Chapter 12.

[29] Ohashi, Y. *Electrospray Ionization Mass Spectrometry*; Cole, R. B., Ed.; Wiley Interscience: New York, **1997**; Chapter 13.

[30] Poon, J. K. *Electrospray Ionization Mass Spectrometry*; Cole, R. B., Ed.; Wiley Interscience: New York, **1997**; Chapter 14.

[31] Gatlin, C. L.; Turecek, F. *Electrospray Ionization Mass Spectrometry*; Cole, R. B., Ed.; Wiley Interscience: New York, **1997**; Chapter 15.

[32] Bruins, A. P.; Covey, T.R.; Henion, J. D. *Anal. Chem.* **1987**, 59, 2642.

[33] Banks, J. F., Jr.; Shen, S.; Whitehouse, C. M.; Fenn, J. B. *Anal. Chem.* **1994**, 66, 406.

[34] Wilm, M. R.; Mann, M. *Int. J. Mass Spectrom. Ion Proc.* **1994**, 136, 167.

[35] Thomson, R. C. *Meas. Sci. Technol.* **1990**, 1, 93.

[36] Stafford, G. C., Jr.; Kelley, P. E.; Syka, J. E. P.; Reynolds, W. E.; Todd, J. F. J. *Int. J. Mass Spectrom. Ion Proc.* **1984**, 60, 85.

[37] Kelley, P. E.; Stafford, G. C., JR.; Stephens, D. R., U.S. Patent 4 540 884, **1985**.

[38] Nourse, B. D.; Cooks, R. G. *Anal. Chim. Acta* **1990**, 228, 1.

[39] March, R. E. *J. Mass Spectrom.* **1997**, 32,351.

[40] Mathieu, E. *J. Math. Pure Appl.* (J. Liouville) **1868**, 13, 137.

[41] Guan, S.; Marshall, A. G. *Int. J. Mass Spectrom. Ion Proc.* **1996**, 157/158, 5.

[42] Yamashita, M.; Fenn, J. B. *J. Phys. Chem.* **1984**, 88, 4451.

[43] Alexandrov, M. L.; Gall, L. N.; Krasnov, V. N.; Nikoleyev, V. I.; Pavelenko, V. A.; Shkurov, V. A. *Dokl. Akad. Nauk SSSR* **1984**, 277, 379.

[44] Yefchak, G. E.; Schultz, G. A.; Allison, J.; Enke, C. G.; Holland, J. F. *J. Am. Soc. Mass Spectrom.* **1990**, 1, 440.

[45] Boyle, J. G.; Whitehouse, C. M. *Rapid Commun. Mass Spectrom.* **1991**, 5, 400.

[46] Dodonov, A. F.; Chernushevich, I. V.; Laiko, V. V. *International Mass Spectrometry Conference; Amsterdam*, **1991**; Extended Abstracts, p.153.

[47] Williams, E. R.; Henry, K. D.; Wang, B. H.; McLafferty, F. W. *Proceedings of the 37th ASMS Conference on Mass Spectrometry and Allied Topics*, Miami Beach, FL, **1989**, p.449.

[48] Van Berkel, G. J.; Glish, L. G.; McLuckey, S. A. *Anal. Chem.* **1990**, 62, 1284.

[49] Doroshenko, V. M.; Cotter, R. J. *Proceedings of the 45th ASMS Conference on Mass Spectrometry and Allied Topics, Palm Springs*, CA, **1997**, p.1107.

[50] McLuckey, S. A.; Van Berkel, G. J.; Goeringer, D. E.; Glish, G. L. *Anal. Chem.* **1994**, 66, 689A.

[51] Cooks, R. G.; Cleven, C. D.; Horn, L. A.; Nappi, M.; Weil, C.; Nappi, M.; Soni, M. H.; Julian, R. K., Jr. *Int. J. Mass Spectrom. Ion Proc.* **1995**, 146/147, 147.

[52] Weil, C.; Cleven, C. D.; Nappi, M.; Cooks, R. G. *Proceedings of the 44th ASMS Conference on Mass Spectrometry and Allied Topics*, Portland, OR, **1996**, p.118.

[53] Doroshenko, V. M.; Cotter, R. J. *Rapid Commun. Mass Spectrom.* **1996**, 10, 65.

[54] Szabo, I. *Int. J. Mass Spectrom. Ion Proc.* **1986**, 73, 197.

[55] Jonscher, K. R.; Yates, J. R. *Anal. Chem.* **1996**, 68, 659.

[56] Gulcicek, E. E.; Whitehouse, C. M. *Proceedings of the 43th ASMS Conference on Mass Spectrometry and Allied Topics*, Atlanta, GA, **1995**, p.101.

[57] Stephenson, J. L., Jr.; Booth, M. M.; Boue, S. M.; Eyer, J. R.; Yost, R. A. *Biochemical and Biotechnological Applications of Electrospray Ionization Mass Spectrometry*; Snyder, A.P., Ed.; ACS symposium series 619: Washington, DC, **1996**, Vol. 619; 519.

[58] Douglas, D. J.; French, J. B. *J. Am. Soc. Mass Spectrom.* **1992**, 3, 398.

[59] Keiser, R. E., Jr.; Cooks, R. G.; Stafford, G. C., Jr.; Syka, J. E. P.; Hemberger, P. E. *Int. J. Mass Spectrom. Ion Proc.* **1991**, 106, 79.

[60] Michael, S. M.; Chien, B. M.; Lubman, D. M. *Anal. Chem.* **1993**, 65, 2614.

[61] Purves, R. W.; Li, L. *J. Microcolumn Separations* **1995**, 7, 603.

[62] Purves, R. W. *The Development and Application of an Electrospray Ionisation Ion Trap/Linear Time-of-Flight Mass Spectrometer*, Ph.D. Thesis, University of Alberta, **1997**.

[63] Purves, R. W.; Li, L. *J. Am. Soc. Mass Spectrom.* **1997**, 8, 1085.

Chapter 2

Investigation of the Quantitative Capabilities of an Electrospray Ionization Ion Trap/Linear Time-of-Flight Mass Spectrometer[a]

2.1 Introduction

Electrospray ionization (ESI) mass spectrometry is increasingly gaining in importance in biochemical and biomedical sciences [1]. For example, ESI has greatly simplified the application of quantitative liquid chromatography-mass spectrometry (LC-MS) methods to highly polar molecules in the pharmaceutical industry [1]. ESI MS and tandem MS are commonly carried out using quadrupole mass analyzers [2, 3]. Recently, however, many new mass spectrometric configurations, based on other types of mass analyzers or hybrid combinations, have been developed for use with ESI [4]. Compared with other mass analyzers, a time-of-flight (TOF) offers several potential advantages, including high sensitivity and extremely fast data acquisition capabilities [5]. High ion transmission (i.e., no slits) coupled with the ability of the TOF to generate a complete mass spectrum with every ion extraction event results in high sensitivity. The fast data acquisition rates of a TOF are desirable for use with fast separation techniques such as capillary electrophoresis [6].

One method of combining the continuous ESI source with a TOF mass analyzer uses a quadrupole ion trap to temporarily store the ions. This method combines the selective ion storage and MS^n capabilities of an ion trap with the sensitivity and speed of the TOF mass analyzer. The use of an ion trap/TOF mass spectrometer for the analysis of ESI ions was first carried out by Michael et al. [7]. ESI ion trap/TOFMS has been used in several applications, including, among the analysis of peptide mixtures [8] and

[a] A form of this chapter has been published as: R. W. Purves, W. Gabryelski and L. Li "Investigation of the Quantitative Capabilities of an ESI Ion Trap/Linear TOF Mass Spectrometer", Rapid Commun. Mass Spectrom. **1998**, 12, 695.

tryptic digests [9]. However, the quantitative capabilities of this type of instrument have not been investigated.

In this chapter, the capabilities and limitations of ESI ion trap/TOFMS for quantitative analysis are explored using sulfonamides. Sulfonamides are antimicrobial agents that are extensively used to combat infections and/or promote growth in farm animals [10]. The level of sulfonamides in food products destined for human consumption is strictly controlled for several reasons. For example, exposure to these residues can reduce the effectiveness of human therapeutic drugs [11] and can also lead to allergic reactions in sensitive consumers [12]. Furthermore, some sulfonamides are thought to be carcinogenic [13]. Only meat products that contain sulfonamide residues below the maximum residue limit are allowed to enter the food chain [14]. Several techniques, including liquid chromatography-ultraviolet detection (LC-UV) [15] have been used to analyze sulfonamide residues. Mass spectrometric techniques, however, have the advantage of providing molecular weight information and structural data that aids in the confirmation of these residues. Detection of various sulfonamide mixtures has been carried out using ESI or ionspray combined with LC [10, 16], capillary electrophoresis [17] or electrochromatography [18].

The focus of this chapter is on the analytical merits of ESI ion trap/TOFMS. These include reproducibility, detection limits, and the linear range of the calibration curves. The factors limiting the detection capabilities of the instrument for a single component and a multicomponent analysis will be discussed. The detectability of sulfonamides using ESI ion trap/TOFMS is compared to results obtained using a quadrupole mass spectrometer.

2.2 Experimental

2.2.1 Instrumentation

A description of the ion trap/linear TOF mass spectrometer has been given in Chapter 1 [19, 20]. In analysis of sulfonamides, analyte was introduced into the 4 μL/min solvent stream, using a 0.5 μL Rheodyne loop injector (Chromatographic Specialties Inc., Brockville, ON). A high voltage (3 to 4 kV) was applied to the ESI needle tip (positioned approximately 1 cm from the nozzle orifice) to initiate the ESI process. Prepurified, heated N_2 gas flowed into this region at a rate of 4 L/min to assist the desolvation of the ions. Electrosprayed ions entered a two-stage interface where the nozzle plate separating the atmospheric and high vacuum regions was operated at 40 V. After passing through the orifice of the sampling plate (operated at 4 V), ions entered the high vacuum region were they were focused by a set of three lenses into a quadrupole ion trap. For this study, the first and third lenses were grounded while the second lens was operated at -80 V. Helium at 0.54 mL/min was added to the ion trap to aid in the trapping. A radio frequency (rf) voltage (800 V_{p-p}) operated at 1 MHz was applied to the ring electrode to temporarily store the ions. The ions were allowed to accumulate in the ion trap for a predetermined period of time (250 ms was used unless otherwise indicated). The rf voltage was then shut off and allowed to decay to 0 V. At this time the exit endcap was pulsed negative (-960 V) to extract the ions into the flight tube, which was operated at -4100 V.

After separating in the 87 cm long flight tube, ions were detected using a modified dual multichannel plate (MCP) detector (Galileo Electro-Optics Corp., Sturbridge, Massachusetts). The ion signal was amplified using a 500 MHz, 20 dB amplifier (CLC 100, Comlinear Corporation, Fort Collins, CO) and monitored using a LeCroy 9374M digital oscilloscope (time resolution of 1 ns/point was used). With this 8-bit digitizer, different oscilloscope voltage settings were used to cover a broad range of

signal variation. Spectra were collected and downloaded to a Pentium PC using data acquisition software that was developed at the University of Alberta [21]. Mass spectra presented in this chapter represent a consecutive sum of 40 ion extraction events obtained during the elution of the analyte, unless otherwise noted. Flow injection profiles were constructed using the following procedure. First, the analyte was injected and the software was used to collect the mass spectra at a given data acquisition rate. For each mass spectrum collected during an injection, the area of the MH^+ peak was calculated. Consequently, a flow injection profile was a plot of the MH^+ peak area as a function of time. Note that the total peak area of an analyte for each injection was calculated by measuring the area under the curve of the flow injection profile.

A previous study of this instrument [19] illustrated that the flow rate of the helium buffer gas into the ion trap is a crucial variable as it has a strong influence on the peak area for low molecular weight analytes (i.e., < 1000 Da). In particular, when a low buffer gas flow rate was used (i.e., < 0.40 mL/min), small changes in the flow rate had a large effect on the peak area. When a higher flow rate was used (i.e., > 0.40 mL/min), the peak area dependence on flow rate was reduced. However, the use of a flow rate greater than 0.7 mL/min degraded the mass resolution. Consequently, a flow rate of 0.54 mL/min was used for this study as it gave the best compromise for maximizing peak area and resolution while minimizing fluctuations in peak area.

Comparative ESI MS experiments were also carried out using a PE Sciex API 100 LC (Concord, ON) quadrupole mass spectrometer. The solvent composition and the flow rate were identical to that used for the ion trap/TOF mass spectrometer. The same 0.5 µL Rheodyne loop injector (Chromatographic Specialties Inc., Brockville, ON) was connected through the capillary line to the electrospray capillary tip. The scan speed was adjusted to 250 ms and a 2 u detection window was monitored in single ion mode using 0.5 u steps. For multicomponent analyses, five detection windows (2 u) were monitored in multiple ion mode using 0.25 u steps.

2.2.2 Sulfonamides and chemicals

Five sulfonamides were examined in this study. Their structures and corresponding molecular weights are presented in Chart 2.1.

Chart 2.1 Structure of the five sulfonamides used in this study.

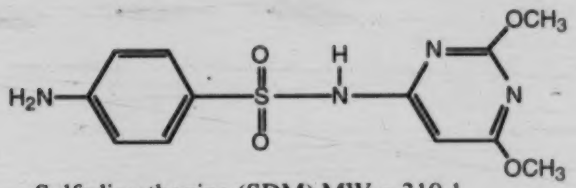

Sulfadimethoxine (SDM) MW = 310.1

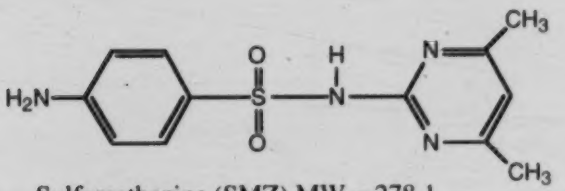

Sulfamethazine (SMZ) MW = 278.1

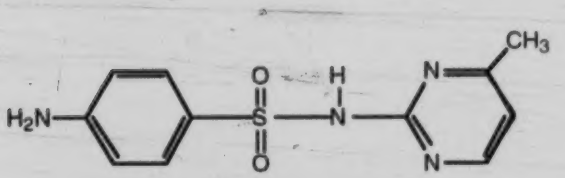

Sulfamerazine (SMR) MW = 264.1

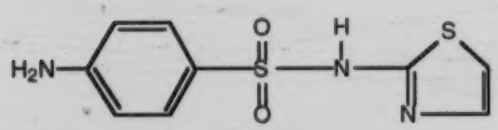

Sulfathiozole (STZ) MW = 256.0

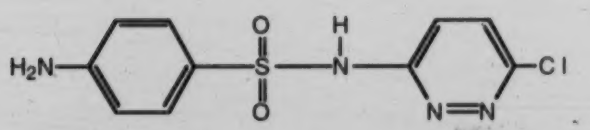

Sulfachloropyridazine (SCP) MW = 284.0

They were analyzed using a solvent combination consisting of 80% acetonitrile, 20% water (v/v) and 2 mM ammonium acetate, unless otherwise indicated. The sulfonamides were purchased from Sigma Chemical Company (St. Louis, MO) and used without further purification. Acetonitrile and HPLC grade water were purchased from BDH Laboratories Inc. (Toronto, ON).

2.3 Results and Discussion

2.3.1 Solution properties

In electrospray, the analyte distribution can be affected by the formation of various cation-analyte adducts when sodium or potassium ions are present in solution [22]. These adducts reduce the signal of the protonated analyte (the principal species in quantitation of sulfonamides) and therefore will adversely affect the quantitative analysis of the analyte. The addition of volatile buffers, such as ammonium acetate, to the analyte solution [17], restricts Na^+ or K^+ adduct formation and therefore is an important factor to be considered when analyzing sulfonamides.

Figure 2.1 shows the effect of varying the concentration of ammonium acetate on the mass spectra obtained from a continuous infusion of 1 µM SDM. Figure 2.1 A shows that with no buffer present, the mass spectrum is dominated by the MNa^+ peak. Figures 2.1 B to D illustrate that the addition of ammonium acetate resulted in preferential formation of the MH^+ ion observed in the mass spectra. Furthermore, the intensity of the sodium adduct peak was dramatically reduced, and ammonium adduct peaks were not observed. However, Figure 2.1 D also shows that the addition of 10 mM ammonium acetate significantly suppresses the analyte signal. Consequently, a concentration of 2 mM ammonium acetate was used as it gave the best compromise between maximizing the peak area of the protonated molecular ion and suppressing the formation of the sodium adduct peak.

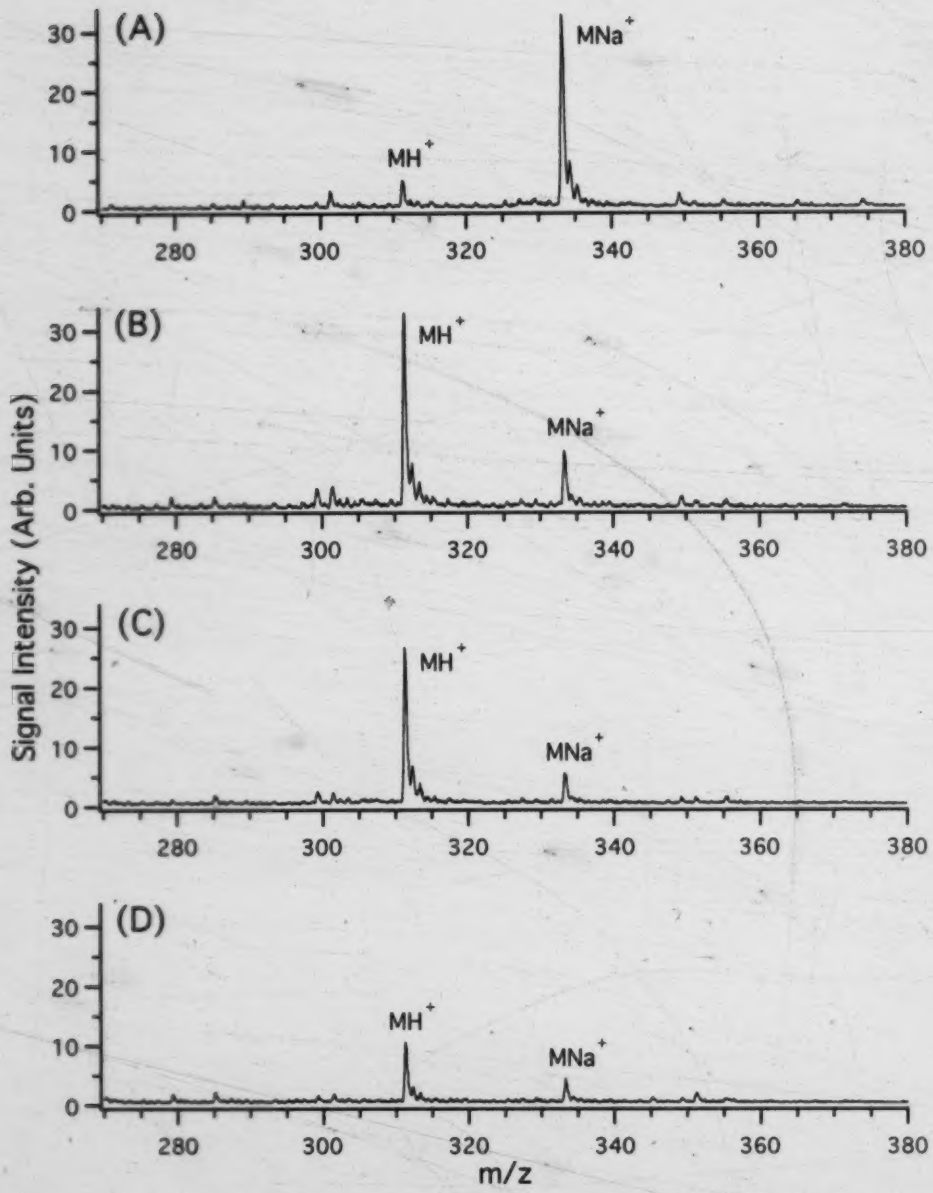

Figure 2.1. Effect of different concentrations of ammonium acetate on the mass spectra of 1 μM SDM in 80% acetonitrile/20% water. (A) No ammonium acetate added, (B) 0.5 mM ammonium acetate, (C) 2 mM ammonium acetate and (D) 10 mM ammonium acetate.

2.3.2 Detection limits and linear range

The detectability of the instrument for five sulfonamides is illustrated in Figure 2.2 and Table 2.1. Figure 2.2 shows a mass spectrum obtained from an injection of a mixture containing 100 femtomole (fmol) of each of the five sulfonamides studied.

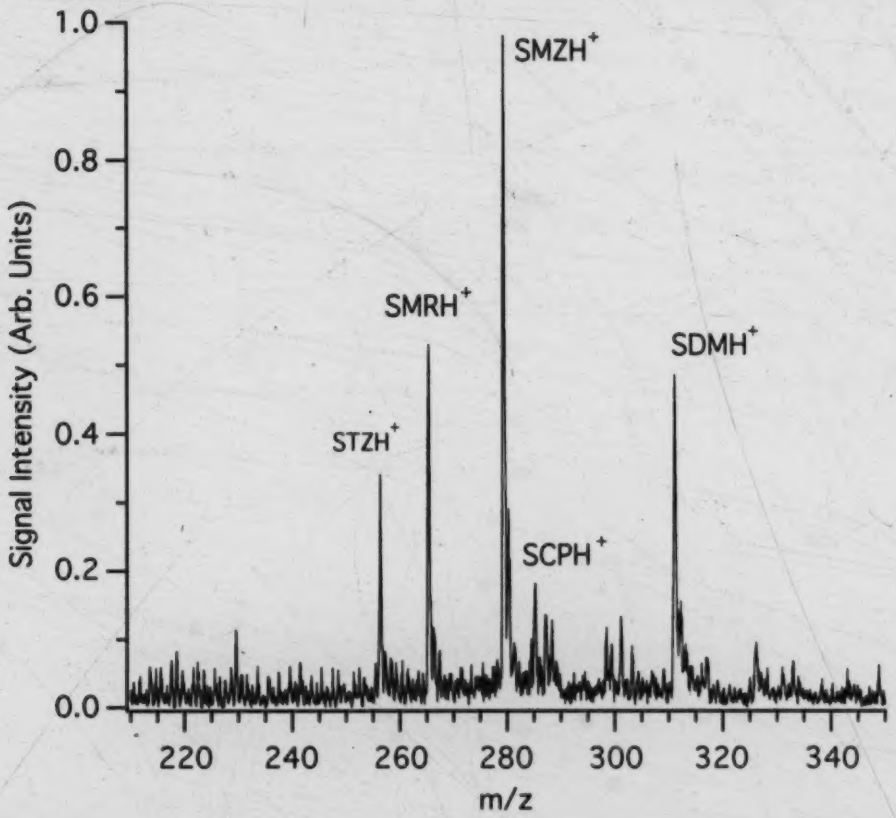

Figure 2.2. Mass spectrum obtained from an injection of a mixture of SDM, SCP, SMZ, SMR, and STZ. The mixture contained 100 fmol of each sulfonamide.

Table 2.1 shows detection limits for sulfamides determined in a flow injection experiment using 2 mM ammonium acetate buffer. The detection limits were estimated based on three times the standard deviation of the blank signal.

Table 2.1. Detection limits for 5 sulfonamides examined in this study.

Sulfonamide	Detection Limit (fmol)
Sulfadimetoxine (SDM)	2.1
Sulfachlorpyridazine (SCP)	11
Sulfamethazine (SMZ)	3.1
Sulfamerazine (SMR)	2.6
Sulfathiazole (STZ)	6.2

It should be pointed out that the detection limits for mixtures prepared using 0.05 mM ammonium acetate are slightly improved (up to a factor of 2) compared with mixtures prepared using 2 mM ammonium acetate. However, the use of 0.05 mM ammonium acetate should be restricted to qualitative determinations because the narrow linear range of a calibration curve using 0.05 mM ammonium acetate.

For all five sulfonamides studied, a linear response for a plot of peak area versus amount injected was obtained for almost 3 orders of magnitude using 2 mM ammonium acetate. Figure 2.3 shows a typical calibration curve for SDM from 10 femtomole (fmol) injected to 7.5 picomole (pmol) injected. The inset shows an expanded view of the low end of the plot from 10 to 500 fmol. For each point on the calibration curve, seven injections were carried out and the error bars represent one standard deviation. The correlation coefficient over the range from 10 fmol to 4 pmol was 0.998. All of the sulfonamides studied exhibited similar behavior; the upper and the lower limit of linearity shifted depending upon which sulfonamide was being studied due to differences in detectability.

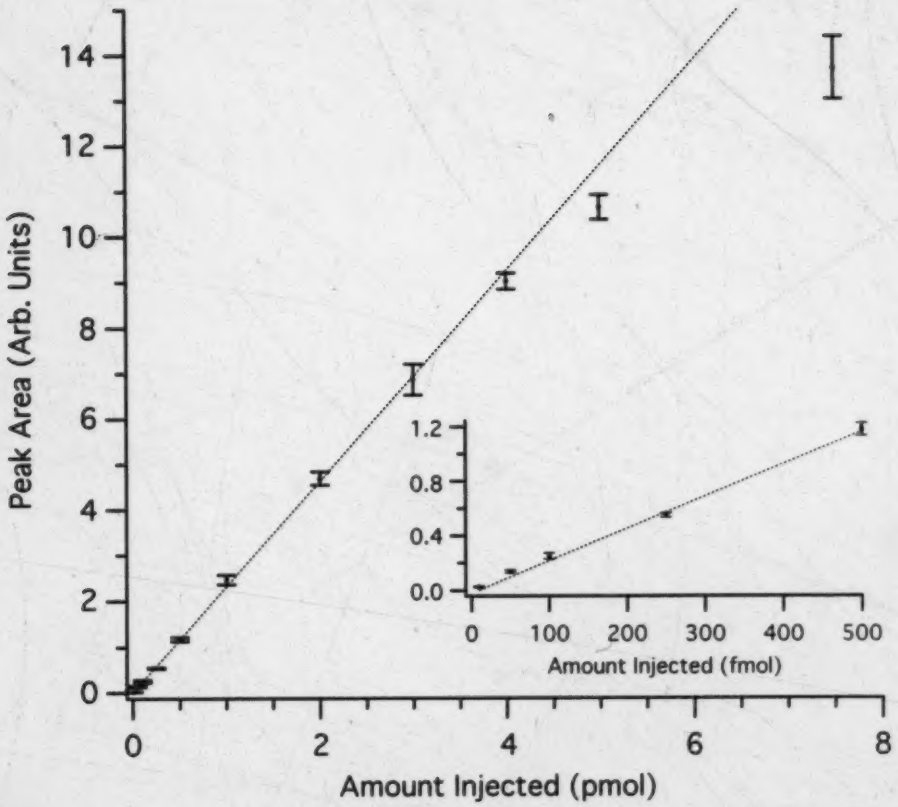

Figure 2.3. Calibration curve for a series of loop injections of SDM with an expanded view of the low end of the plot shown in the inset. 2 mM ammonium acetate buffer in 80% acetonitrile/20% water (v/v) was used. See text for details.

The lower limit of quantitation is restricted by the chemical background noise. Figure 2.4 shows a mass spectrum (only 25 consecutive ion extraction events) obtained from an injection of 5 fmol of SDM. The peak corresponding to the protonated molecule of SDM is barely discernible from the chemical background noise. To improve the detection limit, and hence the lower limit of quantitation, tandem mass spectrometry

techniques could be carried out on the analyte of interest [23] and a corresponding fragment peak monitored. The relative improvement in noise reduction is expected to be significantly larger than the loss of analyte signal, thereby improving the S/N ratio for low level injections.

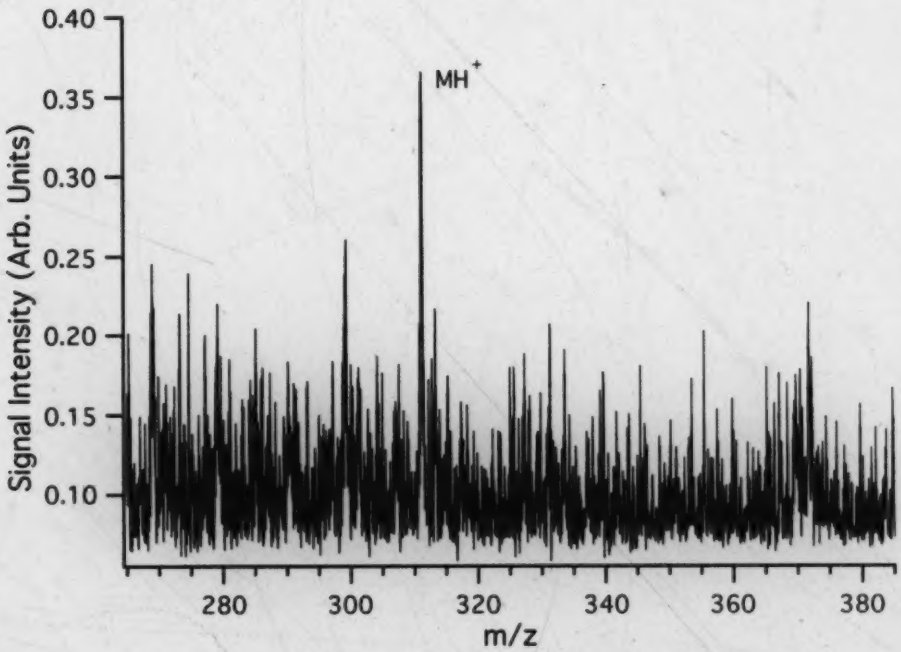

Figure 2.4. Mass spectrum of an injection of 5 fmol of SDM (2 mM ammonium acetate buffer in 80% acetonitrile/20% water (v/v)) showing the limitations due to the chemical background noise using an electrospray ionization ion trap/linear TOFMS. 25 ion extraction events were summed to obtain this mass spectrum.

A negative deviation from linearity is observed at the upper end of the calibration curve shown in Figure 2.3. The detection system, the electrospray ionization source, and the ion trap, are all potential sources of this deviation. When the detection system was

examined, the CLC 100 amplifier (Comlinear Corporation, Fort Collins, CO) provided a linear response over the range in question. Furthermore, the voltage drop across the MCP plates was changed from the usual setting of 900 V across each plate to different values to change the gain. If the detection system was causing the deviation to occur, the injection amount where this deviation was observed would be expected to change as the gain was varied. The deviation in linearity was still observed at the same place in the calibration curve, consequently, the detector was not the cause of the non-linearity.

Several additional experiments were carried out to determine the cause of non-linearity at the upper end of the calibration curve. A comparison of data obtained using ESI ion trap/linear TOFMS with data obtained using ESI quadrupole MS proved to be the most useful. Figure 2.5 shows plots of peak area for SDM versus injection amount using both instrumental configurations. An important observation from this figure is that the shape of the curves for both instruments are similar. This observation suggests that the same limiting factor determines the response function in the high concentration range. The dynamic range of the ion trap can be restricted by the number of ions that can be stored [24]. However, it is not the limiting factor for the upper limit of linearity in this experiment. Based on experiments using multiple components in a mixture (see below), the deviation in the upper limit of calibration curves was determined to be caused by the ESI source.

2.3.3 Reproducibility

The quantitative reproducibility of the ESI ion trap/linear TOFMS was also examined. The reproducibility is sensitive to considerations such as the electrospray needle tip-capillary connection, the condition of the electrospray needle tip, and the inner diameter of the electrospray needle. Generally, RSD values for seven repetitive injections ranged from 4 to 7% for each injection amount. Figure 2.6 shows histograms obtained for injections of SDM at 10 fmol, 100 fmol, and 1 pmol.

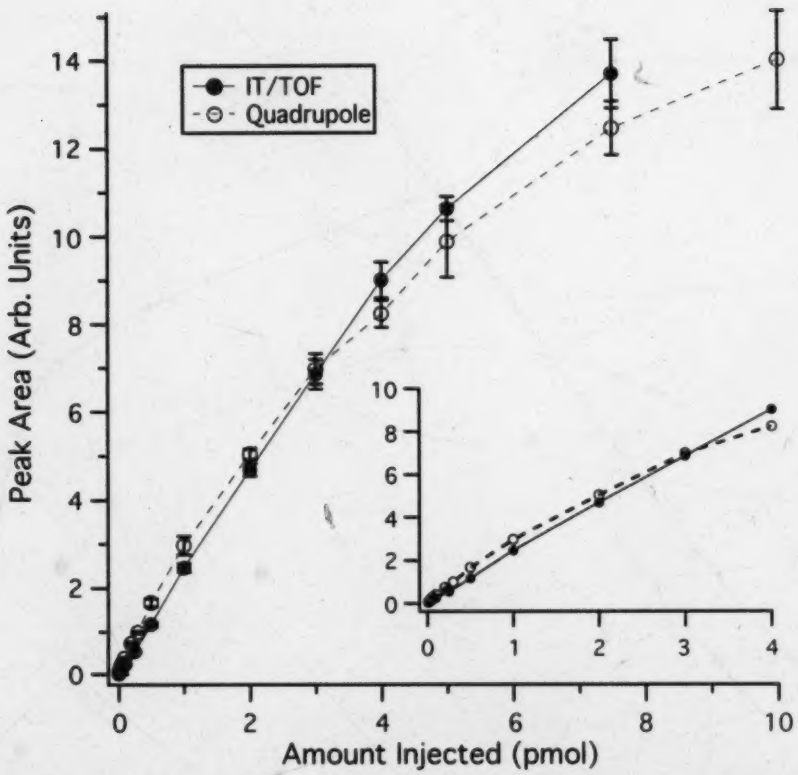

Figure 2.5. Comparison of calibration curves of SDM using ion trap/linear TOFMS and quadrupole MS. Linearity at the low end is shown in the inset. The lines connect the points representing the average of 7 measurements.

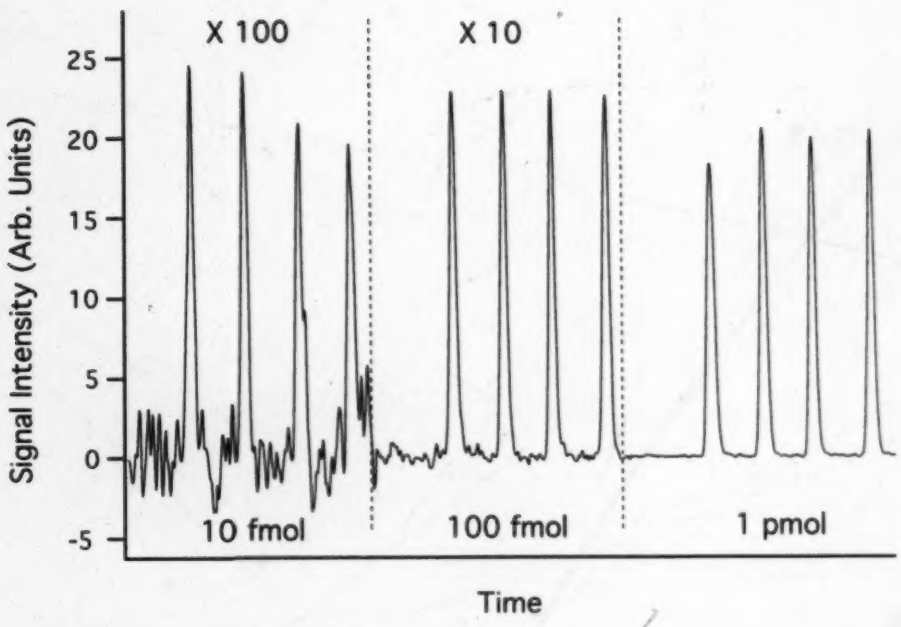

Figure 2.6. Reproducibility of the electrospray ionization ion trap TOFMS illustrated using repeat injections of SDM at 10 fmol, 100 fmol, and 1 pmol.

The reproducibility over the course of an 8 hour day was also examined and a graph of the peak area of SDM obtained during this period is shown in Figure 2.7 A. The use of peak area alone gave a RSD of 8.1%. However, when SMZ was added as an internal standard, the RSD value was reduced to 6.2%, as is shown in Figure 2.7 B.

2.3.4 Multicomponents analyses

Since a TOF mass analyzer records a complete mass spectrum with every ion extraction event, the ESI ion trap/TOFMS is well suited for multicomponent analysis. Multicomponent analysis can be useful for determining co-eluting analytes or for direct analysis of a mixture without separation. Calibration curves established for individual

analytes do not provide information on whether the detectability and linear dynamic range of single component remains constant when analyzed as a part of a mixture.

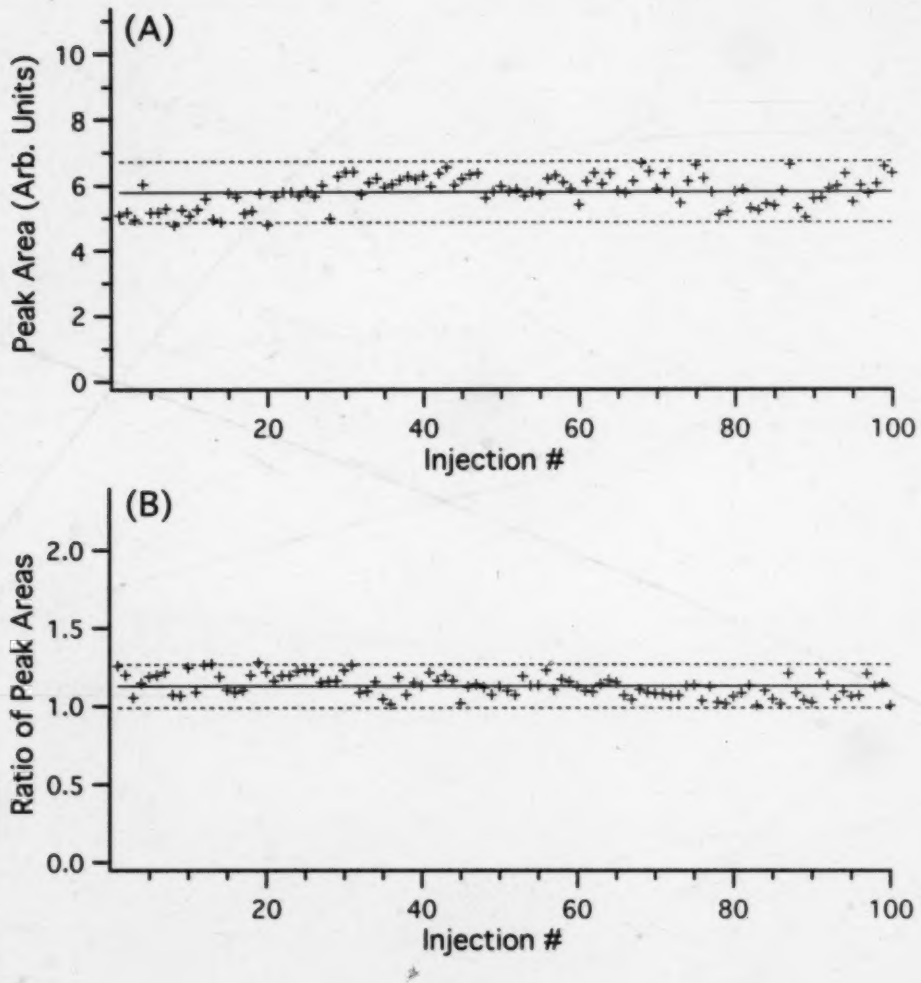

Figure 2.7. Repeat injections of SDM (500 fmol) over an eight hour period. (A) A peak area of SDM as a detector response. (B) A ratio of peak areas (SDM/SMZ) as a detector response (SMZ (500 fmol) used as an internal standard).

Several experiments involving injections of sulfonamide mixtures with varying concentrations of each sulfonamide were carried out to determine the dynamic range of a linear calibration, the detection limits, and the correlation of signal responses.

Figure 2.8 shows the calibration curves of individual components in a mixture obtained by using the ion trap/TOF mass spectrometer. Similar plots obtained using the API 100 quadrupole mass spectrometer are presented in Figure 2.9.

The mixture of sulfamides contained SDM, SMZ, SMR, STZ and SCP in a molar ratio of 1, 1, 1, 2, 4, respectively. To establish the calibration curves, the total amount of all analytes in the mixture was varied while keeping the molar ratios of individual analytes constant. Figure 2.8 and 2.9 show that there are two characteristic regions in the calibration curves for both instruments. One is the linear region, where the signal (peak area) for each analyte in the mixture is proportional to the injected amount of the corresponding analyte. In this low concentration region, the slope and the intercept of the calibration curve for each component in the mixture are found to be the same as those obtained from a single component analysis.

This result indicates that there is no interference among these analytes for the quantitative analysis of the individual analytes in this concentration region. In the non-linear region a negative deviation of the signal responses is observed. An expanded view of the plot in Figure 2.8 B shows that the deviation from linearity starts at the point where the total amount of analyte injected is approximately 13.5 pmol (i.e., 1.5 pmol SDM, 1.5 pmol SMZ, 1.5 pmol SMR, 3 pmol STZ, and 6 pmol SCP). At this point, the suppression for the least sensitive analyte (i.e., SCP) becomes visible. The total peak area for all the analytes present in the mixture, calculated at the deflection point (i.e., ~13.5 pmol for mixture analysis), is comparable with the peak area at the deflection point obtained in the single component experiment (i.e., ~4 pmol for SDM shown in Figure 2.3).

Figure 2.10 illustrates the correlation between the signal intensities of the analytes in the mixture obtained for the ion trap/TOF mass spectrometer.

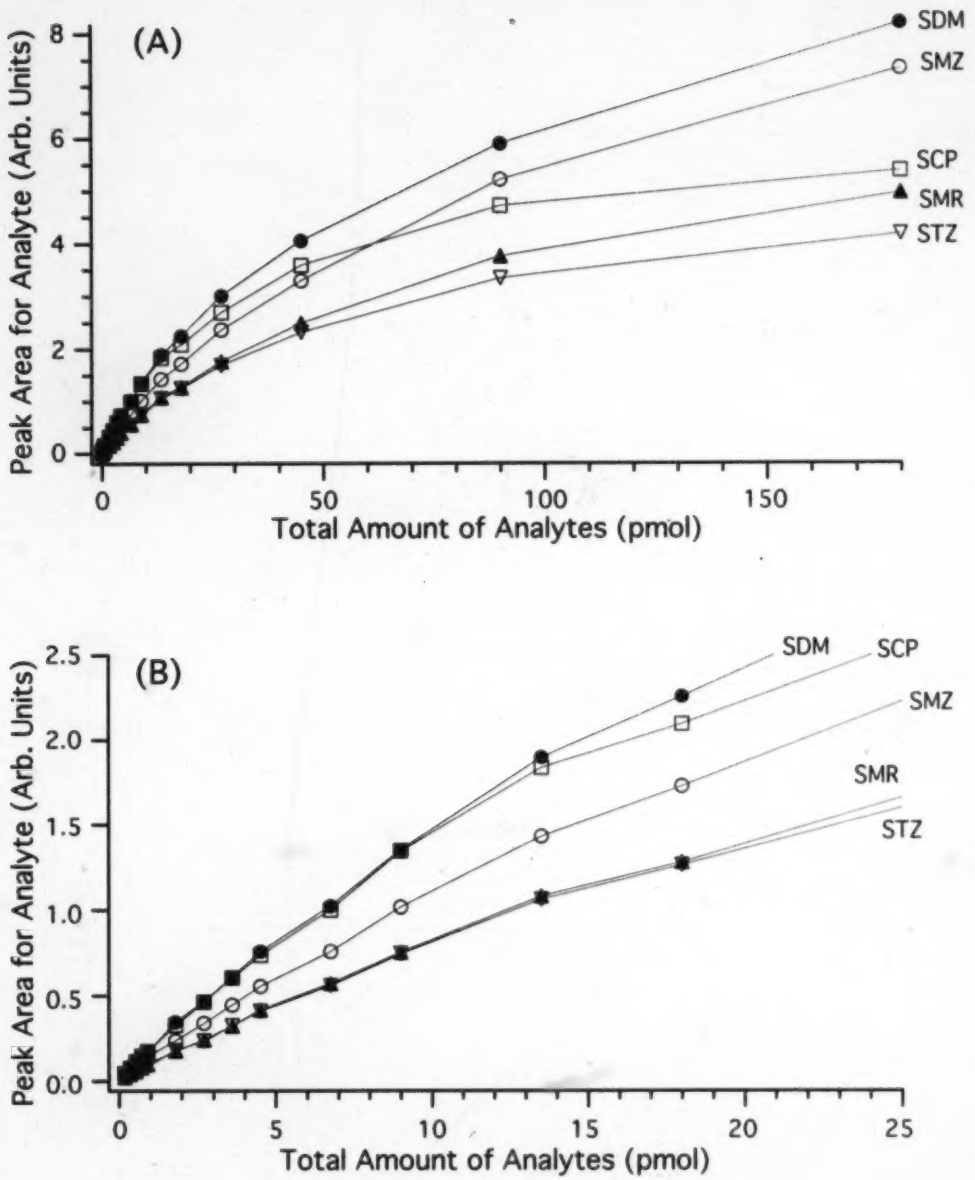

Figure 2.8. Calibration curves for a multicomponent analysis using ion trap/linear TOFMS. (A) The entire calibration range. (B) The linear range at the low end of the calibration curve. The lines connect the points representing the average of 3 measurements.

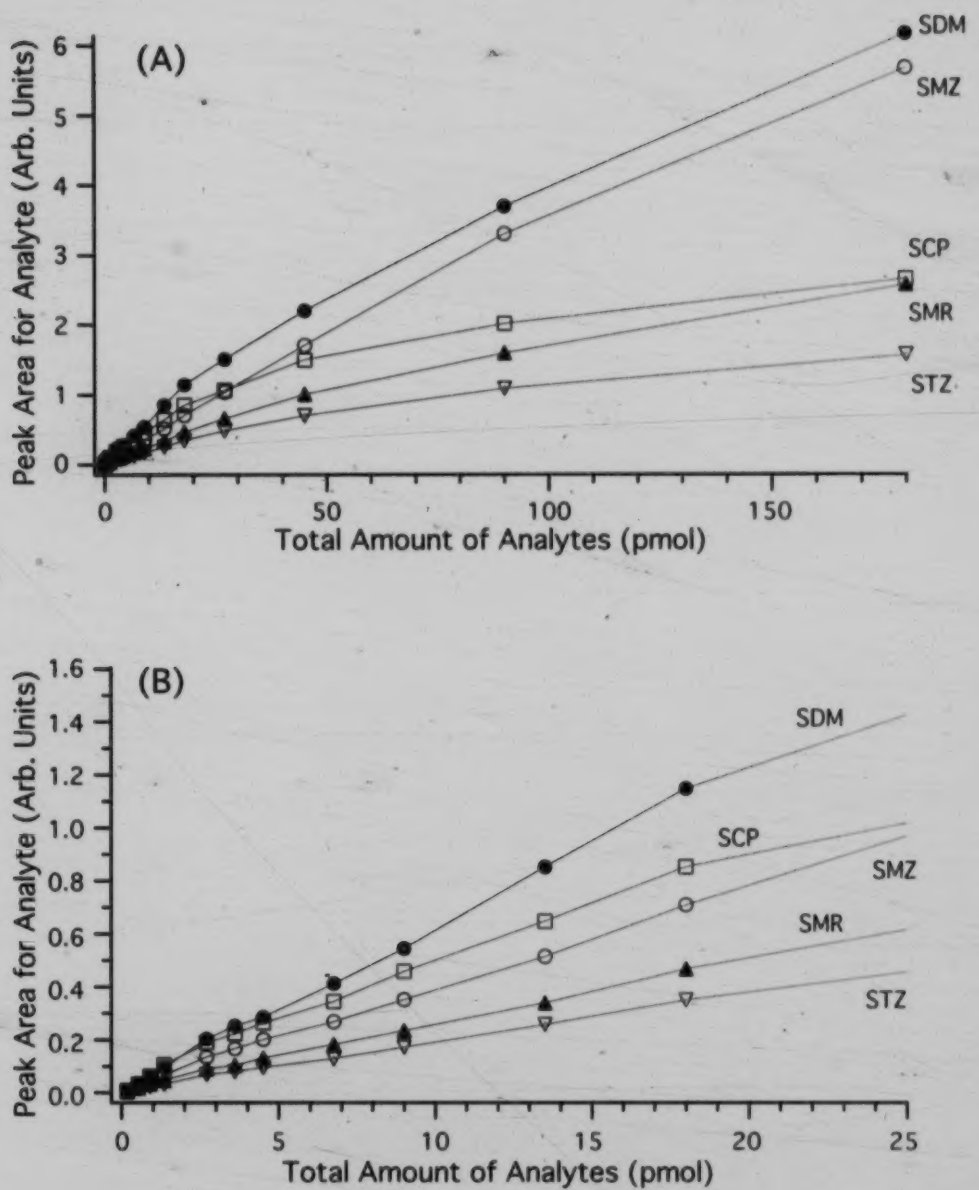

Figure 2.9. Calibration curves for a multicomponent analysis using quadrupole MS. (A) The entire calibration range. (B) The linear range at the low end of the calibration curve. The lines connect the points representing the average of 3 measurements.

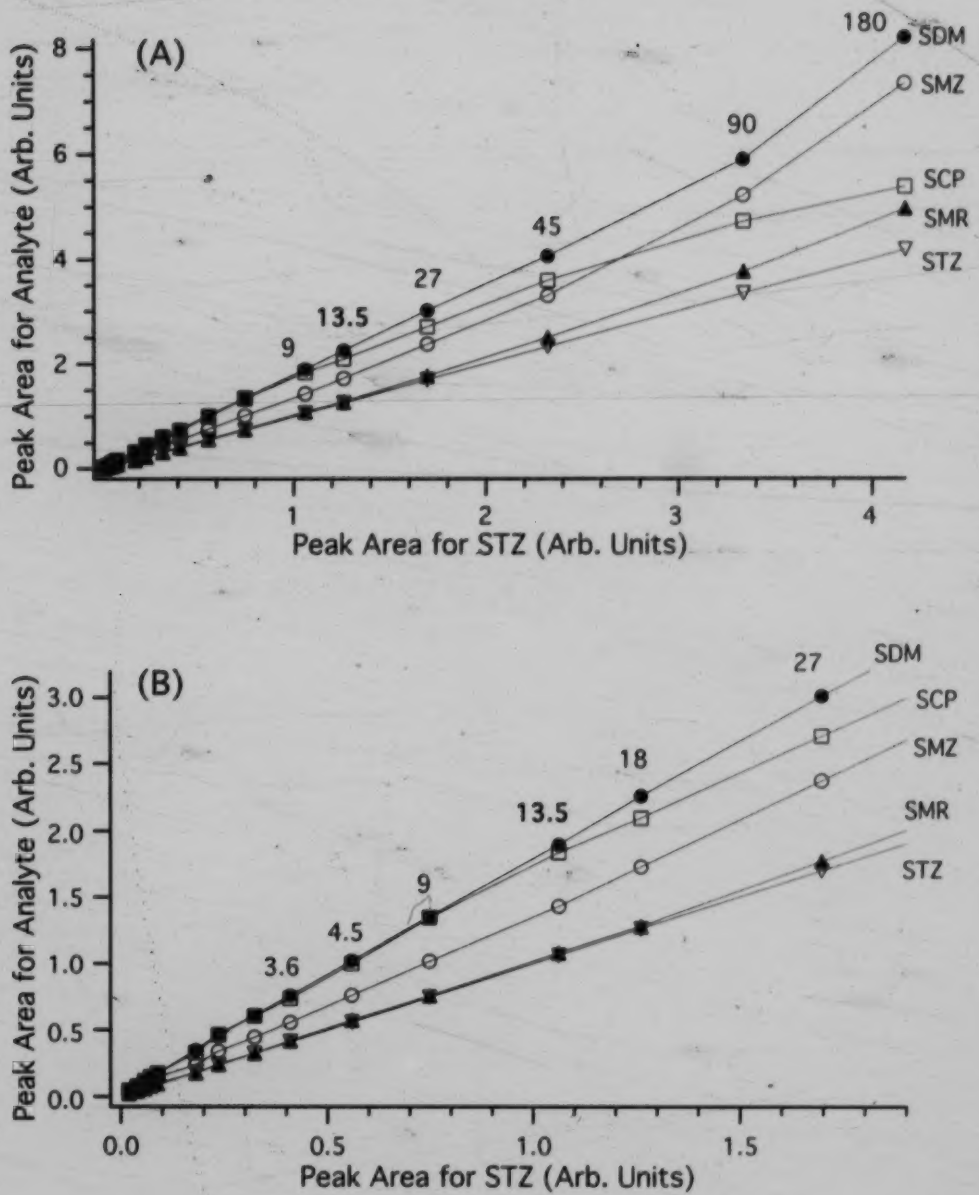

Figure 2.10. Signal correlation for a multicomponent analysis using ion trap/linear TOFMS. (A) The entire calibration range. (B) The linear region. The numbers above each calibration point indicate the total amount of all analytes present in the mixture.

The peak area of each sulfonamide was plotted versus the peak area of STZ at each calibration point. The numbers above each calibration point express the total amount of all the analytes present in the mixture. In the linear calibration range, the relative responses (signal ratios) for all analytes are constant (linear relationship between the analyte signals). However, starting from the deflection point (i.e., 13.5 pmol), a deviation from this linear relationship is observed. Figure 2.10 shows that the extent of signal suppression is not the same for all analytes in the high concentration range. In comparison with STZ, the level of suppression for the more sensitive analytes (SDM, SMZ, SMR) is smaller (positive deviation from linear slope) while it is larger for the less sensitive SCP (negative deviation from linear slope). The plots in the high concentration region in Figure 2.10 could not result from ion trap discrimination effects or ion transmission losses. For a very narrow m/z range of analytes, the m/z discrimination resulting from different trapping efficiencies or preferential m/z storage is negligible [25]. Furthermore, ion transmission losses cannot explain the change in the slopes in the high concentration region relative to the slopes in the low concentration region. A similar plot of signal correlation (not shown) was obtained for the multicomponent analysis using the API 100 LC quadrupole mass spectrometer. Based on these results, it can be concluded that the shape of the calibration plots and the distortion from linearity are caused by the properties of the ESI source.

The results presented here are consistent with a model that predicts the response functions of analytes using ESI [26]. In the low concentration region, analytes compete only with the electrolyte for a position on the surface of the forming droplet and they do not compete with each other. Above a certain critical total amount of analytes (limiting surface capacity for analytes), analyte competition for the surface location occurs. In this process the more sensitive analyte dominates the less sensitive one. This model rationalizes the quantitative behavior for the five component mixture of sulfonamides in the linear range and in the region where the deviation from linear slopes was observed.

In addition, according to the model, the use of high concentrations of electrolyte should extend the upper linear range. However, as pointed earlier, in the analysis of sulfonamides, the addition of ammonium acetate with a concentration higher than 2 mM can significantly reduce the analyte signal. Consequently, the detection of small amounts of analytes is not possible when high concentration of ammonium acetate is used. Nevertheless, it is conceivable that the use of an appropriate electrolyte that gives limited analyte suppression at high concentration may extend the linear range of quantitation in ESI.

There are a few important considerations for multicomponent analyses using ESI ion trap/linear TOFMS. The ESI source characteristics determine the quantitation capabilities of the analysis. The linear range of the calibration curve is the only region where there is proportionality between the signal intensity of the analyte and amount of analyte injected. The upper limit of this range depends on the identity and concentration of an electrolyte, the flow rate of solution to the needle tip, and the ESI current. Increasing the number of components in the analyzed mixture narrows the linear range for a single analyte in the mixture. The appropriate choice of a standard when using the internal standard method may extend the useful quantitation range. As seen in Figure 2.10, STZ is an acceptable standard for SMR. However, SCP is not a reliable standard for SDM, despite the fact that these analytes represent the same class of compounds.

2.3.5 Detectability of ion trap/TOFMS versus quadrupole MS

Detectabilities using ion trap/TOFMS and the API 100 LC mass spectrometer were compared using the same data acquisition rate (4 spectra/sec and 4 scans/sec, respectively). For multicomponent analyses, the API 100 LC mass spectrometer was operated in the multiple ion detection mode (5 windows) and for single component analyses, in the single ion monitoring mode. The detection limits calculated for the single component experiment were comparable for both instruments. However, for the

mixture of five sulfonamides, detection limits for a single constituent were three times lower using ESI ion trap/TOFMS. The advantage of using ESI ion trap/TOFMS should be more pronounced for faster separations and/or for a larger number of analyte components monitored.

2.4 Summary

The characteristics of an ion trap/linear TOFMS for quantitative analysis has been examined. For quantitation purposes, the solution conditions for ESI are a very important variable. For the analysis of sulfonamides, the addition of ammonium acetate to the solvent was a necessary step as it limited the formation of sodium and potassium adducts. Of the five sulfonamides studied, three were detected when 5 fmol were injected. A plot of peak area vs. amount injected for a single compound was linear for almost 3 orders of magnitude. The lower limit of quantitation of this curve is currently restricted by the chemical background noise. Multicomponent analysis showed that the linear range of the calibration curves is restricted by the ESI source properties. The presence of many components in a mixture narrows the linear range for a single analyte that is being monitored in that mixture. The detectability of analytes using ESI ion trap/TOFMS was comparable to results obtained using the API 100 LC mass spectrometer for single ion detection, and was superior for multicomponent analyses. Both the short term and long term quantitative reproducibility of this instrument were examined and the RSD values are in the range of 4 to 8%.

2.5 Literature cited

[1] Gelpi, E. *J. Chromatogr. A* **1995**, 703, 59.

[2] Fenn, J. B.; Mann, M.; Meng, C. K.; Wong, S. F.; Whitehouse, C. M. *Science* **1989**, 246, 64.

[3] Smith, R. D.; Loo, J. A.; Edmonds, C. G.; Barinaga, C. J.; Udseth, H. R. *Anal. Chem.* **1990**, 62, 882.

[4] Gaskell, S. J. *J. Mass Spectrom.* **1997**, 32, 677.

[5] Cotter, R. J. *Time-of-Flight Mass Spectrometry: Instrumentation and Applications in Biological Research*; American Chemical Society: Washington, DC, **1997**.

[6] Banks Jr., J. F.; Dresch, T. *Anal. Chem.* **1996**, 68, 1480.

[7] Michael, S. M.; Chien, B. M.; Lubman, D. M. *Anal. Chem.* **1993**, 65, 2614.

[8] Wu, J. T.; Huang, P. Q.; Li, M. X.; Qian, M. G.; Lubman, D. M. *Anal. Chem.* **1997**, 69, 320.

[9] Qian, M. G.; Lubman, D. M. *Anal. Chem.* **1995**, 67, 2870.

[10] Porter, S. *Analyst* **1994**, 119, 2753.

[11] Haagsma, N.; Pluijmakers, G. J. M.; Aerts, M. M. L.; Beek, W. M. J. *Biomed. Chromatogr.* **1987**, 2, 41.

[12] Brady, M. S.; Katz, S. E. *J. Food Prot.* **1988**, 51, 8.

[13] Woodward, K. N. *Human Exp. Toxic* **1992**, 11, 60.

[14] Boison, J. O.; Keng, L. J.-Y. *J. AOAC Int.* **1995**, 78, 651.

[15] Long, A. R.; Short, C. R.; Barker, S. A. *J. Chromatogr.* **1990**, 502, 87.

[16] Perkins, J. R.; Parker, C. E.; Tomer, K. B. *J. Am. Soc. Mass Spectom.* **1992**, 3, 139.

[17] Johansson, I. M.; Pavelka, R.; Henion, J. D. *J. Chromatogr.* **1991**, 559, 515.

[18] Dekkers, S. E. G.; Tjaden, U. R.; van der Greef, J. *J. Chromatogr. A* **1995**, 712, 201.

[19] Purves, R. W.; Li, L. *J. Am. Soc. Mass Spectrom.* **1997**, 8, 1085.

[20] Purves, R. W.; Li, L. *J. Microcolumn Separations* **1995**, 7, 603.

[21] Coulson, L. D.; Nagra, D. S.; Guo, X.; Whittal, R. M.; Li, L. *Appl. Spectrosc.* **1994**, 48, 1125.

[22] Griffey, R. H.; Sasmor, G.; Greig, M. J. *J. Am. Soc. Mass Spectrom.* **1997**, 8, 155.

[23] Qian, M. G.; Lubman, D. M. *Rapid Commun. Mass Spectrom.* **1996**, 10, 1911.

[24] McLuckey, S. A.; Van Berkel, G. J.; Goeringer, D. E.; Glish, G. L. *Anal. Chem.* **1994**, 66, 689A.

[25] Purves, R. W. *The Development and Application of an Electrospray Ionisation Ion Trap/Linear Time-of-Flight Mass Spectrometer*, Ph.D. Thesis, University of Alberta, **1997**.

[26] Enke, C. G. *Anal. Chem.* **1997**, 69, 4885.

Chapter 3

Characterization of an Electrospray Ionization Ion Trap/Linear Time-of-Flight Mass Spectrometer for Phenylthiohydantoin (PTH)-Amino Acid Analysis[a]

Mass spectrometry offers an attractive method for the detection and identification of PTH-amino acids. The Electrospray Ionization Ion Trap/Linear Time-of-Flight Mass Spectrometer with its speed, sensitivity, and specificity of detection could be used in analysis of these compounds.

3.1 Introduction

The use of Edman sequencing chemistry [1, 2] for determining the primary structure of a protein is a well-established method in biochemical research. The final products of stepwise chemical degradation of proteins, phenylthiohydantoin (PTH) derivatives of amino acids (Figure 3.1), are generally analyzed by high performance liquid chromatography (HPLC) with UV absorbance detection. Despite systematic improvements over the years, the technique still suffers from several limitations [3].

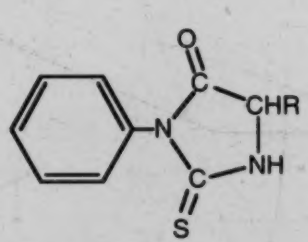

Figure 3.1. Phenylthiohydantoin (PTH)-amino acid. R is the side chain of an amino acid.

---

[a] A form of this chapter has been published as: W. Gabryelski, R. W. Purves and L. Li "Characterization of an ESI Ion Trap/Linear TOF Mass Spectrometer for PTH-Amino Acid Analysis", Int. J. Mass Spectrom. Ion Processes, **1998**, 176, 213.

First, the detection method requires a complete separation of PTH-amino acids by HPLC, which is often slow. For sequencers capable of carrying out short degradation cycles, the detection step is the limiting step for speed. Furthermore, the low detectability of PTH-derivatives by UV detection also limits the overall sensitivity of the sequencing process. At present, partial sequences using low picomole amounts of peptides or proteins can be obtained. Finally, a major drawback with UV detection is that it cannot provide structural information for identification of modified or non-standard amino acids.

The interest in coupling an Edman sequencer with mass spectrometry during the last 25 years has resulted in MS characterization of PTH-amino acids by electron ionization [4, 5], chemical ionization [6], and thermospray ionization [7]. The use of electrospray ionization (ESI) for studying PTH-amino acids in an ion trap mass spectrometer has been reported [8]. There are also several studies on the use of novel sequencing reagents yielding other amino acid derivatives [9-11] that are sensitive for ESI MS detection. Detection limits for the most sensitive derivatives using ESI range from low femtomole in a quadrupole instrument operated in the selected ion monitoring mode [10] to subfemtomole for tandem mass spectrometry (MS/MS) detection [9]. In addition, these studies illustrate that some structural information on amino acid derivatives can be obtained using ESI MS. The actual utility of these novel reagents for sequencing synthetic peptides has been reported [12]. The approach of modifying Edman chemistry to yield compounds, which are sensitive for ESI MS detection, may eventually lead to significant advances in Edman sequencing technology.

Research on combining Edman sequencing with ESI MS explores the capability of the ESI ion trap/time-of-flight mass spectrometer for the identification of products generated in a sequencer. These products include the Edman degradation end products from non-standard and modified amino acids. To assess the analytical merits and limitations of ESI IT/TOFMS for this type of application and to use this technique to

study structural modifications of proteins, understanding of the detectability of standard PTH-amino acids is essential.

In this chapter, ESI mass spectra of 20 standard PTH-amino acids are reported and the source fragmentation patterns of these compounds are discussed. It is shown that ESI IT/TOFMS can be used to differentiate isomers based on their fragmentation patterns. The detection limits and relative detection sensitivity of these PTH-amino acids are also presented. Finally, the comparison of the present method to the technique developed for the detection of PTH-amino acids on a Finnigan MAT LCQ ion trap instrument [8] is given.

3.2 Experimental

3.2.1 ESI IT/TOFMS Instrument

ESI mass spectra of the PTH-amino acids were obtained using an IT/linear TOFMS instrument that has been described in Chapter 1 and Chapter 2 [13, 14]. The instrumental parameters for the analysis of PTH-amino acids were the same as those described in Section 2.2. In addition to the soft ionization used in Chapter 2, source fragmentation was utilized in the current studies of PTH-amino acids.

Fragmentation of organic compounds has been observed in thermospray interfaces [15-17] and ESI or ionspray sources [18]. CID by energetic collisions in the ESI source can be induced by increasing skimmer, nozzle, cone, capillary, and orifice voltage, respectively, depending on the construction of the source [19-22]. Source CID spectra have been acquired with all types of polar compounds, which were analyzed by ESI-MS: e.g., peptides and proteins [19, 23], ruthenium complexes [20], porphyrins [22], sulfonamides [24], penicillin antibiotics [25], selenium-containing ions [26], and benzodiazepines [27]. Several terms have been used for the description of this phenomenon: source CID or ESI/CID [28], up-front CID [26] or CID in the transport

region [29]. Some effort has been made to develop the source fragmentation method [27] which could be used for library searching with different ESI instruments.

The source fragmentation in ESI IT/TOFMS took place in the two-stage electrospray interface shown in Figure 3.2.

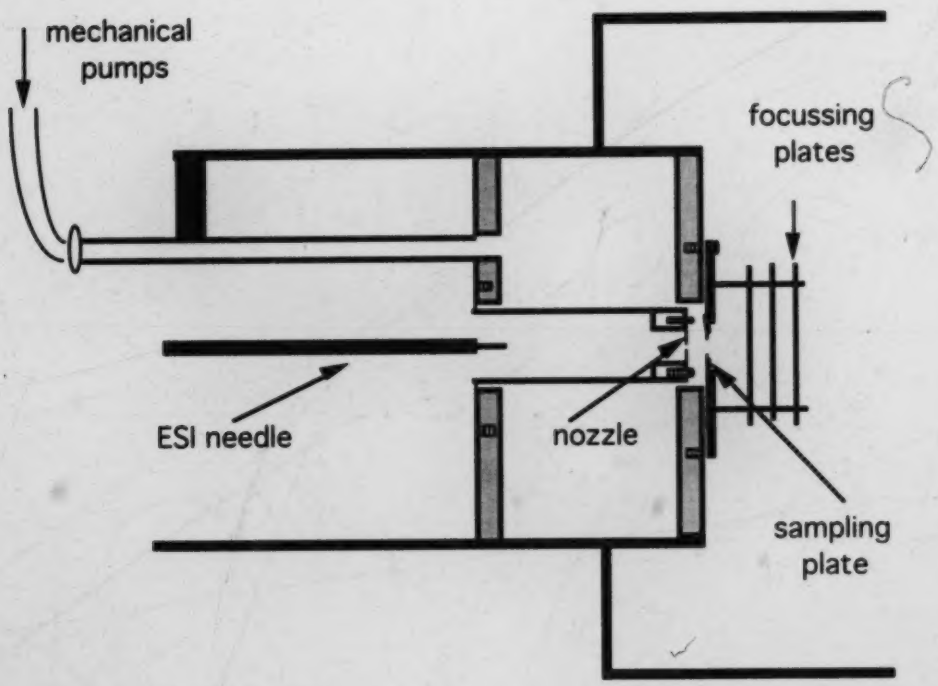

Figure 3.2. Schematic of the two-stage electrospray interface of the ESI IT/TOFMS instrument. Drawing is not to scale.

The nozzle (atmospheric) and the sampling (vacuum) plate have openings of 120 µm and 230 µm, respectively, and are separated by a distance of 4.1 mm. The space between the plates is referred to as the collisionally induced dissociation (CID) region. The CID region is pumped by two mechanical pumps to maintain a pressure of approximately 200

mTorr. A dc voltage of +4.0 V was applied to the vacuum plate while a variable voltage (20 to 70 V) was applied to the atmospheric plate. The degree of dissociation observed in the final spectrum could be manipulated by adjusting the voltage drop between the nozzle and the sampling plate. This potential difference or V_{CID} determines the kinetic energy of the ions colliding with gas molecules at relatively high pressure. Fragmentation conditions were promoted by increasing the atmospheric plate voltage.

3.2.2 Electrospray ionization source

The signal stability for the ESI operation in IT/TOFMS was improved by using a new design for the microspray needle tip. A stainless steel (SS) capillary [inner diameter (i.d.) = 60 μm, outer diameter (o.d.) = 125 μm] was electropolished (as an anode, with copper as the counter electrode in a 1/1/1 solution by volume of orthophosphoric acid/glycerin/water) at one end until the outer diameter was small enough to be inserted into a 100 μm ID fused silica capillary. The most difficult operation was to make a sharp and even cut of the SS capillary piece since the capillary wall was very thin. It was possible to manufacture a satisfactory cut electrolytically. The SS capillary was used as an anode in water/nitric acid solution (1/1 by volume) with a copper wire as a cathode. A constant voltage of 5 V was supplied to the electrodes by a model 6217 A dc power supply (Hewlett Packard, Palo Alto, CA). The SS capillary cut was formed at the air-liquid interface. The narrow end of the modified SS capillary was inserted inside of a fused silica capillary (100 μm i.d., 250 μm o.d.) and protruded 1 mm inside. The tip and fused silica capillary were placed inside a supporting SS capillary (250 μm i.d., 1.59 mm o.d.). The mechanical support for this connection was achieved by soldering the middle part of the SS capillary tip to one end of the supporting SS capillary and gluing the fused silica capillary to the other end. Such an assembly was used as the ESI source and it provided a low dead volume connection. For flow injection experiments, a Rheodyne model 7520 injector (0.5 μL volume of injected sample) was used. The electrospray

source was connected to the injector by using a 30 cm long piece of fused silica (100 μm i.d.). A syringe pump (Harvard Apparatus, South Natick, MA) was used to deliver the solvent at a flow rate of 4 μL/min. For continuous infusion experiments, the sample was delivered directly from a syringe to the electrospray source at a flow rate of 4 μL/min. A dc voltage of 2.8 kV was applied to the ES tip during the ESI process.

3.2.3 Chemicals and sample preparation

All PTH-amino acids and phenylisothiocarbamoyl (PTC) derivatives were purchased from Sigma Chemical Corporation (St. Louis, MO) and used without purification. HPLC-grade acetonitrile, HPLC-grade water and ammonium acetate were purchased from Fisher Scientific Company (Nepean, Ontario). Stock solutions (1 mM) of PTH-amino acids were prepared by dissolving the required amount of sample in HPLC-grade acetonitrile. Standard solutions and mixtures for ESI-MS analysis were prepared from stock solutions by further dilution. The ESI solvent contained 80% acetonitrile and 20% 0.25 mM ammonium acetate in water by volume.

3.3 Results and Discussion

3.3.1 Soft ionization of PTH-amino acids

Figure 3.3 shows some representative mass spectra of PTH-amino acids obtained by continuous infusion of a 5 μM analyte solution through the electrospray source. They were acquired using experimental conditions that favor the formation of the molecular ions (i.e., V_{CID} = 25 V). The buffer-solvent composition used provided the optimal signal intensity of the protonated molecular ion with minimal chemical background.

The spectra of all PTH-amino acids, except PTH-(PTC-cysteine), display prominent protonated molecules, MH^+. In the case of PTH-(PTC-cysteine), the ESI spectrum of this compound shows an intense fragment ion at m/z 205 and no molecular

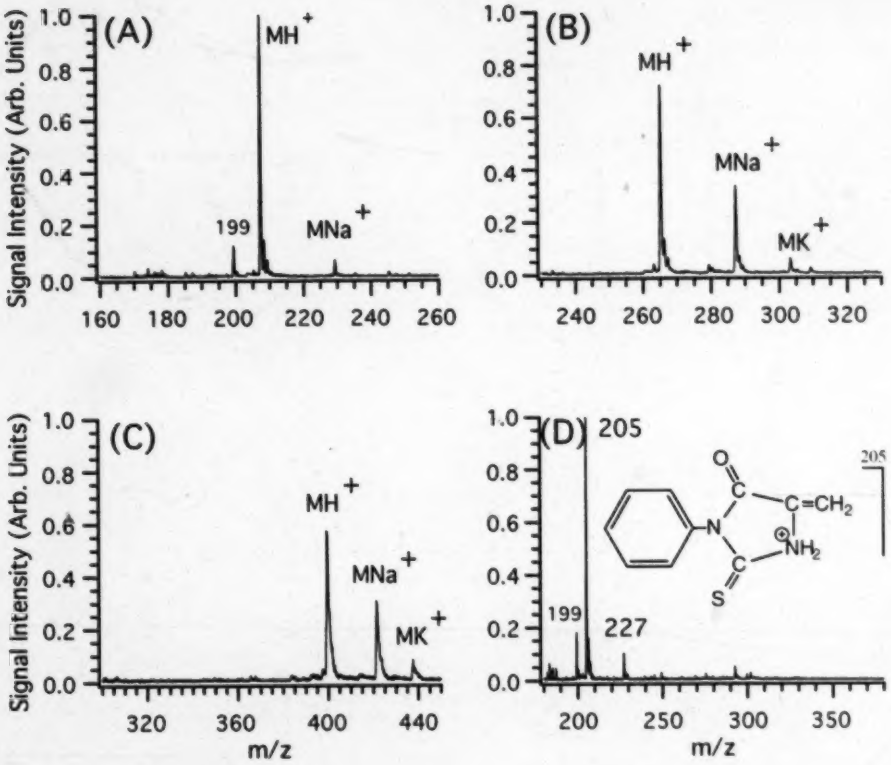

Figure 3.3. Molecular ion regions of mass spectra of PTH-amino acids. (A) PTH-alanine, (B) PTH-glutamic acid, (C) PTH-(PTC-lysine), and (D) PTH-(PTC-cysteine). 5 μM sample solutions in 80% acetonitrile/20% 0.25 mM ammonium acetate in water (v/v) were analyzed at V_{CID}=25 V.

ion peak at m/z 374.5 (see Figure 3.3 D). Figure 3.3 illustrates that ammonium adduct ions, MNH_4^+, are not observed for a low V_{CID} when a relatively low ammonium acetate buffer concentration is used. Alkali metal contamination, likely from the glassware and impurities in the sample, causes the presence of sodium adduct ions MNa^+ and in some instances potassium adduct ions MK^+. The abundance and the composition of these

adduct ions are compound dependent. The signal intensity for these ions decreases slightly when a higher CID voltage is used. Although these adduct ion peaks appear to complicate the spectra, they can be very useful for confirming the presence of a molecular ion peak. The fragment ions generally are not present as alkali adducts. Only singly charged positive ions are observed in the PTH-amino acid mass spectra.

3.3.2 Differentiation of PTH-Leu and PTH-Ile

Table 3.1 (page 60) lists the molecular ion masses of the PTH-amino acids studied. It is clear that the molecular ion mass is unique for many of the PTH-amino acids and it can be used as the basis of identification. However, the isomers, PTH-Leu and PTH-Ile, cannot be distinguished in this way. In addition, the molecular ion mass information obtained for non-standard PTH-amino acids does not provide information about the identity of the analyzed compounds. Fragment ion spectra can be readily obtained in ESI MS. However, the MS distinction of leucine and isoleucine derivatives has been reported to be difficult [7-12]. The extent of fragmentation information depends on the analyzed compound and the instrumental configuration used in the experiment. The possibility of using the ESI IT/TOFMS to distinguish these derivatives based on fragmentation induced in the interface region (i.e., source fragmentation) was examined further.

In ESI IT/TOFMS, the fragmentation of PTH-amino acids is facilitated by increasing the voltage difference between the atmospheric and vacuum plates (i.e., V_{CID}). Figure 3.4 shows the spectra of PTH-Leu and PTH-Ile at various V_{CID}. At low V_{CID}, only the protonated molecular peaks (MH^+=249) for PTH-Leu and PTH-Ile are observed, as shown in Figure 3.4 A and Figure 3.4 D, respectively. The increase in the CID voltage promotes fragmentation of the molecular ion and, as a result, the intensity of a fragment ion at m/z 86 increases for both species (Figures 3.4 B and E). When the fragmentation voltage was increased further, the fragment ion at m/z 69 appeared only in PTH-Ile mass

Table 3.1. Source fragmentation products of PTH-amino acids in ESI IT/TOFMS

PTH-amino acid	MH^+	Major fragment ions	Minor fragment ions
Proline(P)	233	70 (3.8)[a]	
Leucine(L)	249	86 (1.4)	
Isoleucine(I)	249	86 (1.5), 69 (0.3)	
Valine(V)	235	72 (1.6), 55 (0.4)	
Alanine(A)	207	86 (0.2)	
Glycine(G)	193	165 (0.3), 72 (0.2)	
Aspartic acid(D)	251	191 (0.8), 108 (0.8), 233 (0.3), 174 (0.3), 205 (0.3), 88 (0.3)	
Asparagine(N)	250	233 (1.0), 174 (0.7), 191 (0.3), 87 (0.2)	157, 205
Glutamic acid(E)	265	84 (2.3), 247 (0.3)	102, 205
Glutamine(Q)	264	84 (3.2), 247 (1.7)	205
Serine(S)	223	193 (3.1), 60 (0.5), 118 (0.5)	205
Threonine(T)	237	193 (5.5)	219
Tyrosine(Y)	299	136 (2.1), 193 (1.9), 119 (0.4)	
Tryptophan(W)	322	193 (12), 130 (8.4), 132 (1.6)	
Histidine(H)	273	180 (2.0), 152 (2.0), 110 (2.0)	83, 93, 170
Phenylalanine(F)	283	120 (1.6)	103, 162
Arginine(R)	292	70 (2.0), 112 (2.0), 275 (1.1), 233 (0.6), 115 (0.3)	60, 129, 140, 156, 157, 174, 205
Methionine(M)	267	61 (0.7), 146 (0.6), 56 (0.5), 104 (0.5), 174 (0.4)	98, 219
PTC-Lysine(L)	399.5	306 (6.0), 70 (0.8), 143 (0.7), 116 (0.7), 84 (0.6)	247
PTC-Cysteine(C)	374.5[b]	205 (1)	170

[a] 70 (3.8) represents a fragment ion at m/z 70 which was 3.8 times more intense than the corresponding protonated molecular ion in the spectrum obtained at V_{CID} = 45 V.

[b] the molecular peak was not observed.

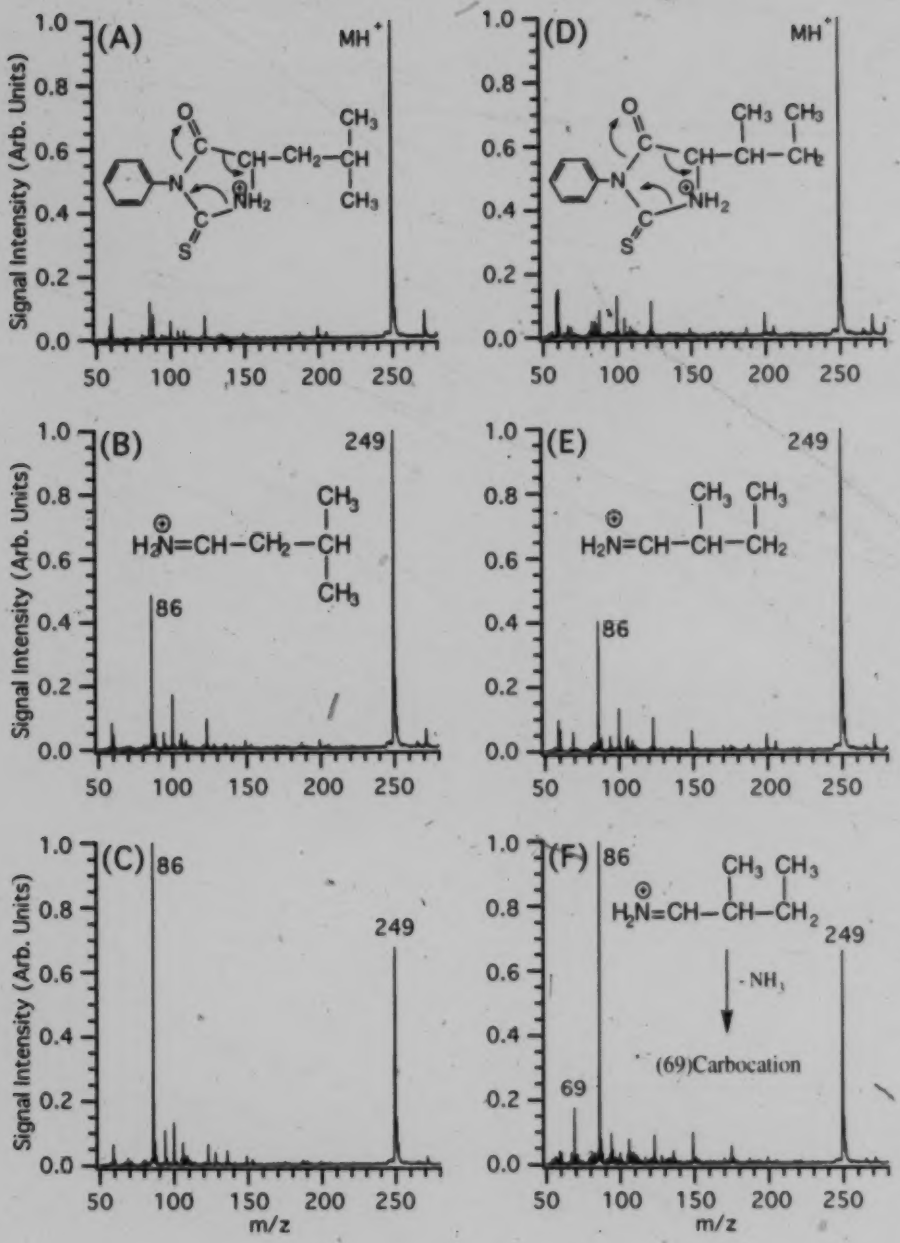

Figure 3.4. Mass spectra of PTH-leucine (A), (B), (C) and PTH-isoleucine (D), (E), (F) at different source voltages. (A) and (D) V_{CID} = 25 V, (B) and (E) V_{CID} = 35 V, (C) and (F) V_{CID} = 45 V.

spectrum (Figure 3.4 F). This characteristic fragmentation pattern can be used to distinguish PTH-Ile and PTH-Leu.

The peaks at m/z 86 shown in Figure 3.4 B and 3.4 E originate from the immonium ions of leucine and isoleucine, respectively. Their structures are presented in the corresponding graphs. The peak at m/z 69 observed only in the PTH-Ile spectra (Figure 3.4 F) is from the ion formed by NH_3 elimination from the isoleucine immonium ion.

It is interesting to compare the fragmentation patterns of PTH-Leu and PTH-Ile observed using different instrumental configurations under the similar fragmentation conditions. The mass spectra (not shown) obtained using a quadrupole mass spectrometer (SCIEX API 100) for both PTH-Leu and PTH-Ile resemble the spectrum of PTH-Leu obtained by IT/TOFMS (Figure 3.4 C). The immonium ion intensities were much smaller and the isoleucine immonium ion fragmentation product at m/z 69 was not present in the PTH-Ile spectrum obtained by the single quadrupole system. Thus, it is not possible to differentiate these isomers by source fragmentation in the SCIEX single quadrupole ESI system. The different effectiveness of source fragmentation observed for IT/TOFMS and quadrupole MS is related to the different designs of the electrospray source. The arrangement of the CID region as well as the pressure maintained in this part of the interface determines the efficiency of source fragmentation.

MS/MS studies of PTH-Ile and PTH-Leu using a commercial ion trap LCQ instrument (Finnigan MAT, San Jose, CA) required a two-step fragmentation process to distinguish between these isomers. In the LCQ ion trap mass spectrometer, fragmentation of the isolated MH^+ of both PTH-Ile and PTH-Leu resulted in the intense m/z 86 immonium ion but did not generated the m/z 69 ion for PTH-Ile. Further isolation and fragmentation of the m/z 86 ion produced the m/z 69 ion exclusively for PTH-Ile. In addition, it was possible to obtain distinct spectra for PTH-Leu and PTH-Ile by using source fragmentation with the LCQ. The key factor for obtaining MS/MS products from

source fragmentation is the time duration from excitation to the detection event. A sufficient increase in the internal energy of the ions in the CID source region (collisional excitation) combined with a long duration of the ion's residence in the ion trap (250 ms) produces very unique fragmentation spectra similar to that shown in Figure 3.4 F. This is likely to be the property not only of IT/TOFMS but also of ion trap MS systems operated at longer trapping cycles.

A triple quadruple system is expected to provide PTH-Leu and PTH-Ile differentiation based on MS/MS spectra of isolated immonium ion, judging from the results obtained by low energy CID in a sector/quadrupole instrument [30]. Nevertheless, this work demonstrates the ability of differentiating PTH-Leu and PTH-Ile in an IT/TOFMS system.

3.3.3 Fragmentation patterns of PTH-amino acids

The fragmentation patterns of other PTH-amino acids were investigated. The operating trapping rf voltage suitable for the detection of all PTH-amino acids sets the limit (LMCO) for the lowest mass-to-charge ratio of a trapped ion at 55. This means that all ions with m/z smaller than 55 could not be trapped and consequently could not be detected. Table 3.1 lists all the peaks present in the fragment ion spectra of PTH-amino acids. The intensity of the fragment ion relative to the intensity of the corresponding protonated molecular ion at V_{CID} = 45 V is also given in parentheses for the major fragment ions. Minor fragments are defined as the ion peaks with intensities < 10% of the intensity of the molecular ion peak.

A close examination of the mass spectral data in Table 3.1 reveals that several groups of PTH-amino acids exhibit similar fragmentation patterns. Fragment ion spectra of aliphatic PTH-amino acids (i.e., PTH-Pro, -Leu, -Ile, and -Val) are dominated by the immonium ions (i.e., $[RCHNH_2]^+$ where R is the side chain of the amino acid). The identity of these ions can be expressed as the fragments formed from the protonated

molecular ion by elimination of stable neutral molecules (i.e., $[MH - PhNCS - CO]^+$). This notation implies that the immonium ions are formed by a nominal elimination of phenylisothiocyanate and carbon monoxide from the protonated molecular ion with the mass loss of 163 (i.e., $[MH - 163]^+$). Val and Ile immonium ions fragment further by NH_3 elimination to generate the ions at m/z 55 and m/z 69, respectively. Immonium ions for PTH-Ala and PTH-Gly are not detected. But the spectrum of PTH-Ala displays a peak at m/z 86 from $[MH - PhNH_2 - CO]^+$. The spectrum of PTH-Gly displays peaks at m/z 165 from $[MH - CO]^+$ and m/z 72 from $[MH - PhNH_2 - CO]^+$.

Acidic and amidic PTH-amino acids (PTH-Asp, -Asn, -Glu, -Gln) show fragmentation products representing H_2O elimination ($[MH - H_2O]^+$ for PTH-Glu at m/z 247 and PTH-Asp at m/z 233) or NH_3 elimination ($[MH - NH_3]^+$ for PTH-Gln at m/z 247 and PTH-Asn at m/z 233). PTH-Asp and PTH-Asn spectra display ion products from further fragmentation of the m/z 233 ion. The peaks at m/z 174 and 205 correspond to the elimination of HNCS and CO, respectively, from the m/z 233 ion. The m/z 191 fragment ion is $[MH - CH_3COOH]^+$ for PTH-Asp and $[MH - CH_3CONH_2]^+$ for PTH-Asn. Immonium ions at m/z 88 for PTH-Asp and at m/z 87 for PTH-Asn are observed. PTH-Glu and PTH-Gln show a dominant fragment ion at m/z 84. This peak is likely from 5-pyrrolin-2-one [31], the product of H_2O elimination from the glutamic acid immonium ion at m/z 102 and the product of NH_3 elimination from the glutamine immonium ion at m/z 101 (the peak at m/z 101 is not present in the spectrum). Less abundant fragment ions at m/z 205 appear in the spectra of PTH-Glu $[MH - CH_3CH_2COOH]^+$ and PTH-Gln $[MH - CH_3CH_2CONH_2]^+$.

The mass spectra of hydroxilic PTH-amino acids (PTH-Ser, -Thr, -Tyr) and PTH-Trp display a common fragment ion peak at m/z 193. This characteristic fragment is produced from the molecular ion by the elimination of a neutral species (e.g., acetone in the case of PTH-Thr, and formaldehyde for PTH-Ser). Immonium fragment ions are present in the spectra of PTH-Tyr at m/z 136 and PTH-Ser at m/z 60. Further elimination

of NH_3 from the PTH-Tyr immonium ion results in the ion peak at m/z 119. The spectrum of PTH-Ser shows a peak at m/z 118 from $[MH - H_2O - CO - HSCN]^+$. Less intense fragments, $[MH - H_2O]^+$, are observed at m/z 205 for PTH-Ser and at m/z 219 for PTH-Thr. The intense fragment at m/z 130 in the mass spectra of PTH-Trp represents the quinolinium ion.

The fragment ion mass spectrum of PTH-His shows $[MH - PhNH_2]^+$ at m/z 180, $[MH - PhNH_2 - CO]^+$ at m/z 152, and the immonium ion at m/z 110. The minor peaks can be attributed to the product of NH_3 elimination from the immonium ion (m/z=93) and the protonated methylimidazole (m/z=83). A similar pattern is observed for PTH-Phe. The intense immonium ion at m/z 120 and a less abundant $[MH - PhNH_2 - CO]^+$ ion at m/z 162 are observed. The product of NH_3 elimination from the immonium ion is also present at m/z 103.

PTH-Arg and PTH-Met spectra show multiple fragment ion peaks due to the breakage of the side chain (R) of the amino acid. The major fragment ions for PTH-Arg include m/z 275 from $[MH - NH_3]^+$, m/z 233 from $[MH - Guanidine]^+$, m/z 112 from $[RCHNH_2 - NH_3]^+$, and m/z 70 from $[RCHNH_2 - guanidine]^+$. The major fragment ions for PTH-Met are m/z 174 from $[MH - PhNH_2]^+$, m/z 146 from $[MH - PhNH_2 - CO]^+$, m/z 104 from $[RCHNH_2]^+$, m/z 61 from $[CH_3SCH_2]^+$, and m/z 56 from $[RCHNH_2 - CH_3SH]^+$.

The mass spectrum of PTH-(PTC-Lys) shows the most intense fragment ion at m/z 306 from $[MH - PhNH_2]^+$, which fragments further to the immonium analog, $[MH - PhNH_2 - PhNCS - CO]^+$, at m/z 143. The elimination of HCN from the ion at m/z 143 results in the product at m/z 116. An alternative fragmentation pathway generates $[MH - PhNH_2 - HNCS]^+$ at m/z 247. This product ion fragments further to $[247 - PhNCS - CO]^+$ at m/z 84 and $[247 - PhNCS - CH_2CO]^+$ at m/z 70. The molecular ion of PTH-(PTC-Cys) is readily fragmented and the spectrum shows a dominant peak at m/z 205 from $[MH - PhNH_2 - CS_2]^+$ and a less intense fragment ion peak at m/z 170.

In all fragment ion spectra of PTH-amino acids, several peaks at m/z 136, 106, and 94 from the product ions of PTH ring cleavage are observed. It should also be noted that the choice of V_{CID} can strongly affect the intensity and identity of the fragments ions in the spectra of PTH-amino acids. If necessary, additional fragmentation information may be obtained by a further increase of the CID voltage. For example, it was possible to observe the hydroxytropylium ion at m/z 107 and the tropylium ion at m/z 91 in the spectrum of PTH-Tyr at V_{CID} = 55 V.

The ESI mass spectral features discussed above indicate that the fragment ion spectra, in combination with the molecular ion information, can provide unambiguous identification of standard PTH-amino acids. Consequently, no chromatographic retention information is required from chemical identification point of view.

3.3.4 Detection of non-standard PTH-amino acids

Understanding the fragmentation patterns should also assist in detecting non-standard PTH-amino acids. Figure 3.5 shows the mass spectra obtained for PTH-α–aminobutyric acid and PTH-α–aminoisobutyric acid. These two isomers can not be distinguished on the basis of their molecular ion. Figure 3.5 shows that the fragmentation pattern for both PTH-nonstandard amino acids resembles those of aliphatic PTH-amino acids (e.g., very intense immonium ion at m/z 58 from $[MH - PhNCS - CO]^+$ and less intense ion at m/z 100 from $[MH - PHNH_2 - CO]^+$). More importantly, different fragment ion mass spectra were obtained for these two isomers. The spectrum of PTH-α-aminoisobutyric acid (Figure 3.5 A) displays a prominent peak at m/z 134 from $[MH - HNCS - CO]^+$, which does not appear in the spectrum of PTH-α–aminobutyric acid. Thus, these two isomers can be readily identified.

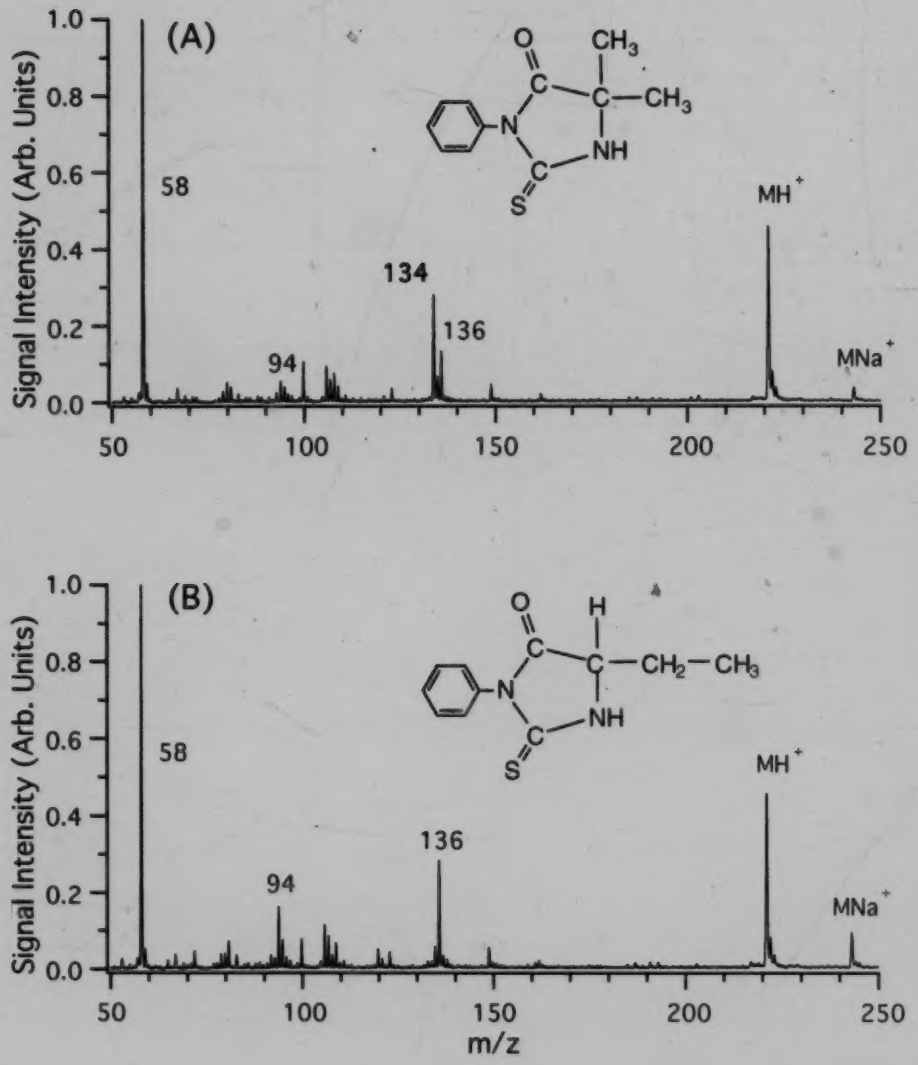

Figure 3.5. Mass spectra of two isomeric non-standard PTH-amino acids obtained at V_{CID} = 45 V. (A) PTH-α-aminoisobutyric acid and (B) PTH-α-aminobutyric acid.

3.3.5 Isobaric interferences in mixture analysis

The data shown in Table 3.1 may suggest possible isobaric interferences for the fragment ions, molecular ions and adducts of different PTH-amino acids. However, this isobaric interference can be controlled for simple mixtures. For example, the peak overlap of MH^+ from PTH-His and MNa^+ from PTH-Asp at m/z 273 is not significant, as either derivative can be identified in the presence of the other. A serious peak overlap may exist for MH^+ of PTH-Gly at m/z 193 with the intense fragment ions at m/z 193 from PTH-Ser, -Thr, -Tyr and -Trp. Figure 3.6 shows the spectrum of the mixture of the PTH-amino acids that are found to easily fragment to generate the m/z 193 ion. When a low CID potential (V_{CID} = 25 V) was used (Figure 3.6 A) the intensity of the m/z 193 peak was at the background level. Using a larger CID potential (V_{CID} = 28 V), as shown in Figure 3.6 B, the intensity of this peak makes the identification of PTH-Gly impossible.

Figure 3.7 shows the mass spectra of a simple mixture of PTH-Ile and PTH-His at different source voltages. At a low CID voltage, the MH^+ peaks are very intense. At a higher fragmentation voltage (V_{CID} = 45 V), even the isomer differentiation information (i.e., m/z 69 for PTH-Ile) can be obtained as shown in Figure 3.7 B. This shows that the identification of PTH-amino acids for a simple mixture is still possible. However, for the analysis of complex mixtures of PTH-amino acids, separation would be beneficial for unambiguous identification. This is particularly true in cases where the relative amount of PTH-amino acids in a mixture varies greatly.

3.3.6 Detectability of PTH-amino acids

The detection sensitivities of PTH-amino acids were examined in ESI IT/TOFMS. This sets the limit of detection, a very important parameter used to judge the applicability of this method. Knowing that PTH-amino acid identification relies mainly on the molecular ion mass, the detectability based on monitoring these ions was evaluated.

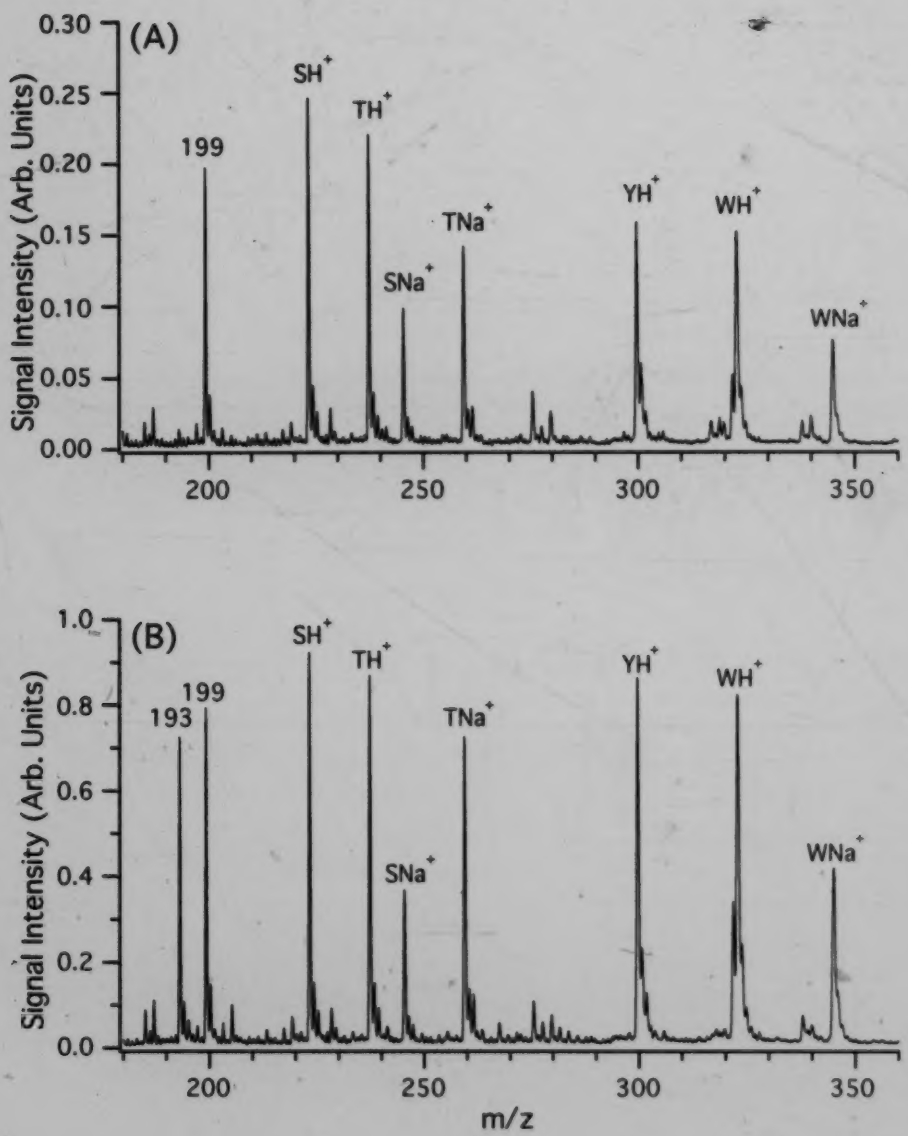

Figure 3.6. Mass spectra of a mixture of PTH-S(serine), PTH-T(threonine), PTH-Y(tyrosine) and PTH-W(tryptophan) obtained at different source voltages: (A) V_{CID} = 25 V and (B) V_{CID} = 28 V. MH^+ represents the protonated molecule and MNa^+ represents the sodium adduct. M is the single letter code of an amino acid.

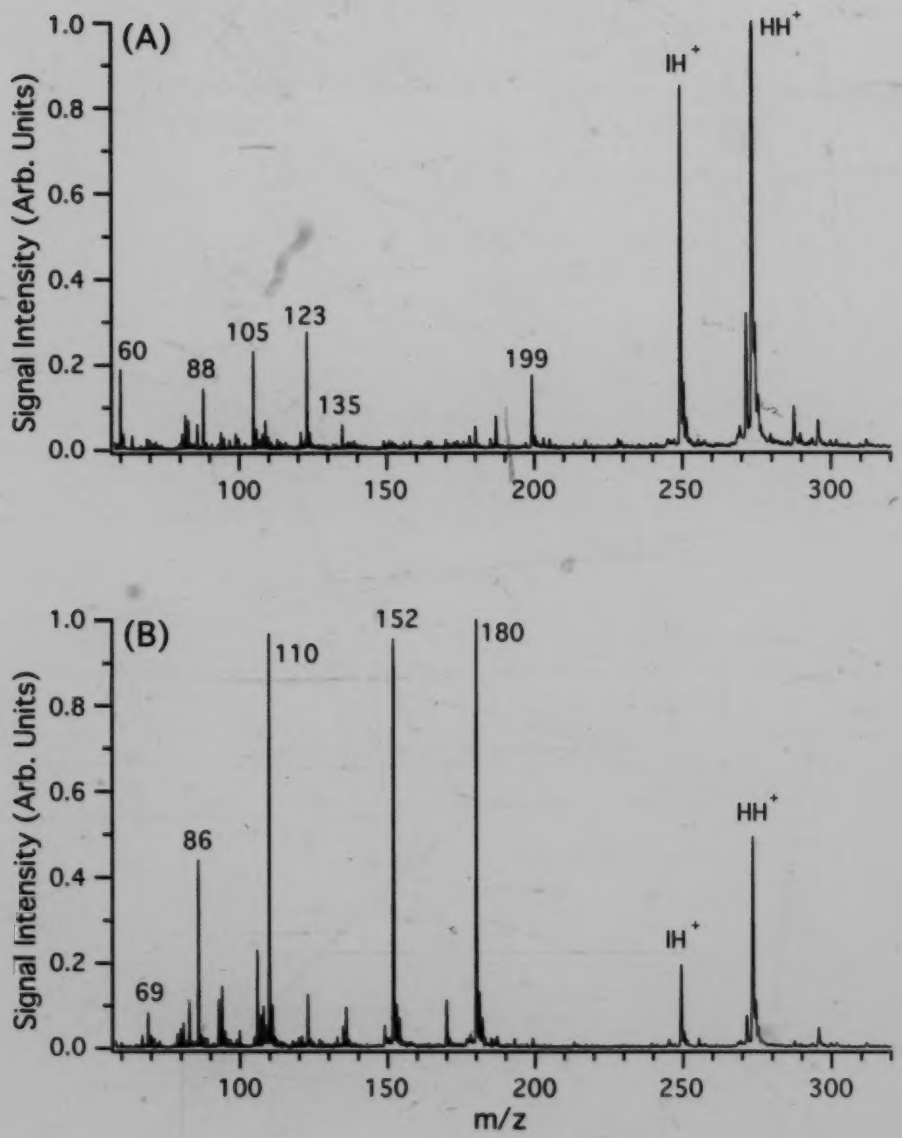

Figure 3.7. Mass spectra of a mixture of PTH-I(isoleucine) and PTH-H(histidine) obtained at (A) V_{CID} = 25 V and (B) V_{CID} = 45 V. MH^+ represents the protonated molecule and M is the single letter code of an amino acid.

Using the ESI setup in the flow injection configuration, a series of injections for various amounts of each PTH-amino acid were performed. The relative signal intensities for 20 PTH-amino acids were determined and the results are shown in Figure 3.8.

Figure 3.8. Signal intensities of PTH-amino acids obtained from an injection of 500 femtomoles of each compound in a flow injection experiment. One letter abbreviation represents the corresponding PTH-amino acid.

An amount of 500 fmol of each compound was injected (5 repetitions). The signal response of the molecular ion peak MH^+ (m/z 205 fragment ion in case of PTH-(PTC-Cysteine)) for each PTH-amino acid was monitored using a spectral recording rate of 4 Hz. The resulting histogram (detector response as a function of time) represents the signal for an injected species, calculated as an integrated peak area above the average level of the baseline.

Two parameters (basicity and hydrophobicity of a compound) appear to influence the ESI signal response for PTH-amino acids. The most basic PTH-amino acids

(arginine, histidine) displayed the highest sensitivity. The basicity of PTH-PTC-Lysine (the lysine-derivative generated in the sequencer) is significantly reduced as a result of derivatization of the free amino group. Among the rest of PTH-amino acids with comparable basicity, ESI signal responses ranged from larger for more hydrophobic species (PTH-Pro, -Val, -Phe) to smaller for less hydrophobic ones (PTH-Glu, -Asp). Data from Figure 3.8 indicate that the response factor differs by 20 for extreme PTH-amino acids. Thus, for non-separation MS detection, the signal intensity of a major product from a particular Edman degradation sequence step could be smaller than the signal intensity for the highly sensitive product carried over from the previous step.

Detection limits for 20 PTH-amino acids were determined from the flow injection experiment using ESI IT/TOFMS as the detector. The protonated molecular ion peak of each PTH-amino acid (m/z 205 fragment ion in the case of PTH-(PTC-Cysteine)) was monitored to create repetitive histograms corresponding to 100, 250 and 500 femtomoles of injected sample. The signal was calculated as the peak height above the average level of the baseline and the noise was represented by the standard deviation of the baseline.

Table 3.2 lists the values for the signal-to-noise (S/N) ratios obtained in the flow injection experiment. Subpicomole levels of detection were achieved for all PTH-amino acids. In fact, it was possible to identify all PTH-amino acids at 100 fmol with a S/N ratio of not less than 5. PTH-Arginine, the most sensitive compound, displayed lower than expected S/N ratio values at 500 fmol and 100 fmol injections. This was the only compound which exhibited sorption in the injection system. Severe band broadening of an injected sample and a long lasting, variable background contributed to the low S/N ratio, especially for large amounts of sample. The increase in data acquisition frequency will reduce the sensitivity of detection. It was determined that even for a trapping time of 50 ms (20 spectra per second) subpicomole detection for all PTH-amino acids would still be possible. The high data acquisition rate achieved gives a measure of the compatibility of the detector with fast separation techniques.

Table 3.2. Detectability of PTH-amino acids in ESI IT/TOFMS

PTH-amino acid	500 fmol	250 fmol	100 fmol	50 fmol	25 fmol
·Arginine	29±6	–	45±5	19±3	10±2
·Histidine	841±42	–	–	83±5	52±4
·Proline	287±15	109±6	77±6		
·Asparagine	125±7	97±5	43±4		
·Valine	130±5	64±4	24±3		
·Phenylalanine	112±6	57±3	24±3		
·Alanine	143±5	49±3	23±2		
·Leucine	143±6	69±4	22±3		
·Tyrosine	69±3	38±3	20±3		
·Isoleucine	79±5	41±4	18±2		
·PTC-Lysine	75±5	35±4	18±3		
·Tryptophan	67±4	37±3	18±2		
·Methionine	61±5	33±3	18±3		
·Threonine	82±6	40±4	16±2		
·PTC-Cysteine	67±4	44±4	15±2		
·Glutamine	55±3	26±2	11±2		
·Glycine	46±3	26±3	10±2		
·Serine	39±2	18±3	7±2		
·Glutamic acid	32±3	18±2	7±2		
·Aspartic acid	30±3	16±2	5±1		

3.3.7 Chemical background

Impurities in samples of PTH-amino acids can complicate the mass spectral interpretation. More importantly, the presence of impurities can cause adverse effect on the detection of PTH-amino acids. Samples from a protein sequencer, can contain impurities from the reagents and various byproducts of the sequencing process.

In an attempt to detect PTH-amino acids directly from a sequencer, aliphatic amines used in the sequencing process totally suppressed the PTH-amino acid signals. This failed attempt suggests that although PTH-amino acid identification using ESI IT/TOFMS can be carried out based on the mass spectral patterns, some type of chromatographic separation is still required for the sensitive detection of PTH-amino acids in a complicated matrix. The purposes of this type of separation are to eliminate any impurities that may interfere with PTH-amino acid detection, and to reduce the possible isobaric interference, rather than to achieve total separation of the PTH-amino acids for retention information. Successful strategies should include the use of alternative reagents in a protein sequencer and the use of a suitable LC separation method to reduce the interference from chemical background.

3.4 Comparison with other studies

At the time the above studies were completed, Zhou et al. reported a study of PTH-amino acid analysis using an ion trap mass spectrometer [8]. In addition to the difference in the type of mass spectrometry instrument used in their experiment, a novel approach was used to increase the detectability for PTH-amino acids. The method relies on the use of a buffer-solvent system containing 5 mM lithium triflate in 1:1 methanol/dichloromethane. PTH-amino acids in such a medium flow through the SS capillary to the nanospray tip at 300 nL/min. The increased sensitivity for PTHs in ESI was achieved by the electrochemical modification of these compounds at the surface of SS capillary electrode. The detection sensitivity and limits of detection were determined from spectral responses with continuous sample introduction and reported as concentration limits.

In the current approach, the solvent system consists of an acetonitrile, water, and ammonium acetate buffer and could be used for separation of PTH-amino acids by HPLC. The detection sensitivity and detection limits were determined for injection of a

fixed volume of sample (0.5 μL) and reported as the absolute amounts detected. As discussed earlier, analysis of PTH-amino acids from a sequencer requires some form of separation before the introduction of the sample to the mass spectrometer. Thus, a study involving analyte injection gives a closer approximation to a real world application, although better concentration limits are always observed with continuous sample introduction in the current experimental setup.

The detectability of the ESI IT/TOFMS method using continuous sample introduction is illustrated in Figure 3.9, which shows a representative ESI spectrum obtained by the continuous infusion of a mixture of PTH-Pro, PTH-Leu, and PTH-Phe at a concentration of 50 fmol/μL per component. The solvent system used was composed of 80% acetonitrile and 20% 0.25 mM ammonium acetate in water (v/v). The sample was delivered at 1 μL/min. The spectrum was acquired by summing the same number of scans (i.e. 100) as in the work by Zhou et al. [8]. Because the scan time used in the current experiment was 250 ms versus 1.5 s in Zhou et al.'s experiment and the flow rate used was 1 μL/min versus 0.3 μL/min, the total sample consumed to obtain the spectrum shown in Figure 3.9 was about half of that used in Zhou et al. 's work (i.e. 21 fmol vs. 38 fmol). The spectrum was smoothed using a 15-point Savitzky-Golay algorithm. The S/N ratios for the molecular ion peaks of PTH-Pro, PTH-Leu, and PTH-Phe were 47, 28, and 15, respectively, compared with 4, 8, and 12 reported by Zhou et al. It is clear that different levels of detection are obtained from the two studies, which reflect the differences in the type of instrument and experimental conditions used. Use of 5 mM lithium triflate in 1:1 methanol/dichloromethane as the ESI solvent in the ESI IT/TOF instrument was attempted. Despite extensive efforts, no signal was obtained for PTH-Pro, PTH-Leu, or PTH-Phe using continuous infusion of 50 fmol/μL solution. It appears that the optimal solvent system used for PTH-amino acid detection, particularly in cases involving electrochemical modification of analytes, is dependent on the design of the ESI needle tip [31]. At this stage, it is difficult to ascertain the contribution of individual

experimental parameters to the observed differences. Nevertheless, some general observation on the experimental results obtained in the ESI IT/TOF instrument can be discussed.

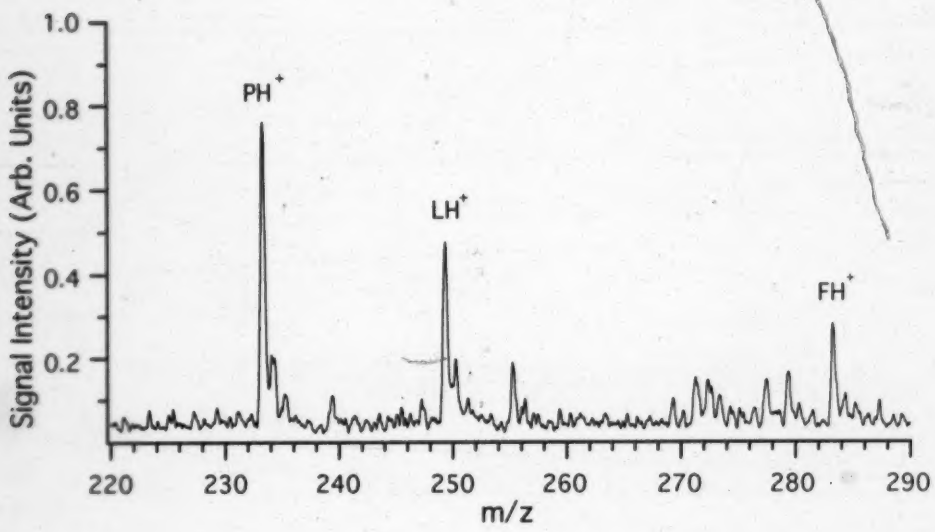

Figure 3.9. Mass spectrum of the mixture containing PTH-P(Proline), PTH-L(Leucine) and PTH-F(Phenylalanine) at 50 fmol/μL obtained by using continuous sample introduction. The sample was delivered at 1 μL/min in the buffer-solvent (80% acetonitrile and 20% 0.25 mM ammonium acetate in water by volume). The spectrum was acquired by summing 100 scans for a period of 25 seconds and smoothed using a 15-point Savitzky-Golay algorithm.

A spectrum similar to that shown in Figure 3.9 can be obtained by summing only 10 scans instead of 100 scans. The detection limit is governed by the chemical background noise. Thus, spectral summing of >10 scans does not reduce the noise level

further. Note that the amount of sample consumed to produce a spectrum like the one shown in Figure 3.9 by summing 10 scans is only 2 fmol. When such an amount was introduced to the system by injection, no signal was observed. In fact, even when 0.5 μL of 50 fmol/μL solution of PTH-Pro, PTH-Leu, or PTH-Phe was introduced by injection, only PTH-Pro could be detected. The injection experiment accounts for the analyte dispersion or dilution effects in a continuos stream of carrier solvent as well as adsorption losses during the transport of the sample plug. It is clear that one cannot infer the absolute amount of detection from a continuous injection experiment.

The effect of flow rate on the detection sensitivity was also studied. It was found that for continuous injection the signal intensity was independent of flow rate used in the range 0.5-6 μL/min. A flow rate <0.5 μL/min causes the spray to become unstable. For a flow rate >6 μL/min, the desolvation process was less effective resulting in the presence of cluster peaks in the spectrum and a decrease in sensitivity.

Two different methods of generating CID spectra were used for studying gas-phase ion chemistry of PTH-amino acids for identification. Zhou et al. used ion trap CID while IT/TOFMS relies on the use of source fragmentation. The later method lacks control over the selection (isolation) of the parent ion for fragmentation and possible sources of interferences have to be reduced by an efficient separation. However, the ability to generate unique fragmentation patterns for PTH-amino acid identification by source fragmentation should facilitate on-line HPLC/MS analysis of these compounds, when selection of precursor ion for fragmentation is difficult.

Different fragmentation products of PTH-amino acids were recorded in CID spectra of corresponding methods. Considering a comparable amount of energy deposited to a precursor ion during the source excitation and the ion trap excitation, the population of generated fragment products should be similar in both techniques [32]. Some significant differences, however, are observed. Generally, there is a good agreement in a population of high mass fragment ions but the absence of a number of low

mass fragments is typical for ion trap CID spectra. As an example, the m/z 69 ion originated from PTH-Ile is not present in the ion trap CID spectrum [8]. By contrast, the ion trap CID spectrum of PTH-Ile [8] contains m/z 189, m/z 193, and m/z 221 ions, which were not detected in source fragmentation. A direct comparison of source fragmentation and ion trap CID became possible, when an ESI IT/TOFMS was equipped with ion trap CID capability. Details about the instrumental modifications of the IT/TOFMS and the design of the ion trap CID experiment can be found in Chapter 6 (Sections 6.2.1 and 6.2.2).

MS/MS spectra for PTH-amino acids obtained in the ion trap CID are strongly dependent upon operating conditions used in the dissociation process. The ion trap pressure, amplitude of rf trapping voltage, and shape and amplitude of the excitation waveform are three important parameters related to the amount of energy deposited to the fragmenting ion and have a major effect on the resulting CID spectra. An elevated buffer gas pressure favors the dissociation process, because of a larger number of energetic collisions between fragmenting species and gas molecules. However, this surplus energy uptake controlled by the magnitude of excitation waveform is not large enough to change the fragmentation pattern. The population of dissociation products remains the same, although the intensity of particular species is affected by the buffer gas pressure and the energy of excitation waveform. The major factor affecting MS/MS spectra is the magnitude of rf trapping voltage. This parameter determines the highest amount of energy deposited to an ion in CID process (equation 1.11) and also the low mass limit for trapping (equation 1.10).

Figure 3.10 shows the ion trap CID spectrum of PTH-Ile acquired by using two different amplitudes of rf trapping voltage in ion trap CID. The spectrum in Figure 3.10 A was obtained at a lower amplitude of rf trapping voltage than the spectrum in Figure 3.10 B. It was possible to deposit more energy into the molecular ion in the ion trap CID experiment represented in Figure 3.10 B.

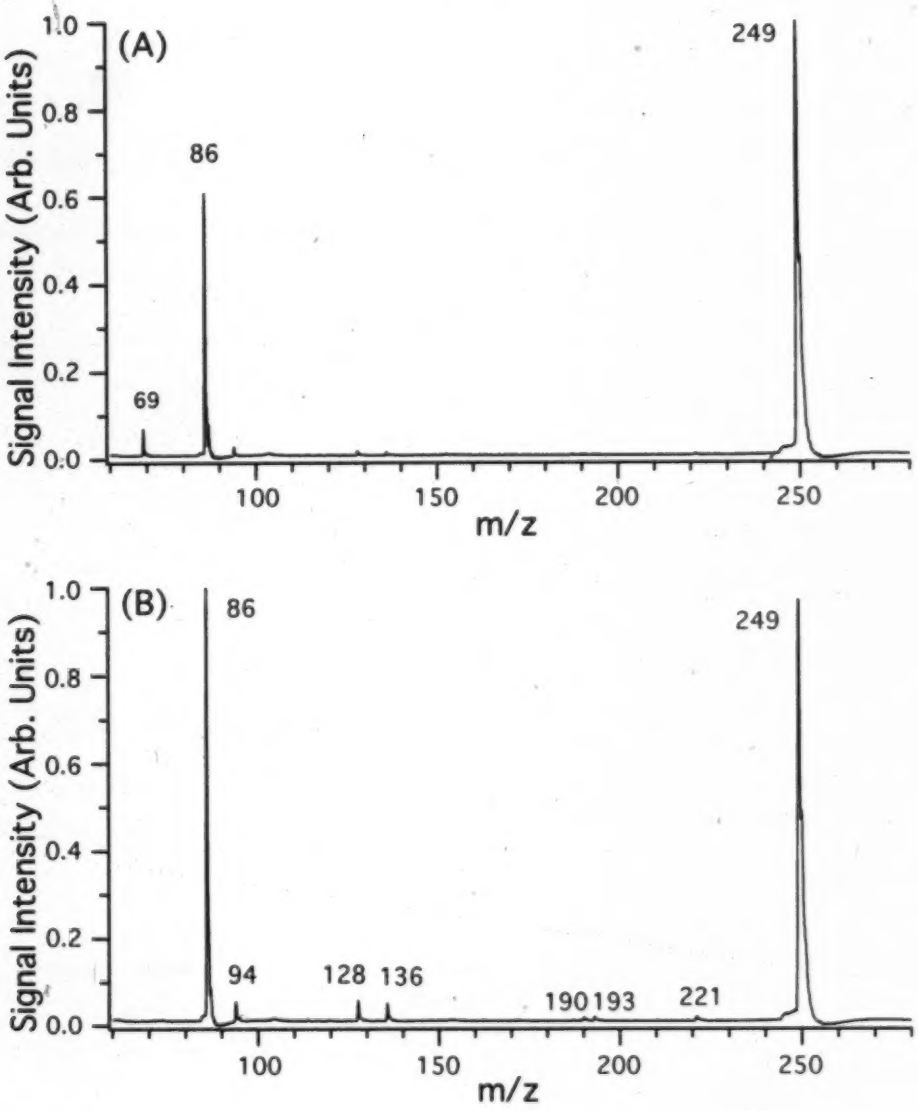

Figure 3.10. Ion trap CID spectra of PTH-isoleucine obtained in IT/TOFMS. (A) Spectrum obtained at $q_z = 0.149$ and $V_{P-P} = 920$ V, (B) Spectrum obtained at $q_z = 0.210$ and $V_{P-P} = 1300$ V.

The evidence for this, in Figure 3.10 B, is the presence of CID products at m/z 94, 128, and 136 originating from the cleavage of the PTH ring. The ring cleavage is energetically more demanding than the formation of the immonium ion at m/z 86. However, as can be seen in Figure 3.10 B, in the process of creating conditions for more effective CID excitation, the ability for trapping the ion at m/z 69 was lost. The low mass ion at m/z 69 is still formed but is not trapped and cannot be detected under such conditions. Results from similar experiments for all PTH-amino acids show the strong relationship between the magnitude of the CID energy implemented for fragmentation and ability to trap all fragmentation products. In contrast, CID excitation in source fragmentation does not impose any restrictions on trapping.

It is clear, that even under optimal conditions, ion trap CID does not provide the detection capability for ions at m/z below the LMCO in MS/MS experiment. However, the choice of rf voltage amplitude or q_z should not be arbitrary, as it is in some commercial ion trap instruments, and one should also consider the properties of analyzed species. The lowest possible, and common for all PTH-amino acids, amplitude of rf voltage providing efficient fragmentation with the lowest observable m/z of fragment ions at m/z 50 was determined. For these conditions, fragmentation products from ion trap CID of PTH-amino acids were analogous to those obtained from source fragmentation and listed in Table 3.1.

3.5 Summary

An ESI IT/TOFMS system was evaluated as a detector for identification of PTH-amino acids. Each of the PTH-amino acids studied can be characterized by well-defined ion peaks in the mass spectra of these compounds. With the exception of PTH-(PTC-Cysteine), a protonated molecular peak can be used for identification of these derivatives. Fragmentation patterns obtained by source excitation followed by a long trapping period (250 ms) gave rise to unique fragmentation products. The source fragmentation patterns

allow for the differentiation of isomers (PTH-Leu/PTH-Ile and PTH-α–aminobutyric acid/PTH-α–aminoisobutyric acid). The detectability of PTH-amino acids for the ESI IT/TOFMS was examined. Results for the relative signal responses of the 20 standard PTH-amino acids indicate that the response factor between the most sensitive and the least sensitive compound can be as high as 20. Sensitivity disproportionation must be considered in the identification procedure. Subpicomole detection of PTH-amino acids was demonstrated. However, samples from a sequencer require purification to achieve sensitive detection. The purpose of such a step is not the total separation of PTH-amino acids, but rather the elimination of interfering species such as aliphatic amines. The electrospray interface used in the studies does not accept high flow rates required for liquid chromatography separations. The on-line purification of samples from a sequencer will be evaluated with the new electrospray interface.

3.6. Literature cited

[1] Edman, P. *Acta Chem. Scand.* **1950**, 4, 283.

[2] Edman, P.; Begg, G. *Eur. J. Biochem.* **1967**, 1, 80.

[3] Smillie, L. B.; Carpenter, M. R. *HPLC of Peptides and Proteins: Separation, Analysis, and Conformation;* Mant, C. T.; Hodges, R. S., Ed.; CRC Press: Boca Raton, Florida, **1991**, 875.

[4] Hagenmaier, H.; Ebbighausen, W.; Nicholson, G.; Votsch, W. *Z. Naturforsch.* **1970**, 25b, 681.

[5] Sun, T.; Lovins, R. E. *Anal. Biochem.* **1972**, 45, 176-191.

[6] Fairwell, T.; Brewer, J. H. B. *Anal. Biochem.* **1980**, 107, 140.

[7] Pramanik, B. C.; Hinton, S. M.; Millington, D. S.; Dourdeville, T. A.; Slaughter, C. A. *Anal. Biochem.* **1988**, 175, 305.

[8] Zhou, J.; Hefta, S.; Lee, T. D. *J. Am. Soc. Mass Spectrom.* **1997**, 8, 1165.

[9] Aebersold, R.; Bures, E.J.; Namchuk, M.; Goghari, M. H.; Shushan, B.; Covey, T. C. *Protein Science* **1992**, 1, 494.

[10] Bures, E. J.; Nika, H.; Chow, D. T.; Morrison, H. D.; Hess, D.; Aebersold, R. *Anal. Biochem.* **1995**, 224, 364.

[11] Basic, C.; Bailey, J. M.; Lee, T. D. *J. Am. Soc. Mass Spectrom.* **1995**, 6, 1211.

[12] Hess, D.; Nika, H.; Chow, D. T.; Bures, E. J.; Morrison, H. D.; Aebersold, R. *Anal. Biochem.* **1995**, 224, 373.

[13] Purves, R. W.; Li, L. *J. Microcolumn Separations* **1995**, 7, 603

[14] Purves, R. W.; Li, L. *J. Am. Soc. Mass Spectrom.* **1997**, 8, 1085.

[15] Yinon, J.; Jones, T. L.; Betowski, L. D. *Proceedings of the 38th ASMS Conference on Mass Spectrometry and Allied Topics*, Tucson, AZ, **1990**, p.43.

[16] Voyksner, R. D.; Pack, T.; Cornish, T. J. *Proceedings of the 38th ASMS Conference on Mass Spectrometry and Allied Topics*, Tucson, AZ, **1990**, p.1218.

[17] Heeremans, C. E. F.; van der Hoeven, R. A. M.; Niessen, W. M. A.; Tjaden, U. R.; van der Greef, J.; Nibbering, N. M. M. *Proceedings of the 38th ASMS Conference on Mass Spectrometry and Allied Topics*, Tucson, AZ, **1990**, p.1216.

[18] Loo, J. A.; Udseth, H. R.; Smith, R. D. *Rapid Commun. Mass Spectrom.* **1988**, 2, 207.

[19] Katta, V.; Chowdhury, S. K.; Chait, B. T. *Anal. Chem.* **1991**, 61, 174.

[20] Katta, V.; Chowdhury, S. K.; Chait, B. T. *Proceedings of the 38th ASMS Conference on Mass Spectrometry and Allied Topics*, Tucson, AZ, **1990**, p.214.

[21] Henion, J. D.; Conboy, J.; Mordehai, A.; Hopfgartner, G.; Huggins, T.; Rule, G.; Wachs, T. *Proceedings of the 40th ASMS Conference on Mass Spectrometry and Allied Topics*, Washington, DC, **1992**, p.499.

[22] Van Berkel, G. J.; McLuckey, S. A.; Glish, G. L. *Anal. Chem.* **1991**, 63, 1098.

[23] Loo, J. A.; Edmonds, C. G.; Udseth, H. R.; Smith, R. D. *Proceedings of the 38th ASMS Conference on Mass Spectrometry and Allied Topics*, Tucson, AZ, **1990**, p.140.

[24] Perkins, J. R.; Parker, C. E.; Tomer, K. B. *J. Am. Soc. Mass Spectrom.* **1992**, 3, 139.

[25] Grindstaff, D. J.; Allen, M. H.; Voyksner, R. D. *Proceedings of the 40th ASMS Conference on Mass Spectrometry and Allied Topics*, Washington, DC, **1992**, p.37.

[26] Wachs, T.; Henion, J. D. *Proceedings of the 40th ASMS Conference on Mass Spectrometry and Allied Topics*, Washington, DC, **1992**, p.1663.

[27] Keever, J.; Voyksner, R. D.; Hough, J. *Proceedings of the 46th ASMS Conference on Mass Spectrometry and Allied Topics*, Orlando, FL, **1998**, p.86.

[28] Josephs, J. L. *Rapid Commun. Mass Spectrom.* **1995**, 9, 1270.

[29] Straub, R.; Voyksner, R. D. *Proceedings of the 40th ASMS Conference on Mass Spectrometry and Allied Topics*, Washington, DC, **1992**, p.1879.

[30] Dookeran, N. N.; Yalcin, T.; Harrison, A. G. *J. Mass Spectrom.* **1996**, 31, 500.

[31] Van Berkel, G. J.; Zhou, F. *Anal. Chem.* **1995**, 67, 2916.

[32] Van Dongen, W. D.; van Wijk, J. I. T.; Heerma, W.; Haverkamp, *J. Rapid Commun. Mass Spectrom.* **1999**, 13, 1712.

Chapter 4

Dissociation of Protonated Phenylthiohydantoin-Amino Acids and Phenylthiocarbamoyl-Dipeptides[a]

In Edman sequencing of a peptide, the reagent phenylisothiocyanate (PITC) couples to the free α-amino group of at the N-terminus of the peptide to form a phenylthiocarbamyl (PTC)-peptide derivative. The N-terminal resdue is then cleaved from the peptide chain as a thiazolone-amino acid, leaving the rest of the peptide intact. Before detection a thiazolone-amino acid is converted to its isomeric form, phenylthiohydantoin (PTH)-amino acid. The investigation of a simlar process which may occur in the gas phase is presented in this chapter.

4.1 Introduction

The phenylthiocarbamoyl (PTC) derivatives of peptides and the phenylthiohydantoin (PTH) derivatives of amino acids are the two major types of products generated in the Edman sequencing method. Understanding the fragmentation pathways of these species should facilitate structural elucidation and chemical identification based on the fragment ion mass spectra, particularly when mass spectrometry is combined with Edman sequencing for the analysis of non-standard and modified amino acids. It is clear that studies of the fragmentation pathways of PTH-derivatives have significance not only in understanding the fundamentals of ion chemistry but also in practical applications, particularly now when with the advance of electrospray ionization, sensitive analysis of PTH-derivatives has become possible.

---

[a] A form of this chapter has been published as: T. Yalcin, W. Gabryelski, and L. Li "Dissociation of Protonated Phenylthiohydantoin-Amino Acids and Phenylthiocarbamoyl-Dipeptides", J. Mass Spectrom., **1998**, 33, 543.

Mass spectrometry has previously been used for identification of thiohydantoin [1-3], methyl [4] and phenylthiohydantoin [5-9] amino acid derivatives. For PTH-amino acids, major fragment ions observed in chemical ionization [5] and thermospray ionization [6] MS have been reported; but no detailed studies of the fragmentation mechanisms were given. Gaskel and co-workers [9] have examined several PTC derivatives and presented a study of fragmentation pathways of major product ions using ESI with low-energy collisional activation.

In this chapter, an in-depth investigation of the collisionally-induced dissociation (CID) reactions of phenylthiohydantoin (PTH) amino acids and N-terminal phenylthiocarbamoyl (PTC) derivatives of several amino acids and dipeptides is presented. The purpose of this study, in particular, was to determine whether there is any isomerization of thiazolone to phenylthiohydantoin derivatives in the gas phase during the fragmentation similar to that which occurs in solution. Several common fragment ions were observed in ESI mass spectra of studied dervatives from source fragmentation. These source-formed ions were subjected to CID and their product ions were recorded. The proposed fragmentation mechanisms of these ions are presented.

4.2 Experimental

4.2.1 High-energy CID experiments

All high-energy CID experiments were carried out on a ZabSpec (ZAB) orthogonal acceleration (OA) time-of-flight (TOF) instrument from Micromass (Manchester, UK). The ESI method was used for creating gas-phase ions. The precursor ions were accelerated by a voltage of 4 kV and mass selected with the EBE mass spectrometer. The ions were introduced into the collision cell floated at 3600 V. Thus, for high-energy CID, the laboratory kinetic energy of a singly charged precursor ion is 400 eV. Argon was used as the collision gas, and on average, the abundance of the

precursor ions was attenuated by ~30 %. The ions exiting the collision cell were guided into the OA-TOF spectrometer and pulsed into the flight tube for mass separation. Ions were detected with a microchannel plate detector.

4.2.2 Low-energy CID experiments

Low-energy CID experiments were performed using a Quattro tandem quadrupole instrument (VG Biotech, Winsford, Cheshire, UK) equipped with an electrospray interface. The voltage of the collision cell was 20 V. The laboratory kinetic energy of a singly charged precursor ion for low-energy CID was about 20 eV. Argon was used as the collision gas and, on average, the abundance of the precursor ion was attenuated by ~30 %. The tandem mass spectra reported represent sums of 20 to 30 scans.

4.2.3 Chemicals

The dipeptides (Gly-Leu, Ser-Leu, Thr-Leu, Trp-Leu and Tyr-Leu), PITC, and PTH derivatives were purchased from Sigma Chemical Corporation (St. Louis, MO) and used without purification. HPLC-grade acetonitrile, HPLC-grade water and ammonium acetate were purchased from Fisher Scientific Company (Nepean, Ontario). PTC-derivatives of dipeptides were synthesized by dissolving a dipeptide (30 µmol) in 500 µL of ethanol-pyridine-water (1:1:1, v/v/v) and by adding sevenfold molar excess of PITC. The solvent was removed under a stream of nitrogen. The product was analyzed without further purification. Solutions for ESI MS analysis were prepared by dissolving a sample compound in a mixture of 80 % acetonitrile and 20 % (v/v) 0.25 mM ammonium acetate in water (v/v). For continuous infusion experiments the sample solution (100 µM) was delivered directly from the syringe to the electrospray source at a flow rate of 6 µL/min.

4.3 Results and Discussion

Electrospray ionization mass spectra of several N-terminal PTC derivatives of dipeptides and the underivatized dipeptides were recorded. The b_1 ion or thiazolone ion, corresponding to a cleavage product in solution chemistry, was detected in the ESI spectra of the PTC derivatives of dipeptides, PTC-X-Leu (where X=Thr, Ser, Trp, or Tyr) and PTC-Gly-Leu. The underivatized dipeptides did not display the b_1 ion peaks in the ESI spectra. These findings are consistent with the results obtained by others [9, 11]. The thiazolone ions formed from PTC-X-Leu were of sufficient intensity in the ESI mass spectra that they could be mass-selected to study the CID fragmentation reactions. Figure 4.1 A shows the product ion spectrum of the thiazolone-Thr ion from PTC-Thr-Leu obtained using low-energy collisional activation in a triple quadrupole mass spectrometer. The low-energy product ion spectrum of the protonated PTH-Thr is shown in Figure 4.1 B for comparison. The spectrum shown in Figure 4.1 A is in good agreement with that obtained by fragmentation of the b_1 ion originated from a larger PTC-TLLELA peptide [9]. In Figure 4.1 A, four major fragmentation products are observed. These are: the ions at m/z's 209 and 193 generated from the m/z 237 ion with the loss of 28 u and 44 u, respectively; the threonine immonium ion at m/z 74; and the phenylisothiocyanate ion at m/z 136. The product ion spectrum of the protonated PTH-Thr ion shows one prominent fragmentation product at m/z 193 corresponding to the loss of 44 u, and several minor fragment ions corresponding to the immonium ion of the threonine at m/z 74, the m/z 84 ion and the phenylisothiocyanate ion at m/z 136.

Figure 4.1 clearly shows that the product ion spectrum of the m/z 237 ion derived from PTC-Thr-Leu is different from that of PTH-Thr. This indicates that the fragmentation pathways of the b_1 ion derived from PTC-Thr-Leu are significantly different from those of the phenylthiohydantoin ion. One of the common product ions observed in Figures 4.1 A and 4.1 B is the ion at m/z 193. In a previous study [9], it was proposed that this ion is produced by the loss of CS after isomerization of the thiazolone

ion (the b_1 ion) to the phenylthiohydantoin ion. In order to explore the gas-phase ion chemistry for both isomers, more detailed studies on PTH-derivatives and PTC-derivatives were carried out using high energy CID in a sector/OA TOF system.

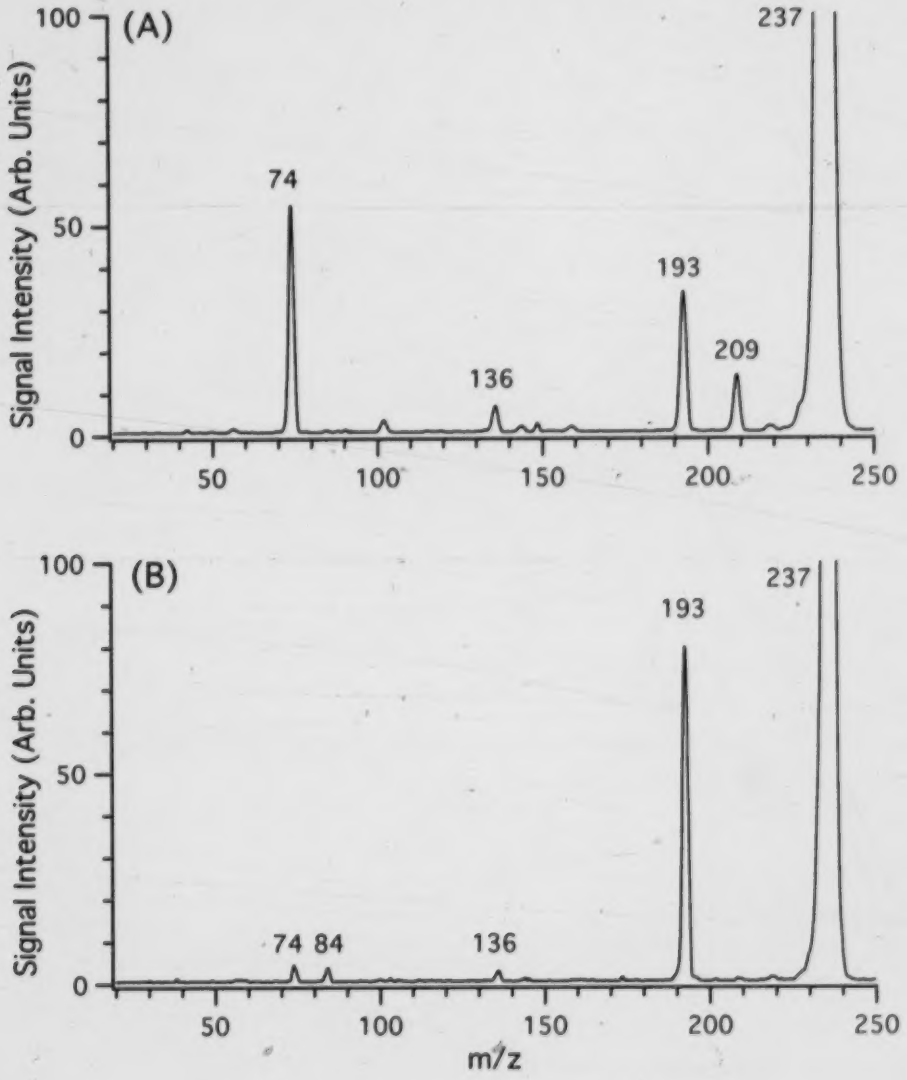

Figure 4.1. Low-energy CID mass spectra of the m/z 237 ion derived from (A) PTH-Thr-Leu and (B) PTH-Thr.

Figure 4.2 shows the product ion spectra of the protonated PTH-X (where X=Thr, Ser, Trp, or Tyr) obtained using the high-energy CID technique.

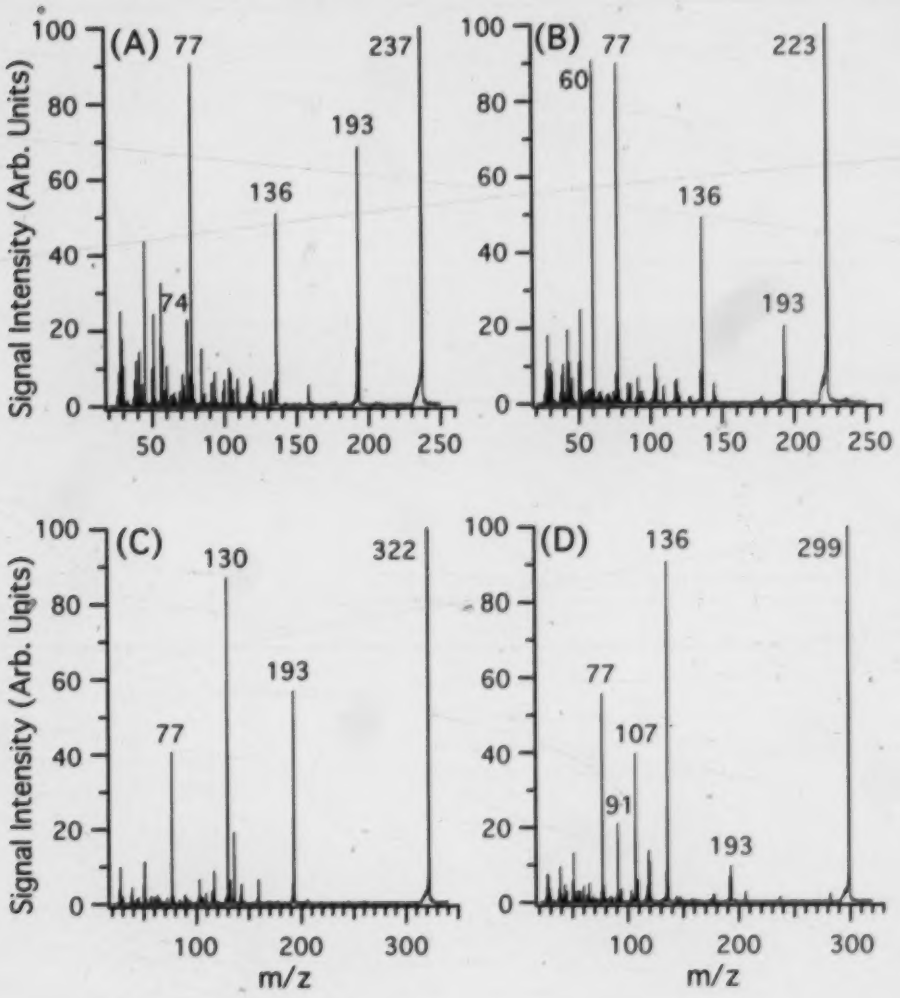

Figure 4.2. High-energy CID mass spectra of the protonated PTH-amino acids: (A) PTH-Thr, (B) PTH-Ser, (C) PTH-Trp, and (D) PTH-Tyr.

Surprisingly, the ion peak expected to be from the elimination of CS from the protonated PTH-amino acids is absent for PTH-Ser, PTH-Trp, and PTH-Tyr (Figures 4.2 B-D). The most intense peaks in the spectra are from the immonium ion (i.e., m/z 74 for PTH-Thr, 60 for PTH-Ser, 130 for PTH-Trp, and 136 for PTH-Tyr which overlaps with phenylisothiocyanate ion), phenylisothiocyanate at m/z 136, the phenyl ion at m/z 77, and the ion at m/z 193. According to the observation in the previous chapter, the m/z 193 ion, a common fragment ion product of PTH-X, appears to be from side chain (R) elimination with hydrogen migration from the R-group to the ion at m/z 193. Note that the loss of the side chain neutral species (CH_3CHO) produces a product ion with a mass of 44 u less than the mass of the protonated PTH-Thr ion.

The CID spectra of the thiazolone ions derived from PTC-X-Leu are shown in Figure 4.3. The fragment ions observed in the spectra include the immonium ion, phenylisothiocyanate at m/z 136, the phenyl ion at m/z 77, and the product ion corresponding to CO elimination from the molecular ion. Only the thiazolone ions derived from PTC-Thr-Leu and PTC-Trp-Leu produce the ion at m/z 193 by a loss of 44 u and 129 u from its respective precursor ion.

Since fragment ions at m/z 193 are observed in both PTH and PTC derivatives, understanding the origins of these ions and their fragmentation pathways should provide additional information on the ion chemistry. The attention was focused on studying the product ion spectra of the m/z 193 ion from different sources. Figure 4.4 shows the product ion mass spectra of the m/z 193 ions derived from PTH-X. Similar spectra were obtained from these ions indicating similar fragmentation reaction pathways of these ions. If the loss of CS from the phenylhydantoin ion derived from PTH-Thr took place, it would result in an ion with significantly different structure from that produced by the side chain elimination from the phenylhydantoin moiety. From the results shown in Figure 4.4, one can conclude that the $[b_1\text{-}44]^+$ peak from PTH derivatives is not from the loss of CS from the phenylhydantoin ion, even in the case of PTH-Thr.

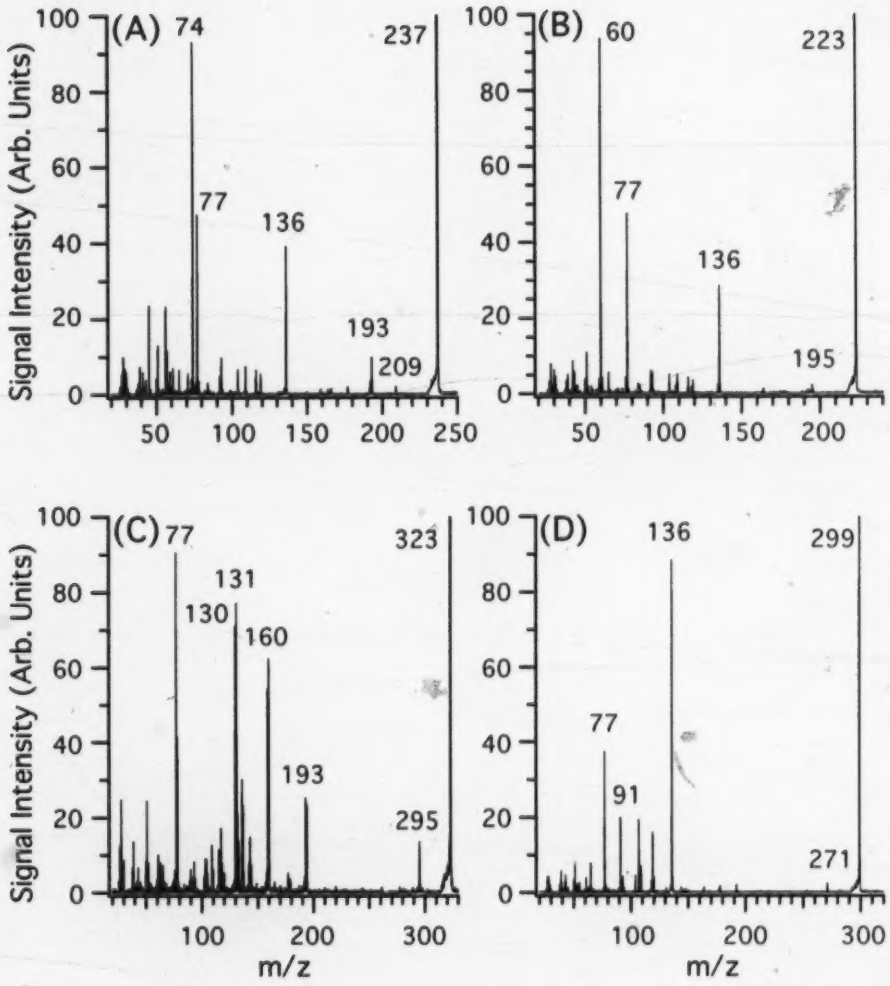

Figure 4.3. High-energy CID mass spectra of the thiazalone ions derived from (A) PTC-Thr-Leu, (B) PTC-Ser-Leu, (C) PTC-Trp-Leu, and (D) PTC-Tyr-Leu.

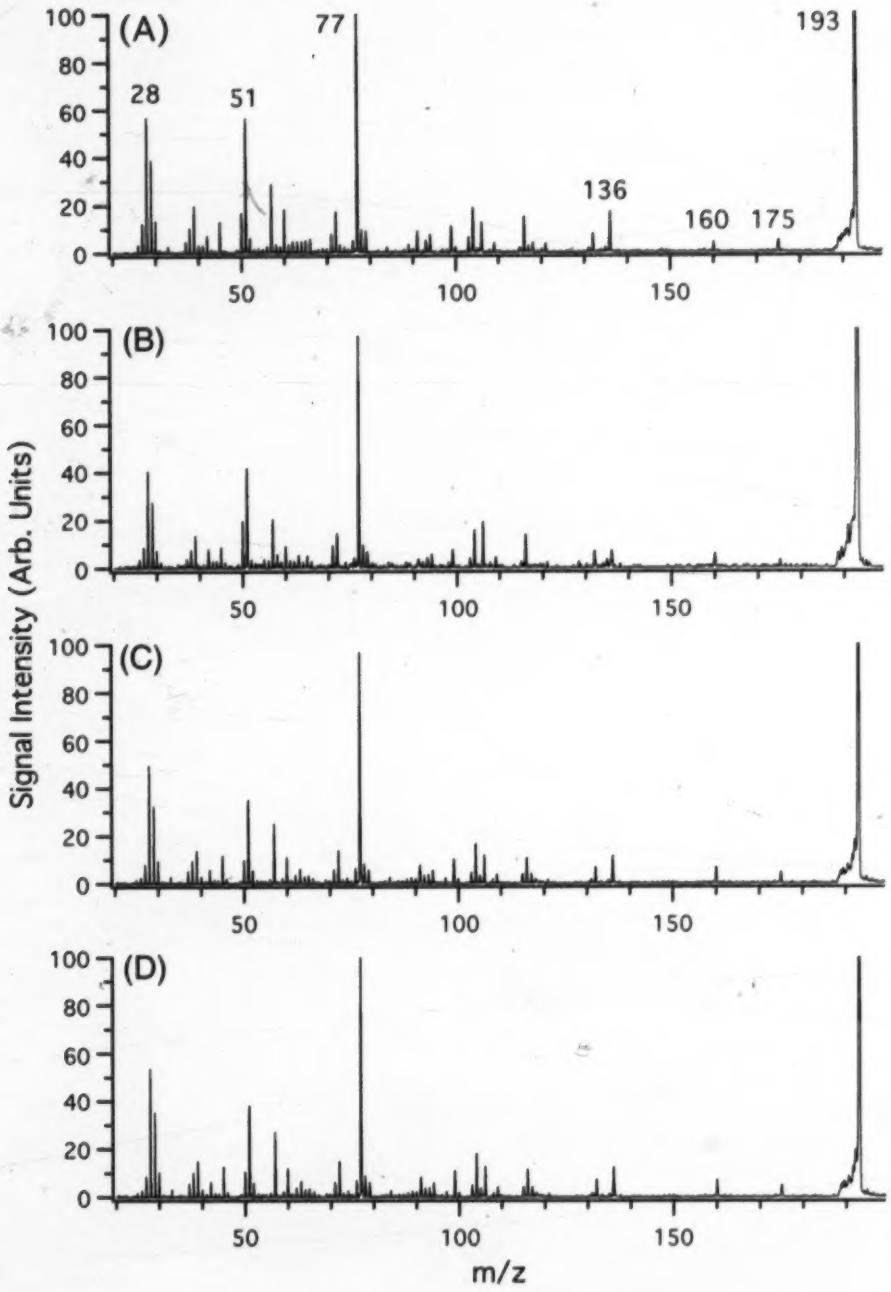

Figure 4.4. High-energy CID mass spectra of the m/z 193 ions derived from (A) PTH-Thr, (B) PTH-Ser, (C) PTH-Trp, and (D) PTH-Tyr.

As was indicated above, there is hydrogen migration from the R group to the charge-retaining moiety, yielding the m/z 193 ion, with the rest of the R group leaving the ion as a neutral species. It seems that the structure of the ion at m/z 193 derived from PTH-X should be identical to the ion of the protonated PTH-Gly, i.e.,

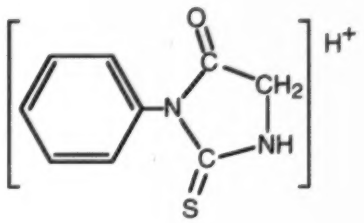

Indeed, this structure of the m/z 193 ion was proposed previously by others in the analysis of PTH derivatives by chemical ionization [5]. If this is the case, the CID product ion spectrum of the ion at m/z 193 derived from PTH-X should be the same as the CID spectrum of PTH-Gly. Figure 4.5 shows high-energy CID mass spectrum of the protonated PTH-Gly.

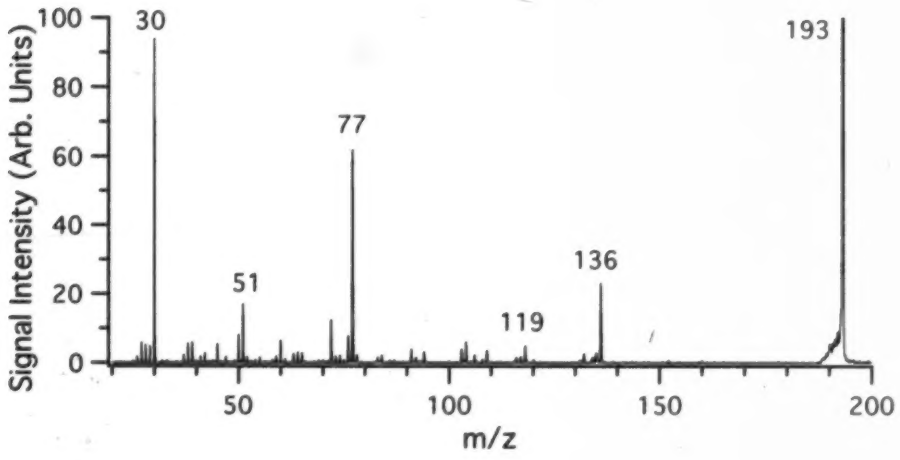

Figure 4.5. High-energy CID mass spectra of the m/z 193 ion derived from PTH-Gly.

The spectrum in Figure 4.5 is different from that shown in Figure 4.4. The spectrum of protonated PTH-Gly shows three prominent fragmentation ions. Namely: phenylisothiocyanate at m/z 136; phenyl ion at m/z 77; and glycine immonium ion at m/z 30. By contrast, the spectrum of the m/z 193 ion derived from PTH-X shows an intense m/z 28 ion peak, with a much less intense glycine immonium ion peak. Another major spectral difference is that, in Figure 4.4, two product ions at m/z's 175 and 160 are observed whereas the spectrum shown in Figure 4.5 from the protonated PTH-Gly does not display these peaks. It is obvious that the fragmentation pathways of the ions at m/z 193 derived from PTH-X are not entirely the same as that of PTH-Gly.

In the process of generating the m/z 193 ion from PTH-X, the elimination of the neutral species from the side chain group is postulated. The structures of the neutral species eliminated from PTH-X are shown in Figure 4.6.

The fragmentation of the m/z 193 ion derived from PTH-X follows the postulated scheme shown in Figure 4.7 (PTH-Ser is shown as an example). The hydrogen transfer takes place via hydrogen bonding with the carbonyl oxygen in the phenylhydantoin moiety. As shown in Figure 4.7, water is subsequently eliminated to form the ion at m/z 175. This process is driven by the migration of one of the labile hydrogens to the hydroxy group in the m/z 193 ion. A fragmentation pathway involving formation of the m/z 160 ion is unclear. It may be generated by the elimination of SH from the m/z 193 ion.

Figure 4.8 shows the proposed fragmentation mechanism for the m/z 193 ion derived from PTH-Gly. Depending on the location of the proton in the phenylhydantoin moiety, two dissociation paths are proposed. If the protonation occurs at phenylated amide nitrogen, the reaction follows path 1. If the protonation occurs at the other amide nitrogen, the reaction follows path 2. This scheme accounts for the production of the major ions at m/z 136 and m/z 30.

PTH-X	Neutral
PTH-Thr	$CH_3-CH=O$
PTH-Ser	$CH_2=O$
PTH-Tyr	
PTH-Trp	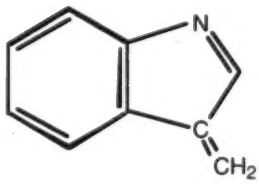

Figure 4.6. Structures of neutral species eliminated from the side chains of X during the formation of the m/z 193 ion from PTH-X.

The formation of the common ion at m/z 193 from PTH-X along with the product ion spectrum of this ion (Figure 4.4) provides an ideal diagnostic tool on the presence of the protonated PTH-derivatives in the gas phase. Examining the spectra shown in Figure 4.3 from PTC-X-Leu, it can be seen that no ion peak at m/z 193 is detected in the product ion spectra of the b_1 ions derived from PTC-Tyr-Leu and PTC-Ser-Leu. Hence there is no isomerization of thiazolone to phenylhydantoin for the b_1 ions of these two PTC derivatives. In the cases of PTC-Thr-Leu and PTC-Trp-Leu, an ion peak at m/z 193 is observed. Examination of the fragmentation patterns of the m/z 193 ions originated from these thiazolone ions was done. Figure 4.9 shows the product ion spectra of the m/z 193 ions derived from PTC-Thr-Leu, PTC-Trp-Leu, as well as PTC-Gly-Leu. As, Figures 4.9 A and B illustrate, common product ions are observed for the fragmentation of the

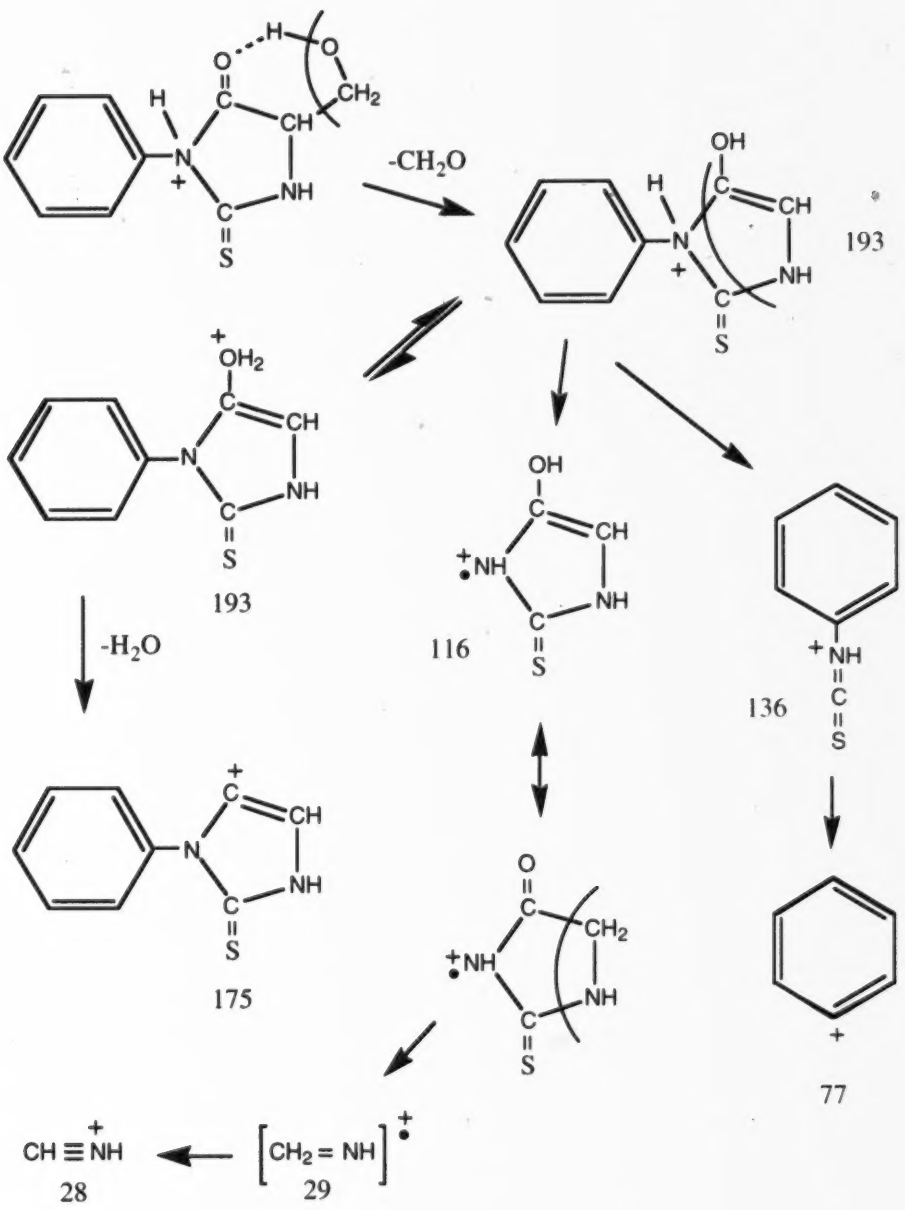

Figure 4.7. Proposed mechanism of fragmentation of the m/z 193 ions derived from PTH-X using PTH-Ser as an example.

thiazolone ions derived from PTC-Thr-Leu and PTC-Trp-Leu. These ions include the phenylisothiocyanate ion at m/z 136 and the phenyl ion at m/z 77. However, these spectra are different from those shown in Figure 4.4. In Figures 4.9 A and B, peaks corresponding to the ions from H_2O elimination are not observed. In contrast, H_2O elimination were observed for the m/z 193 ion originating from PTH-X (Figure 4.4). The fragmentation pathways of the m/z 193 ions originated from PTC-Thr-Leu and PTC-Trp-Leu are different from those of the m/z 193 ions originated from PTH-derivatives. Hence there is no evidence for isomerization of thiazole to phenylhydantoin for the b_1 ions of these two PTC derivatives.

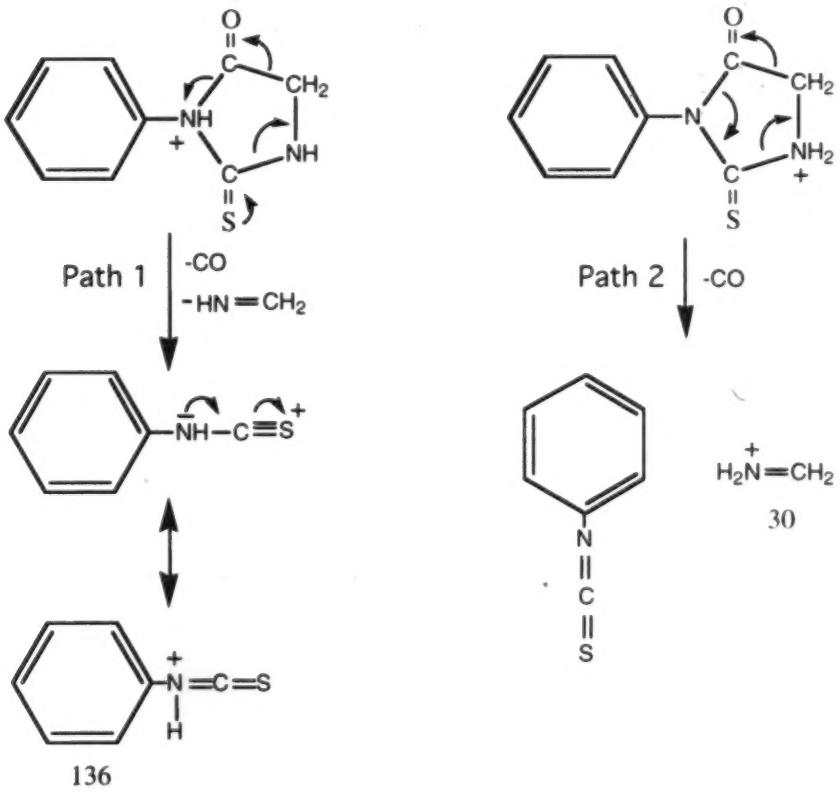

Figure 4.8. Proposed mechanism of fragmentation of the m/z 193 ion derived from PTH-Gly.

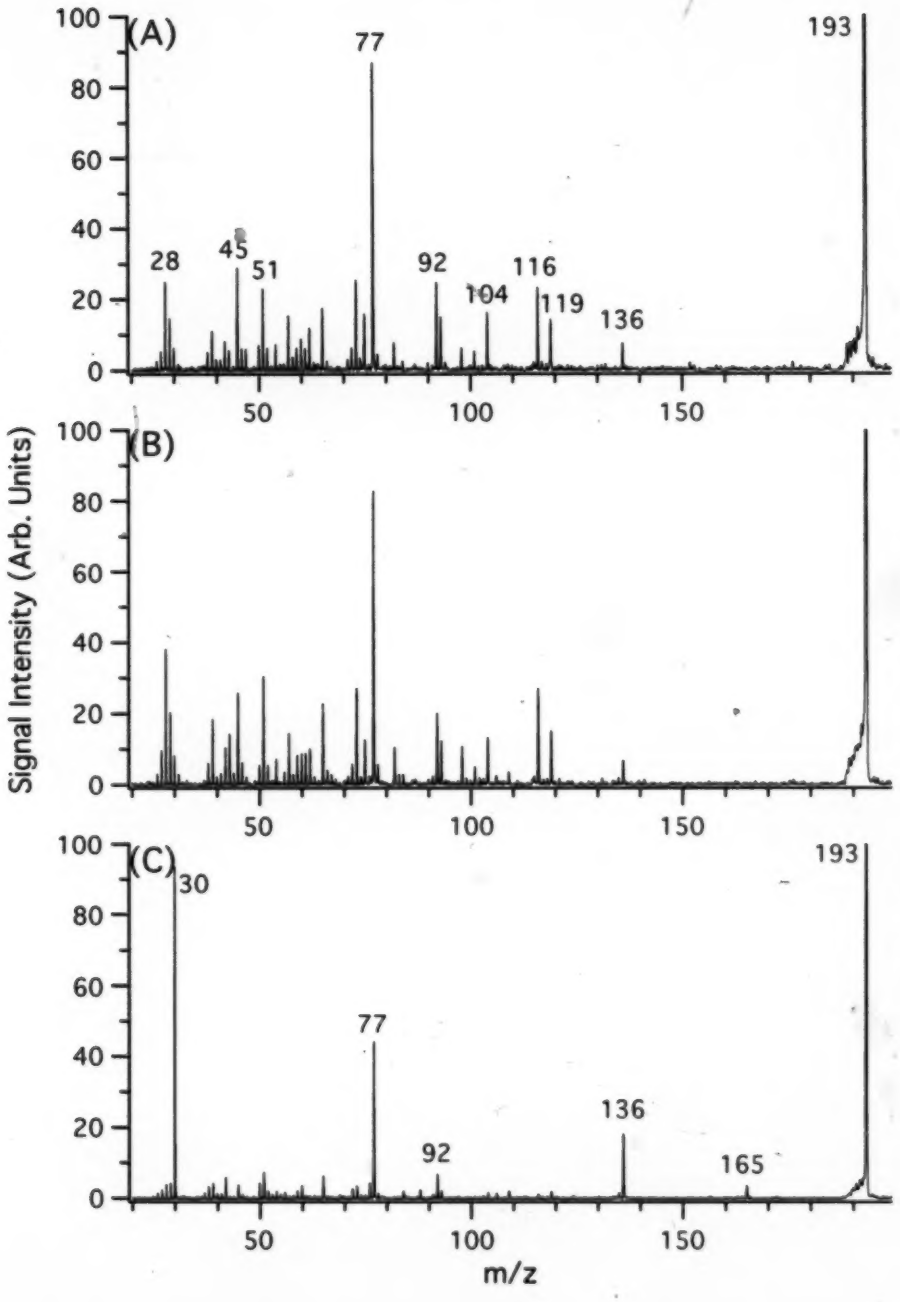

Figure 4.9. High-energy CID mass spectra of the m/z 193 ions derived from (A) PTC-Thr-Leu, (B) PTC-Trp-Leu, and (C) PTC-Gly-Leu.

The spectrum shown in Figure 4.9 C (the m/z 193 ion from PTC-Gly-Leu) is different from those shown in Figures 4.9 A and B. It resembles the spectrum shown in Figure 4.5 for the m/z 193 ion from PTH-Gly with the exception that the product ion spectrum from PTC-Gly-Leu contains the m/z 165 peak which is probably from CO elimination of the m/z 193 ion.

By analogy with the proposed mechanism of fragmentation for PTH-X, Figure 4.10 shows the formation and fragmentation mechanism of the m/z 193 ion derived from PTC-Thr-Leu and PTC-Trp-Leu. A thiazolone ion/neutral complex is formed [12] followed by the C-terminal group leaving the complex as a neutral species, resulting in a cyclic ion like the b ions [11]. A hydrogen migration from the side chain group takes place during the formation of the m/z 193 ion. Figure 4.11 shows the proposed structure and fragmentation mechanism of the m/z 193 ion derived from PTC-Gly-Leu.

4.4 Summary

The fragmentation pathways of the protonated PTH-X (where X=Thr, Ser, Trp, or Tyr), PTH-Gly, PTC-X-Leu, and PTC-Gly-Leu generated by ESI have been examined. The high-energy CID spectra of the m/z 193 ions from PTH-X are the same, suggesting they have the same structure. However, the spectrum of the m/z 193 ion from PTH-Gly is different from those of PTH-X. It was shown that the source-formed ion at m/z 193 derived from PTH-X originates from the side chain elimination of the R group with a hydrogen migration from the R group to the phenylhydantoin moiety. The hydrogen migration is proposed to occur via a hydrogen bond with the carbonyl group in the phenylhydantoin moiety. Hence the structure of the m/z 193 ions from PTH-X is different from that from PTH-Gly. This gives the rationale of the observed differences in product ion spectra of the m/z 193 ions from PTH-X and PTH-Gly. Since a common ion at m/z 193 is generated from PTH-X, it is argued that this ion along with its CID spectrum can be used to examine the presence of these ions in the gas phase.

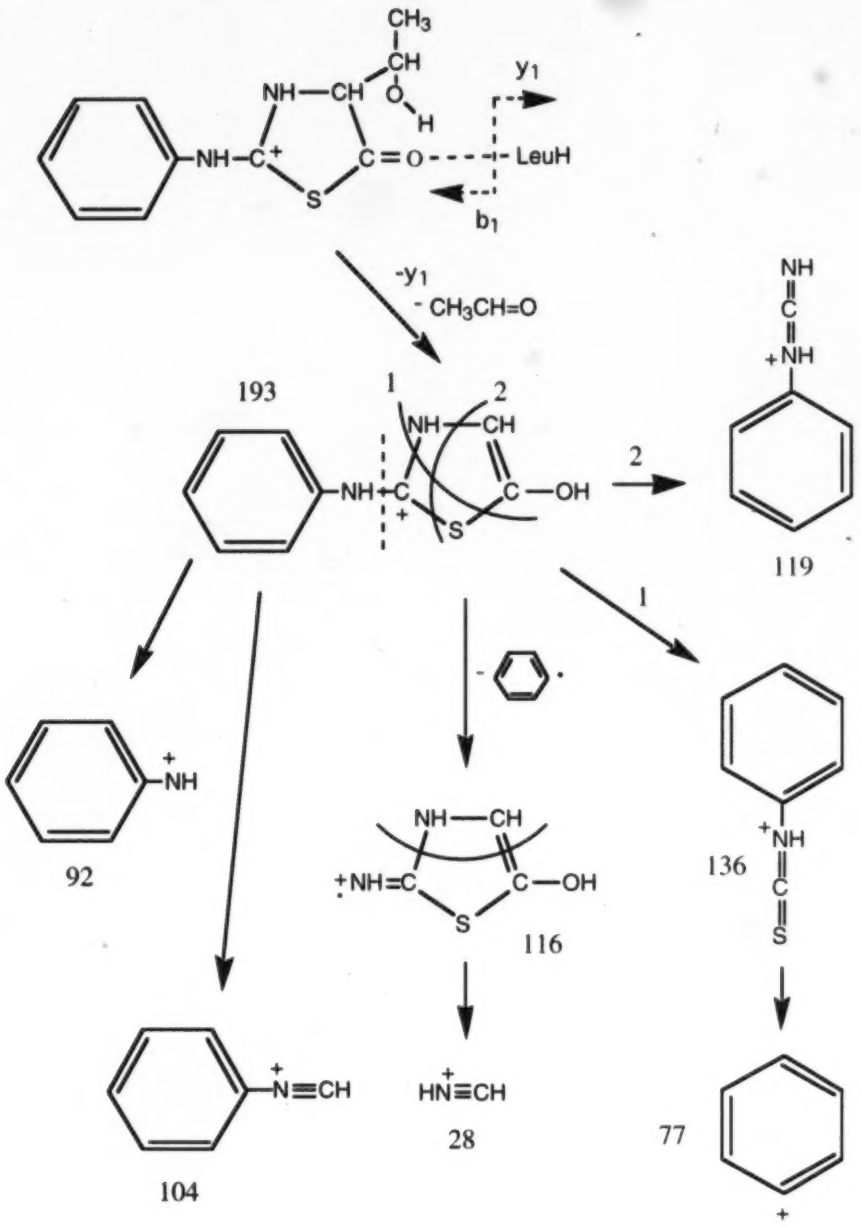

Figure 4.10. Proposed mechanism of formation and fragmentation of the m/z 193 ions derived from PTC-Thr-Leu and PTC-Trp-Leu using PTC-Thr-Leu as an example.

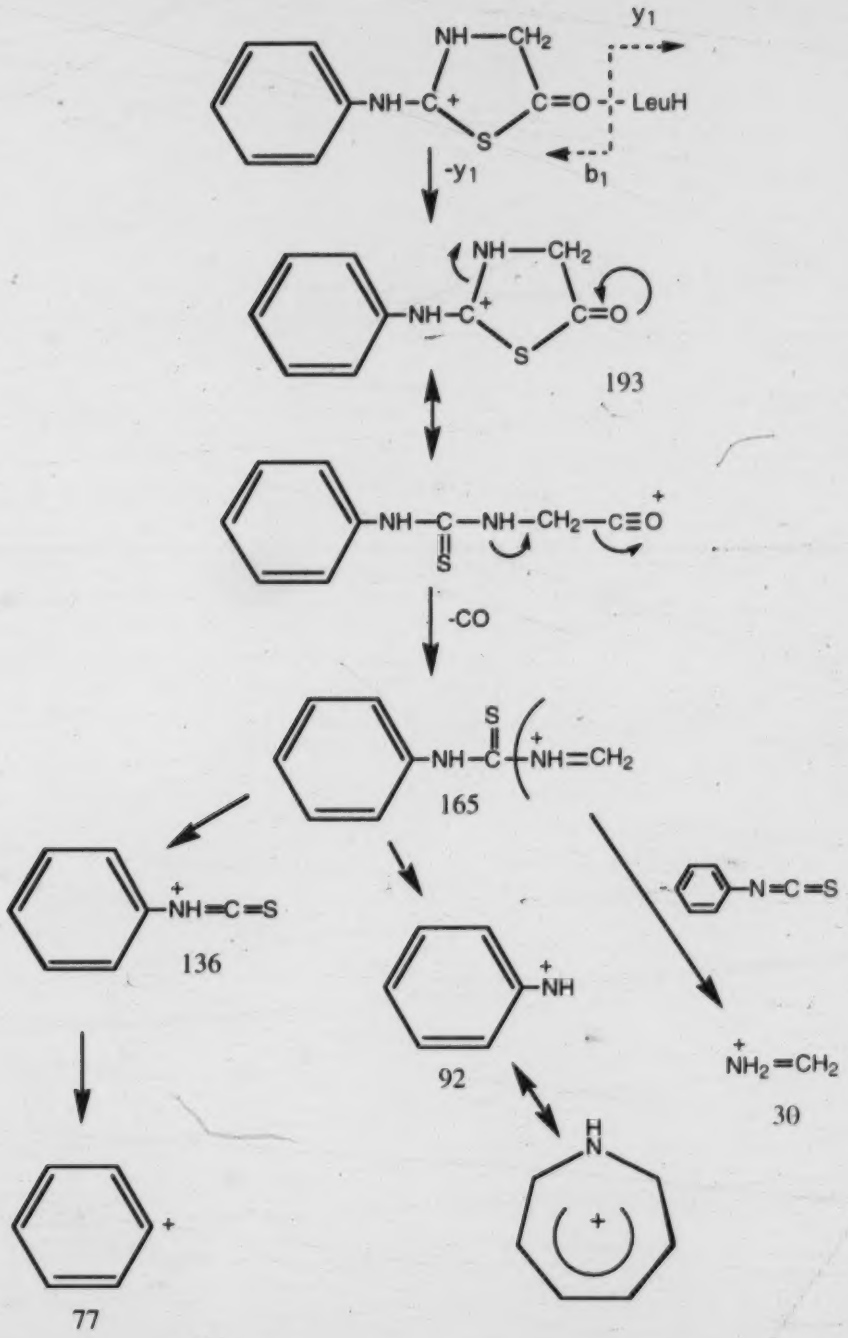

Figure 4.11. Proposed mechanism of fragmentation of the m/z 193 ion derived from PTC-Gly-Leu.

CS elimination from the thiazolone was not observed. The $[b_1\text{-}44]^+$ peak in the CID spectrum of the protonated PTH-Thr was from the loss of a neutral species (CH_2O) by side chain elimination, rather than CS elimination.

For PTC-X-Leu, only PTC-Thr-Leu and PTC-Trp-Leu gave rise a peak at m/z 193 in the source fragmentation spectra. Examination of the CID spectra of the m/z 193 ions derived from these two derivatives reveals that these ions had different fragmentation pathways from that of the m/z 193 ion from PTH-X. Furthermore, the fragmentation pathways of these ions were different from the m/z 193 ion derived from PTC-Gly-Leu. The spectral information obtained in the experiment strongly suggests that there is no isomerization of thiazolone to phenylthiohydantoin in the gas phase.

4.5 Literature cited

[1] Basic, C.;. Baley, J. M.; Lee, T. D. *J. Am. Soc. Mass Spectrom.* **1995**, 6, 1211.

[2] Okada, K.; Sakuno, A. *Org. Mass Spectrom.* **1978**, 9, 535.

[3] Rangarajan, M.; Ardery, R. E.; Darbre, A. *J. Chromatogr.* **1973**, 87, 499.

[4] Sun, T.; Lovins, R. E. *Anal. Biochem.* **1972**, 45, 176.

[5] Fairwell, T.; Brewer, H. B., Jr. *Anal. Biochem.* **1980**, 107, 140.

[6] Pramanik, B. C.; Hinton, S. M.; Millington, D. S.; Dourdeville, T. A.; Slaughter, C. A. *Anal. Biochem.* **1995**, 224, 373.

[7] Hess, D.; Nika, H.; Chow, D. T.; Bures, E. J.; Morrison, H. D.; Aebersold, R. *Anal. Biochem.* **1995**, 224, 373.

[8] Bures, E. J.; Nika, H.; Chow, D. T.; Morrison, H. D.; Hess, D.; Aebersold, R. *Anal. Biochem.* **1995**, 224, 364.

[9] Summerfield, S. G.; Bolgar, M. S.; Gaskell, S. J. *J. Mass Spectrometry* **1997**, 32, 225.

[11] Yalcin, T.; Khouw, C.; Csizmadia, I. G.; Peterson, M. R.; Harrison, A. G. *J. Am. Soc. Mass Spectrom.* **1995**, 6, 1165.

[12] Harrison, A. G.; Wang, J.-Y. *Int. J. Mass Spectrom. Ion Proc.* **1997**, 160, 157.

Chapter 5

Structural Analysis of Polymer End Groups by ESI MS/MS[a]

In polymer research, the chemical structures of the polymer end groups play an important role in determining the functional properties of a polymeric system. Polymer end group determination is often an essential part of a polymer characterization program. The tandem mass spectrometry technique, presented in the previous chapter, can be applied to solve problems in this area of chemical analysis.

5.1 Introduction

Despite the chemical diversity of polymeric systems, an increasing number of different types of polymers, including most commonly used industrial polymers, can now be analyzed by mass spectrometry. At present, matrix-assisted laser desorption ionization (MALDI) time-of-flight mass spectrometry (TOFMS) is perhaps the most widely used technique for polymer analysis [1, 2]. With MALDI-TOF, the molecular weight, molecular weight distribution and polymer composition can be rapidly and accurately determined [3-18]. However, structural information generated from MALDI-TOF is often limited. This is particularly true for end group characterization. At best, the oligomer masses in a MALDI spectrum can only be used to deduce information about the total mass of the end groups of a polymer.

Tandem mass spectrometry combined with MALDI has been developed for polymer structural characterization [19-22]. Very impressive fragment ion spectra can be produced in tandem sector/time-of-flight mass spectrometry with collision-induced dissociation (CID). Derrick and coworkers recently demonstrated the use of high energy

[a] A portion of the work described in this chapter was submitted to *Anal. Chem.* for publication as: T. Yalcin, W. Gabryelski, and L. Li "Structural Analysis of Polymer End Groups by Electrospray Ionization High-Energy Collision-Induced Dissociation Tandem Mass Spectrometry"

CID in sector/TOF MS for end group characterization [22]. The need for high energy CID to gain information on end group structures was clearly illustrated [22]. However, in CID spectra of oligomers, ion peaks from end-groups tend to mix with many low mass peaks that are the result of internal fragmentation of the polymer chains, rendering some difficulty in spectral interpretation for end-group structure analysis, particularly for unknowns. Since MALDI generates predominately singly charged oligomers, only low mass polymers are amendable to MALDI MS/MS. These difficulties are also associated with MALDI-TOF having post-source decay or CID capability.

Electrospray ionization (ESI) MS is another important method for polymer analysis [23-39]. In ESI, multiple charged polymeric ions are generated and these ions can be readily fragmented in the source region of an ESI interface [37]. However, polymeric species and their fragments such as those from poly(ethylene glycol)s (PEGs) appear to be difficult to fragment into low-mass ions with low-energy CID. This was observed in the studies of a series of PEGs in MALDI Fourier transform ion cyclotron resonance (FT-ICR) experiment [22] and in fast atom bombardment ionization CID experiment [40].

In this chapter, a new MS method that provides structural information on polymer end groups is presented. This method is based on the use of source fragmentation of polymer ions generated by electrospray ionization. Ions formed in the source are subjected to high-energy collision-induced dissociation analysis in a tandem sector/time-of-flight mass spectrometer. The application of this method is demonstrated for the end-group analysis of two slow-releasing drugs, poly(oxyethylene) bis(acetaminophen) and poly(oxyethylene) bis(ephedrine). The limitations of a ESI IT/TOFMS instrument for this type of application are also discussed.

5.2 Experimental

5.2.1 High-energy CID experiments with source fragmentation

All high-energy CID experiments were carried out by using ZabSpec (ZAB) orthogonal acceleration (OA) time-of-flight (TOF) instrument from Micromass (Manchester, UK). The ESI method was used for creating gas phase ions. Source fragmentation of polymer ions was controlled by adjusting the voltage difference V_{CID} between the atmospheric plate and the skimmer. The precursor ions were accelerated by a voltage of 4 kV and mass selected with the EBE mass spectrometer. The ions were introduced into the collision cell floated at 3600 V. Thus, for high-energy CID, the laboratory kinetic energy of a singly charged precursor ion is 400 eV. Argon was used as the collision gas, and on average, the intensity of the precursor ions was attenuated by ~30 %. The ions exiting the collision cell were guided into the OA-TOF spectrometer, and pulsed into the flight tube for mass separation. Ions were detected with a microchannel plate detector.

5.2.2 Polymers and chemicals

Poly(oxyethylene)bis(acetaminophen), Poly(oxyethylene)bis(ephedrine), acetaminophen and ephedrine were purchased from Sigma Chemical Corporation (St. Louis, MO) and used without purification. The structures of these two polymers are shown in Chart 5.1. HPLC-grade acetonitrile, HPLC-grade water and ammonium acetate were purchased from Fisher Scientific Company (Nepean, ON). Solutions for ESI-MS analysis were prepared by dissolving an analyzed compound in a mixture of 80 % (v/v) acetonitrile and 20 % (v/v) 0.25 mM ammonium acetate in water. The sample solution (100 μM) was delivered from the syringe to ESI source at a flow rate of 6 μL/min using the continuous infusion method.

Chart 5.1 Structures of the polymers used in this study.

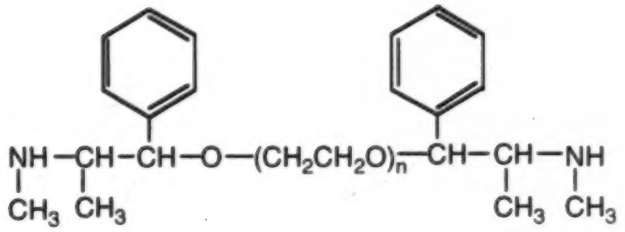

Poly(oxyethylene) bis(ephedrine)

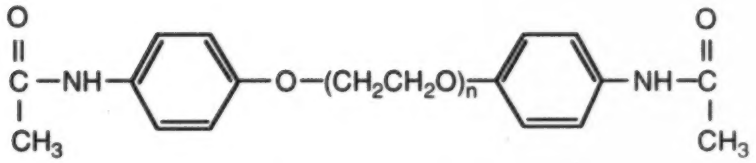

Poly(oxyethylene) bis(acetaminophen)

5.3 Results and Discussion

5.3.1 Poly(oxyethylene) bis(ephedrine)

Electrospray ionization of the polymers (average molecular weight ~ 3500 u) resulted in the mass spectra displaying several polymer distributions arising from oligomers with different charge states. The oligomers at the +2, +3, and +4 charge state were observed. However, only the oligomers at the charge state of +4 could dissociate. Figure 5.1 A shows the low mass region of the high-energy CID spectrum of an ion (+4 charge state) at m/z = 1014 from poly(oxyethylene) bis(ephedrine). Series of peaks G_n (i.e., m/z at 148, 192, and 236) and A_n (i.e., m/z at 45, 89, 133, 177) (see Figure 5.5 for fragment ion notations) were observed with a mass difference corresponding to the repeat unit of the polymer (i.e., 44 u). These fragment ions are generated by cleavage of the polymer backbone and may contain end group information [40].

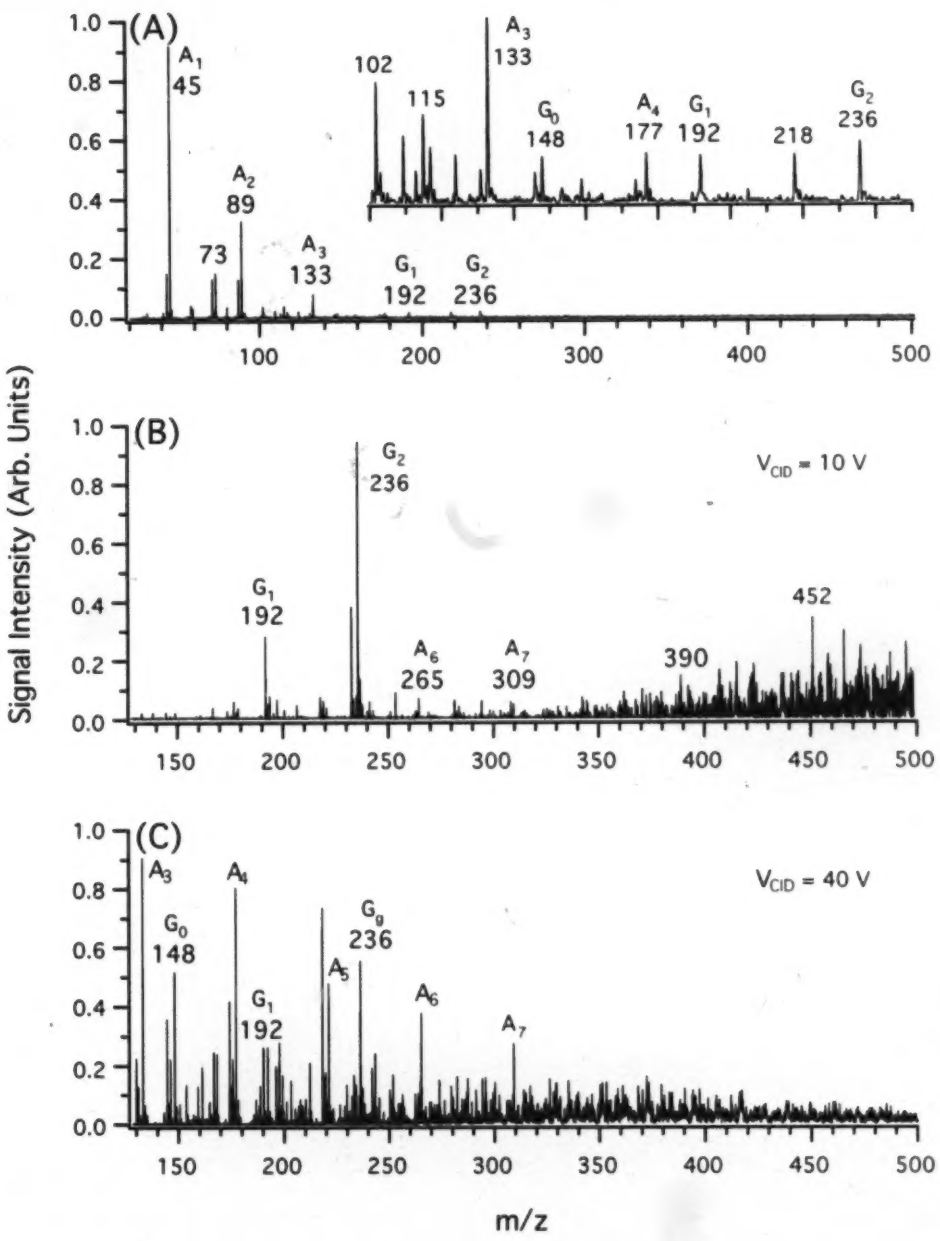

Figure 5.1. CID spectra of poly(oxyethylene) bis(ephedrine) using tandem sector/time of flight MS. (A) High-energy CID spectrum of the m/z 1014 oligomer at +4 charge state, (B) Source CID of the polymer at V_{CID} = 10 V, and (C) Source CID of the polymer at V_{CID} = 40 V.

However, no intense peaks corresponding to the ephedrine structure can be assigned. This illustrates a major shortcoming of the method using CID MS/MS of high mass oligomers for structural characterization of end groups. The lack of a sufficient number of fragment ions from the particular structures of end groups is quite understandable, in light of the fact that the internal energy gained from the CID process redistributes among many energy levels of such a large ion. Chain cleavage appears to be the dominant process in CID.

It would appear that further dissociation of the fragment ions after selection should potentially generate structural information on the end group. Unfortunately, the ZAB-TOF system used does not provide MS/MS/MS capability. Thus an alternative tandem mass spectrometry experiment was examined. Source fragmentation was used to produce fragment ions from a polymer, followed by high-energy CID of these fragments. Figure 5.1 B and C show the source fragmentation spectra of poly(oxyethylene) bis(ephedrine) obtained using different source voltages (V_{CID}). A number of fragment ions are generated in source fragmentation; however, the ions from the G_n series at m/z 148, 192, 236 are preferentially formed (Figure 5.1 B and C). When V_{CID} increases to 40 V, lower mass fragments become more intense. These ions were selected for high-energy CID. Examining all of the recorded spectra, some fragmentation patterns can be readily recognized. This is illustrated in Figure 5.2. The high-energy CID spectrum of the m/z 236 ion (Figure 5.2 A) exhibits a fragment ion at m/z 148 generated by elimination of two monomer units of the polymer (88 u). Figure 5.2 B shows that the fragment ion at m/z 148 is also produced by high-energy CID of the m/z 192 ion (elimination of one monomer unit). However, as shown in Figure 5.2 C, there are no fragment ions originating from the m/z 148 ion that correspond to further monomer elimination. In addition, the presence of common fragment ions in the mass spectral regions from m/z 20 to 150 is observed in Figure 5.2 B and Figure 5.2 C. From these results, one can tentatively assign the m/z 148 ion as an ion from the end group of the polymer.

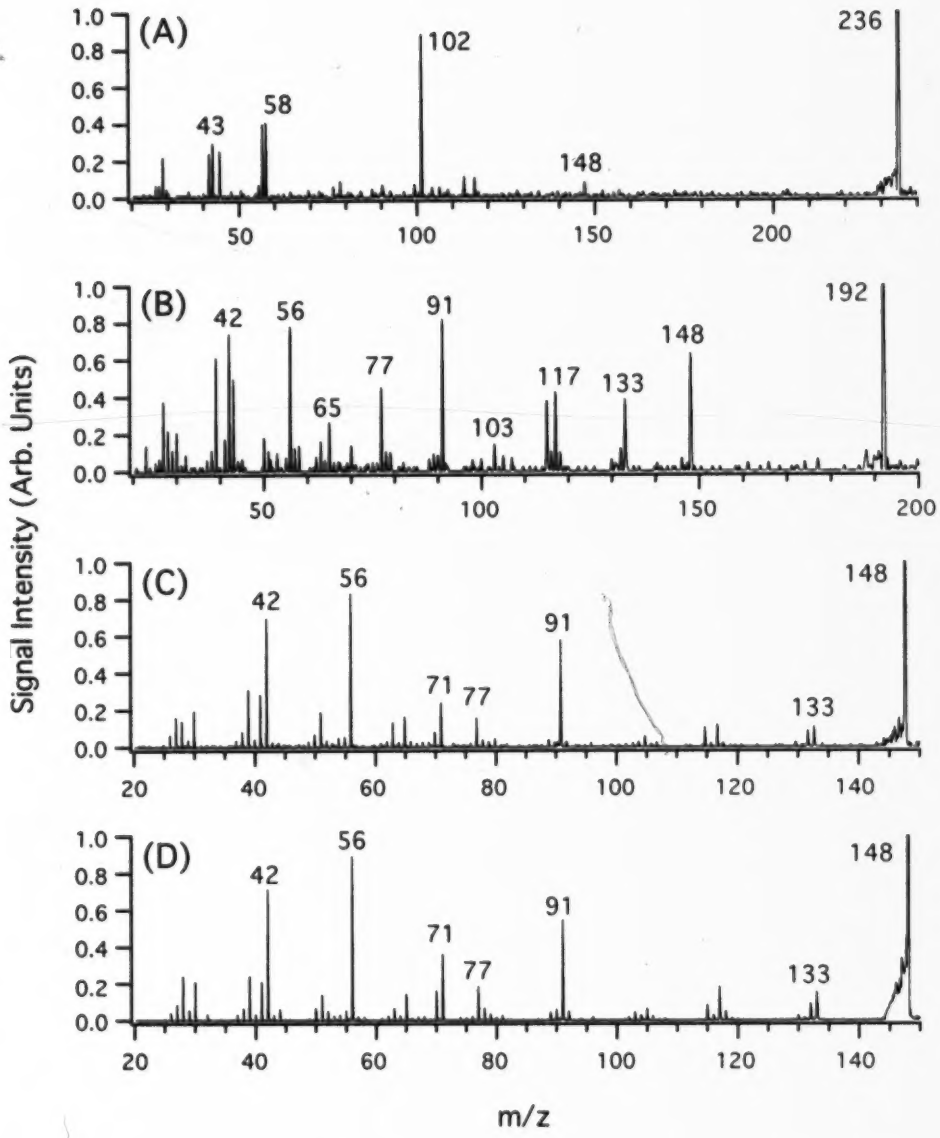

Figure 5.2. High-energy CID spectra of ions generated in source fragmentation. (A) G_2 ion at m/z 236, (B) G_1 ion at m/z 192 and (C) G_0 ion at m/z 148, all derived from poly(oxyethylene) bis(ephedrine). (D) The m/z 148 ion originating from ephedrine.

For unambiguous structural assignment, fragment ion spectra of standard compounds can be obtained and compared to a spectrum of an unknown. In this case, a high-energy CID spectrum of an ion originating from the standard compound, ephedrine, was recorded under the same experimental conditions. This is shown in Figure 5.2 D. The spectra shown in Figures 5.2 C and 5.2 D are similar, confirming the end-group structure.

5.3.2 Poly(oxyethylene) bis(acetaminophen)

Similar results were obtained in the analysis of poly(oxyethylene) bis(acetaminophen). Figure 5.3 A shows the expanded high-energy CID spectrum of a poly(oxyethylene) bis(acetaminophen) oligomer at +4 charge state. At the mass range up to about m/z 133, this CID spectrum is similar to that in Figure 5.1 A obtained from poly(oxyethylene) bis(ephedrine), despite the significant differences in end group structures of the two polymers. Unfortunately, this is also the mass region in which one hopes to obtain useful information on end group structures. It is clear that high-energy CID MS/MS of oligomers has limited use in end group structure characterization for these two slow-releasing drugs. Figure 5.3 B and C show the source fragmentation spectra of a poly(oxyethylene) bis(acetaminophen) obtained using different source voltages (V_{CID}). These spectra are different from those of poly(oxyethylene) bis(ephedrine) (see Figures 5.1 B and 5.1 C). The source-formed ions from the G_n series at m/z 134, 222, 310 were subjected to high-energy CID and the resulting spectra are shown in Figure 5.4. The m/z 134 ion, related to the identity of the end group, was formed in high-energy CID by elimination of an appropriate number of monomer units from larger species. Figure 5.4 C shows the high-energy CID spectrum of the m/z 134 ion originated from poly(oxyethylene) bis(acetaminophen) and it can be compared to the high-energy CID spectrum of the m/z 134 ion originated from acetaminophen. In this case, the confirmation of the identity of the end group was also obtained.

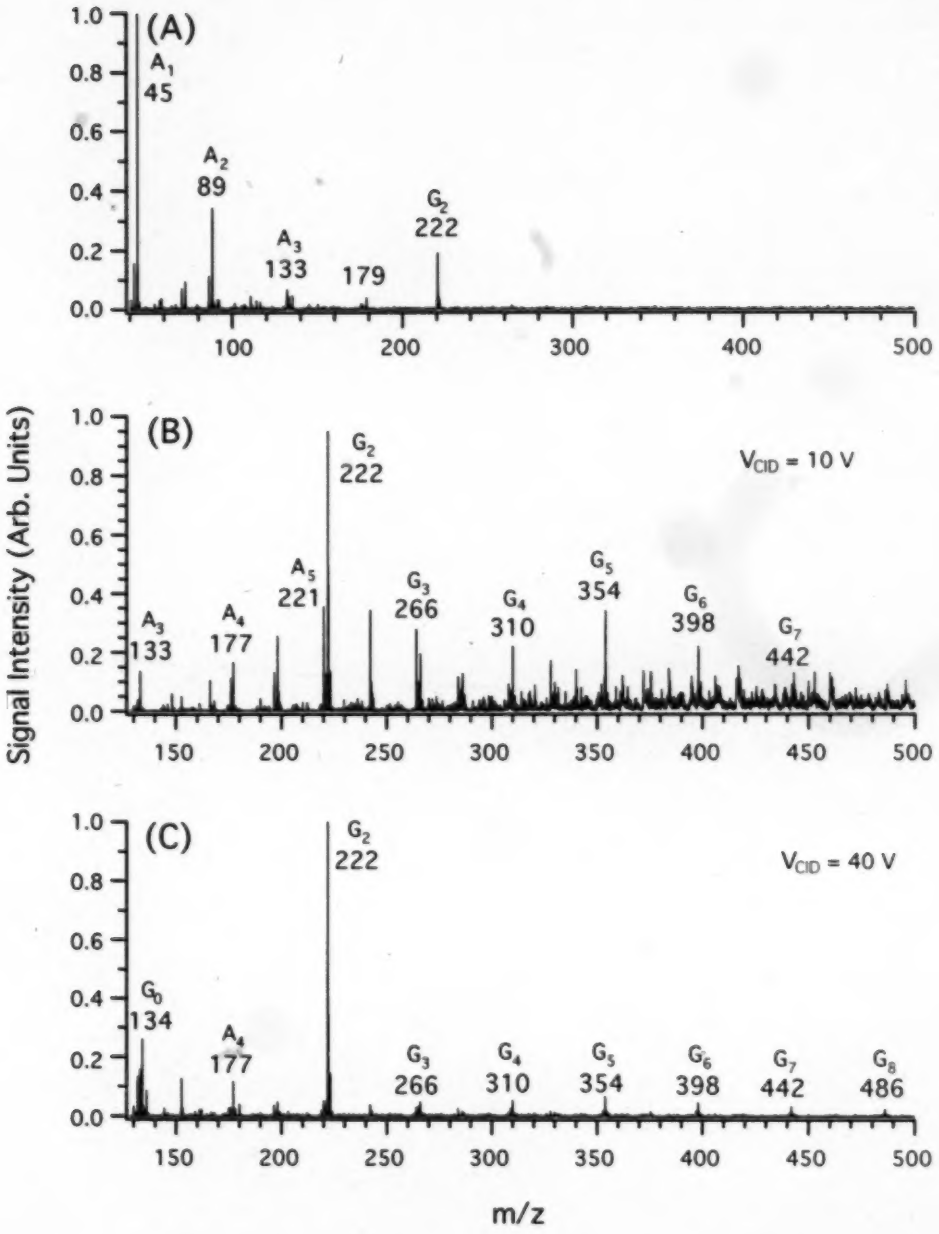

Figure 5.3. CID spectra of poly(oxyethylene) bis(acetaminophen) using tandem sector/time of flight MS. (A) High-energy CID spectrum of the m/z 1007 oligomer at +4 charge state, (B) Source CID of the polymer at V_{CID} = 10 V and (C) Source CID of the polymer at V_{CID} = 40 V.

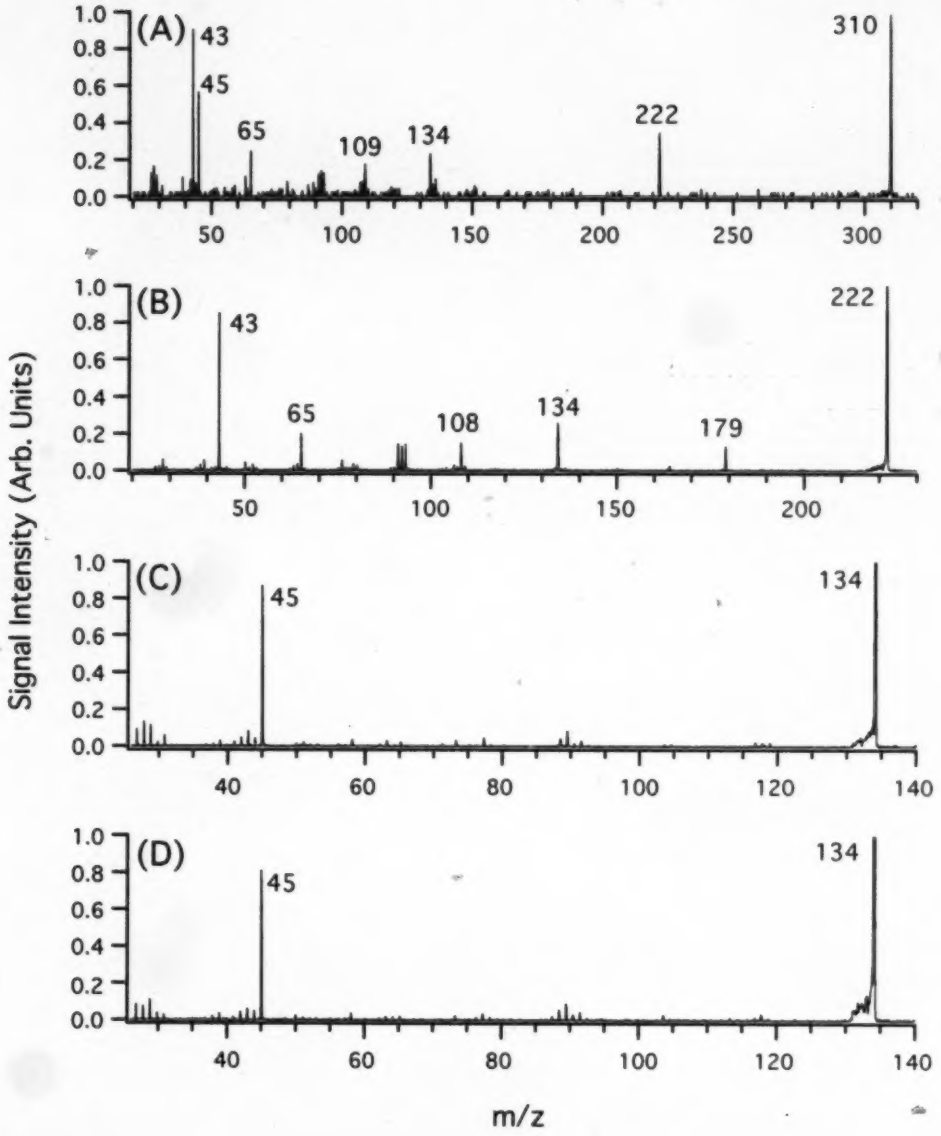

Figure 5.4. High-energy CID spectra of ions generated in source fragmentation. (A) G_4 ion at m/z 310, (B) G_2 ion at m/z 222 and (C) G_0 ion at m/z 134, all derived from poly(oxyethylene) bis(acetaminophen). (D) The m/z 134 ion originating from acetaminophen.

5.3.3 Other considerations

The above examples demonstrate that the method of source fragmentation/MS/MS can be very useful in obtaining structural information of polymer end groups. In applying this method for end group analysis, several important issues need to be considered. The first one is related to the generation of source-fragment ions for different types of polymers. It appears that source fragmentation is quite efficient for a number of polymeric systems [27-38]. In fact, source fragmentation is one of the major concerns in determining molecular weights of polymers by ESI. For polymers that do not fragment efficiently, variation of ESI conditions such as solvents and types of cation can influence the extent of source fragmentation [39].

For two identical end groups, the described method does not indicate the number of the end groups linked to the polymer. In addition to that, the careful examination of the source fragmentation (Figure 5.1 B and Figure 5.3 B) or high-energy CID fragmentation (Figure 5.1 A and Figure 5.3 A) spectra of both polymers reveals, according to the A_n ion series, that another candidate for the end group can be postulated. A consecutive loss of the monomer unit (44u) from all A_n ions implies that a $H(OCH_2CH_2)_n$ terminal satisfies requirements to be considered as an alternative end group. However, complementary information can be obtained from an ESI MS or MALDI MS of the intact polymer that provides the total mass of the end groups attached to the polymer terminals. Thus, the correct number and identity of the end groups can be conclusively determined by the combination of polymer MS and ESI source fragmentation MS/MS. In the case of poly(oxyethylene) bis(acetaminophen) and poly(oxyethylene) bis(ephedrine), the desired polymeric product has ephedrine or acetaminophen linked to the polymer at both ends. Dosage determination of these slow-releasing drugs is partly dependent upon the success of derivatization of the polymer. For the two species examined in this work, both ESI and time-lag focusing MALDI-TOF mass analysis of the oligomer indicated that there are two end groups attached to the

polymer [41]. In the case of a non-symetric polymer with different termini, the end group assignment would depend on the concomitant generation of source-fragment ions that contain a terminal group.

5.3.4 The origin of the fragment ions in CID spectra of the polymers

The presence of the fragment ions not related to the end groups in CID spectra raises the question about the nature of these ions. Figure 5.5 shows the proposed mechanism of the formation of the ions present in low-energy CID spectra of poly(oxyethylene) bis(ephedrine) and poly(oxyethylene) bis(acetaminophen). In the electrospray ionization process, the oligomer of the polymer subjected to dissociation accommodates four protons. Considering the proton affinity of amines or amides versus that of ethers [42] protonation should take place at the NH functionality of a polymer end group. It is represented in Figure 5.5 by the end group R carrying the charge. Such protonated sites posses a well stabilized charge center and will favor charge-remote fragmentation [40] in CID. The reaction scheme for this process is shown in Figure 5.5 A. Charge-remote decompositions can account for all major CID fragments from the G_n series containing end group information. Note, that ions from the B_n series are not observed in the CID spectra. The remaining labile protons randomly move along a polymer chain and interact with ether oxygen atoms. The random location of protons creates many possible reaction sides. Figure 5.5 B illustrates formation of A_n series ions. They are generated by charge-site catalyzed (inductive) cleavages [40]. The incipient ionic products of these decompositions would be primary carbonium cations. Such ions are prone to further fragmentation, isomerization and may rearrange to more stable structures during or after formation. The ions from A_n series do not contain end group information.

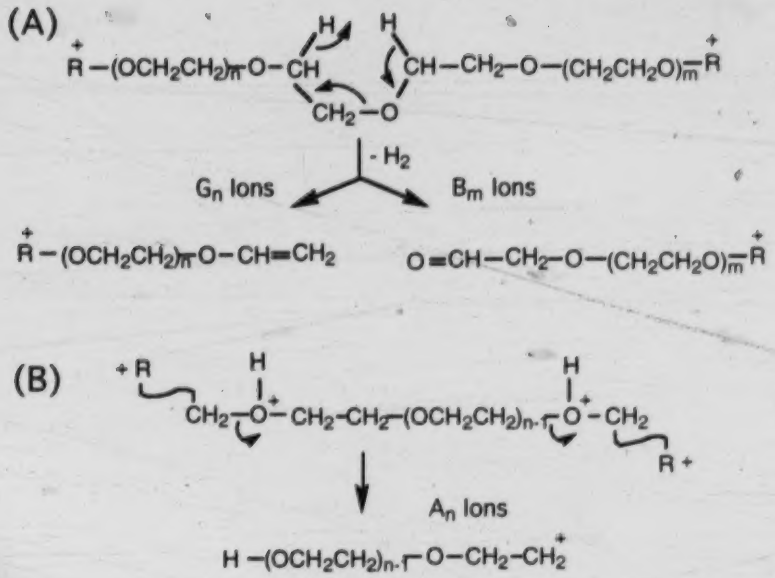

Figure 5.5. Proposed mechanism of polymer fragmentation. (A) Formation of G_n and B_m ions and (B) Formation of A_n ions.

5.3.5 Ion stability diagrams in source fragmentation

For the production of end group fingerprint spectra, the described method does not require the use of an on-line separation technique. This provides the advantage of simplicity and no need of compromising ESI and separation conditions. The infusion experiment also provides polymeric ion signals over a long period, ensuring the selection of many different source-fragment ions for CID. However, one has to be aware of the possible presence of any low mass impurities in the polymer sample that may cause complications in spectral interpretation. For instance, the fragment ion peak observed at m/z 148 in Figure 5.1 C could be simply from ephedrine that might be present in the sample. While off-line separation by liquid chromatography to remove low mass impurities prior to MS/MS experiments is an obvious option, another way to check the

origins of low mass peaks is to examine the source fragmentation behavior of different species with common groups. This is illustrated in Figure 5.6.

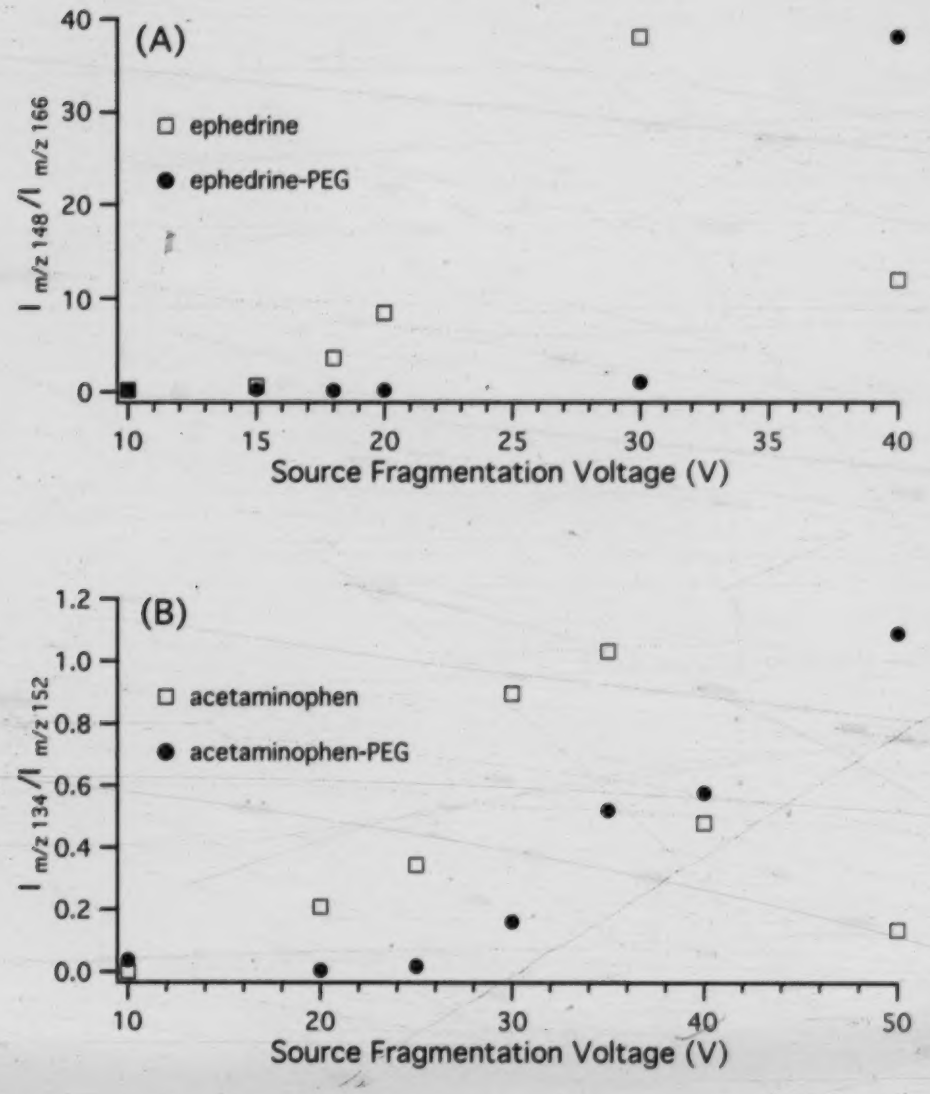

Figure 5.6. Ion stability diagrams in source fragmentation. (A) Poly(oxyethylene) bis(ephedrine) and ephedrine, (B) Poly(oxyethylene) bis(acetaminophen) and acetaminophen.

Figure 5.6 shows the distributions of important diagnostic ions formed in source fragmentation. The two sets of data shown in Figure 5.6 A were obtained by source fragmentation of ESI generated ephedrine and poly(oxyethylene) bis(ephedrine), respectively. In the case of ephedrine, the intensity of the ion R^+ at m/z 148 was measured relative to the intensity of the protonated molecular ion of ephedrine ROH_2^+ at m/z 166 at various fragmentation voltages (V_{CID}). For ephedrine-attached PEG, the signal at m/z 166 was at the background level and the ratio of peak intensities at m/z 148 and m/z 166 was calculated for comparison. Figure 5.6 A illustrates that at V_{CID} of 30 V, only the formation of the m/z 148 ion originating from ephedrine takes place. A further increase in V_{CID} causes dissociation of the m/z 148 ion derived from ephedrine and formation of the m/z 148 ion initiated from ephedrine-PEG. The corresponding graphs for acetaminophen and acetaminophen-attached PEG are presented in Figure 5.6 B. The intensity of the ion R^+ (m/z 134) was measured relative to the intensity of the ion at m/z 152 (i.e., the protonated molecular ion peak of acetaminophen) at various fragmentation voltages (V_{CID}). Figure 5.6 clearly shows that in both cases higher V_{CID} is required to produce a significant amount of end group related species from the polymer. Thus, the presence of strong ion signals at m/z corresponding to the intact molecular ion peak of end group initiators (i.e., m/z 166 for ephedrine and m/z 152 for acetaminophen) and end-group containing fragment ions (i.e., m/z 148 for ephedrine and m/z 134 for acetaminophen at low source voltages would suggest the presence of some impurities in the sample.

5.3.6 ESI IT/TOFMS in end group determination of polymers

Ion trap instruments provide multiple stages of ion selection and dissociation in a MS^n process. This asset is especially valuable in experiments involving structural elucidation of ionic species using several consecutive dissociation steps to obtain structural details of investigated ions. Thus an ESI IT/TOF mass spectrometer is a

logical instrumental alternative to the expensive tandem sector/time-of-flight mass spectrometer in polymer studies. Figure 5.7 and 5.8 show results obtained for analysis of poly(oxyethylene) bis(ephedrine) using the ESI IT/TOF instrument.

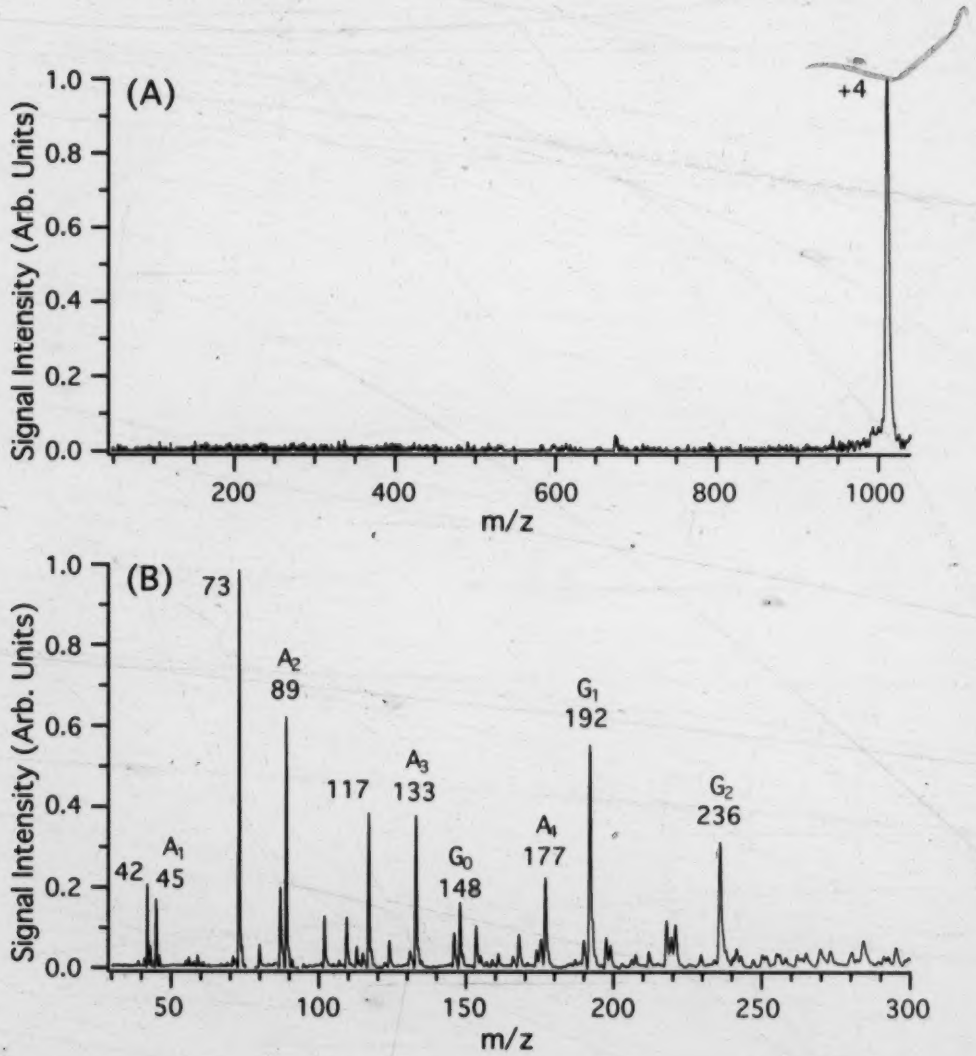

Figure 5.7. CID spectra of poly(oxyethylene) bis(ephedrine) using ion trap/time-of-flight MS. (A) Ion trap CID spectrum of the m/z 1014 oligomer at +4 charge state and (B) Source CID of the polymer at V_{CID} = 40 V.

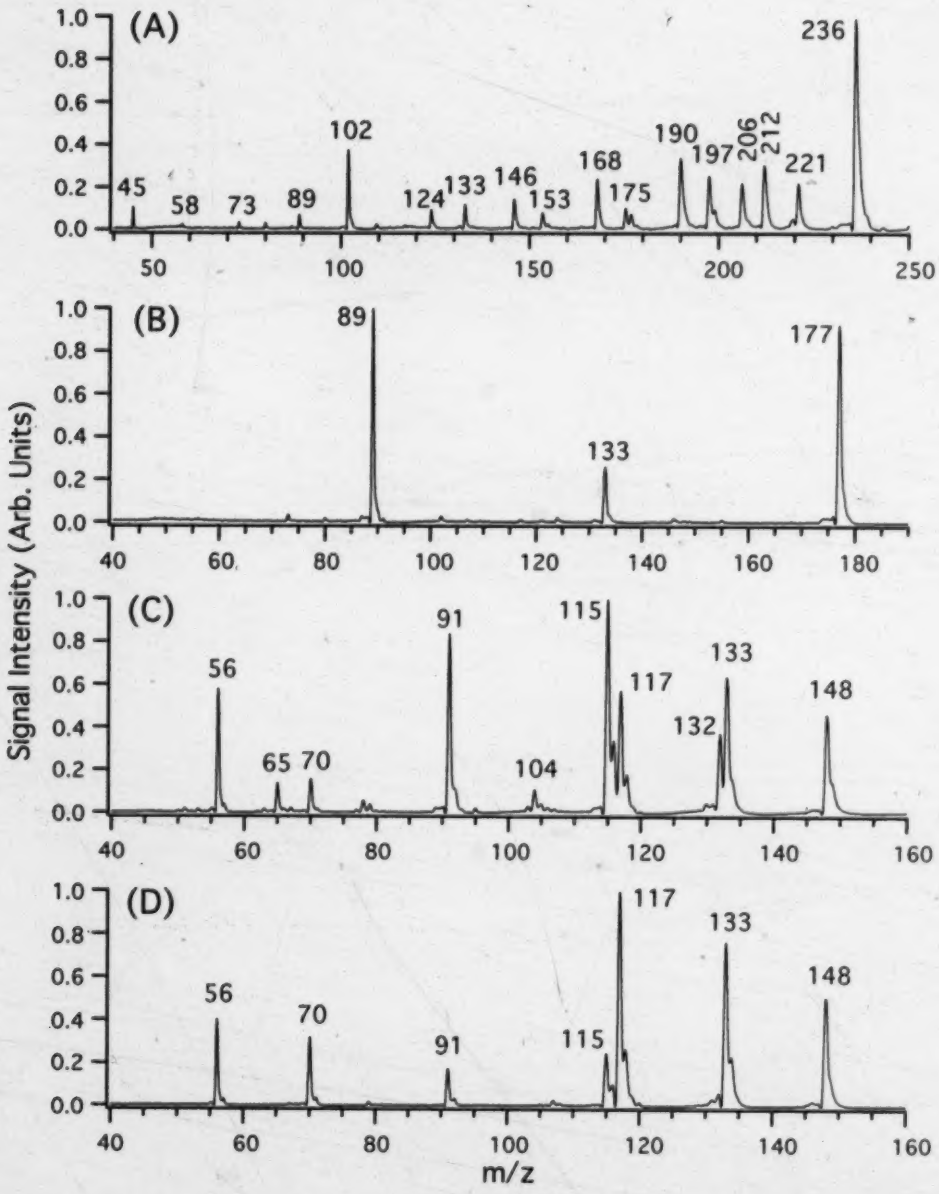

Figure 5.8. Ion trap CID spectra of ions generated in source fragmentation. (A) G_2 ion at m/z 236, (B) A_4 ion at m/z 177 and (C) G_0 ion at m/z 148, all derived from poly(oxyethylene) bis(ephedrine). (D) The m/z 148 ion originating from ephedrine.

The spectrum shown in Figure 5.7 A illustrates the experiment in which the ion of an oligomer at +4 charge state (m/z 1014) was isolated inside the ion trap. In the next step, the selected ion was excited to induce fragmentation. As can be seen in Figure 5.7 A, the ion trap CID excitation did not generate dissociation products. A further increase in excitation energy resulted in the total loss of the molecular ion from the trap. This characteristic behavior is typical for large ions that can not be fragmented in ion trap CID. The highest energy deposited to an ion in CID without losing it from the trap is related to the magnitude of rf trapping voltage and is expressed as q_z parameter. The failure to dissociate the molecular ion at the highest available q_z does not imply that a similar CID process for a commercial ion trap instrument will be ineffective. In an operation of the commercial instrument, a higher amplitude of rf trapping voltage (3000 V_{P-P} is the limit for IT/TOF) could be used increasing q_z and an amount of energy involved in CID.

Ions that were not able to dissociate inside the trap were fragmented in a more energetic source excitation process. Figure 5.7 B shows the spectrum of dissociation products from the polymer in source fragmentation. Previously identified ions from G_n and A_n series are present in the spectrum. These ions were selected for ion trap CID and Figure 5.8 shows their ion trap CID spectra. Comparison of spectral features for the m/z 236 ion obtained in ion trap CID (Figure 5.8 A) and high-energy CID (Figure 5.2 A) is astonishing. The presence of the common ions at m/z 45, 58, 102 in both spectra provides evidence that the same ion was analyzed. The number of products in the ion trap CID (Figure 5.8 A) is impressive. However, the diagnostic peak at m/z 148 formed by elimination of two monomer units from the m/z 236 ion in high-energy CID does not appear in the ion trap CID spectrum. This complication does not allow deduction of a correlation between ions as was possible in the analogous procedure for high-energy CID. The presence of all "extra" peaks in the ion trap CID spectrum raises an intriguing question about their nature. Figure 5.8 B shows the ion trap CID spectrum of the m/z 177

from the A_n series. This ion, in contrast to the m/z 236, does not contain the end group moiety in its structure. The ion trap CID spectrum of the m/z 177 does not show such complexity and is similar to the high-energy CID spectrum of this ion (not shown). As one can see, there is a significant influence of the presence of the end group on the population of fragments in ion trap CID. It is not surprising when one considers the environment of ion trap CID. An ion trap is a reaction chamber with an abundance of ions and neutrals formed in CID. All of these reactive species have been allowed to interact for tens or hundreds of milliseconds. The final products of this process may be completely different than the products obtained from high-energy CID. In high-energy CID, ions are separated in space and possible interactions are limited to a few microseconds between excitation and detection. Figure 5.8 C and D compare ion trap CID spectra acquired for the m/z 148 ion originated from ephedrine-PEG (Figure 5.8 C) and derived from ephedrine (Figure 5.8 D). The match between these two spectra is also not as convincing as in high-energy CID. Not only are differences in intensity of corresponding fragmentation products observed, but also the exclusive presence of the m/z 65 peak and the m/z 132 peak can be noticed in Figure 5.8 C. It is very difficult to explain this observation. The effect of instrumental conditions on spectral information is negligible when these conditions are properly controlled and very reproducible ion trap CID spectra can be obtained. It might be possible that depending upon the origin, two different types (structures) of m/z 148 ion could be generated and this difference could only be spotted by the ion trap. It would be a very useful property of ion trap systems. On the other hand, the above results clearly indicate that ion chemistry in the trap can complicate mass spectral analysis based on MS/MS methods.

5.4 Summary

A new tandem mass spectrometry method was used to obtain structural information on polymer end groups. This method relies on the use of source

fragmentation to generate low mass fragment ions from polymer ions formed by electrospray ionization. Two types of ions, similar to those observed in high-energy CID of oligomer ions, were generated from source fragmentation of poly(oxyethylene) bis(acetaminophen) and poly(oxyethylene) bis(ephedrine). One group of ions generated by cleavage of the polymer chain did not contain end group information. Ions from a second group retaining end group information were subjected to high-energy collision-induced dissociation in a tandem sector/time-of-flight mass spectrometer. High-energy CID spectra of selected ions provided information on polymer end groups. These spectra can be used as a fingerprint to compare with the CID spectra of standard compounds for unambiguous structural identification of end groups. This method, along with oligomer mass information obtained from techniques such as ESI-MS or MALDI-TOF, should be useful for studying "unknown" end group structures. This method does rely on the availability of CID library spectra in order to find a satisfactory match. Fortunately, in polymer analysis, some prior-knowledge of the end group chemistry is always available from the polymer chemistry used for the synthesis. The initiators and their analogs are available and can be used to generate a CID library for spectral comparison. The laborious aspect of the method will depend upon the complexity of the polymeric system under investigation.

The described method could not be applied to the ESI IT/TOFMS. Two major instrumental limitations were discovered. The ion trap was not capabile of dissociating large ionic species. Secondly, ion trap CID of polymer fragments generated in the ESI source resulted in an abundance of ions exhibiting very limited spectral information. It shows a need for designing a new dissociation method effective for larger ions as well as studying processes involving reaction of all species present in the trap.

5.5 Literature cited

[1] Bahr, U.; Deppe, A.; Karas, M.; Hillenkamp, F. *Anal. Chem.* **1992**, 64, 2866.

[2] Danis, P. O.; Karr, D. E. *Org. Mass Spectrom.* **1993**, 28, 923.

[3] Juhasz, P.; Costello, C. E. *Rapid Commun. Mass Spectrom.* **1993**, 7, 343.

[4] Montaudo, G.; Montaudo, M. S.; Puglisi, C.; Samperi, F. *Rapid Commun. Mass Spectrom.* **1994**, 8, 1011.

[5] Cottrell, J. S.; Koerner, M.; Gerhards, R. *Rapid Commun. Mass Spectrom.* **1995**, 9, 1562.

[6] Mowat, I. A.; Donovan, R. J. *Rapid Commun. Mass Spectrom.* **1995**, 9, 82.

[7] Danis, P. O.; Karr, D. E.; Simonsick, W. J. Jr.; Wu, D. T. *Macromolecules* **1995**, 28, 1229.

[8] Larsen, B. S.; Simonsick, W. J. Jr.; McEwen, C. N. *J. Am. Soc. Mass Spectrom.* **1996**, 7, 287.

[9] Lloyd, P. M.; Suddaby, K. G.; Varney, J. E.; Scrivener, E.; Derrick, P. J.; Haddleton, D. M. *Eur. Mass. Spectrom.* **1995**, 1, 293.

[10] Belu, A. M.; DeSimone, J. M.; Linton, R. W.; Lange, G. W.; Friedman, R. M. *J. Am. Soc. Mass Spectrom.* **1996**, 7, 11.

[11] Danis, P. O.; Karr, D. E.; Xiong, Y.; Owens, K. G. *Rapid Commun. Mass Spectrom.* **1996**, 10, 862.

[12] Wallace, W. E.; Guttman, C. M.; Antonucci, J. M. *J. Am. Soc. Mass Spectrom.* **1999**, 10, 224.

[13] Burger, H. M.; Muller, H. M.; Seebach, D.; Bornsen, K. O.; Schar, M.; Widmer, M. *Macromolecules* **1993**, 26, 4783.

[14] Weidner, S.; Kuhn, G.; Friedrich, J.; Schroeder, H. *Rapid Commun. Mass Spectrom.* **1996**, 10, 40.

[15] Wilczek-Vera, G.; Danis, P. O.; Eisenberg, A. *Macromolecules* **1996**, 29, 4036.

[16] Whittal, R. M.; Li, L.; Lee, S.; Winnik, M. A. *Macromol. Rapid Commun.* **1996**, 17, 59.

[17] Schriemer, D. C.; Li, L. *Anal. Chem.* **1996**, 68, 2721.

[18] Schriemer, D. C.; Whittal, R. M.; Li, L. *Macromolecules* **1997**, 30, 1955.

[19] Jackson, A. T.; Yates, H. T.; Scrivens, J. H.; Critchley, G.; Brown, J.; Green, M. R.; Bateman, R. H. *Rapid Commun. Mass Spectrom.* **1996**, 10, 1668.

[20] Jackson, A. T.; Yates, H. T.; MacDonald, W. A.; Scrivens, J. H.; Critchley, G.; Brown, J.; Deery, M. J.; Jennings, K. R.; Brookes, C. *J. Am. Soc. Mass Spectrom.* **1997**, 8, 132.

[21] Scrivens, J. H.; Jackson, A. T.; Yates, H. T.; Green, M. R.; Critchley, G.; Brown, J.; Bateman, R. H.; Bowers, M. T.; Gidden, J. *Int. J. Mass Spectrom. Ion Proc.* **1997**, 165/166, 363.

[22] Bottrill, A. R.; Giannakopulos, A. E.; Waterson, C.; Haddleton, D. M.; Lee, K. S.; Derrick, P. J. *Anal. Chem.* **1999**, 71, 3637.

[23] Fenn, J. B.; Mann, M.; Meng, C. K.; Wong, S. F.; Whitehouse, C. M. *Science*, **1989**, 24, 64.

[24] Smith, R. D.; Loo, J. A.; Orgorzalek-Loo, R. R.; Busman, M.; Udseth, H. R. *Mass Spectrom. Rev.* **1991**, 10, 359.

[25] Chen, R.; Cheng, X.; Mitchel, D. W.;Hofstadler, S. A.;Rockwood, A. L.; Scherman, M. G.; Smith, R. D. *Anal. Chem.* **1995**, 67, 1159

[26] Kallos, G. J., Tomalia, D. A.; Hedstrand, D. M.; Lewis, S.; Zhou, J. *Rapid Commun. Mass Spectrom.* **1991**, 5, 383.

[27] Prokai, L.; Simonsick, W. J., Jr.; *Rapid Commun. Mass Spectrom.* **1993**, 7, 853.

[28] Sherrard, K. B.; Marriott, P. J.; McCormick, M. J.; Colton, R.; Smith, G. *Anal. Chem.* **1994**, 66, 3394.

[29] McEwan, C. N.; Simonsick, W. J. Jr.; Larsen, B. S.; Ute, K.; Hatada, K. *J. Am. Soc. Mass Spectrom.* **1995**, 6, 906.

[30] Hunt, S. M.; Binns, M S.; Sheil, M. M. *J. Appl. Polym. Sci.* **1995**, 56, 1589.

[31] O'Connor, P. .; McLafferty, F. W. *J. Am. Chem. Soc.* **1995**, 117, 12826.

[32] Mahon, A.; Kemp, T. J.; Buzy, A.; Jennings, K. R. *Polymer* **1996**, 37, 531.

[33] Saf, R.; Schitter, R.; Mirtl, C.; Stelzer, F.; Hummel, K. *Macromolecules* **1996**, 29, 7651.

[34] Guittard, J.; Tessier, M.; Blais, J. C.; Bolbach, G.; Rozes, L.; Marechal, E.; Tabet, J. C. *J. Mass Spectrom.* **1996**, 31, 1409.

[35] Parees, D. M.; Hanton, S. D.; Cornelio Clark, P. A.; Willcox, D. A. *J. Am. Soc. Mass Spectrom.* **1998**, 9, 282.

[36] Yalcin, T.; Gabryelski, W.; Li, L. Structural Analysis of Polymer End-Groups by Using ESI MS/MS, *Proceedings of the 46th ASMS Conference on Mass Spectrometry and Allied Topics*, Orlando, Florida, May 31-June 4, **1998**, p. 1053.

[37] Hunt, S. M.; Sheil, M. M.; Belov, M.; Derrick, P. J. *Anal. Chem.* **1998**, 70, 1812.

[38] Nielen, M. W.; Buijtenhuijs, F. A. *Anal. Chem.* **1999**, 71, 1809.

[39] Chen, R.; Dunlop, K.; Gabryelski, W; Li, L. unpublished results (**1999**).

[40] Selby, T. L.;Wesdemiotis, C.; Lattimer, R. P. *J. Am. Soc. Mass Spectrom.* **1994**, 5, 1081.

[41] Whittal, R. M.; Schriemer, D. C.; Li, L. *Anal. Chem.* **1997**, 69, 2734.

[42] Lias, S. G.; Liebman, J. F.; Levin, R. D. *J. Phys. Chem. Ref. Data* **1984**, 13, 695.

Chapter 6

Photo-Induced Dissociation of Electrospray Generated Ions in an Ion Trap/Time-of-Flight Mass Spectrometer using a Nd:YAG Laser[a]

6.1 Introduction

Collision-induced dissociation presented in previous chapters, is the most prevalent method for structural elucidation of biological molecules in tandem mass spectrometry. Among several mass spectrometric configurations being used for MS/MS, ion trap mass spectrometry has been demonstrated to be a very useful tool for highly efficient production and subsequent analysis of CID products. However, due to the limited amount of energy deposited into larger ions in the collisional activation process inside an ion trap (collisional and kinetic effects), the efficiency of CID is observed to decrease with increasing mass-to-charge ratio. In extreme cases, the ions to be excited are resonantly ejected from the trap without fragmentation. The attractiveness of photo-induced dissociation (PID) comes from the fact that energy deposition by photon absorption is independent of mass. In addition, PID can be highly selective, because the efficiency of PID is dependent on the wavelength of the photon used for dissociation. This can be very useful in applications such as selective analysis of photo-labeled peptides from peptide mixtures resulting from enzyme digestion of proteins covalently bonded with a photo-labeled inhibitor. Because of mechanistic difference in energy absorption in PID and CID, the fragmentation patterns from these two processes can be different. Thus PID and CID may provide complementary structural information of biomolecules.

There are a number of reported studies on the development and applications of PID for chemical analysis. The first report on photodissociation of chemical ionization

[a] A form of this chapter has been published as: W. Gabryelski and L. Li "Photo-Induced Dissociation of Electrospray Generated Ions in an Ion Trap/Time-of-Flight Mass Spectrometer", Rev. Sci. Instrum. **1999**, 11, 4192.

generated peptide ions was published fifteen years ago [1]. It used a high power pulsed UV laser and a Fourier transform-ion cyclotron resonance (FT-ICR) mass spectrometer. Results from early experiments [2, 3] showed the compatibility of PID with the instrumental requirements of FT-ICR. Hunt and coworkers [4] showed that this technique is applicable to larger (up to m/z 3100) peptide ions. Recent advances in ionization techniques such as electrospray ionization (ESI) for large biomolecules open a new opportunity in the application of PID for structural characterization using FT-ICRMS and a wide range of wavelength from IR to vacuum UV. Williams et al. [5] reported photodissociation efficiencies on order of 100% for the peptide alamethicin using 193-nm light, much higher than that of CID. Little et al. [6] demonstrated the capability of infrared multiphoton dissociation (IRMPD) to obtain sequence information for peptides/proteins and nucleotides. IRMPD was shown to have less mass discrimination and ability to dissociate much more stable ions than CID [6].

The first successful use of a quadrupole ion trap for photodissociation involved the study of proton-bound dimer of 2-propanol utilizing a continuous wave CO_2 laser [7]. A 266-nm laser beam was used in an ion trap dissociation experiment of ionized perfluoropropylene with a simple fiber-optic interface [8]. The PID technique performed inside an ion trap for electrospray generated ions proved to be feasible for molecular structure determination. Stephenson et al. [9] described an ion trap with a multi-pass optical arrangement for PID. This elegant arrangement extends the optical pathlength; hence partially overcoming the inherent disadvantage of low photoabsorption-cross-section often associated with PID. This technique was successfully applied to representatives of biologically important molecules such as oligosaccharides, peptides, oligonucleotides and antibiotics [10].

In conventional ion trap systems such as those previously used for PID experiments [7-10], mass spectra of PID products are recorded by mass scan in the trap. An alternative method of recording mass spectrum is to use a time-of-flight (TOF) mass analyzer.

This chapter describes the application of ion trap/TOFMS for PID studies of electrospray generated ions and reports results from PID and CID of peptides. In contrast to an ion trap with slow mass scan, ion trap/TOF provides the unique capability for fast detection of all ions formed via PID and any quick excitation process in general. This unique feature is demonstrated and explored to study the time dependence of generation of PID fragment ions after laser excitation.

6.2 Experimenal

6.2.1 Modifications of the instrument

The ion trap/linear time-of-flight mass spectrometer equipped with an electrospray ionization source has been described in previous chapters. For CID and PID experiments, the instrument was modified to perform isolation and activation of ions inside the ion trap. The personal computer (PC) output signals were used for synchronization of laser pulses and all ion trap events (i.e., ion accumulation, ion isolation, ion excitation, and ion ejection for detection). The arbitrary waveform generator AWG PCI-311 (PC Instruments Inc., Akron, OH) was used to generate the broadband SWIFT (Stored Waveform Inverse Fourier Transform [11]) isolation and excitation waveforms according to the algorithm implemented by Doroshenko and Cotter [12]. The AWG output was connected to the ion trap entrance end-cap.

As an example, Figure 6.1 A represents the SWIFT waveform used for isolating the protonated molecular ions of leucine enkaphalin (m/z 556.6) inside the ion trap. The waveform was designed by calculating the fundamental secular frequency of ions to be isolated and building a magnitude spectrum from 10 to 500 kHz with the notch (width 0.8 kHz) centered at the fundamental secular frequency. The transformation (inverse Fourier transform) of the tailored magnitude spectrum resulted in the time-domain sweep-like waveform shown in the Figure 6.1 A. An acceptable amplitude range for this waveform

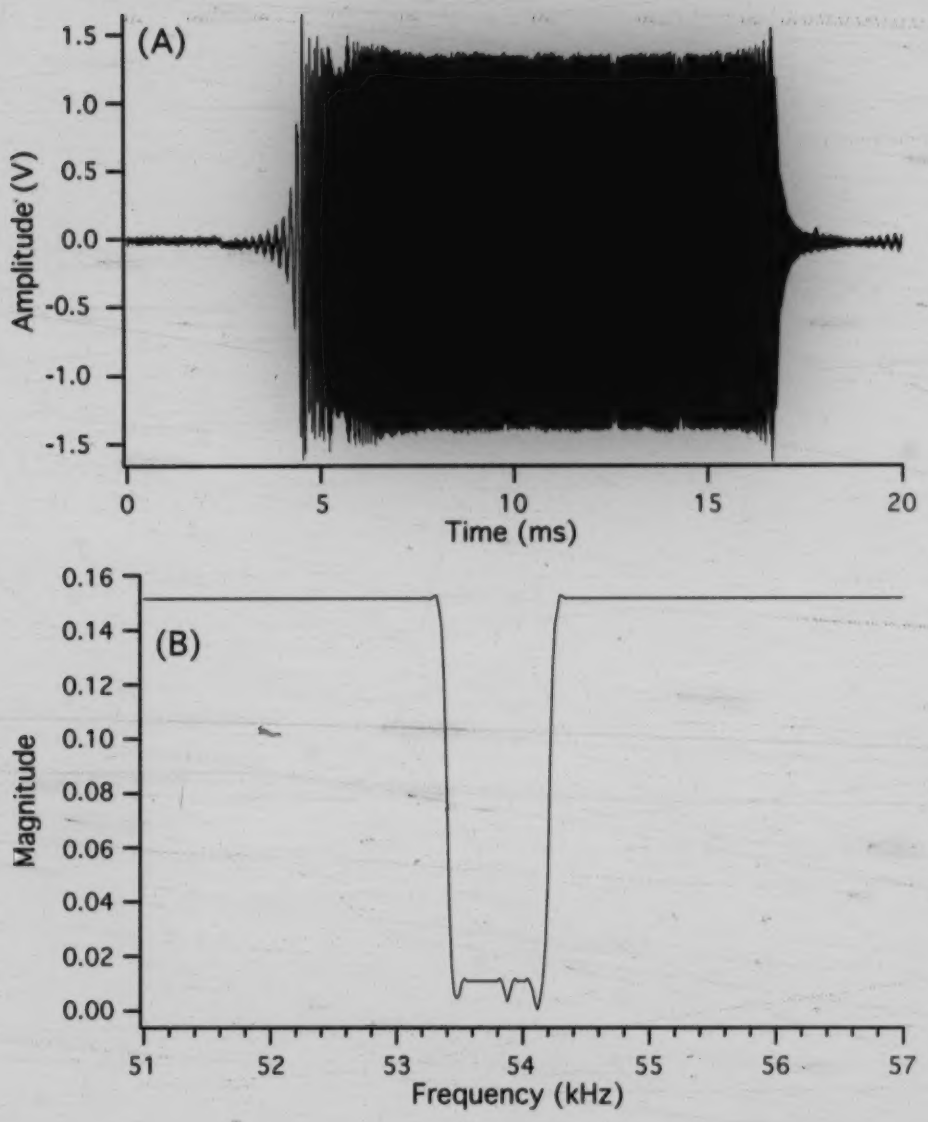

Figure 6.1. SWIFT waveforms used in isolation of the protonated ion of leucine-enkephalin at m/z 556.6. (A) Time-domain SWIFT notched waveform used for ion isolation. (B) Magnitude spectrum of the SWIFT notched waveform used for isolation.

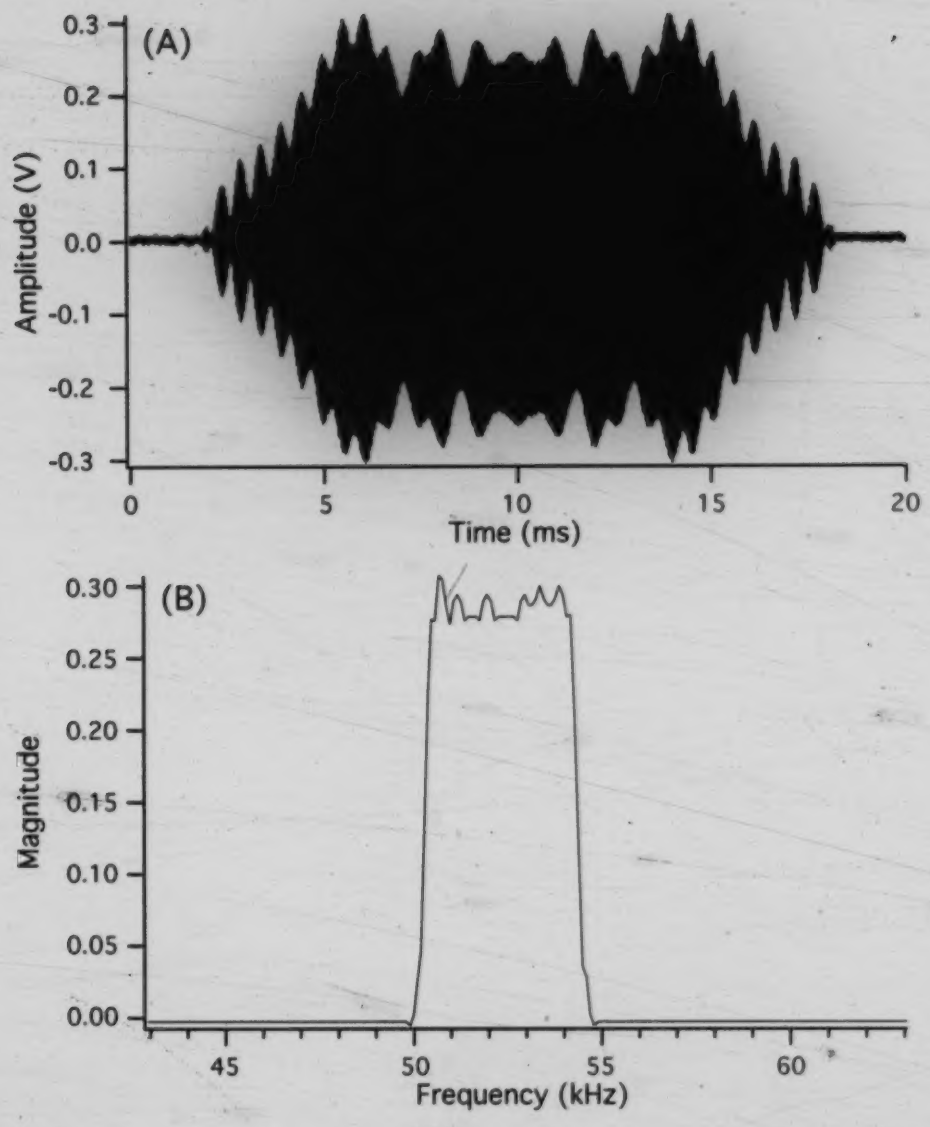

Figure 6.2. SWIFT waveforms used in activation of the protonated ion of leucine-enkephalin at m/z 556.6. (A) Time-domain SWIFT waveform used for excitation. (B) Magnitude spectrum of the SWIFT waveform used for excitation.

was achieved by using the quadratic phase modulation method [12]. Figure 6.1 B shows the magnitude spectrum (Fourier transform product) obtained for the SWIFT waveform from Figure 6.1 A at the vicinity of the secular frequency. In all experiments, the same notch width was used and the amplitude of the SWIFT waveform was adjusted to provide the best ion isolation resolution and minimal ion loses in the isolation process. Excitation waveforms were constructed in a similar fashion. Figure 6.2 A shows the SWIFT excitation waveform implemented in the ion trap CID process of leucine enkaphalin (m/z 556.6) and the resulting magnitude spectrum of this excitation waveform is shown in Figure 6.2 B. In this case, the waveform in frequency domain contains the excitation frequency band at a width of 4 kHz. The frequency band overlaps the isolation frequency notch and extends to lower frequencies. The broadband excitation provides better control over the excitation energy deposition, compared to a single frequency excitation method.

6.2.2 Excitation experiments

Three types of ion excitation experiments with corresponding sequence of events are depicted in Figure 6.3. In the CID method (Figure 6.3 A), the positive edge of a master trigger pulse (A) from the PC triggers a pulser which applies a negative voltage pulse (-800 V and 30 μs wide) to the exit endcap. This negative pulse (less than 1μs delay to the master trigger) removes ions from the trap and represents the starting point for TOF detection. The gating signal (2) in Figure 6.3 A from PC is connected to a gating electric plate in the ESI interface. Only when the value of signal (2) is low (60 volts for high and 0 for low), ions enter the ion trap. The ion accumulation event takes place from B to C. This is followed by a short cooling period (C-D) and then by the application of several repeat isolation-waveforms (D). After a subsequent cooling period (D-E), the selected ions are excited by the application of an activation waveform (E). After a short waiting period, the fragment ions are ejected from the trap into the TOF detector by applying pulse A. The entire sequence in the CID experiment was controlled by software developed in house.

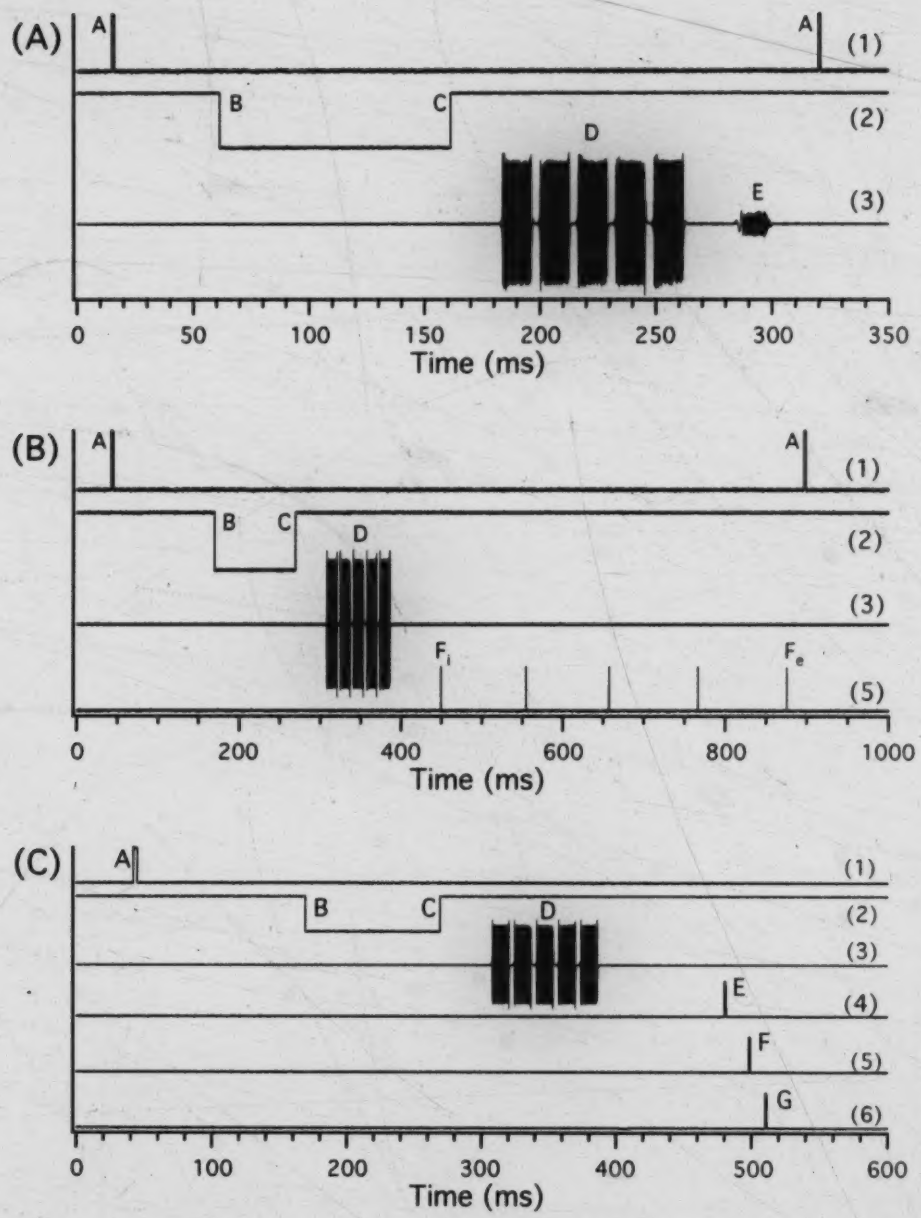

Figure 6.3. Sequence of events of an ion trap/time-of-flight mass spectrometer for (A) CID, (B) PID with multiple laser pulses and (C) PID with a single laser pulse and time-dependent detection. See text for details.

In the PID method with the use of multiple laser pulses for dissociation (Figure 6.3 B), the accumulation process (B-C) is followed by short cooling period (C-D), isolation event (D) and post-isolation cooling (D-F_i). Instead of CID, the isolated ions are subjected to a series of laser pulses (F_i to F_e). The fragment ions are ejected from the trap into the TOF detector by applying the master pulse A. The time delay between the last laser pulse and the ion ejection pulse (i.e., from F_e to A) can be adjusted with the software. With a PC master clock to control the entire sequence of the events in a cycle, the time jitter of the delay from F_e to A is in the order of several microseconds. For instance, for the 1-s duration of entire cycle of events shown in Figure 6.3 B, when a time delay from F_e to A is set at 10 μs with the software, the actual delay is in the range 5-15 μs after the last laser pulse. This time jitter is not a concern for ordinary experiments where the main interest is to produce fragment ions. However, in the case of studying the time dependence of the generation of PID ions shortly after the photoexcitation of the precursor ions, the time jitter must be kept at minimum to ensure reproducible PID spectra.

In order to limit the time uncertainty of the detection event the sequence shown in Figure 6.3 C was used. Master trigger (A) starts a new cycle (ion accumulation B-C, isolation D) and triggers the laser (E). The delay time between the laser pulse (F) (Q-switch trigger out) and detection pulse G was controlled by digital delay generator model I2IBR (California Avionics Laboratory Inc., Palo Alto, CA). This set up allowed to probe time-dependence of events as low as 1 μs apart with time delay from 1 microsecond to several milliseconds following the dissociation laser pulse.

A 266 nm laser beam from a Nd:YAG laser was used in PID experiments. The laser light was collimated by two lenses (convex, f = 300 mm; concave, f = 100 mm) into the 1.5-mm diameter hole in the ring electrode. In a typical PID experiment, an isolated parent ion was subjected to a single laser pulse (5-ns pulse width) or a series of laser pulses (2 to 10), at an energy of 30 to 50 mJ per pulse. Each pulse was separated by a 100 ms delay time. PID spectra were corrected for background ions by subtracting the spectrum

obtained using the same experimental sequence but without introducing ions into the ion trap.

6.2.3 Chemicals and electrospray conditions

Peptides were purchased from Sigma Chemical (St Louis, MO) and used without purification. HPLC-grade acetonitrile, HPLC-grade water and ammonium acetate were purchased from Fisher Scientific (Nepean, ON, Canada). Peptide solutions (10 to 100 μM) (80% [v/v] acetonitrile, 20% [v/v] 0.25 mM ammonium acetate in water) were delivered to the electrospray source with a 60 μm ID stainless steel capillary tip at 3 μL/min.

6.3 Results and Discussion

The peptide sequence ions (e.g.,b_1) are indicated following the conventions of Roepstorff and Fohlman [13] or Biemann [14]. A short description of these conventions can be found in Appendix A.

6.3.1 Selectivity of PID at 266-nm wavelength

The choice of the laser wavelength in PID experiment is dictated by the absorption properties of the analyzed species. Peptides do not absorb appreciably in the visible or near-UV region. At shorter wavelengths the absorption coefficient for peptides increases. With the use of low laser power where single photon absorption dominates and multiphoton processes are minimal, the PID at 266 nm is expected to be efficient only for peptides containing aromatic rings. To evaluate the selectivity of the experimental conditions for aromatic and nonaromatic peptides at 266 nm, PID spectra for a series of peptides were obtained by varying the laser power and concentration of ions in the ion trap. Among all analyzed peptides only the species containing tryptophan, tyrosine, and phenylalanine could be fragmented using the PID process at 266 nm.

6.3.2 PID of peptides

6.3.2.1 The effect of multiple laser pulses on PID spectra

Figure 6.4 shows the PID spectra of protonated Trp-Ala obtained with the use of various numbers of laser pulses for excitation. After two laser shots (Figure 6.4 A), the spectrum contains sequence relevant fragments as well as several dissociation products of the tryptophan absorbing group at m/z 130, 83, and 64. After five laser shots (Figure 6.4 B), the number and intensity of sequence relevant fragment ions decreases. It is clear that the sequence relevant fragment ions produced by the first two laser shots are further dissociated with the additional laser pulses. Because the low mass cutoff for ion storage in the ion trap is set at m/z=55, any low-mass ions (m/z < 55) formed in PID with the excessive excitation are not detected in the PID spectra. After ten laser pulses of excitation, the mass spectrum obtained, as shown in Figure 6.4 C, represents only deep fragmentation products with a less intense tryptophan immonium ion peak (W). Figure 6.4 clearly shows that the PID fragmentation pattern is strongly influenced by the number of laser pulses used for excitation in the ion trap/TOF system.

6.3.2.2 The effect of the laser power on PID spectra

Another factor controlling the population of PID products is the laser power. Figures 6.5 A and 6.5 B show the PID spectra from protonated Tyr-Gly obtained by using 5 laser pulses at laser energy of 40 mJ and 50 mJ, respectively. As the laser power increases, deeper fragmentation products are generated at the expense of larger ions (e.g., MH^+-NH_3). Figure 6.5 C shows the CID spectrum of the same peptide ion. The major difference observed in comparing the CID and PID spectra is the preferential formation of MH^+-NH_3 or z_2 ion in PID and b_2 ion in CID. In addition, deeper fragment ions (e.g., m/z 91 and 59) are only observed in PID.

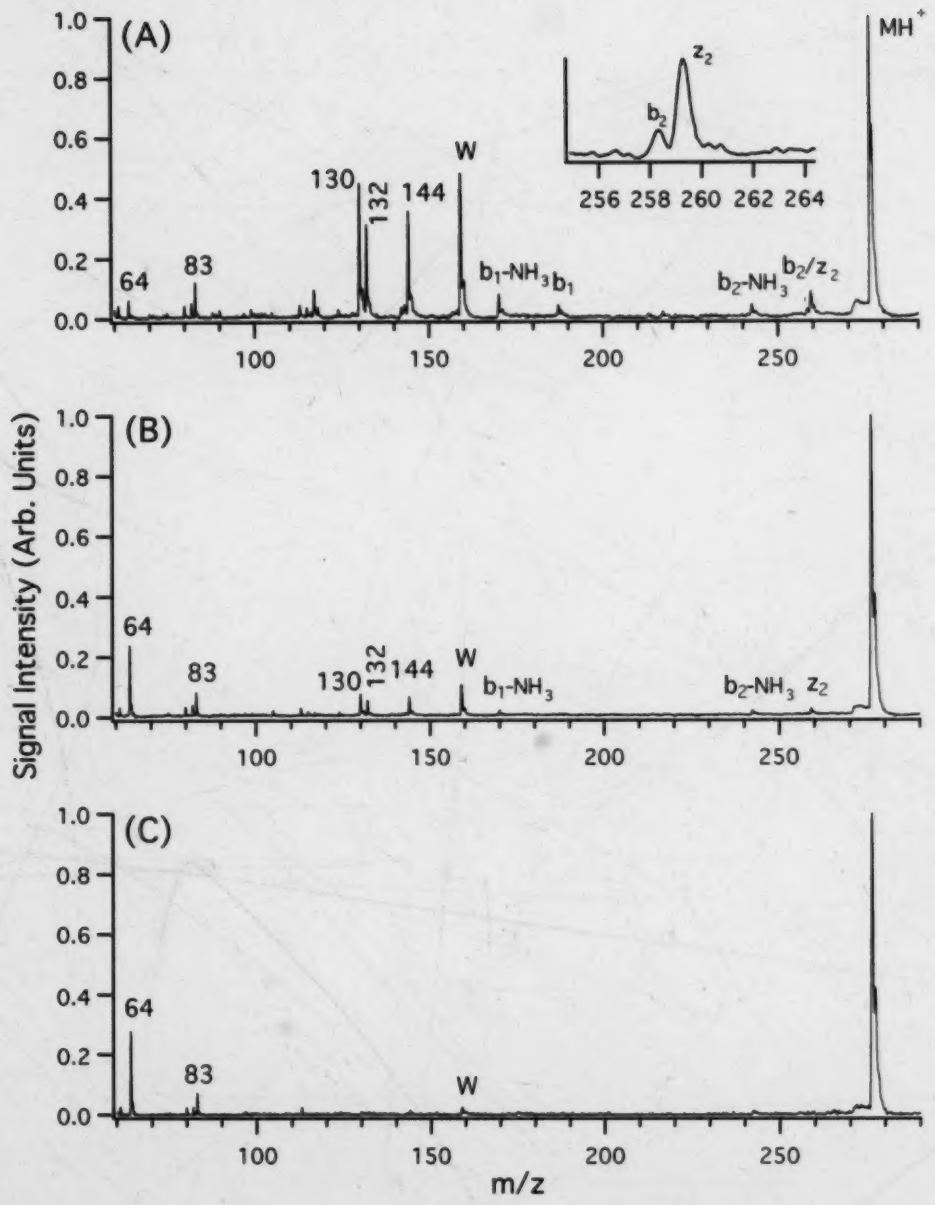

Figure 6.4. PID spectra of protonated Trp-Ala at $q_z = 0.133$ with helium as a buffer gas at P = 0.6 μTorr in the TOF tube and laser energy of 40 mJ per pulse: (A) 2 pulses, (B) 5 pulses and (C) 10 pulses.

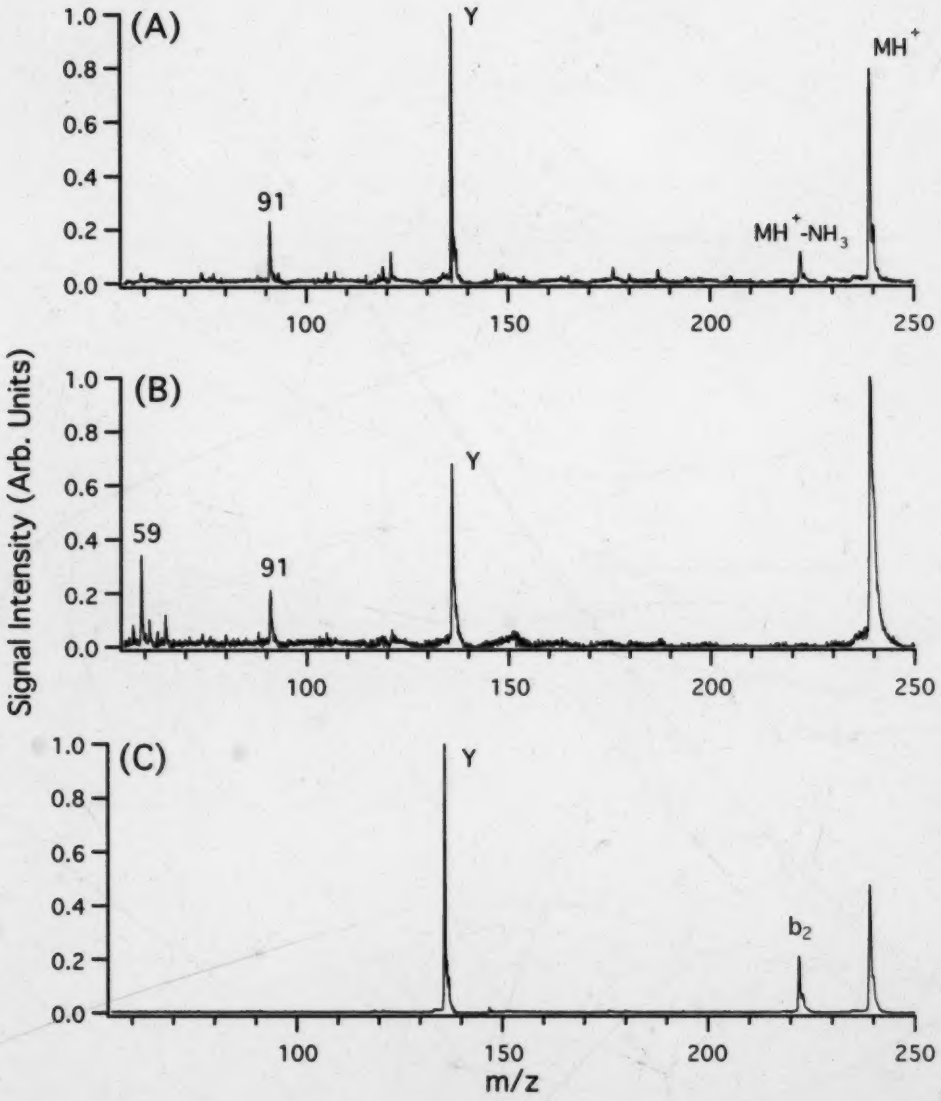

Figure 6.5. Dissociation spectra of protonated Tyr-Gly at $q_z = 0.154$ with helium as a buffer gas: at P = 0.6 μTorr in the TOF tube. (A) PID from 5 laser pulses with laser energy of 40 mJ per pulse. (B) PID from 5 laser pulses with laser energy of 50 mJ per pulse and (C) CID. The buffer gas pressure in the TOF tube was 0.6 μTorr.

6.3.2.3 The effect of the buffer gas pressure inside the ion trap on PID spectra

The buffer gas pressure inside the ion trap has a major effect on the population of sequence related ion products in PID. Because it is difficult to measure the pressure inside the ion trap directly, the pressure in the TOF flight tube is used as a measure of a pressure inside the ion trap. Figure 6.6 A to C show the PID spectra of protonated Tyr-Gly-Gly molecular ions obtained at different pressures inside the trap with the use of the same laser power. The CID spectrum of this ion is shown in Figure 6.6 D for comparison. Variations in population and intensities of formed ions can be observed in PID spectra when the pressure inside the ion trap is increased. The comparison of CID and PID spectra shown in Figure 6.6 rises a few important points. Despite specific differences in PID and CID products, PID is as efficient as CID for providing structural information. The larger number of sequence related PID products was obtained at the lower ion trap pressure. Considering the minimal effect of buffer-gas collision-deactivation process at low pressure, PID should be the most efficient under such a condition. Surprisingly, careful examination of all PID spectra suggests that a moderate increase in pressure resulted in more efficient dissociation. This is best illustrated in PID experiment of morphiceptin (YPFP) and leucine-enkephalin (YGGFL).

Figure 6.7 A to C show the PID spectra of the protonated molecular ion of morphiceptin obtained under similar conditions with the pressure inside the ion trap decreasing from A to C. The CID spectrum of YPFP (Figure 6.7 D) reflects the specific fragmentation pattern of a peptide containing proline residue. Significant spectral differences for PID and CID include lack of a_4, b_4, y_3, a_2, y_1 and exclusive presence of c_2 and two unidentified fragments at m/z 272 and m/z 296 in PID. Internal fragments (e.g., a_3y_3, b_3y_3) and their spectral intensities are used as probes for determination of energy deposited in the dissociation process. Usually a highly energetic excitation or multiple collision process increases the probability of cleavage of the two amide bonds. These types

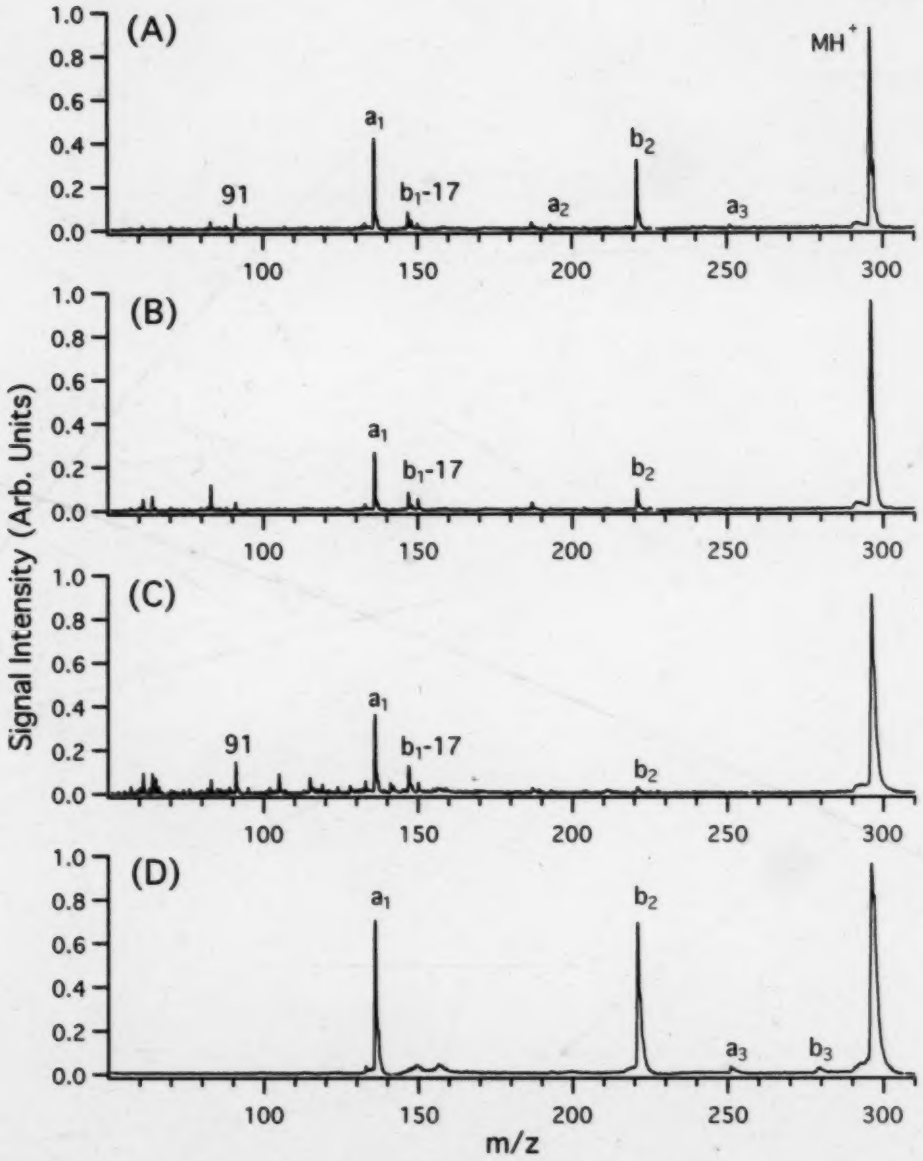

Figure 6.6. Dissociation spectra of protonated Tyr-Gly-Gly at $q_z = 0.124$ with helium as a buffer gas: (A) PID at P = 0.8 μTorr in the TOF tube, (B) PID at P = 0.6 μTorr, (C) PID at P = 0.4 μTorr, (D) CID at P = 0.8 μTorr. 5 laser pulses with laser energy of 50 mJ per pulse were used for PID.

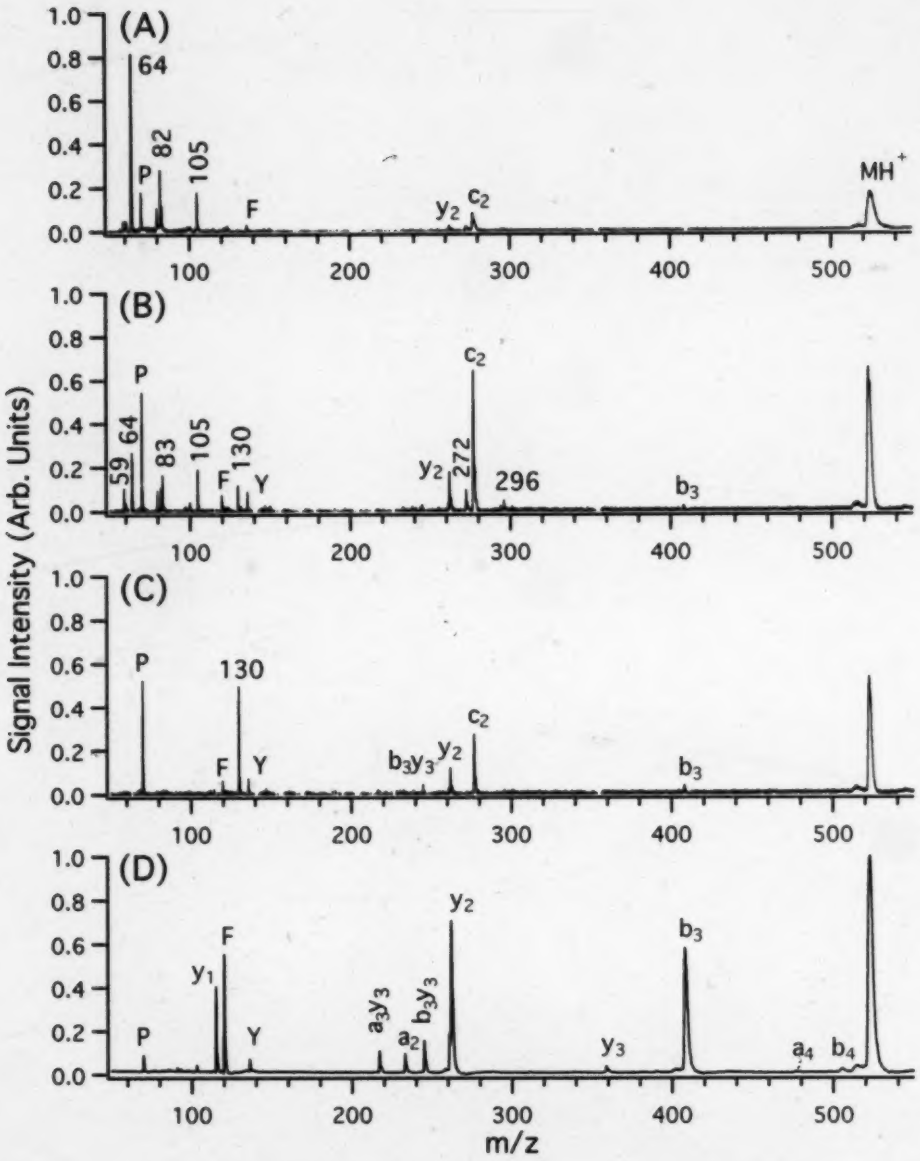

Figure 6.7. Dissociation spectra of protonated morphiceptin (YPFP) at $q_z = 0.141$ with helium as a buffer gas: (A) PID at P = 0.8 μTorr in the TOF tube, (B) PID at P = 0.6 μTorr, (C) PID at P = 0.4 μTorr, (D) CID at P = 0.8 μTorr. 5 laser pulses with laser energy of 50 mJ per pulse were used for PID.

of ions were very intense in the PID process at 193 nm [3]. The results shown in Figure 6.7, however, indicate that PID at 266 nm does not produce these internal fragment ions. Nevertheless, observation of different fragment ions in PID and CID spectra, as shown in Figure 6.7 for morphiceptin, suggests that the combination of these two processes can be useful in providing complementary structural information.

The unusual effect of elevated buffer gas pressure making the dissociation more efficient is apparently due to an artifact introduced by the presence of oil vapor in the trap. This can be seen in the PID experiment of leucine-enkephalin (Figures 6.8 and 6.9).

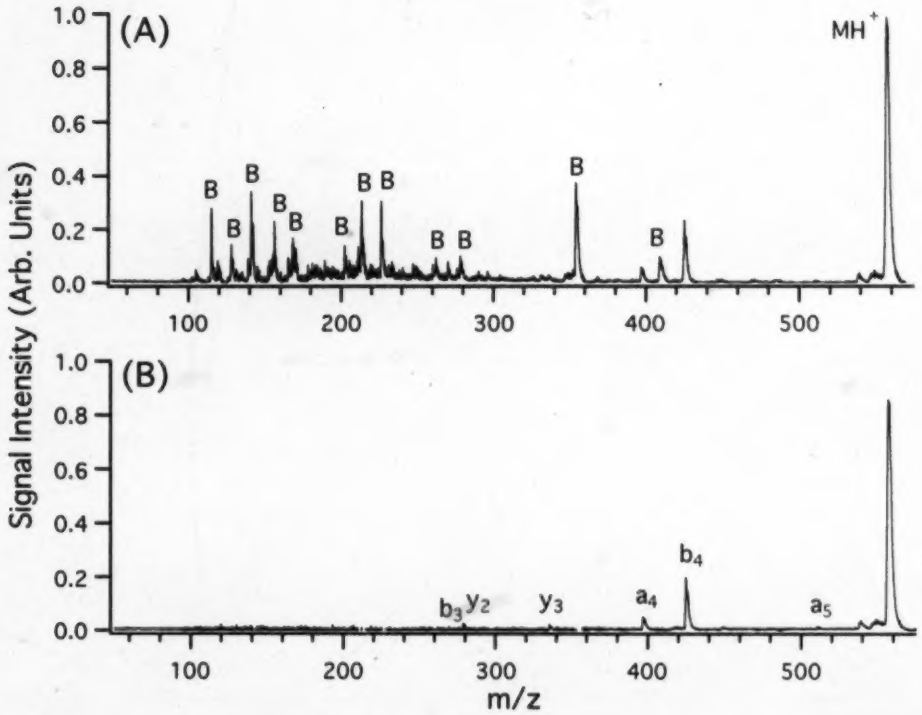

Figure 6.8. PID spectra of protonated leucine-enkephalin (YGGFL) at q_z = 0.132 with helium as a buffer gas at P = 0.6 μTorr in the TOF tube: (A) PID and (B) Background-subtracted PID. Major background ions are labeled as "B". 5 laser pulses with laser energy of 50 mJ per pulse were used for PID.

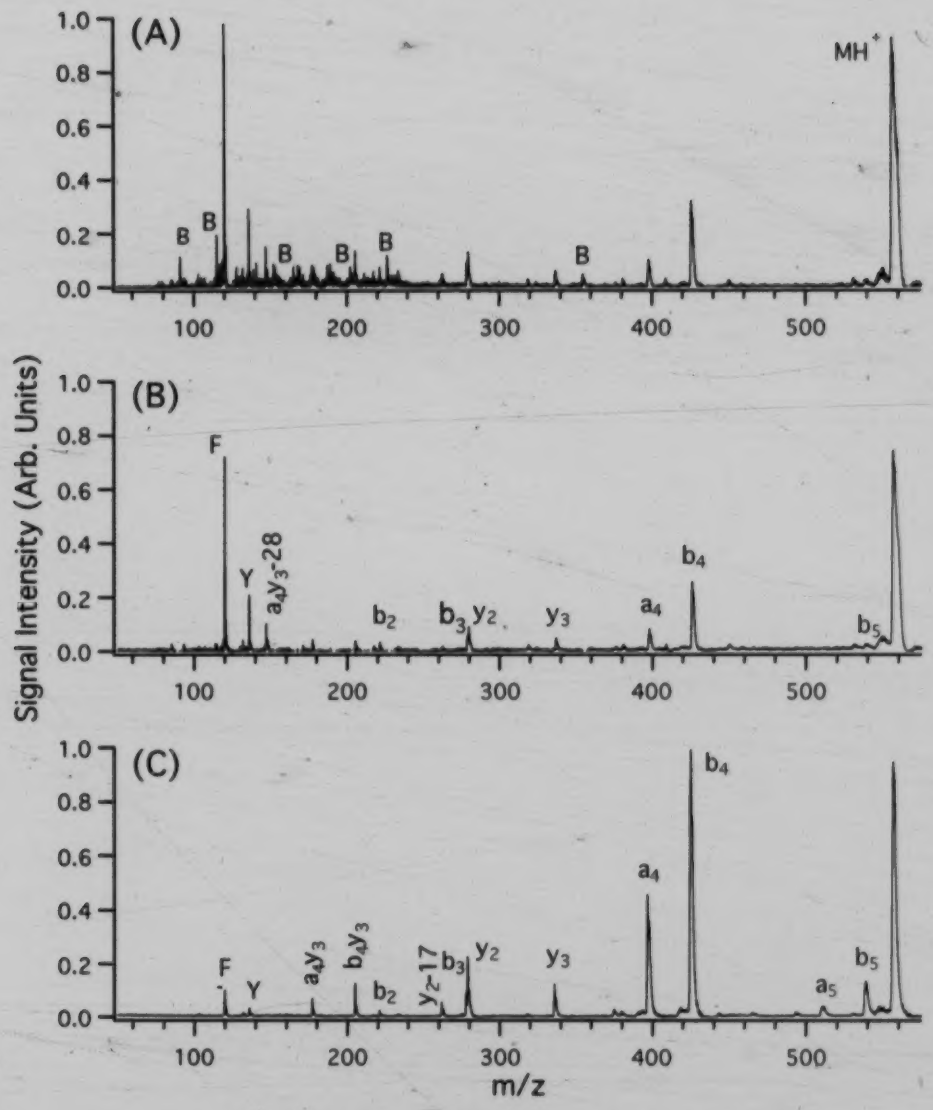

Figure 6.9. Dissociation spectra of protonated leucine-enkephalin (YGGFL) at q_z = 0.132 with helium as a buffer gas at P = 0.6 μTorr in the TOF tube: (A) PID, (B) Background-subtracted PID and (C) CID. (A) and (B) were obtained after buffer gas "purging" step. The major background ion peaks are labeled as "B". 5 laser pulses with laser energy of 50 mJ per pulse were used for PID.

The source of the intense background is from the diffusion pump oil (SANTAVAX 5 or polyphenyl ether), a component of the vacuum system. Introducing a relatively larger amount of helium to the trap to sweep away the oil vapor residing in the trap can reduce the background. The reduction of the amount of oil vapor in the trap also reduces the attenuation of laser beam from the vapor. This increase in laser power results in the increase in fragment ion signal.

Note that further background reduction was possible when the ion trap was "purged" with buffer gas for a long time (e.g., half-hour) before the experiment. Figure 6.9 A shows the background level after "purging" the trap with buffer gas and the corresponding background-subtracted PID spectrum of leucine-enkephalin (Figure 6.9 B). The CID spectrum of protonated leucine-enkephalin is presented in Figure 6.9 C for comparison. The noticeable difference between PID and CID is the abundant presence of low mass immonium ions of tyrosine (Y) and phenylalanine (F), reduced intensity of high mass fragments, and the absence of a_3 in PID.

6.3.2.4 PID of oxytocin

Because of the possibility of imparting more energy to the molecular ions with PID, PID can be used to fragment ions that cannot be readily fragmented by the CID process inside the ion trap [5]. This was also observed in the ion trap/TOF set up with a 266-nm laser. Figure 6.10 shows the PID spectrum of protonated peptide oxytocin (CYIQNCPLG). Oxytocin contains an intramolecular disulphide bridge. CID could not fragment the protonated molecular ion of this stable peptide. The CID spectrum presented in the inset of Figure 6.10 was acquired at the highest possible q_z value (maximum energy deposition in CID) in the ion trap/TOF instrument and exhibits no fragment ions. . A number of fragment ions are observed in the PID spectrum, although the sequential information obtained is still limited. This example illustrates that the PID technique can potentially be very useful in generating structural information not readily obtained by CID.

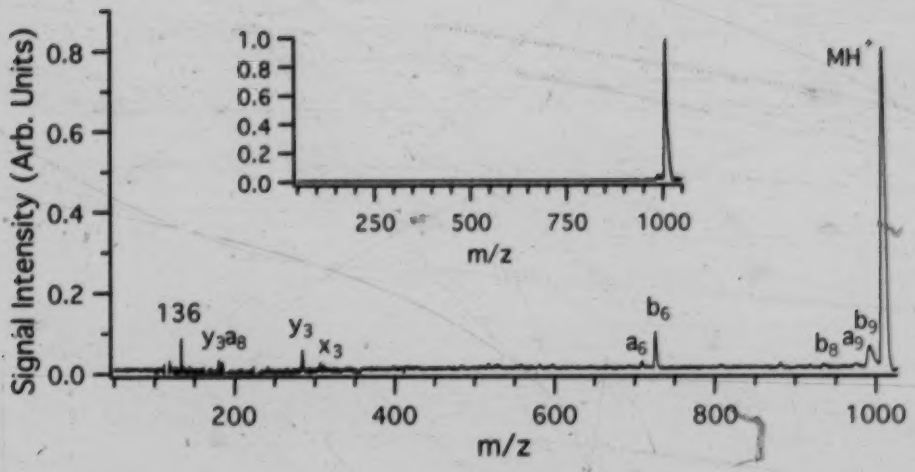

Figure 6.10. PID spectrum of protonated oxytocin (CYIQNCPLG) at q_z = 0.073 with helium as a buffer gas at P = 0.6 μTorr in the TOF tube. 10 laser pulses with laser energy of 50 mJ per pulse were used for PID. The CID spectrum at q_z = 0.110 is shown in the inset.

6.3.3 Time-dependent detection in PID

The combination of the ion trap with its ion selection capability and the TOF detector provides a unique tool for fast detection of ions formed via PID. The time delay for probing the population of ions formed in PID inside the ion trap can be as short as 1 microsecond in the current setup. Figure 6.11 shows the time dependence of relative intensities (fragment ion/molecular ion) of several fragment ions formed by PID. In this case, the protonated molecular ion of Trp-Ala was generated by electrospray and mass-selected by ion trap. The time scale represents the time difference between the laser pulse and the detection pulse.

The time-resolved detection experiment, as shown in Figure 6.11 reveals a few interesting features. It is clear that the intensities of the PID products vary as a function of

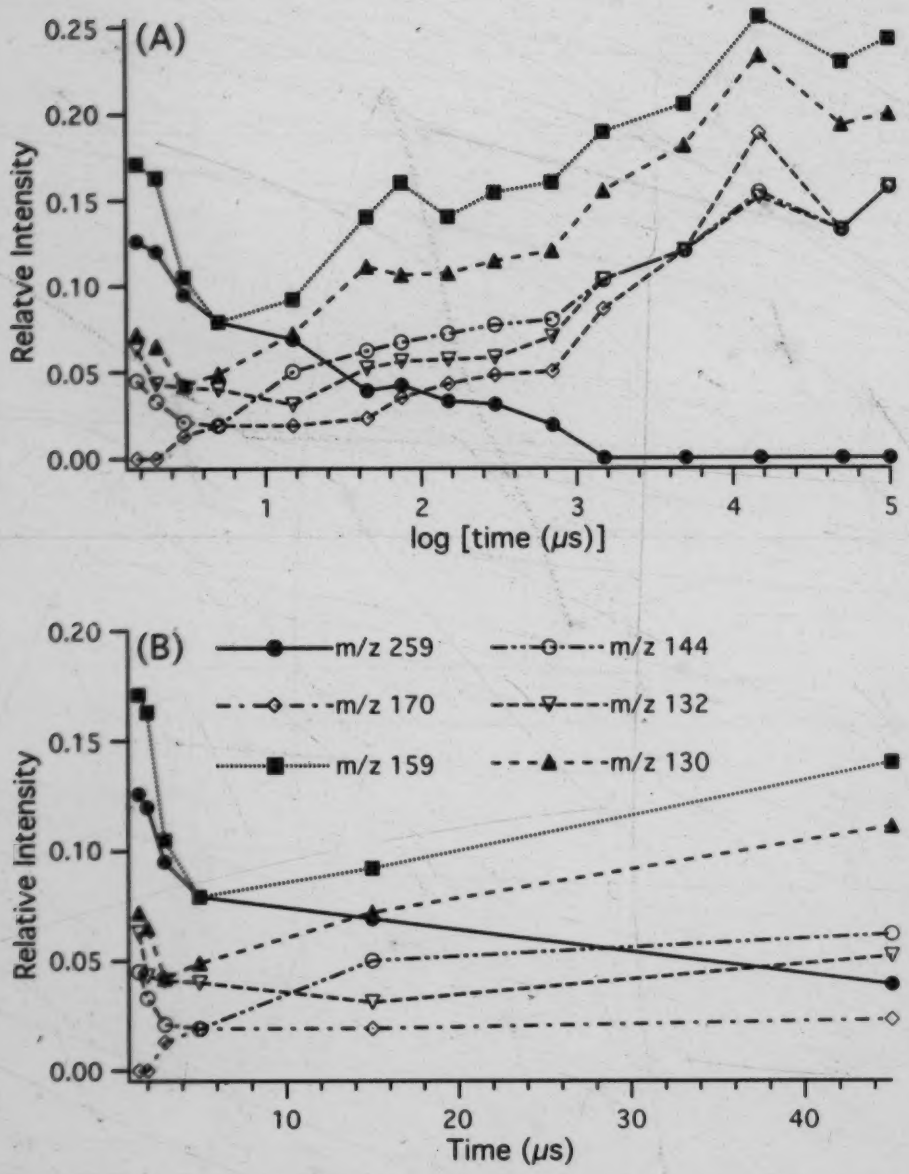

Figure 6.11. Relative intensities of PID products as a function of time after the laser pulse for protonated Trp-Ala at $q_z = 0.133$. Helium was used as a buffer gas at P = 0.4 μTorr in the TOF tube and the laser energy was 40 mJ per pulse. (A) Logarithmic time scale, (B) Linear time scale. The lines connect the points representing the average of 3 measurements.

the time delay. With the exception of m/z 259 (z_2), intensities of all fragmentation products are higher at a longer delay, leveling off at about 10 ms. The ion intensity variation is more pronounced in the first few microseconds delay after the laser pulse (see Figure 6.11 B with an expanded time scale). The population of ions inside the ion trap, as probed by the TOF detector, may be dictated by kinetics and also by the efficiency of ion extraction from the trap after the laser pulse. It seems that an instantaneous detection (< 2 μs) provides more ions for detection or more efficient ion ejection comparing to the 3-50 μs delay range. A time of several tens of microseconds might be required for ions to collisionally cool down to the center of the trap to be more efficiently ejected. It is also possible that, in a few microseconds after excitation, ions have a sufficient time to dissociate further into much smaller undetected ions (m/z below LMCO).

The results from these time-resolved studies have practical implications. It can be seen from Figure 6.11 that detection of the m/z 259 ion is possible only within the detection time frame of 1 ms. This detection time frame may not be compatible with commercial ion trap detection schemes. Thus an ion trap using mass scan with a detection time frame larger than 1 ms would not detect this particular ion. On the other hand, the detection of m/z 170 can be achieved at least a few microseconds after the laser excitation event.

Another time dependence study of fragment ions is shown in Figure 6.12 for protonated Tyr-Gly-Gly. In this case, the intensity variation of PID products with time are especially noticeable for the deep fragmentation products at m/z 63, 77, and 91 supporting the notion that a long delay time favors the formation of smaller ions. These fragment ions are likely from long-lived metastable ions, analogue to those observed in ion trap with matrix-assisted laser desorbtion ionization [15]. It is clear that much needs to be done in understanding the time dimension of the fragmentation process in the ion trap. Nevertheless, the results showed in Figures 6.11 and 6.12 demonstrate the capability of the ion trap/TOF mass spectrometer to generate time-dependent spectra from PID. It opens a

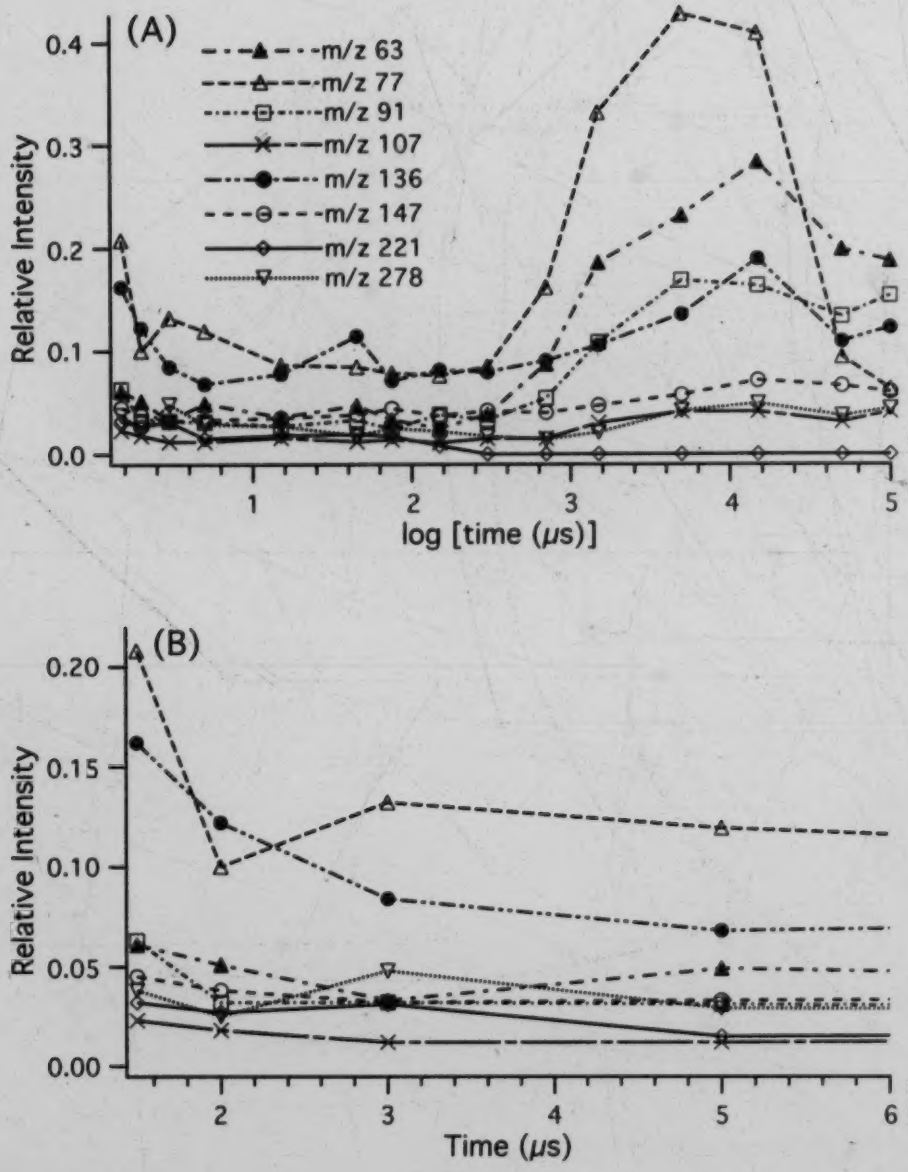

Figure 6.12. Relative intensities of PID products as a function of time after the laser pulse for protonated Tyr-Gly-Gly at $q_z = 0.124$. Helium was used as a buffer gas at P = 0.4 μTorr in the TOF tube and the laser energy was 50 mJ per pulse. (A) Logarithmic time scale, (B) Linear time scale. The lines connect the points representing the average of 3 measurements.

new venue for studying the PID process and provides a new tool for analytical applications.

6.4 Summary

An ion trap/time-of-flight mass spectrometer has been developed for the studies of photo-induced dissociation of ions generated by electrospray ionization. A pulsed 266-nm laser beam from a Nd:YAG laser was used for PID of several peptides. The amount of photoenergy deposited for fragmentation can be controlled by the identity of absorbing group, laser power, number of laser pulses, and ion trap buffer gas pressure. Energetically optimal PID process results in spectra providing sequential information similar to that obtained from CID. The excessive amount of photoenergy deposited to fragmenting ion favors the formation of deep fragmentation products at the cost of sequence related ions. The PID technique has the potential to probe the structural features of larger species that cannot be fragmented by CID. The quality of the vacuum is critical in PID experiments of such ions because an unattenuated high laser power is required to make the dissociation process effective. Fast and time-dependent detection of the PID ions by the ion trap/TOF mass spectrometer was demonstrated. The time-dependent spectra obtained can potentially be very useful for understanding the PID process as well as analytical applications.

6.5 Literature cited

[1] Bowers, W. D.; Delbert, S. S.; Hunter, R. L.; McIver, R. T., Jr. *J. Am. Chem. Soc.* **1984**, 106, 7288.

[2] Bowers, W. D.; Delbert, S. S.; McIver, R. T., Jr. *Anal. Chem.* **1986**, 58, 969.

[3] Lebrilla, C. B.; Wang, T. S.; Mizoguchi, T. J.; McIver, R. T., Jr. *J. Am. Chem. Soc.* **1989**, 111, 8593.

[4] Hunt, D. F.; Shabanowitz, J.; Yates, J. R.; Griffin, P. R.; Zhu, N. Z. *Anal. Chim. Acta* **1989**, 225, 1.

[5] Williams, E. R.; Furlong, J. J. P.; McLafferty, F. W. *J. Am. Soc. Mass Spectrom.* **1990**, 1, 288.

[6] Little, D. P.; Speir, P. J.; Senko, M. W.; O'Connor, P. B.; McLafferty, F. W. *Anal. Chem.* **1994**, 66, 2809.

[7] Hughes, R. J.; March, R. E.; Young, A. B. *Int. J. Mass Spectrom. Ion Phys.* **1982**, 42, 255.

[8] Louris, J. N.; Brodbelt, J. S.; Cooks, R. G. *Int. J. Mass Spectrom. Ion Proc.* **1987**, 75, 345.

[9] Stephenson, J. L., Jr.; Booth, M. M.; Shalosky, J. A.; Eyler, J. R.; Yost, R. A. *J. Am. Soc. Mass Spectrom.* **1994**, 5, 886.

[10] Stephenson, J. L., Jr.; Booth, M. M.; Boue, S. M.; Eyler, J. R.; Yost, R. A. *Biochemical and Biotechnological Applications of Electrospray Ionization Mass Spectrometry*; Snyder, A.P., Ed.; ACS symposium series 619: Washington, DC, **1996**, 512.

[11] Guan, S.; Marshall, A. G. *Int. J. Mass Spectrom. Ion Processes* **1996**, 157/158, 5.

[12] Doroshenko, V. M.; Cotter, R. J. *Rapid Commun. Mass Spectrom.* **1996**, 10, 65.

[13] Roepstorff, P.; Fohlman, J. *Biomed. Mass Spectrom.* **1984**, 11, 601.

[14] Biemann, K. *Ann. Rev. Biochem.* **1992**, 61, 977.

[15] Fountain, S. T.; Lee, H.; Lubman, D. M. *Rapid Commun. Mass Spectrom.* **1994**, 8, 407.

Chapter 7

Photo-Induced Dissociation of Electrospray Generated Ions in an Ion Trap/Time-of-Flight Mass Spectrometer using a Pulsed CO_2 Laser[a]

7.1 Introduction

The ion trap/time-of-flight mass spectrometer in conjunction with a pulsed 266-nm laser beam from a Nd:YAG laser has the potential to probe the structural features of ions generated by electrospray ionization. The limiting factor of this PID technique, presented in Chapter 6, was related to the selective absorption of uv-irradiation by the analyzed species. To evaluate ion trap photodissociation methods for a broad range of compounds, the use of an alternative laser wavelength in ion excitation is required. A 10.6-μm light used in Infrared Multiphoton Dissociation (IRMPD) is a reasonable choice because nearly every type of organic bond can absorb an infrared photon.

IRMPD is a technique that is gaining acceptance as a versatile method for fragmentation of both small and large ions [1-3]. Following the earlier work [4, 5], McLafferty and co-workers demonstrated that IRMPD with FT-ICR detection is an effective method by which proteins as large as 29 kDa can be dissociated and further characterized [6]. This PID method compared favorably with CID with respect to efficiency of fragmentation and reduction in ion losses from scattering or other collisional effects. IRMPD was combined with a quadrupole ion trap mass spectrometer for the analysis of oligosaccharides, ribonucleic acid dimers and peptides [7] and also in conjunction with SWIFT to characterize dissociation pathways of antibiotics and hydrogen-bonded complexes [8, 9]. IRMPD is generally performed on mass spectrometers based on Penning or Paul traps by combining the external optical scheme and modifications to

---

[a] A form of this chapter is in preparation for publication: W. Gabryelski, L. Li "Photo-Induced Dissociation of Electrospray Generated Ions in an Ion Trap/Time-of-Flight Mass Spectrometer using a Pulsed CO_2 Laser".

trapping electrodes which allow the laser beam to traverse the ion trapping volume [10]. It seems that the key to successful implementation of IRMPD in a trapping mass spectrometer or even an external ion reservoir [11] is the ability to store ions for long periods, thus allowing multiphoton absorption followed by delayed detection. These requirements determined conditions at which IRMPD experiments are carried out. Trapped ions are irradiated by continuous wave IR light for a period of tens to hundreds of milliseconds and the progress of dissociation is monitored on the same time scale.

The effective use of pulsed lasers to fragment large ions has proven to be difficult with ion beam mass spectrometers because the interaction region between the laser and the ion beam is very small. The results from the dissociation of peptides up to 14 kDa in a time-of-flight instrument showed that much higher energy photons (6.4 eV) were required to induce dissociation because the time-of-flight time-scale was not sufficient for absorption of multiple photons [12]. Another difficulty is that a complete mass spectrum for scanning instruments cannot be obtained for each laser pulse because the scan speed is far slower than the duration of the laser pulse. These limitations are alleviated in trapping mass spectrometers but IRMPD on this type of instrument was rarely used with pulsed lasers [7].

One of the most fundamental questions concerning the development of photodissociation of high molecular weight analytes surrounds the ability to activate and dissociate ions that have large numbers of degrees of freedom. Statistical theories, in the form of quasi-equilibrium theory (QET) and Rice-Ramsperger-Kassel-Marcus (RRKM) theory [13, 14], suggest that dissociation of high molecular weight analytes on a microsecond time scale would require unrealistic amounts of activation energy. For instance, theoretical calculations [15] imply that 12 to 19 eV of energy are needed to fragment a 2.1-kDa peptide at rates detectable in the microsecond time scale. Further, more than 58 eV would be required to fragment a 13.7-kDa protein. IRMPD of several electrosprayed peptides and proteins via a continuous wave CO_2 laser and a FT-ICR

instrument [6] showed the formation of structurally significant fragment ions. However it is not clear whether these ions were formed by multiphoton processes or by further photodissociation of photofragment ions.

Another interesting issue related to the photodissociation process is the time factor for monitoring the progress of dissociation. Ion trap systems used for IRMPD and CID experiments [16, 17] are capable of recording spectra only tens of milliseconds after the beginning of the excitation. The sub-millisecond time scale experiments were performed using ion trap/reflectron time-of-flight mass spectrometer to study the decay of large ions following activation by matrix-assisted laser desorption/ionization at 355-nm [18]. It was shown that these ions undergo fragmentation over long period of time, extending even to milliseconds in some cases [18]. The alternative method of recording PID mass spectra, presented in the previous chapter, may bring some understanding about the ion trap environment at short times (i.e., microsecond time frame) after photoexcitation.

This chapter focuses on the application of an ion trap/time-of-flight mass spectrometer for IRMPID studies of electrospray generated ions. Experiments with a pulsed CO_2 laser demonstrate that sufficiently high photon fluxes are available to photodissociate irradiated ions of proteins. Time-resolved detection is used to characterize the photodissociation process inside the quadrupole ion trap and this technique is compared to CID. Finally, the feasibility of IRMPD on the ion trap/time-of-flight instrument for differentiation of isomers is examined.

7.2 Experimental

7.2.1 IRMPD and time-resolved CID experiments

The ion trap/linear time-of-flight mass spectrometer modified to perform tandem mass spectrometry in CID and PID experiments has been described in the previous chapter.

Only minor modifications were necessary to implement a high-power pulsed CO_2 laser into the experimental scheme. Figure 7.1 A illustrates the sequence of events in IRMPD.

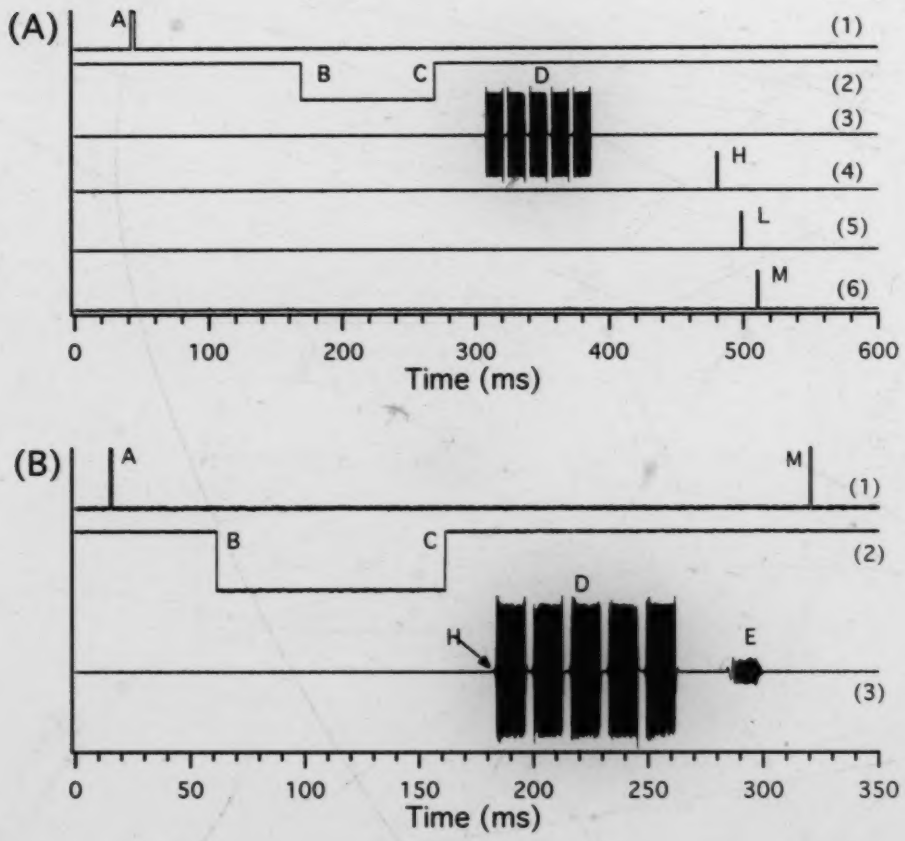

Figure 7.1. Sequence of events of an ion trap/time-of-flight mass spectrometer for (A) IRMPD with a pulsed CO_2 laser, and (B) Time-resolved CID. See text for details.

Master trigger pulse (A) from the PC triggers a pulser which applies a negative voltage to the exit end-cap. This removes ions from the trap. The master trigger (A) also initiates a

new cycle in which ions are accumulated in the trap (B-C) and the selected ions are isolated (D). In the next step a pulse (H) is sent simultaneously to the trigger input of the CO_2 laser and to the input of a digital delay generator model I2IBR (California Avionics Laboratory Inc., Palo Alto, CA). The delay time between the laser pulse (L) and the trigger input pulse (H) is constant (30.2 μs). The output of the digital delay generator is used to trigger the TOF detection pulse (M). A delay time between excitation (L) and detection (M) is set up by adjusting the time delay H-M introduced by the digital delay generator. Note that this design allows for detection of ions from 30.2 μs before the laser pulse to up to 1 s after the laser pulse with uncertainty of ± 0.5 μs.

CID is usually performed with a PC master clock to control the entire sequence of the events in a cycle. However, for probing the population of ions during the CID process, the detection pulse (M) has to be synchronized with the excitation waveform to ensure reproducible CID spectra. Figure 7.1 B shows the sequence of events in a time-resolved CID experiment. The master trigger (A) from the PC starts a new cycle in which ions are accumulated in the trap (B-C) and the selected ions are isolated (D). To limit the time uncertainty of the detection (M) relatively to the CID excitation event (E), a digital delay generator was used to control a time delay between the detection pulse (M) and the starting point of the series of isolation waveforms (H). This set up allowed probing the population of ions inside the trap before, during, or after CID excitation with the uncertainty of ± 0.5 μs by adjusting the delay time (H-M).

A 10.6-μm laser beam from an Allmark pulsed (30-ns pulse width) CO_2 laser (A-B Lasers, Acton, MA) was used in the IRMPD experiments. The laser was operated at the full power mode and the 1-cm-diameter IR laser beam was attenuated by reflection from a stainless steel mesh located at the laser output. The beam was directed by a set of IR-compatible mirrors to the 25 cm focal length germanium lens. After passage through a sodium chloride window, the focused laser light was directed into a 1.5-mm diameter hole in the ring electrode of the ion trap. The laser energy was measured with an Model 10A-

MED-AN laser power/energy meter (Diamond Ophir Optics, Wilmington, MA) located in front of the sodium chloride window at the entrance to the mass spectrometer. No attempt was made to measure the actual laser power in, or beyond, the ion trap. The energy of the laser beam inside the ion trap was monitored by measuring photodissociation efficiency for the standard compound (PTH-isoleucine). In IRMPD experiments, isolated parent ions were subjected to a single laser pulse in an energy range from 80 mJ to 4 J per pulse.

7.2.2 Chemicals and electrospray conditions

Peptides and proteins were purchased from Sigma Chemical (St Louis, MO) and used without purification. HPLC-grade acetonitrile, HPLC-grade water, ammonium acetate and acetic acid were purchased from Fisher Scientific (Nepean, ON, Canada). Disaccharide isomers were kindly provided by Dr. Ole Hindsgaul. 5-100 μM sample solutions (80% [v/v] acetonitrile, 20% [v/v] 0.25 mM ammonium acetate in water) were delivered to the electrospray source with a 60 μm ID stainless-steel capillary tip at 3 μL/min. The solvent composition in electrospray of equine cytochrome c consisted of 95% [v/v] water, 5% [v/v] acetonitrile and 0.1% [v/v] acetic acid in order to generate molecular ions of the protein at lower charge states.

7.3 Results and Discussion

7.3.1 IRMPD of peptides

Figure 7.2 shows IRMPD spectra obtained for peptides analyzed previously in PID with a Nd:YAG laser at 266-nm. The IRMPD spectrum of Trp-Ala (Figure 7.2 A) was acquired for comparable laser energy conditions as the PID spectrum of the dipeptide presented in Figure 6.4 A (Chapter 6). IRMPD was effected by applying one laser pulse at 80 mJ per pulse and two consecutive laser pulses at 40 mJ per pulse were used in PID. The increase in the intensity of dissociation products originated from a tryptophan group at

m/z 115 and 117 and a lack of sequence relevant fragment ions (b_2, b_2-NH_3) in IRMPD indicates that this method provides a more energetic excitation. The IRMPD spectrum of morphiceptin (YPFP) in Figure 7.2 B resembles the PID spectrum of this peptide in Figure 6.7 C. To achieve the spectral information presented in the figures different excitation conditions were used. IRMPD relied on a single (100 mJ) laser pulse while PID required 5 laser pulses at 50 mJ per pulse. The presence of internal fragments (e.g., a_3y_3, b_3y_3) in IRMPD implies, that despite of the smaller energy input, the IRMPD technique deposits more energy into the irradiated ions. At the same time, the structure relevant fragments (e.g., y_1, y_2, y_3) are preserved in the IRMPD process and thus sequential information is retained. The examples in Figure 7.2 illustrate the advantage of using a single laser pulse versus a series of pulses or a continuous irradiation. This is particularly true when the laser beam is more destructive to the sequence relevant fragments than for the molecular ion. In the case of leucine-enkephalin (YGGFL), IRMPD (Figure 7.2 C) produces the same number of diagnostic ions as PID (Figure 6.9 B) but the intensities of a particular type of ions are different. All immonium ions (F, Y, L) providing compositional information are detected in IRMPD. PID does not generate the immonium ion of leucine (L) but the intensity of larger fragment ions (a_4, b_4) is higher in PID than IRMPD. The abundance of these ions depends on the energy of the excitation. For instance, a_4 and b_4 are observed in IRMPD only when the energy of the excitation is smaller than 110 mJ. They appear in the spectrum as the latest products at a time of 7 μs after the 100 mJ excitation laser pulse. The formation of these ions represents slow and low energy reactions. For the same reason, the more energetic IRMPD discriminates against fragmentation channels of the molecular ion leading to the formation of the b_5 and a_5 type of ions generated in CID. The energy of a laser pulse is a critical and practically the only parameter determining the ability to generate maximum number of informative fragments in IRMPD. The method gives enough compositional and sequential information to make it useful for sequence verification.

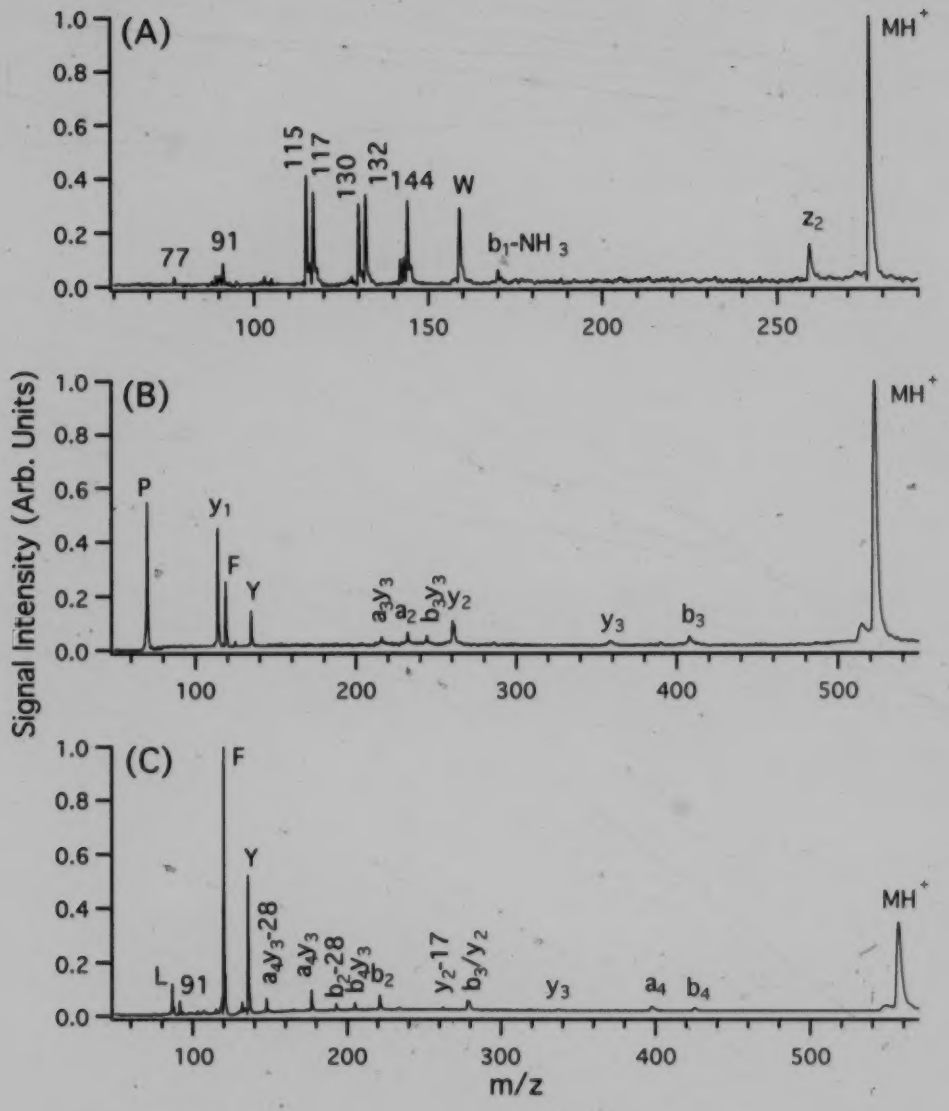

Figure 7.2. IRMPD spectra using a pulsed CO_2 laser with helium as a buffer gas at P = 0.6 μTorr in the TOF tube. (A) Trp-Ala at q_z = 0.1332 and a single laser pulse with laser energy of 80 mJ per pulse, (B) Morphiceptin (YPFP) at q_z = 0.141 and a single laser pulse with laser energy of 100 mJ per pulse, (C) Leucine-enkephalin (YGGFL) at q_z = 0.132 and a single laser pulse with laser energy of 100 mJ per pulse.

7.3.2 IRMPD of equine cytochrome c

The capability of depositing more energy into the ions with IRMPD, as demonstrated above, can be utilized in the analysis of large ions. Equine cytochrome c is a 12361 Da protein that generates a series of multiply protonated molecular ions in electrospray ionization. Figure 7.3 shows the IRMPD spectra of equine cytochrome c when a molecular ion of that protein at +13 charge state was isolated inside the ion trap and subjected to IRMPD. Only one laser pulse at energy of 180 mJ was used. The progress of photodissociation can be observed starting at 1 μs after the excitation (Figure 7.3 A) to 10 ms following the laser pulse (Figure 7.3 D). The spectrum in Figure 7.3 A acquired shortly after the laser pulse contains intense low m/z ion peaks. These ions can be detected only in the first few microseconds after excitation because their intensities decrease quickly with time. It is not surprising when one considers that the LMCO in the experiment was set up at m/z of 140. All formed ions with the m/z smaller than LMCO could not be trapped and are lost after the first few cycles of rf trapping voltage. The formation of these ions is characteristic for a higher energy excitation and was not observed in IRMPD of the same molecular ion at a laser pulse energy of 130 mJ. The intensity and number of ions in the m/z ranges of 140 to 250, and 450 to 650, increase with time in the spectra representing detection at longer time delays. IRMPD spectra acquired at time delays longer than 10 ms look like the spectrum in Figure 7.3 D. This indicates that the formation of products is completed in 10 ms after the excitation.

PID with 266 nm light relied on the use of multiple laser pulses to effect photodissociation. IRMPD is capable of fragmenting large ions using a single laser pulse. Figure 7.4 shows IRMPD spectra of the +13 charge state molecular ion of equine cytochrome c acquired 10 ms after the excitation at increasing energy of the laser pulse. At the laser energy of 130 mJ (Figure 7.4 A) and 180 mJ (Figure 7.4 B), photofragmentation of a molecular ion generates a different population of products. The increase in the laser pulse energy to 460 mJ results in the total dissociation of the molecular ion (Figure 7.4 C).

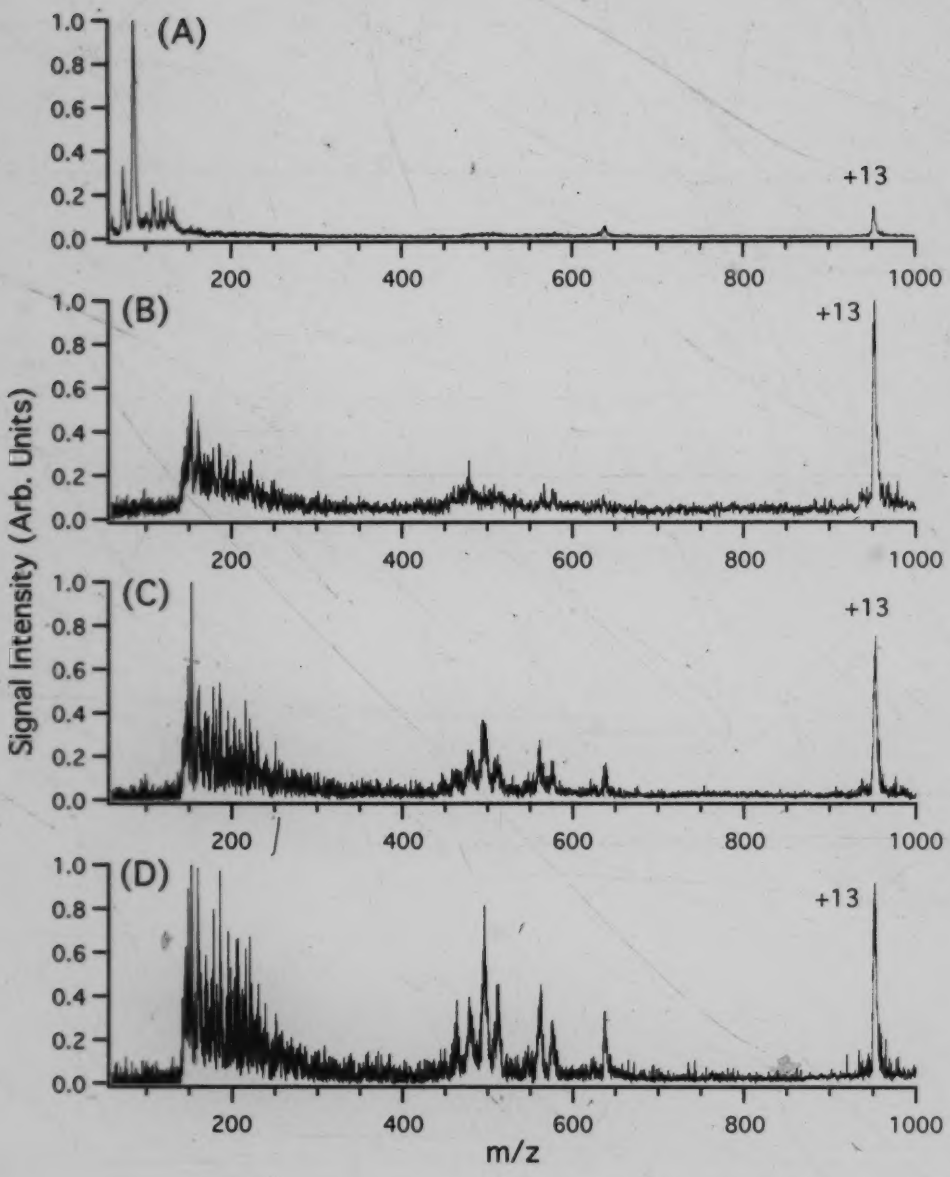

Figure 7.3. IRMPD spectra of equine cytochrome c at +13 charge state with helium as a buffer gas at P = 1 μTorr in the TOF tube and a single laser pulse with laser energy of 180 mJ per pulse. (A) 1 μs after excitation, (B) 100 μs after excitation, (C) 1 ms after excitation, (D) 10 ms after excitation.

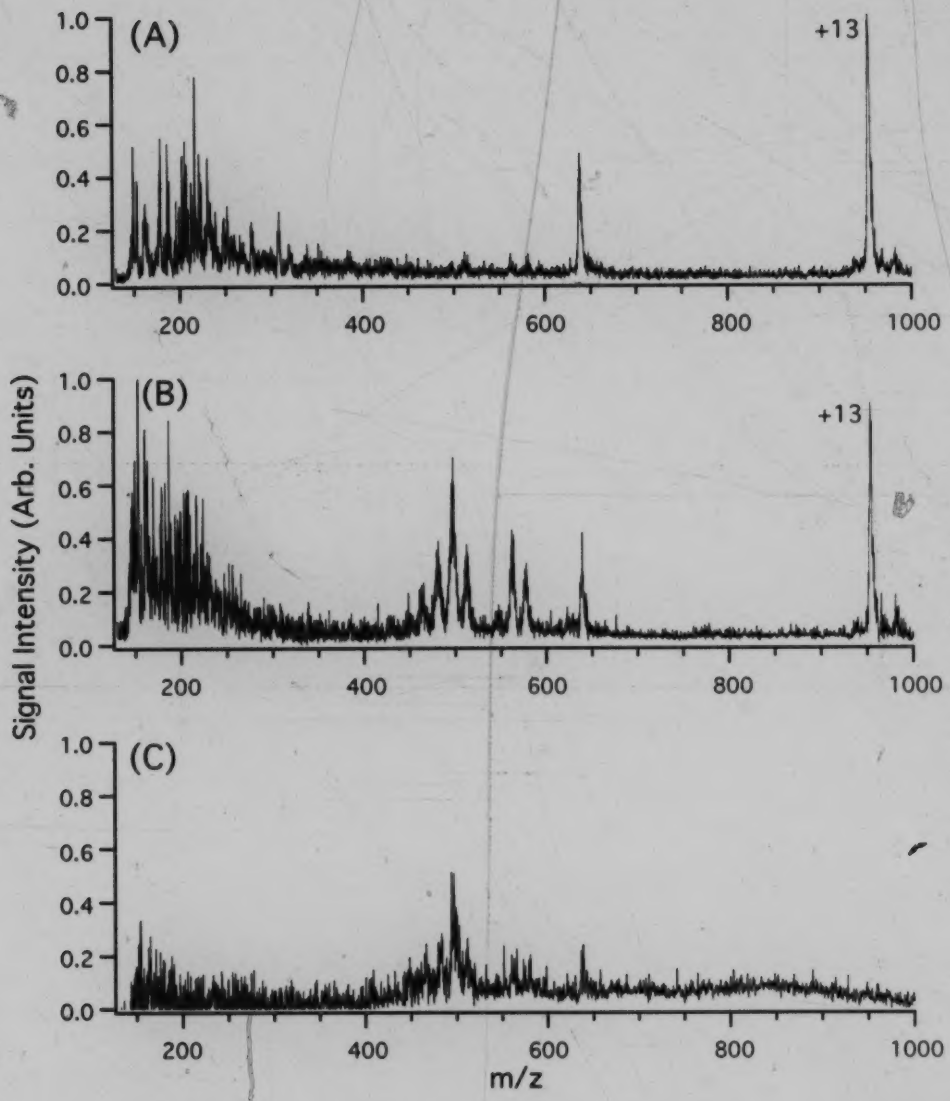

Figure 7.4. IRMPD spectra of equine cytochrome c at +13 charge state acquired 10 ms after excitation with helium as a buffer gas at P = 1 μTorr in the TOF tube and a single laser pulse. (A) Laser energy of 130 mJ per pulse, (B) Laser energy of 180 mJ per pulse, (C) Laser energy of 460 mJ per pulse.

Note that the abundance of fragments generated by the total dissociation of the molecular ion and detected in the trapping mass range is reduced relative to that obtained for a softer excitation. The multiple charging of the protein makes the identification of formed products difficult. However, the presence of the protein in various forms of gas-phase ions provides an opportunity to examine IRMPD in a context of a protein ionic charge state or a protein conformation. In order to completely dissociate the molecular ion of equine cytochrome c at the +12 charge state, a laser pulse energy of 500 mJ was required. Further, to totaly dissociate the +8 charge state molecular required 1.2 J. Different energy levels of excitation required to promote the total dissociation of a particular ionic form of equine cytochrome c suggests that IRMPD spectra of different conformers obtained at the same experimental conditions may be different.

Figure 7.5 shows the IRMPD spectra of the molecular ion of equine cytochrome c at the +12 charge state obtained for the same experimental conditions as were used for IRMPD of the +13 charge state of the protein (Figure 7.3). The comparison of the spectra acquired at various time delays following one excitation laser pulse at 180 mJ shows that in the case of the +12 charge state, relative to the +13 charge state, a smaller number of less intense fragment peaks was generated. This is especially pronounced for the ion peaks in the m/z range of 450 to 650. The intensity of the fragment peaks compared to the intensity of the molecular ion peak for each charge state indicates that it is more difficult to photodissociate the +12 ion than the +13 ion. The formation of fragment ions for both ionic forms of the protein was accomplished in 10 ms.

IRMPD of a molecular ion of equine cytochrome c at charge states from +10 to +13 at the same excitation energy showed that the spectra of the molecular ion at the +11 charge state resemble that presented in Figure 7.3 for the +13 charge state. In contrast the spectra of the molecular ion at the +10 charge state are similar to that presented in Figure 7.5 for the +12 charge state. The higher m/z ion at the +11 charge state dissociated more effectively than the lower m/z ion at the +12 charge state. For a series of molecular ions

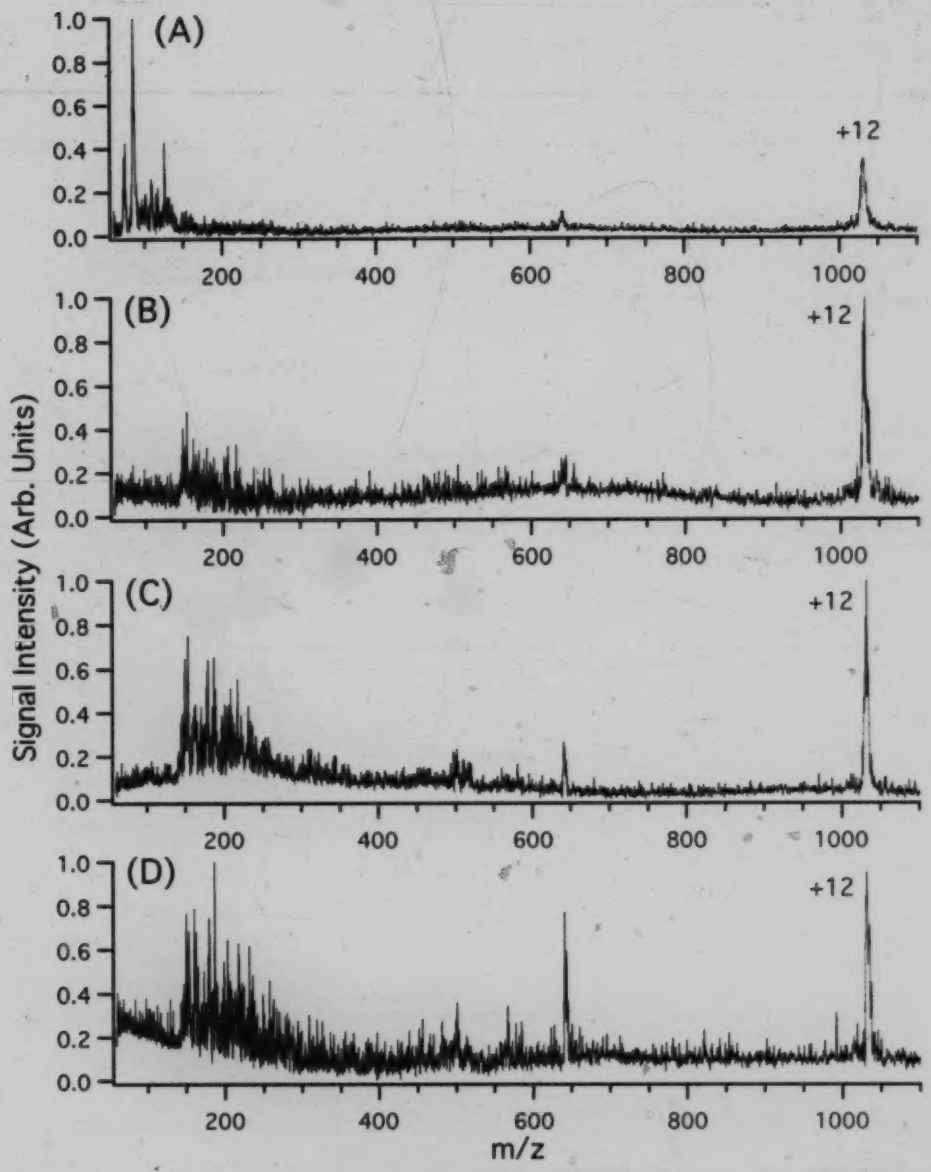

Figure 7.5. IRMPD spectra of equine cytochrome c at +12 charge state with helium as a buffer gas at P = 1 μTorr in the TOF tube and a single laser pulse with laser energy of 180 mJ per pulse. (A) 1 μs after excitation, (B) 100 μs after excitation, (C) 1 ms after excitation, (D) 10 ms after excitation.

(either even or odd charge state) the dissociation efficiency was observed to decrease with increasing m/z.

In addition to the energy of the laser excitation, the efficiency of photodissociation could be determined by a competitive process of collisional deactivation of irradiated ions. The energy deposited to the molecular ion of the protein may be transferred to buffer gas molecules that collide with the molecular ion and make the dissociation process less effective. The collisional deactivation affecting photoactivation and dissociation of ions is typical for operation of the quadrupole ion traps at high helium pressures [8]. The effects of buffer gas pressure, in conjunction with laser energy and structural identity of the molecular ion in IRMPD of equine cytochrome c, was examined and results are presented in Figure 7.6. The influence of the buffer gas pressure on the dissociation efficiency of the +12 ion is demonstrated in Figure 7.6 A as a decay diagram describing time dependent depletion of the molecular ion following the laser pulse. The area of the molecular ion peak (A) was measured in the IRMPD spectrum obtained at a certain time delay after the excitation. The area (A) was then correlated to the area of a molecular ion peak (A_0) acquired in the same sequence but without the application of the laser. The calculated dissociation efficiency (A / A_0) was then plotted as a function of the time delay between excitation and detection. Each point on the graph represents an average of 5 measurements with an error bar corresponding to 2 standard deviations. The ion trap buffer gas pressure (not measured directly) is related and expressed nominally by the pressure measured in the tube of the TOF detector. The range of examined pressures (0.5 to 1 μTorr) represents a condition in which the ion trap/TOF instrument provides a reasonable trapping efficiency for large ions. Figure 7.6 A summarizes an experiment when the laser energy of 180 mJ was used to dissociate the molecular ion at +12 charge state. The depletion of the molecular ion signal detected 1 μs after excitation is significant. Only 20% of molecular ions survived the dissociation process. The intensity of the molecular ion declines for 20 μs, after which no change in the intensity of the molecular ion is observed. Decay curves

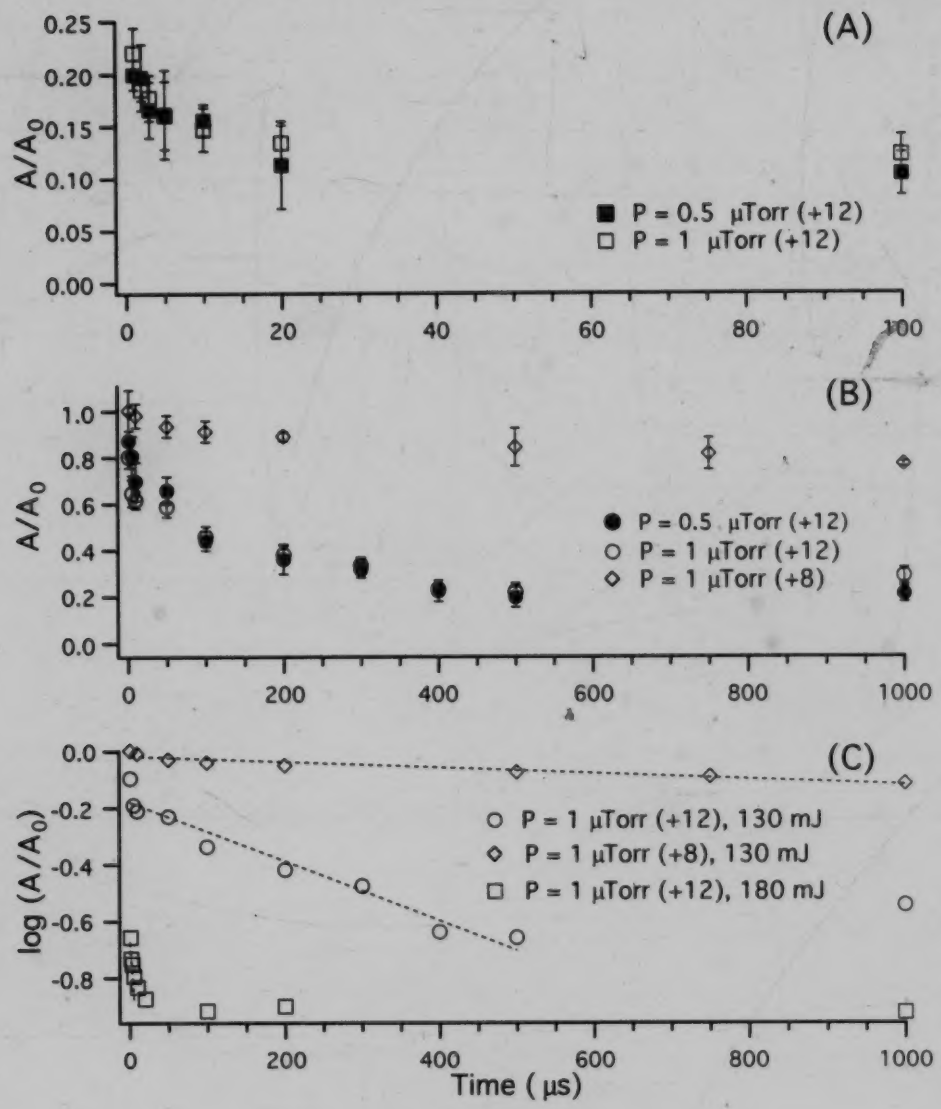

Figure 7.6. Time-resolved detection in IRMPD of equine cytochrome following a single excitation laser pulse. (A) Laser energy of 180 mJ per pulse, (B) Laser energy of 130 mJ per pulse, (C) The log (A / A_0) versus time plots for +12 and +8 charge state molecular ions at laser energy of 130 mJ per pulse and for the +12 molecular ion at laser energy of 180 mJ per pulse.

for a low and a high pressure condition are similar. Taking into account the precision of the experiment, the dissociation efficiency is not affected by the buffer gas pressure in the operational range of the instrument. The same result was obtained in the IRMPD experiment when the lower energy (130 mJ) laser pulse was used to fragment the +12 molecular ion (Figure 7.6 B). At examined helium pressures and laser energies, the dissociation efficiency of ions is not impacted by collisions with helium. A softer excitation resulted in a different shape of the decay curve. Almost 90% of the molecular ions remained intact 1 μs after the excitation and their further dissociation can be observed for next 500 μs until there is no visible progress in the dissociation. The decay curve for the molecular ion at the +8 charge state obtained for the same excitation energy level is presented for comparison. The information contained in Figures 7.6 A and 7.6 B can be used for determination of parameters describing the kinetics of the dissociation process.

Figure 7.6 C presents log (A / A_0) versus time plots for experiments where the +12 charge state molecular ion was subjected to excitation at laser energies of 130 mJ and 180 mJ and the +8 ion was photoexcited at a laser energy of 130 mJ. A linear relationship determined in the plots suggests that dissociation follows the first order reaction with the rate constants obtainable from the slopes of the plots in Figure 7.6 C. The decrease in energy of a laser pulse from 180 mJ to 130 mJ changes the dissociation rate constant for the +12 ion from $k=7.3 \cdot 10^4$ s^{-1} to $k=2.4 \cdot 10^3$ s^{-1}. The +8 ion following the excitation at 130 mJ dissociates slower with the rate constant of $k=2.6 \cdot 10^2$ s^{-1}.

The ability to monitor photodissociation shown in the decay curves in Figure 7.6 is a unique capability of the ion trap/time-of-flight analyzer. All commonly used trapping mass spectrometers including quadrupole ion traps and FT-ICR instruments are limited to the detection of photodissociation products only tens of milliseconds after the excitation laser pulse. Thus, it was not previously possible to monitor events occurring in the sub-millisecond time scale. The results presented for this new method confirm reports related to IRMPD of multiply charged ions with continuous laser excitation. In such experiments,

the irradiation time required to reach the onset of fragmentation for individual ions is a measure of the energy involved in the photodissociation. The amount of energy required to dissociate ubiqutin (a 8.6 kDa protein) was shown to decrease with increasing charge state [6]. This result is consistent with the observation described above for equine cytochrome c with IRMPD. Cytochrome c with higher charge states dissociates at higher rates.

The difference in dissociation rates observed for different charge states ions of cytochrome c can be readily explained by considering their structural differences [19]. The internal energy content of ions determines their fragmentation efficiencies. It derives from two sources: the internal energy of the ion before ionization (thermal energy); and the amount of energy deposited in the excitation process. The contribution of thermal energy to the internal energy of ions is directly proportional to the number of degrees of freedom associated with the ions [20]. For equine cytochrome c ions at various charge states, the thermal energy component should be the same. The size of the multiply charged ions of equine cytochrome c increases with the increase in charge state [21]. Accommodation of protons to form new charge centers may also affect other properties of the ion associated with its conformation. Ions at higher charge states are more rigid than their low charge state analogs. Photoexcitation energy deposited into a rigid ion results in dissociation, whereas a more labile ion has an ability to undergo conformational changes upon excitation without fragmenting. Thus, even if the more rigid ions (i.e., higher charge state ions) absorb less energy, their fragmentation can still be favored.

The detection capability of the ion trap/time-of-flight can provide additional characterization of photodissociation process for large molecules. The genealogical relationships between ions in IRMPD can not be elucidated in experiments carried out with continuous-wave excitation. IT-TOF detection following a single laser pulse established two types of products generated. Some ions were formed from the molecular ion just after the excitation (Figure 7.5 A) whereas other ions were generated at longer times (Figure 7.5 B-D). The population of ions formed instantaneously can suggest that excitation may

remain localized in large ions [22] such that the effective number of degrees of freedom is much smaller than the total number in the ion. Localized heating would be a way to increase the fragmentation of large ions on mass spectrometry time scales, since the amount of energy added by that means is not related to ion size.

7.3.3 IRMPD of PTH-isoleucine

The results of IRMPD experiments for smaller and singly charged ions are somehow surprising. When a low energy laser pulse is used, decay curves for photodissociating species resemble the curves presented in Figure 7.6 B. A sufficient increase in laser energy should theoretically result in total dissociation of irradiated ions. However, it was not possible to achieve complete dissociation of small singly charged species at high excitation energies. Among different classes of compounds analyzed in IRMPD at high laser energy, two distinct types of responses were observed. Multiply charged ions followed the post-excitation response of equine cytochrome c (Figure 7.6 A). "Decay curves" of singly charged ions resembled that of the m/z 249 molecular ion of PTH-isoleucine shown in Figure 7.7 A.

Figure 7.7 A shows relative intensities of ions involved in IRMPD (180 mJ) of PTH-isoleucine as a function of a time delay between excitation and detection. The logarithmic time scale is used to include a wider range of delay times. The intensity of each ion produced in IRMPD was measured as a peak area (A_x) and related to the peak area of the molecular ion peak subjected to photodissociation (A_0). As a result, the plot for the molecular ion represents its relative dissociation efficiency and a plot for a fragment ion corresponds to a relative fragment yield of this particular ion. Each point on the graph represents an average of 3 measurements and error bars for a relative dissociation efficiency of the molecular ion represent 2 relative standard deviations. Photodissociation products generated from the molecular ion of PTH-isoleucine are shown in the IRMPD spectra in Figure 7.7 B and Figure 7.7 C.

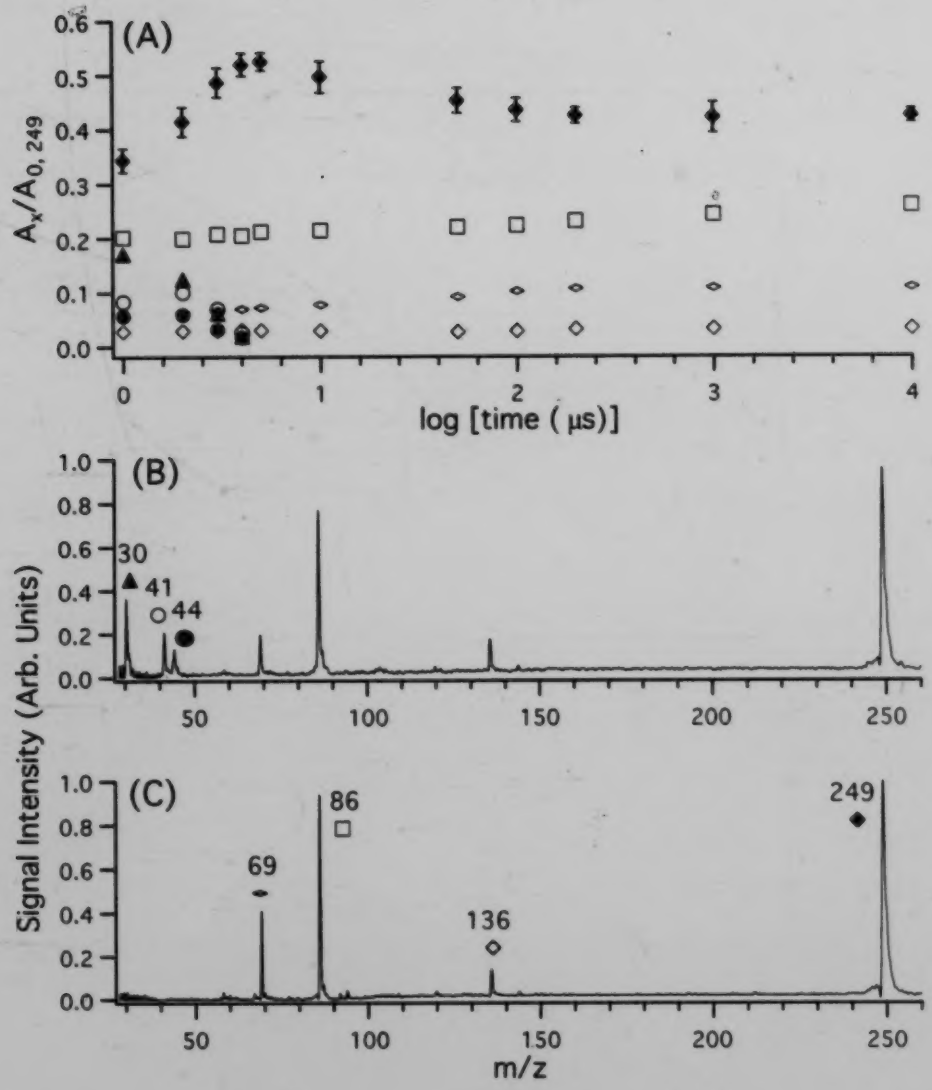

Figure 7.7. Time-resolved detection in IRMPD of PTH-isoleucine following a single excitation laser pulse with helium as a buffer gas at P = 0.8 μTorr in the TOF tube and a single laser pulse with laser energy of 180 mJ per pulse. (A) The IRMPD spectrum acquired 1 μs after excitation, (B) The IRMPD spectrum acquired 10 ms after excitation, (C) Relative intensities of IRMPD products as a function of time after excitation.

The spectrum in Figure 7.7 B was acquired 1 μs after the application of a single laser pulse. In addition to fragments at m/z of 136, 86, and 69, the spectrum reveals the presence of ions originating from the dissociation of the side chain of PTH-isoleucine at m/z 44, 41, and 30. These small ions with m/z below LMCO (set at m/z 55) have unstable trajectories of motion within the ion trap. As can be seen in Figure 7.7 A, the intensity of these ions decreases with time and they can be detected only in first 4 microseconds after excitation. The IRMPD spectrum in Figure 7.7 C was obtained 10 ms after the excitation and contains only those photofragments which are effectively trapped. Relative intensities of these ions (m/z 69, 86, 136) measured from 1 μs after excitation increase only slightly with time. It implies that formation of these fragments occurred very rapidly (< 1 μs). Side chain fragmentation products (m/z 30, 41, 44) are also formed at sub-microsecond time scale. The dissociation of the molecular ion at this level of excitation occurred rapidly but the plot representing the relative intensity of the molecular at m/z 249 following the laser excitation indicates a new phenomenon. The increase in intensity of this ion during 5 microseconds of detection is followed by a slow decrease of its intensity that can be observed up to 1 ms after the excitation.

Figure 7.8 illustrates data obtained in the same IRMPD experiment of PTH-isoleucine. Time dependence of the ion signals (peak areas) is presented in Figure 7.8 A. A_0 is the total peak area of the molecular ion subjected to photodissociation. $A_{\text{TOTAL DETECTED}}$ is the total peak area of all ions originating from photodissociation, including the molecular ion, and detected by the ion trap/time-of-flight system. $A_{\text{TOTAL TRAPPED}}$ is the total peak area of all ions generated in IRMPD including the molecular ion and excluding ions that are below LCMO (m/z = 55). $A_{\text{TOTAL MAXIMUM}}$ is a hypothetical total peak area of ions produced by photodissociation. It includes all ions that are efficiently trapped and also includes m/z 30, 41, 44 ions at intensities (peak areas) determined 1 μs after the excitation. $A_{\text{TOTAL MAXIMUM}}$ approximates the nominal intensity of all ions present in the IRMPD spectra in the case when the loss of the ions at m/z below 55 would not take place.

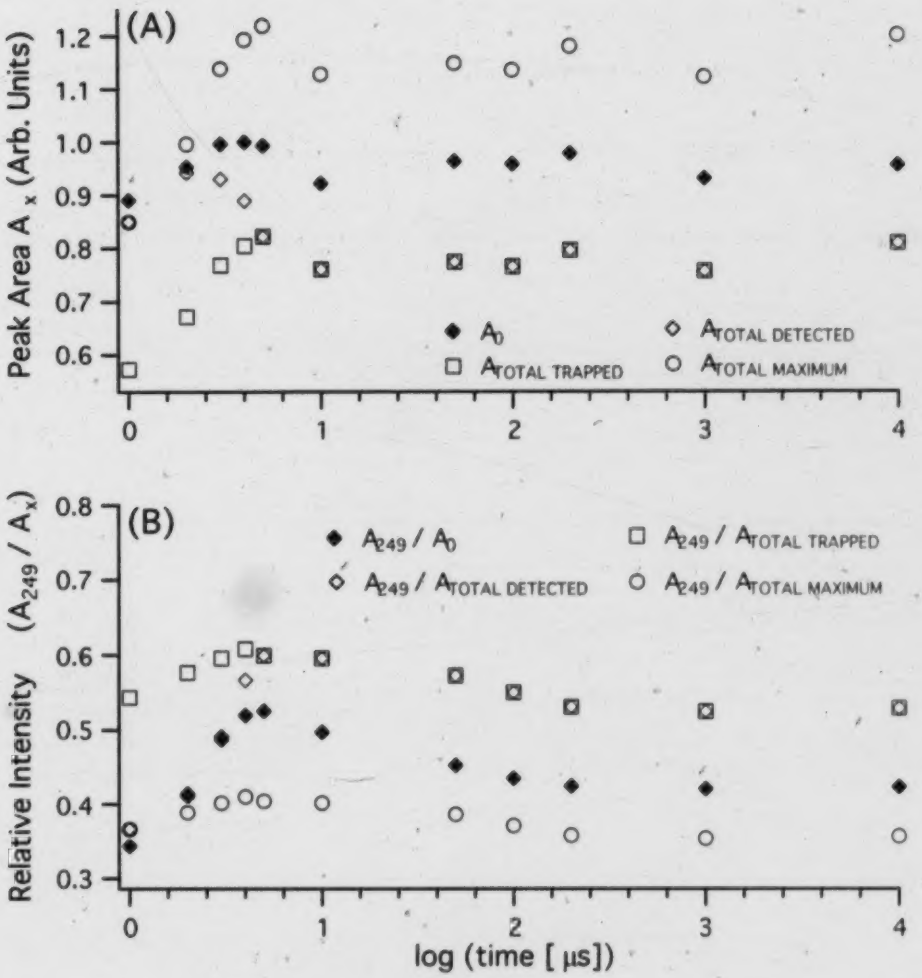

Figure 7.8. Time-resolved detection in IRMPD of PTH-isoleucine following a single excitation laser pulse with helium as a buffer gas at P = 0.8 μTorr in the TOF tube and a single laser pulse with laser energy of 180 mJ per pulse. (A) The total intensity of the ions after the excitation, (B) Relative intensities of the molecular ion after the excitation. See text for details.

A comparison of $A_{TOTAL\ DETECTED}$ to A_0 shows that some ions are being lost in the first 5 microseconds of detection. The ion loss is not substantial during the first 3 microseconds, which means that the ion loss is not induced by the laser pulse. The ion loss has to be attributed to the ions at m/z below LMCO. At the same time, $A_{TOTAL\ TRAPPED}$ increases mainly because of the increase in the intensity of the molecular ion. It is proposed that the increase in molecular ion intensity is due to the reformation of the molecular ions in the ion trap. The reformation of the molecular ion observed as the increase in its intensity with time is an implication of the photodissociation process. The formation of reactive species capable of donating a proton to a neutral species generated in IRMPD may result in the reformation of the molecular ion. It is possible that small fragment ions with m/z<55, present in the excited energy state after irradiation, participate in reactions leading to formation of the molecular ion.

Figure 7.8 B shows relative intensities of the molecular ion associated with A_0, $A_{TOTAL\ DETECTED}$, $A_{TOTAL\ TRAPPED}$, and $A_{TOTAL\ MAXIMUM}$ as a function of detection time. A_{249} / $A_{TOTAL\ MAXIMUM}$ defines the photodissociation efficiency of the molecular ion with an assumption that ions with m/z below LMCO formed at the intensity determined in first microsecond after excitation would be lost only due to the ion trap instability factor. A_{249} / $A_{TOTAL\ TRAPPED}$ represents the photodissociation efficiency of the molecular ion when only ions at m/z above LMCO are considered. It exemplifies the dissociation efficiency in the case when all ions with m/z below LMCO formed at intensity determined in first microsecond after excitation would be lost due to the donation of a proton to form an ionic species efficiently stored in the trap. The photodissociation efficiency A_{249} / A_0 calculated as the intensity of the molecular ion effected by dissociation to the intensity of the molecular ion subjected to this process falls in between two curves (A_{249} / $A_{TOTAL\ MAXIMUM}$ and A_{249} / $A_{TOTAL\ TRAPPED}$) depicted in Figure 7.8 B. It means that ions with m/z below LMCO are lost not only due to the trapping instability but also due to the gas phase proton transfer to neutral PTH-isoleucine molecule present in the trap after excitation. A_{249} / $A_{TOTAL\ DETECTED}$

represents the photodissociation efficiency of the molecular ion calculated for all ions detected in the dissociation process. The A_{249} / A_0 curve in the Figure 7.8 B follows closely the A_{249} / $A_{TOTAL\ DETECTED}$ curve in a short time after the excitation. This indicates that during the first 3 microseconds after the excitation there is no substantial ion loss affected by trapping instability. In this time the proton donation is responsible for the decrease in the signal of the ions at m/z below LMCO. Trapping instability becomes significant in the fourth microsecond after the excitation.

The photodissociation inside the ion trap with possible interactions of confined species is a complex process. In IRMPD of PTH-isoleucine, a rapid dissociation of the molecular ion is belived to be followed by post-excitation reformation of this ion. The controlling factors such as gas phase basicity and energy state of generated species, determine the direction of chemical reactions in a post-excitation period. The reformation process is followed by a moderate dissociation of the molecular ion observed from 5 μs up to 1 ms after the excitation. This process may be influenced by remaining energy that was deposited to the ion during laser excitation. However, the dissociation occurring in the millisecond time scale may result from reformation process in which an excited molecular ion experiences subsequent dissociation. The reformation of the molecular ion is typical for all examined singly charged ions (PTH-amino acids, peptides, oligosaccharides) subjected to IRMPD in a single laser pulse experiment at high energy. Results of equine cytochrome c, presented earlier, indicate that a similar process could occur in IRMPD of this species. The dissociation of a molecular ion at +12 charge state at excitation energy of 180 mJ determined in a time-resolved detection experiment was completed in 20 μs (Figure 7.6 A). However, the formation of the most intense fragment in the m/z range of 450 to 650, most likely related to a singly charged ion of the heme moiety, was observed up to 10 ms after the application of the laser pulse (Figure 7.5). This ion is generated from the molecular ion just after the excitation (Figure 7.5 A) but also at longer times by a process

that is not related directly to the rapid dissociation of the molecular ion. A charge transfer to a neutral fragment produced in IRMPD may be responsible for the formation of the ion.

The detection of ions at m/z below the LMCO provides the mass extension of the ion trap. The application of this property to ion trap/time-of-flight in IRMPD is illustrated in Figure 7.9. The presented spectra of the PTH-amino acid isomers were acquired 1 μs after the single laser pulse excitation at energy of 180 mJ. For this quick detection, ions in the range below LMCO (m/z 55) are observed in the spectra of PTH-isoleucine (Figure 7.9 A), PTH-leucine (Figure 7.9 B), and PTH-norleucine (Figure 7.9 C). Analyzed isomers differ only in the structure of the aliphatic side chain group. PTH-norleucine that contains an unbranched aliphatic side chain could not de distinguished from PTH-leucine based on source or ion trap CID methods presented in Chapter 3. IRMPD with the ion trap/time-of-flight detection provides additional information about the fragmentation of the molecular ion. Ions at m/z 30, 41, and 44 are related to the fragmentation of the immonium ion at m/z 86 and are formed by elimination of butene, ethylamine, and propene respectively. Based on the relative intensities of m/z 69, 44, 41, and 30 ions in the IRMPD spectra, it is possible to differentiate these PTH-amino acid isomers.

7.3.4 Time-resolved CID of PTH-isoleucine

In the IRMPD experiment of PTH-isoleucine, the reformation of the protonated molecular ion was observed only at high excitation energy. Results from ion trap CID presented in the analysis of polymer end groups in Chapter 5, suggest that a similar process is possible in collisional excitation. A time-resolved CID experiment was designed to monitor ions involved in collisional excitation. Figure 7.10 presents results obtained from such an experiment for PTH-isoleucine. The inset in Figure 7.10 A shows the CID waveform applied to the entrance end-cap of the ion trap and used in excitation of the molecular ion of PTH-isoleucine. The waveform was designed according to the principles described in Chapter 6. It consists of a range of frequencies (55.0-60.0 kHz) applied in

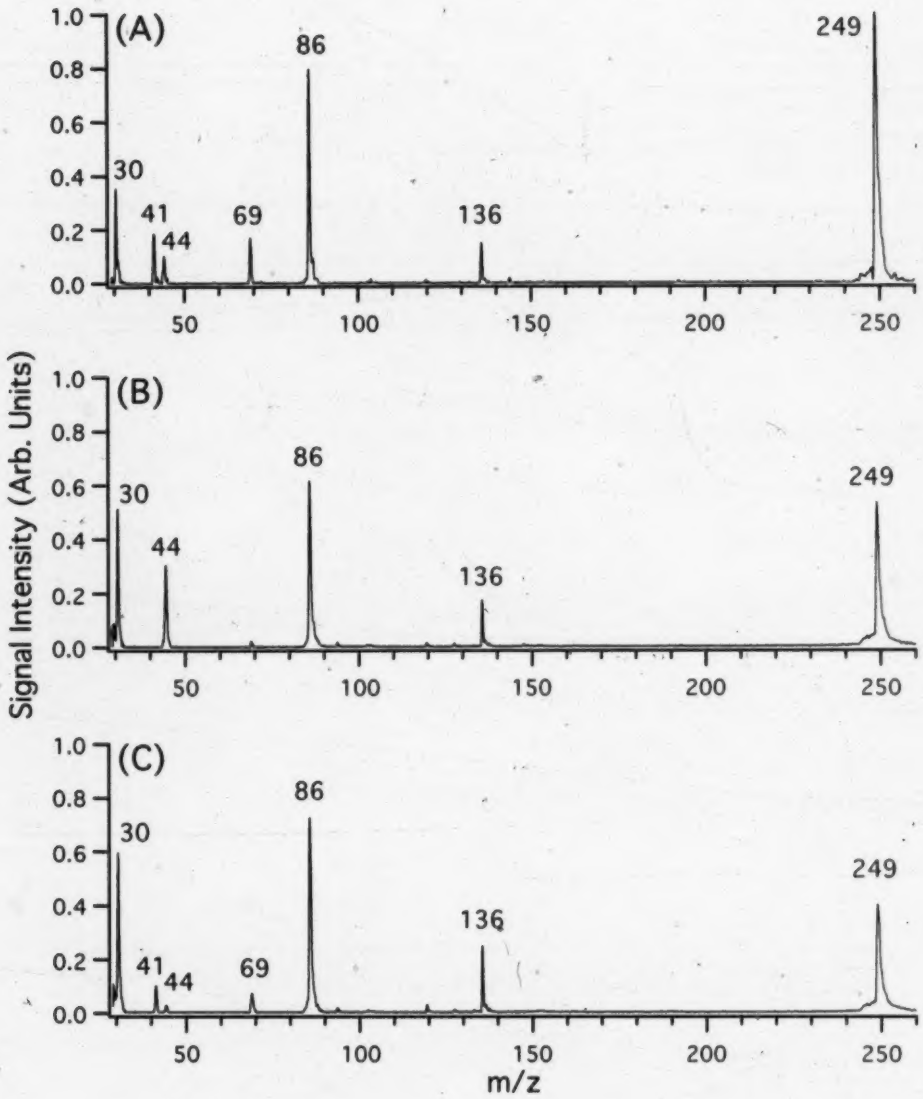

Figure 7.9. IRMPD spectra of PTH-amino acid isomers acquired 1 μs after excitation with helium as a buffer gas at P = 1 μTorr in the TOF tube and a single laser pulse with laser energy of 180 mJ per pulse. (A) PTH-isoleucine, (B) PTH-leucine , (C) PTH-norleucine.

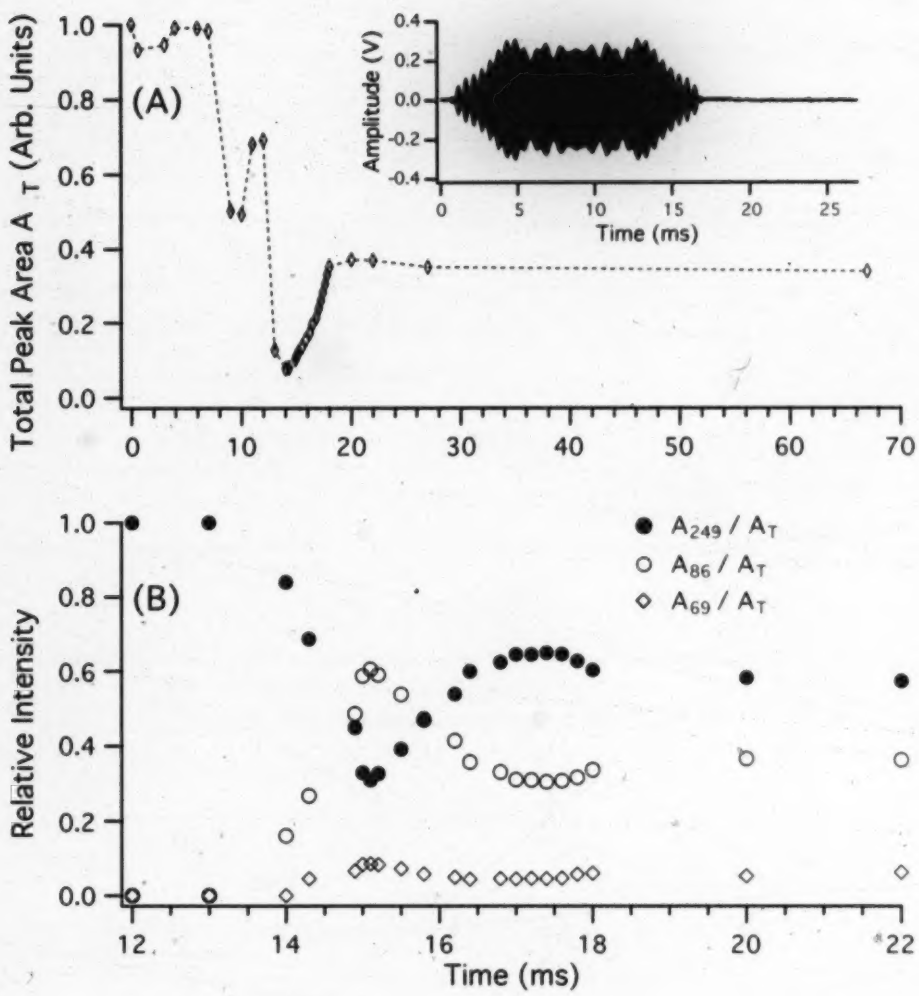

Figure7.10. Time-resolved detection in CID of PTH-isoleucine. (A) The total intensity of the ions present in the ion trap during CID, (B) Relative intensities of ions involved in CID. The inset shows the CID used for excitation of the molecular ion of PTH-isoleucine.

a sweep frequency fashion and swept from lower to higher frequencies. The calculated secular frequency responsible for resonant excitation of the molecular ion is 59.7 kHz. By using ion trap/time-of flight detection, it is possible to probe the population of ions participating in CID with time. Figure 7.10 A shows the total intensity of the ions present in the ion trap during the application of the excitation waveform. CID relies on the increase in the oscillation amplitude of resonating ions which results in a significant ion loss during the excitation. Approximately two-thirds of the total ion signal is lost in the process. Figure 7.10 B shows relative intensities of ions involved in CID. In addition to the molecular ion, only ions formed at a significant yield (>1%), namely the m/z 86 and m/z 69 ion, are considered. After application of the excitation waveform, there is no fragment ion formation during the first 13 milliseconds. This is because, at that moment, the applied frequencies are different than the secular resonant frequency of the molecular ion. However, molecular ions experience a slight excitation at frequencies different from the secular one. This excitation is observed at the time when the measured total ion intensity is reduced. It must be stressed that the drop in the ion signal at the moment of detection is caused by two factors. First, some ions are lost during excitation. Second, ions that move far away from the center of the trap are ejected less efficiently into the flight tube than ions located in the center of the trap. The effect of resonant excitation at frequencies close to the secular frequency is observed at 13 ms when the intensity of the total ion signal decreases. Figure 7.10 B shows that at this moment the molecular ions start to dissociate and form the m/z 86 and m/z 69 fragments. The progress of dissociation is observed during the next 2 ms when ions are located outside the center of the trap. After that, the collisional focusing gradually restores the position of the ions to the center of the trap. During this process, the intensity of the m/z 249 molecular ion increases at the cost of the intensity of the m/z 86 fragment ion. This process lasts for about 2 ms and the relative intensity of the ions, as well as total intensity of the ions involved in CID, remains the same there after. These observations suggest that the reformation of the molecular ion for PTH-isoleucine, similar

to this encountered in IRMPD, takes place in CID. The immonium ion seems to participate in the protonation of the neutral molecule of PTH-isoleucine detected in the millisecond time scale. The time-resolved CID experiment can not be performed on ion traps with commercial detection schemes for the simple reason that detection can not be accomplished at the same time as CID excitation. This type of experiment provides clear evidence for ion-neutral reactions taking place inside the ion trap as an implication of CID excitation. Time-resolved CID offers a tool to determine the genealogy of CID products by monitoring a time of formation for a particular species. Secondary fragments formed as a result of gas phase reactions appear in a time-resolved spectrum much later than primary fragments originating directly from a molecular ion. Such secondary ions (m/z 189 and m/z 193) at a low intensity (refer to Figure 3.10 in Chapter 3) emerge in the CID spectrum of PTH-isoleucine at a time of 3 ms after the appearance of primary fragments.

7.3.5 Analysis of disaccharide isomers by IRMPD and CID

Development of new analytical methodologies for analyses of carbohydrates is an important topic of current analytical research. Mass spectrometry of carbohydrates constitutes the subject of review articles [23, 24]. Among MS techniques, tandem mass spectrometry has the potential to provide structural information on these species [25]. A challenging part of structural analysis of carbohydrates is gaining unambiguous linkage information for linear and branched carbohydrates. These include different anomers (α- and β-linked saccharides) as well as isomers linked at different positions. The three dominant processes in the fragmentation of protonated or cation-coordinated oligosaccharides [26] include: the loss of a proton or a cation; glicosidic bond cleavage; and cross-ring cleavage. Glycosidic bond cleavages are important for the determination of the sequence of monosaccharides. While cross-ring cleavages are useful for determining linkages between component monosaccharides and the branching arrangements. Carbohydrates exhibit a wide structural variety and the abundance of fragment ions

depends on many structure-related factors [27]. Figure 7.11 shows the structures of analyzed disaccharide isomers that provide rather limited structural information in tandem

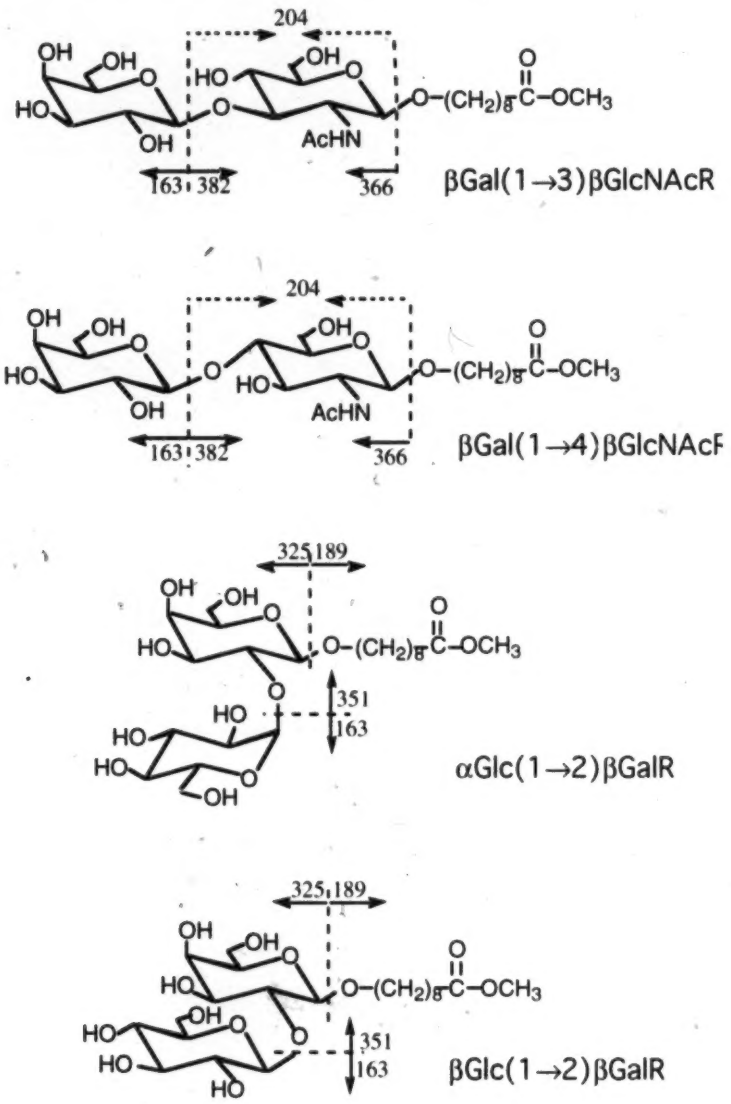

Figure 7.11. Structures and fragmentation pathways of linkage isomers (βGal(1→3)βGlcNAcR, βGal(1→4)βGlcNAcR) and anomers (βGlc(1→2)βGalR and αGlc(1→2)βGalR) analyzed by IRMPD.

mass spectrometry. βGal(1→3)βGlcNAcR and βGal(1→4)βGlcNAcR are examples of isomers with different linkage positions. βGlc(1→2)βGalR and αGlc(1→2)βGalR are examples of different anomers. The absence of a free hydroxyl group on the anomeric carbon for these compounds prevents a type of fragmentation that would lead to cross-ring dissociation products which are especially useful in structural analysis [28]. Examples shown in this section should be regarded as a brief consideration of the potential of an IRMPD ion trap/time-of flight technique, not as an elaborate structural analysis.

Figure 7.12 shows the fragmentation spectra of βGal(1→3)βGlcNAcR and βGal(1→4)βGlcNAcR obtained in ion trap CID and IRMPD under the same experimental conditions. CID of a protonated molecular ion of βGal(1→4)βGlcNAcR (Figure 7.12 A) and βGal(1→3)βGlcNAcR (Figure 7.12 B) resulted in products from the dissociation of glycosidic bonds. The fragmentation pathways following the dissociation of glyciosidic bonds are depicted in Figure 7.11. The most intense fragment ion (m/z 366) is formed from the molecular ion by elimination of the linker (HOR). Further elimination of galactose from the m/z 366 ion with a proton transfer to the glucose moiety leads to the formation of the m/z 204 ion. A similar process for the elimination of galactose from the protonated molecular ion and a proton transfer to the glucose moiety generates the m/z 382 ion. The CID spectrum of the (1→4) linked isomer (Figure 7.12 A) also contains low intensity ions at m/z 138 and 168. The intensity of these ions increases in the CID spectra of the m/z 366 ion originated from βGal(1→4)βGlcNAcR (Figure 7.12 C) and βGal(1→3)βGlcNAcR (Figure 7.12 D). The m/z 366 ion dissociates to produce the m/z 204 ion and a series of ions at m/z 186, 168, 138, and 127. The elimination of neutral molecules from the m/z 204 ion accounts for formation of the observed fragments. The loss of H_2O from m/z 204 results in the m/z 186 ion, the loss of $2H_2O$ in the m/z 168 ion, the loss of $2H_2O+CH_2O$ in the m/z 136 ion, the loss of $H_2O+CH_3CONH_2$ in the m/z 127 ion, and the loss of $H_2O+CH_3CONH_2+ CH_2O$ in the m/z 97 ion. Ions at m/z 127 and m/z 97 could be potentially generated from the m/z 163 ion (galactose moiety) by elimination of $2H_2O$ and

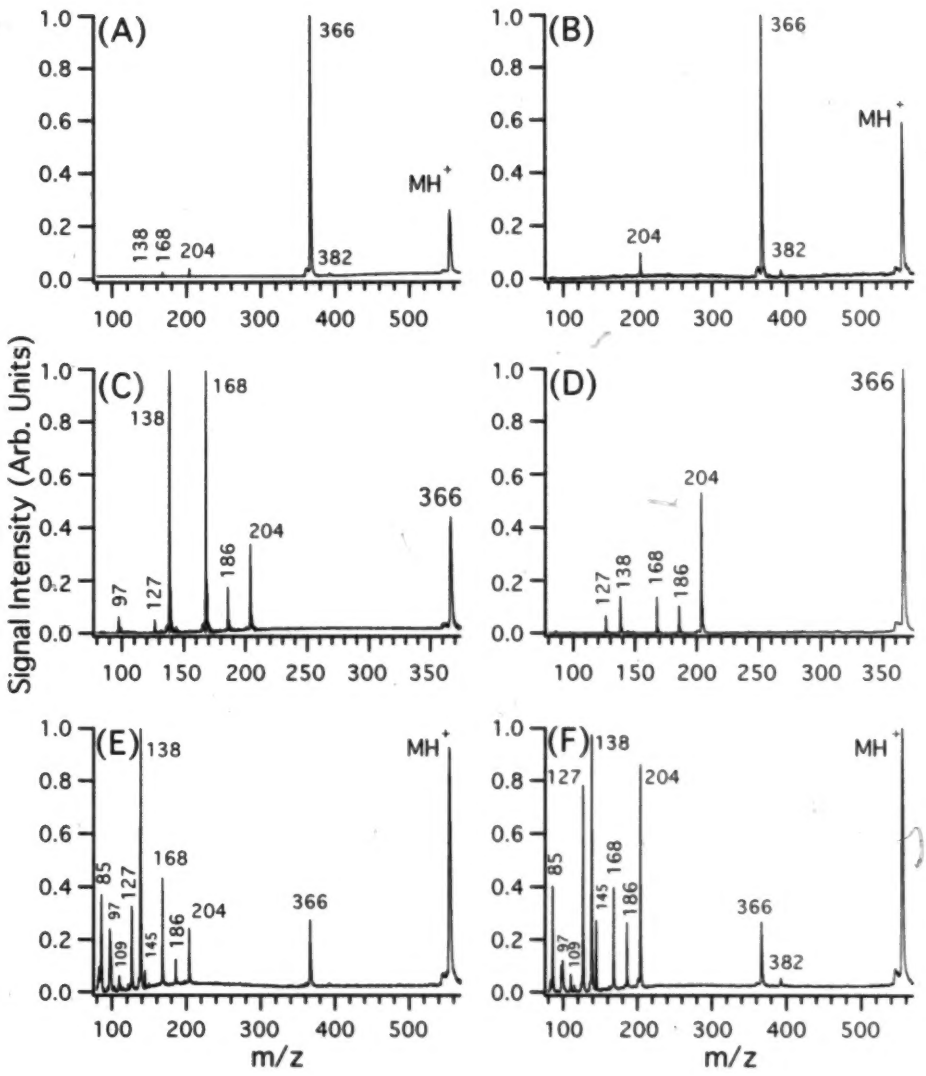

Figure 7.12. Dissociation spectra of disaccharide linkage isomers. (A), (C), (E) βGal(1→4)βGlcNAcR. (B), (D), (F) βGal(1→3)βGlcNAcR. (A), (B) CID of the protonated molecular ion. (C), (D) CID of the m/z 366 ion. (E), (F) IRMPD spectra of the protonated molecular ion acquired 1 ms after excitation with helium as a buffer gas at P = 0.8 μTorr in the TOF tube and a single laser pulse with laser energy of 180 mJ per pulse.

elimination of $2H_2O+CH_2O$, respectively. The comparison of the MS/MS/MS spectra in CID of two linkage isomers in Figures 7.12 C and 7.12 D indicates that based on the intensity difference of ions at m/z 168, 138, and 97 one can distinguish between these isomers. The similar distinction can be made based on the MS/MS process effected by a single laser pulse. Figure 7.12 E and 7.12 F show the IRMPD spectra of βGal(1→4)βGlcNAcR and βGal(1→3)βGlcNAcR, respectively. In addition to the ion peaks present in CID, new products are observed in both IRMPD spectra. The ions at m/z 145 and 109 may be formed from the m/z 204 ion by elimination of CH_3CONH_2 and elimination of $2H_2O+CH_3CONH_2$, respectively. They may also be generated from a galactose moiety when elimination of H_2O from the m/z 163 ion produces the m/z 145 ion and elimination of $3H_2O$ from the m/z 163 ion produces the m/z 109 ion. The m/z 85 ion is the only product of the cross-ring cleavage of the m/z 145 ion. Two bond cleavage in a monosaccharide ring with the elimination of $C_2H_4O_2$ is responsible for the formation of this ion. Compared to CID, IRMPD is capable of generating more fragments with more energetic excitation. The differentiation of two linkage isomers in IRMPD is possible based on a MS/MS experiment when the intensity of m/z 204, 186, 145, 127, and 97 fragment ions is compared.

Figure 7.13 shows results from similar CID and IRMPD experiments for the two disaccharide anomers. The molecular ion selected for dissociation was the ammonium cation adduct (preferentially formed in ESI). Figure 7.13 A shows the CID spectrum of αGlc(1→2)βGalR and Figure 7.13 B shows the CID spectrum of βGlc(1→2)βGalR acquired at the same experimental conditions. The fragmentation products generated by the cleavage of glycosidic bonds, provide sequential information corresponding to ion peaks at m/z of 351, 325, and 163. The fragmentation pathways following the dissociation of glycosidic bonds are depicted in Figure 7.11. The most intense fragment ion at m/z 351, in this case, is formed from the molecular ion by elimination of glucose and ammonia with a proton transfer to the galactose moiety. The cleavage of a glycosidic bond between glucose

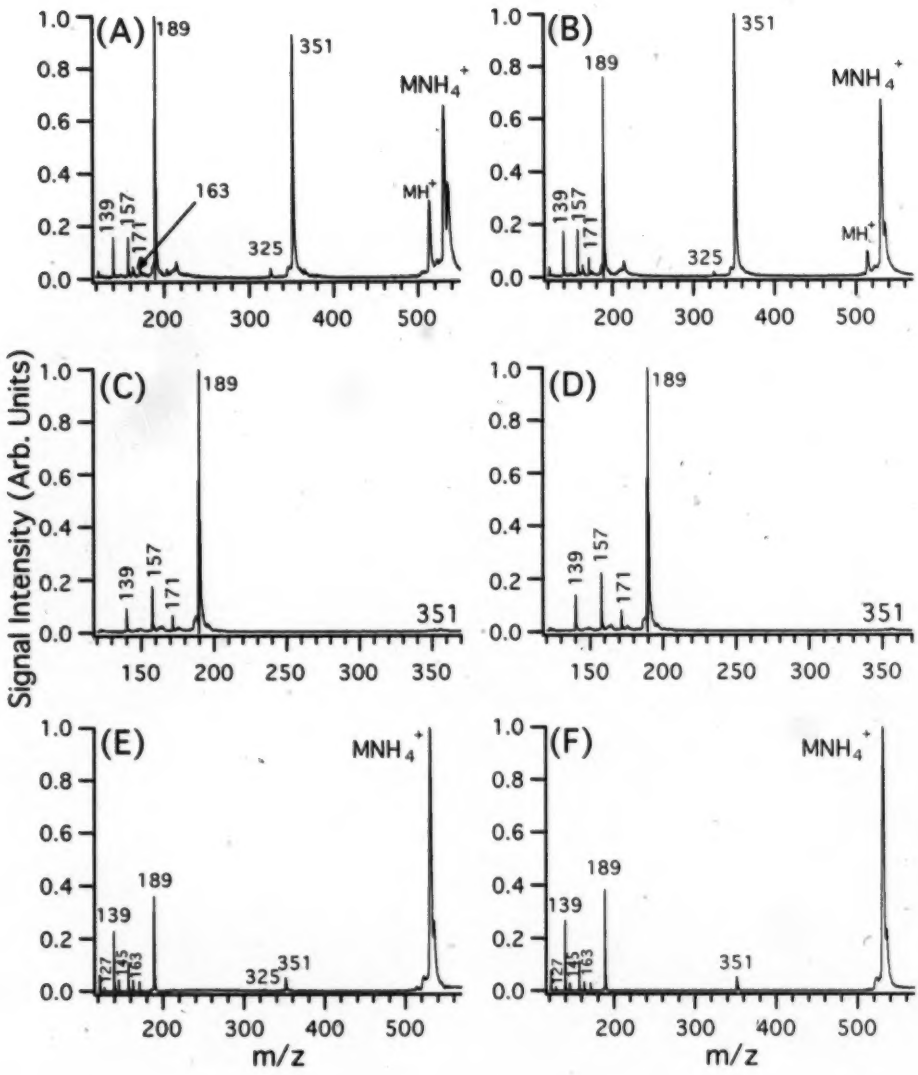

Figure 7.13. Dissociation spectra of disaccharide anomers. (A), (C), (E) αGlc(1→2)βGalR. (B), (D), (F) βGlc(1→2)βGalR. (A), (B) CID of the ammoniated molecular ion. (C), (D) CID of the m/z 351 ion. (E), (F) IRMPD spectra of the ammoniated molecular ion acquired 1 ms after excitation with helium as a buffer gas at P = 0.8 μTorr in the TOF tube and a single laser pulse with laser energy of 180 mJ per pulse.

and galactose leads to the formation of the m/z 163 ion with the charge retained on the glucose moiety. The most useful fragment ion at m/z 325 containing the linkage information is generated by elimination of HOR and ammonia from MNH_4. The intensity of this ion is not high enough to select and dissociate this ion in the MS/MS/MS stage. CID of these anomers is dominated by formation of fragments related to the linker group (R). The most intense peaks in the spectra in Figure 7.13 correspond to the protonated linker $[H_2OR]^+$ at m/z of 189 and its products at m/z 171 (elimination of H_2O), at m/z 157 (elimination of CH_3OH), and at m/z 139 (elimination of H_2O+CH_3OH). Figure 7.13 C and 7.13 D show the CID spectra of the m/z 351 ions originated from αGlc(1→2)βGalR and βGlc(1→2)βGalR, respectively. The spectra were acquired at high excitation energy, so the intensity of a fragmenting ion is very small. Even for these conditions, only ion peaks related to the linker structure are detected and the products corresponding to the galactose ring are not observed.

IRMPD spectra of αGlc(1→2)βGalR (Figure 7.13 E) and βGlc(1→2)βGalR (Figure 7.13 F) are similar to the CID spectra. The intensity of the fragment peaks originated from monosaccharide rings at m/z 163, 145, and 127 relative to the intensity of the fragment peaks related to the linker group (R) is higher in IRMPD. However, the spectra do not provide the information necessary to differentiate these anomers. A significant difference in dissociation pathways of the anomers relative to the linkage isomers was observed. The analyzed anomers as underivatized carbohydrates provided limited structural information [27]. In case of the analyzed linkage isomers, the presence of a derivatizatized monosaccharide subunit contributed to the successful application.

The examination of various metal cations (Na^+, K^+, Li^+, Cs^+) involved in the formation of molecular ion adducts [26] and subjected to dissociation was also not effective in differentiating the anomers. In fact, the ammonium adducts of analyzed compounds were found to provide the most intense fragmentation. The most distinctive feature for the two anomers is the formation of the MH^+ ion in CID. As can be seen in Figures 7.13 A

and 7.13 B, the intensity of this product is much higher in CID of the ammoniated molecular ion of αGlc(1→2)βGalR. This ion originates from MNH_4^+ by elimination of NH_3 to form the protonated molecular ion. This observation indicates that properties of a molecular ion that are not related to backbone fragmentation of the ion may be useful in differentiating of these anomers.

A time-resolved IRMPD method characterizes the behavior of an ion subjected to irradiation not only in the contest of fragmentation but also in the contest of all gas-phase processes occurring inside the ion trap. Figure 7.14 shows results from the time-resolved IRMPD experiment of the ammoniated molecular ions of αGlc(1→2)βGalR and βGlc(1→2)βGalR.

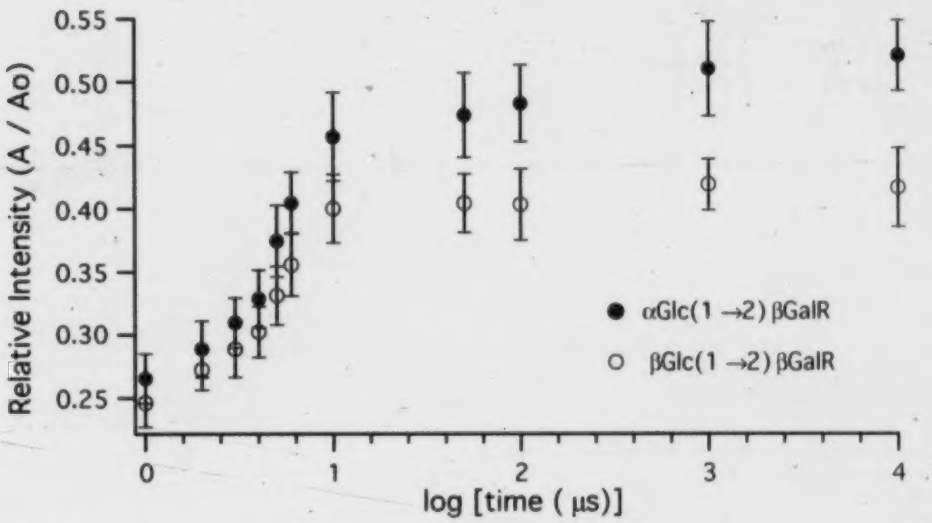

Figure 7.14. Time-resolved detection in IRMPD of βGlc(1→2)βGalR and αGlc(1→2)βGalR anomers following a single excitation laser pulse with helium as a buffer gas at P = 0.8 μTorr in the TOF tube and a single laser pulse with laser energy of 180 mJ per pulse. See text for details.

The relative intensity (A / A_0) of each molecular ion monitored with time was calculated as follows. The area of a molecular peak (A) was measured in the IRMPD spectrum obtained at a delay time after application of a single excitation laser pulse (180 mJ). The area (A) was then correlated to the area of a molecular ion peak subjected to photodissociation (A_0). The dissociation efficiency (A / A_0) was then plotted as a function of the time delay (logarithmic scale) between excitation and detection. Each point on the graph represents an average of 3 measurements with an error bar corresponding to 2 standard deviations. The relative intensity of the molecular ions increases sharply during the first 10 μs following the laser excitation. This is the effect of the reformation of the molecular ion. The reformation of the molecular ions, in contrast to PTH-isoleucine, continues for the remaining time. Comparison of the curves for αGlc(1→2)βGalR and βGlc(1→2)βGalR indicates that the molecular ions were photofragmented with similar efficiency. However, the rate of the reformation process of each anomer determined from 1 μs to 10 ms is different. The relative intensity of the molecular ion for the α-anomer is higher than for the β-anomer and this difference becomes more pronounced with longer delay (reaction) times. A distinct response of ammoniated molecular ions of αGlc(1→2)βGalR and βGlc(1→2)βGalR to a pulsed laser excitation allows for differentiation of examined anomers. Due to the complexity of the process, it is difficult to comprehend this observation. A rate of a reformation process, in case of anomers, is likely related to structure stability of an ammoniated molecular ion determined by an anomeric configuration.

7.4 Summary

An ion trap/time-of-flight mass spectrometer was applied to IRMPD studies of ions generated by electrospray ionization. A pulsed 10.6-μm laser beam from a CO_2 laser was used for excitation of trapped ions. Results from IRMPD of peptides showed that the method provides information about the composition and sequence of analyzed species. IRMPD spectra are similar to those obtained by uv-excitation. However, in contrast to the

excitation at 266-nm by multiple laser pulses in PID, the energy of a single laser pulse in IRMPD is sufficient to effect dissociation of peptides. The laser power is practically the only parameter which has to be controlled to obtain IRMPD spectra providing the optimal sequential information. The IRMPD technique has the potential to probe the structural features of larger species that cannot be fragmented by CID. Equine cytochrome c in the form of a multiply charged ion was successfully fragmented in a single laser pulse experiment. The progress of the dissociation process was monitored in a sub-millisecond time frame. Results from this experiment indicate that the conformation of the protein plays an important role in its dissociation ability in IRMPD.

The behavior of smaller and singly charged ions subjected to the laser excitation at a high energy is different than that of the protein. The dissociation of these ions is followed by a reformation process which is clearly observed in the first few microseconds after excitation. The reformation process leads to an increase in the intensity of the molecular ion, and is due to the gas-phase reactions between species generated by highly energetic irradiation. A similar effect on a longer time scale was observed in CID when this excitation technique was monitored by the time-resolved detection. IRMPD with quick detection of products that are not trapped in the quadrupole field provides an extension to the low mass limit of the ion trap and was used for differentiation of PTH-amino acid isomers.

The application of the technique to the analysis of anomers and linkage isomers of disaccharides showed that IRMPD in one stage of tandem mass spectrometry can provide a spectral information no worse than that obtained in two stages of tandem mass spectrometry in CID. The success of this application is strongly dependent on the properties of disaccharides influencing the fragmentation pathways rather than the dissociation method used. Nevertheless, the time-resolved detection of two anomers subjected to IRMPD indicates that the distinction between these two isomers is possible.

7.5 Literature cited

[1] Little, D. P.; McLafferty, F. W. *J. Am. Soc. Mass Spectrom.* **1996**, 7, 209.

[2] Dufresne, C. P.; Wood, T. D.; Hendrickson, C. L. *J. Am. Soc. Mass Spectrom.* **1998**, 9, 1222.

[3] Fridriksson, E. K.; Baird, B.; McLafferty, F. W. *J. Am. Soc. Mass Spectrom.* **1999**, 10, 453.

[4] Bomse, D. S.; Berman, D. W.; Beauchamp, J. L. *J. Am. Chem. Soc.* **1981**, 103, 3967.

[5] Baykut, G.; Watson, C. H.; Weller, R. R.; Eyler, J. R. *J. Am. Chem. Soc.* **1985**, 107, 8036.

[6] Little, D. P.; Speir, P. J.; Senko, M. W.; O'Connor, P. B.; McLafferty, F. W. *Anal. Chem.* **1994**, 66, 2809.

[7] Stephenson, J. L., Jr.; Booth, M. M.; Boue, S. M.; Eyler, J. R.; Yost, R. A. *Biochemical and Biotechnological Applications of Electrospray Ionization Mass Spectrometry*; Snyder, A.P., Ed.; ACS symposium series 619: Washington, DC, **1996**, 512.

[8] Colorado, A.; Shen, J. X.; Brodbelt, J. S. *Anal. Chem.* **1996**, 68, 4033.

[9] Goolsby, B. J.; Brodbelt, J. S. *J. Mass Spectrom.* **1998**, 33, 705.

[10] Stephenson, J. L., Jr.; Booth, M. M.; Shalosky, J. A.; Eyler, J. R.; Yost, R. A. *J. Am. Soc. Mass Spectrom.* **1994**, 5, 886.

[11] Hofstadler, S. A.; Sannes-Lowery, K. A.; Griffey, R. H. *Anal. Chem.* **1999**, 71, 2067.

[12] Gimon-Kinsel, M. E.; Kinsel, G. R.; Edmondson, R. D.; Russell, D. H. *J. Am. Soc. Mass Spectrom.* **1995**, 6, 578.

[13] Robinson, P. G.; Holbrook, K. A. *Unimolecular Reactions*, Wiley: New York, **1972**.

[14] Rosenstock, H. M.; Wallenstein, M. B.; Wahrhaftig, A. L.; Eyring, H. *Proc. Natl. Acad. Sci. U.S.A.* **1952**, 38, 667.

[15] Griffin, L. L.; McAdoo, D. J. *J. Am. Soc. Mass Spectrom.* **1993**, 4, 11.

[16] McLuckey, S. A.; Ramsey, R. S. *J. Am. Soc. Mass Spectrom.* **1994**, 5, 324.

[17] Asam, M. R.; Glish, G. L. *J. Am. Soc. Mass Spectrom.* **1999**, 10, 119.

[18] Fountain, S. T.; Lee, H.; Lubman, D. M. *Rapid Commun. Mass Spectrom.* **1994**, 8, 407.

[19] Price, W. D.; Schnier, P. D.; Williams, E. R. *Anal. Chem.* **1996**, 68, 859.

[20] Drahos, L.; Vekey, K. *J. Am. Soc. Mass Spectrom.* **1999**, 10, 323.

[21] Chen, Y-L.; Collings, B. A.; Douglas, D. J. *J. Am. Soc. Mass spectrom.* **1997**, 8, 681.

[22] Schlag, E. W.; Levine, R. D. *Chem. Phys. Lett.* **1989**, 163, 523.

[23] Burlingame, A. L.; Boyd, R. K.; Gaskell, S. J. *Anal. Chem.* **1994**, 66, 667R.

[24] Burlingame, A. L.; Boyd, R. K.; Gaskell, S. J. *Anal. Chem.* **1996**, 68, 630R.

[25] Bahr, U.; Pfenninger, A.; Stahl, B.; Karas, M. *Anal. Chem.* **1997**, 69, 4530.

[26] Cancilla, M. T.; Wong, A. W.; Voss, L. R.; Lebrilla, C. B. *Anal. Chem.* **1999**, 71, 3206.

[27] Laine, R. A.; Yoon, E.; Mahier, T. J.; Abbas, S.; de Lappe, B.; Jain, R.; Matta, K. *Biol. Mass Spectrom.* **1991**, 20, 505.

[28] Spengler, B.; Dolce, J. W.; Cotter, R. J. *Anal. Chem.* **1990**, 62, 1731.

Chapter 8

Conclusions and Future Work

The work presented in this thesis involves the development and application of an electrospray ionization ion trap/linear time-of-flight mass spectrometer.

The capabilities and limitations of using this instrument for quantification of sulfonamides are investigated in Chapter 2. Calibration curve exhibiting a linear response for almost 3 orders of magnitude were observed. The lower limit of the linear range was restricted by the chemical background noise while the upper limit was governed by the ESI source. Multicomponent analysis showed that the presence of many components in a mixture narrows the linear range for a single analyte that is being monitored in that mixture. The properties of an ESI source characterized in this chapter provides an explanation for the selective effectiveness of electrospray ionization. The detectability of analytes using ESI ion trap/TOF MS was comparable to results obtained using the API 100 LC mass spectrometer for single ion detection, and was superior for multicomponent analyses.

In Chapter 3, the ESI IT/TOFMS was evaluated as a detector for the identification of PTH-amino acids. Each of the 22 PTH-amino acids studied was characterized by well-defined mass spectral patterns. The source fragmentation gave rise to unique and intense fragmentation products which allowed for the differentiation of isomers. The detectability of PTH-amino acids for the ESI IT/TOFMS was examined. Results for the relative signal responses of the 20 standard PTH-amino acids indicate that the response factor between the most sensitive and the least sensitive compound can be as high as 20. Sensitivity disproportionation must be considered in the identification procedure. Subpicomole detection of PTH-amino acids was demonstrated. However, samples from a sequencer would require a purification procedure in order to achieve sensitive detection. The purpose of such a step is not the total separation of PTH-amino acids, but rather simply the

elimination of interfering species. The comparison of the developed detection method to a technique using a novel solvent system and a commercial ion trap instrument indicated superior detection capability for ESI IT/TOFMS. Optimal conditions, determined for ion trap CID of PTH-amino acids, yielded fragmentation information analogous to that provided by source fragmentation.

An in-depth investigation of the CID reactions of PTH-amino acids and N-terminal PTC derivatives of several amino acids and dipeptides, as major types of products generated in the Edman protein sequencing, is presented in Chapter 4. The purpose of this study was to determine whether the processes taking place in the gas phase during the fragmentation are similar to these occurring in solution. The spectral information obtained in the experiment strongly suggests, that at a detection time scale of a sector instrument, there is no isomerization of thiazolone to phenylthiohydantoin in the gas phase. Understanding the fragmentation pathways of the examined species should also facilitate structural elucidation and chemical identification for non-standard and modified amino acids.

A new tandem mass spectrometry method was used to obtain structural information on polymer end groups. This method, presented in Chapter 5, relied on the use of source fragmentation to generate low mass fragment ions from polymer ions formed by electrospray ionization. These ions were then subjected to high-energy collision-induced dissociation in a tandem sector/time-of-flight mass spectrometer. The spectral information obtained from MS/MS studies enabled confirmation of the identity of the end group. This method, complemented by time-lag focusing MALDI, can be extended to study unknown end group structures. The described method could not be applied to the ESI IT/TOFMS. Two major instrumental limitations were discovered. The ion trap was not capable of dissociating large ionic species. Secondly, ion trap CID of polymer fragments generated in the ESI source resulted in an abundance of ions exhibiting very limited spectral information.

An alternative to CID in probing structural features of biomolecules, photo-induced dissociation, was implemented and is presented in Chapters 6 and 7. Experiments with a 266-nm laser beam from a pulsed Nd:YAG laser, in Chapter 6, showed that the amount of photoenergy deposited for fragmentation is governed by the absorption property of the ions, the laser power, the number of laser pulses, and the ion trap buffer gas pressure. Energetically optimal PID process resulted in spectra providing sequential information similar to that obtained from CID. It was demonstrated that the PID technique has the potential to probe the structural features of peptides that can not be fragmented in ion trap CID process. A combination of the ion trap with the TOF detector was found to provide a unique capability for fast detection of ions formed in PID.

Chapter 7 focused on the application of the ion trap/time-of-flight mass spectrometer for IRMPID studies of electrospray generated ions. In contrast to the excitation at 266-nm by multiple laser pulses in PID, the energy of a single pulse from a CO_2 laser in IRMPD is sufficient to effect dissociation of peptides. The laser power is practically the only parameter which has to be controlled in obtaining IRMPD spectra providing the optimal sequential information. Experiments with a pulsed CO_2 laser demonstrated that sufficiently high photon fluxes are available to photodissociate irradiated ions of proteins. Equine cytochrome c in the form of multiply charged ions was successfully fragmented in the single laser pulse experiment. The progress of the dissociation process was monitored in a sub-millisecond time frame. Results from this experiment indicate that the conformation of the protein plays an important role in its dissociation. Photodissociation of smaller and singly charged ions is followed by the reformation (increase in intensity) of the molecular ion observed clearly in the first few microseconds after excitation. Time-resolved detection was used to characterize the dissociation processes occurring inside the quadrupole ion trap. Finally, IRMPD on the ion trap/time-of-flight instrument was found to be useful for differentiation of anomers and linkage isomers of disaccharides as well as PTH-amino acid isomers.

In future applications, an ion trap/time-of-flight spectrometer can be used in analyses demanding fast and sensitive detection of multicomponent samples. The function of the instrument in this type of operation will not be restricted to providing molecular weight. Tandem mass spectrometry techniques may help in solving problems with identification of species analyzed by mass spectrometry. Within the limitations presented and discussed in this work, the instrument is a useful addition to the analytical tools for obtaining compositional or structural information. Time-resolved detection, which provides the opportunity to monitor very fast processes occurring inside the ion trap, could expand the application of mass spectrometry for studying new phenomena. This new technique was applied to monitor dissociation of ions but its potential could be practically extended to all processes taking place inside the ion trap. Rapid detection is required for a variety of applications. Monitoring of reactions between ions and reactants introduced to the trap (e.g., hydrogen-deuteron exchange for proteins in conformational studies) belongs to this category. The current detection system can not probe events (e.g., photodissociation of small ions) occurring at a time delay less than 1 μs. A time-of-flight detector is potentially capable of providing submicrosecond detection time frame. The instrumental modifications necessary to implement submicrosecond detection should be explored.

Tandem mass spectrometry techniques on an ion trap/time-of-flight spectrometer can provide unique information especially for large species generated by electrospray ionization. To improve performance of the instrument in analysis of large molecules, a new ESI source was constructed at the University of Alberta. It contains an octopole guide mediating in the transport of ions into the ion trap and a turbomolecular pump that provides an improvement in vacuum quality. Field assisted aerospray ionization, instead of electrospray ionization, is used in the new source to generate ions. The new source can also be combined with liquid chromatography. The effect of these modifications will be evaluated in the future.

Appendix A

Fragmentation of peptide ions

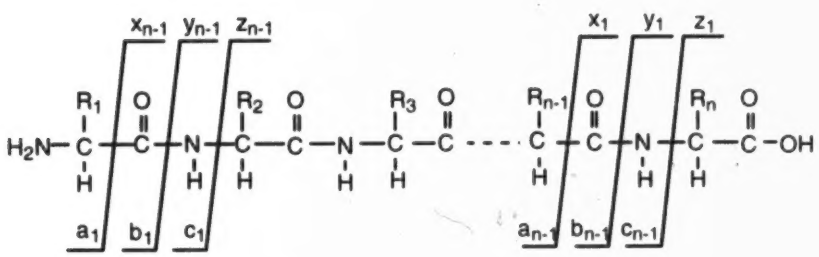

Figure A.1. Nomenclature for the backbone fragmentation of peptide ions. Subscripts refer to the amino acid position in the sequence, determined from the N-terminus (for **a**, **b**, **c** ions) or C-terminus (for **x**, **y**, **z** ions). R refers to the amino acid side chain.

In dissociation of singly charged peptides, fragmentation along the peptide backbone is often accompanied by the transfer of one or two protons for stability of formed ions. Fragments with charge retention on the N-terminus of a peptide are denoted as **a**, **b**, **c** ions, whereas fragments with charge retention on the C-terminus of a peptide are denoted as **x**, **y**, **z** ions (see Figure A.1). An internal fragment ion generated by two backbone cleavages (eg. $\mathbf{y}_{n-1}\mathbf{b}_{n-1}$) is indicated by a **y**-type fragment at position n-1 from the peptide C-terminal, and a **b**-type of fragment at position n-1 from the peptide N-terminal. Other internal fragment ions are produced from $\mathbf{y}_{n-1}\mathbf{b}_{n-1}$ after loss of carbon monoxide ($\mathbf{y}_{n-1}\mathbf{a}_{n-1}$), ammonia, or water. Immonium ions (HN=CH-R) are labeled with the single-capital letter code of the particular amino acid.

References:

[1] Roepstorff, P.; Fohlman, J. *Biomed. Mass Spectrom.* **1984**, 11, 601.

[2] Biemann, K. *Ann. Rev. Biochem.* **1992**, 61, 977.